Dielectric and lattice dynamical properties of molecular crystals via density functional perturbation theory: implementation within a first principles code

Tulip, Paul Robert

Dielectric and Lattice Dynamical Properties of Molecular Crystals via Density Functional Perturbation Theory: Implementation within a First Principles Code

Paul Robert Tulip

A thesis submitted in partial fulfilment
of the requirements for the degree of
Doctor of Philosophy

The University of Durham
Department of Physics
2004

Abstract

Organic molecular crystals form a condensed solid phase offering a rich vein of physical phenomena which are open to investigation. The desire to harness these properties for technological and biological purposes has led to extensive experimental and theoretical investigations. The naturally occurring α-amino acids form molecular crystals in the solid state; to date there have been very few studies of these systems. The work in this thesis is concerned with attempting to understand the relationship between the properties of the molecular crystal, and how these relate to the properties of the constituent molecules in isolation. To this end, density functional calculations of the structural and electronic properties of amino acids in both the crystalline and gaseous states are performed, and the results reported. The bonding mechanisms responsible for the crystal being stable are elucidated, and used to explain the zwitterionisation of the molecules upon formation of the solid state. In order to investigate the lattice dynamical and dielectric properties, the implementation of a variational density functional perturbation theory (DFPT) scheme within the plane wave pseudopotential formalism is described in detail. This scheme is fully self-consistent, and its computational cost is comparable to that of a single-point self-consistent total energy calculation. The long wave method is used to alleviate well-known problems associated with the application of homogeneous fields to crystal systems, viz. that such fields break the crystal symmetry, and the adequate treatment of electronic screening. Calculation of the first order perturbed wavefunctions and the second order change in the Kohn-Sham functional allows properties such as the polarisability, dielectric matrix, dynamical matrix and Born effective charge tensors to be determined. The treatment of crystalline symmetries is described in detail. The DFPT formalism is extended to allow IR absorption spectra to be obtained. The lattice dynamical and dielectric behaviour of the isolated molecules and the molecular crystals are obtained; calculation of the IR spectra facilitates an insight into the effects of the crystalline environment and zwitterionisation upon the lattice dynamics. Results indicate the importance of the molecular shape and structure upon the intermolecular interactions, and hence the crystal structure formed. It is these intermolecular interactions that are found to play the major part in modification of the lattice dynamical and dielectric behaviour.

Declaration

I confirm that no part of the material offered has previously been submitted by me for a degree in this or in any other University. If material has been generated through joint work, my independent contribution has been clearly indicated. In all other cases material from the work of others has been acknowledged and quotations and paraphrases suitability indicated.

P. R. Tulip
Durham, 22nd September 2004

Acknowledgements

I would like to thank all those who have made my time here at Durham so enjoyable. Thanks to the CMT group for coffee time discussions, particularly Ian Bolland (and for his help with computing too). Thanks to Stewart for his supervision, curries and single malt Scotches. I'd like to mention, in no particular order, Sean, Nik and Eleni, for being the general target of thesis-related moans, and actually listening. Fenia for labelling me a possible resident of Guantanomo Bay, Elizabeth for labelling me everything else. Thanks to Mike for many a long computer gaming session, and Sarah for her refreshing cynicism. I'd like to acknowledge Keith Refson for his help in dealing with computing issues. Thanks to Phil Inness work on the IR stuff. Finally, I'd like to thank my parents and Rachael for their support throughout.

It is a capital mistake to theorise before one has data. Insensibly one begins to twist facts to suit theories instead of theories to suit facts.

Sherlock Holmes in *A Scandal in Bohemia*, Sir Arthur Conan Doyle

Contents

List of Figures

Chapter 1

Introduction

1.1 Organic Molecular Crystals

Molecular crystals offer a rich vein of physical phenomena considerably different from the optical, electronic and mechanical properties exhibited by conventional solids such as covalent or ionic crystals. This arises partly because of the generally weak intermolecular interactions such as van der Waals and dipolar interactions [1], and partly because of the subtle interplay that may arise between inter- and intra-molecular degrees of freedom.

In recent years, molecular crystals have become the subject of intense theoretical and experimental research [2, 3, 4, 5, 6, 7, 8, 9, 10]. Much of this has centred around developing an understanding of the physics of these systems in order to harness it for technological applications such as molecular electronics [6, 11, 12, 13], and to this end, there have been concerted efforts to attempt to understand the nature of charge carriers in these systems. An area of equally intense activity is that of "crystal engineering" or super-molecular chemistry [14, 15]. This fascinating area is based upon the use of individual molecules in order to attempt to design functional molecular crystals that may be used for a variety of technological applications. The key behind this philosophy is that the crystal structure and packing formed by an array of molecules is determined to a large extent by the intermolecular interactions such as hydrogen bonds and van der Waals interactions; thus one can, given enough understanding of these interactions, manipulate them advantageously in order to

produce materials with technologically useful properties, such as non-linear optical response [14].

Molecular crystals of organic molecules are also interesting from the biological and biochemical perspective. An understanding of the hydrogen bond is essential to comprehend many important biological processes and molecules such as proteins and peptides. Molecular crystals offer an ideal test-bed in which to understand the nature of the hydrogen bond in biochemical systems in more detail.

It is possible to define a molecular crystal as a solid that is formed by electrically neutral molecules interacting via weak non-bonding interactions, primarily van der Waals. If the constituent molecules possess specific functional groups then the possibility also exists for the formation of hydrogen bonds and dipolar interactions that will also serve to stabilise the crystal. In general, there is little electronic charge overlap between molecules, and therefore the constituent molecules retain their identity to a large extent. This is in contrast to covalent or ionic solids, where the individual properties of constituent particles in the crystal are completely lost [1]. This has led to a number of studies in which the solid state environment is treated as a perturbation to a molecular calculation [9], or in which *ab initio* or experimental molecular charge densities are used in conjunction with classically derived intermolecular potentials in order to study the behaviour of molecular crystal systems [16].

Approaches such as these have the advantage of being relatively simple and computationally cheaper than attempting a full *ab initio* treatment of the molecular solid; however, considering that the molecular structure itself may change in response to the crystal environment, in addition to the actual electronic density itself, questions must arise over the validity of such treatments. Furthermore, such approaches are based upon the idea of zero overlap between molecular wavefunctions; this implicitly assumes that space may be partitioned into Wigner-Seitz-type cells associated with each molecule [9]. Such an approximation may not always be valid, and neglects quantum mechanical interactions such as the exchange repulsion. For these reasons, a full *ab initio* approach is more appealing: the crystal itself is dealt with quantum mechanically, and no assumptions need to be made about the nature of the

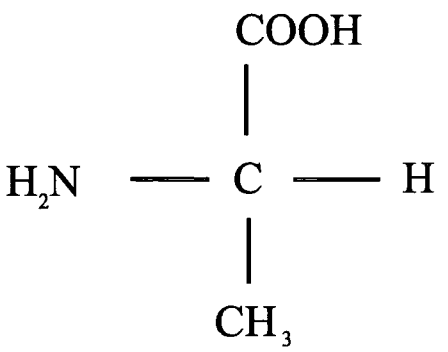

Figure 1.1: Structure of alanine: the carboxylic and amine groups are common to all amino acids. The central carbon atom is the C_α atom.

interactions or the level of molecular overlap; rather only the cell contents need be specified. This is conceptually more satisfying, and aesthetically more appealing.

The work in this thesis concerns applying density functional theory, and density functional perturbation theory, to amino acids in both the solid and gaseous states. In particular, the emphasis is on the determination of the geometric, electronic, dielectric and vibrational properties, and elucidating the effects of the crystal structure upon the molecular properties. The amino acids are the building blocks of peptides and proteins, and, given the increasing interest in the life sciences evidenced in projects such as the Human Genome Project [17], are candidates for *ab initio* calculations. A thorough understanding of their detailed physical and chemical properties as provided by *ab initio* calculations will allow a complete understanding of the biological processes that they participate in.

1.2 Amino Acids

The amino acids are characterised by possessing acidic and basic groups on the same molecule. These are a carboxylic COOH and an amine NH_2 group respectively. In the so-called α-amino acids, both functional groups are attached to the same carbon atom, the C_α. A representative structure, that of alanine, is shown in figure 1.1.

In aqueous solutions and the solid state, these molecules often form dipolar ions, or *zwitterions*, whereby the carboxylic group donates a proton to the amine group.

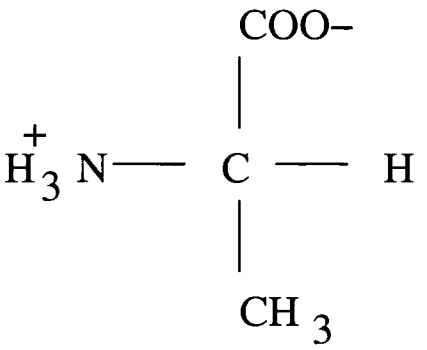

Figure 1.2: Structure of alanine: the effects of zwitterionisation. The molecule now has two oppositely charged functional groups.

This leads to two oppositely charged functional groups on the same molecule. This is shown in figure 1.2. In the gaseous phase, zwitterionisation is energetically unfavourable, but the interactions present in solution and the solid state can act as a stabilising influence.

The relevance of the amino acids lies in their biological importance; not only do they form the building blocks of peptides and proteins, all cellular tissue and fluid in living organisms contains a reservoir of free amino acids: an "amino acid pool". These take part in metabolic reactions, including the biosynthesis of polypeptides and proteins, and the synthesis of nucleotides.

The asymmetric carbon atoms present in all amino acids except for glycine leads to stereoisomerism: one may obtain optically active D- and L-amino acids, or optically inactive DL-amino acids. The majority of naturally occurring amino acids are of the L-type, for reasons that are unclear. However, the ratio of D- to L-type may alter naturally in archaeological samples via the process of racemisation; combined with the use of standard laboratory analytical techniques, this allows a method of dating samples other than C_{13} dating [18].

Further interest can be motivated from potential technological applications of bio-organic molecules [19] such as the proposed use of DNA for creating electronic circuits [20] and the development of light-emitting organic polymers [21]. The importance of amino acids to the pharmaceutical industry and their useage in drug synthesis [18], coupled with the prospect of drug design from first principles, also provides a powerful motivation.

A more unexpected and perhaps quixotic motivation for examining the amino acids is in understanding the origins of life, and the possibilities of extra-terrestrial life, which may be aided by examining cool interstellar space for signs of biomolecules [22, 23]. Traces of amino acids have been found on meteorites, whilst both glycine and alanine have been detected in lunar samples. Providing a satisfactory explanation for their presence requires a comprehensive knowledge of amino acid chemistry; *ab initio* techniques can serve as a useful companion to experimental approaches in such an endeavour.

A complete understanding of the role of amino acids in these important processes requires a thorough understanding of the underlying biochemistry, and consequently, a full and adequate treatment of the quantum mechanics underpinning this biochemistry is required. They are thus ideal candidates for the application of *ab initio* methods.

In light of the above, it is no surprise that a comprehensive body of *ab initio* work on amino acids already exists [22, 24, 25, 26, 27]. However, the majority of this work has concerned conformational analyses of a limited subset of the 20 naturally occurring α-amino acids, in particular alanine and glycine. Numerous works also exist in which *ab initio* methodologies have been combined with Onsager models [28, 29] in order to model the behaviour of amino acids in solution. Very little work has been carried out on determining the normal modes and dielectric behaviour. It is possible that this is due to the fact that the majority of work has been carried out using quantum chemical techniques such as restricted Hartree-Fock (RHF), methods which are not ideally suited to the study of large and complicated molecules. Less work exists concerning amino acids in the solid state, where they typically form molecular crystals. Indeed, this aspect has attracted surprisingly little interest from theorists, the only work in the literature appearing to concern the shielding tensors of carbon-13 [30, 31].

1.3 The Hydrogen Bond in Organic Molecules

Given the central role played by the hydrogen bond in the chemistry and biochemistry of amino acids it is useful at this point to consider what a hydrogen bond is, how they arise, and why they are so significant. The hydrogen bond is an ubiquitous presence in structural chemistry and biology. Hydrogen bonds span a wide spectrum of energies, and lie intermediate in strength between covalent and van der Waals interactions. It is this that accounts for their importance in biological reactions, permitting hydrogen bonds to associate and dissociate rapidly at ambient temperatures, which is a vital prerequisite for biological reactions to take place.

The definition of what constitutes a hydrogen bond is currently controversial [32, 33]. The earliest definition is that due to Pauling, in his *Nature of the Chemical Bond*: "Under certain conditions an atom of hydrogen is attracted by rather strong forces to two atoms instead of only one, so that it may be considered to be acting as a bond between them. This is called a hydrogen bond". In this view, the nature of the bond is largely ionic, or electrostatic. Such a definition would, however, seem to restrict hydrogen bonding to interactions of the form X-H A, where X and A may be any of the following: F, O, Cl, N, Br and I. This therefore excludes functional groups such as C-H, P-H, and X-H amongst others [32]. A more open definition is that due to Pimentel and McClellan (1960): *A hydrogen bond is said to exist when (1) there is evidence of a bond, and (2) there is evidence that this bond sterically involves a hydrogen atom already bonded to another atom.* This makes no assumptions about the character of the the donor and acceptor groups, but is sufficiently open that it leaves open the possibility of any X-H group being a potential hydrogen bond donor [32]. Perhaps a more useful refinement is that of Steiner and Saenger [34], where a hydrogen bond is defined as: "any cohesive interaction X-H A where H carries a positive and A a negative (partial or full charge) and the charge on X is more negative than on H". This definition, although focusing only upon the electrostatic aspects of the hydrogen bond, and hence restrictive with respect to weak hydrogen bonds, is sufficient for the types of hydrogen bonds that will be encountered in this work.

1.3.1 Theoretical Treatment

Although Pauling's original work envisaged the hydrogen bond as being largely explicable in terms of electronegativities and pure electrostatics, this interpretation is unsatisfactory for many bonds, as has been pointed out by Coulson [35]. It is possible to decompose the potential energy for hydrogen bonded dimers following the method of Morokuma [36], with contributions from electrostatics, polarisation, exchange-repulsion, charge-transfer, and coupling terms, which reflects the fact that none of the other contributions is truly independent of the others. Although such a decomposition is largely artificial, it is useful from a conceptual point of view. Strong hydrogen bonds are largely electrostatic in nature, that is, the interaction may be represented as multipole-multipole interactions of undisturbed charge densities; weaker interactions, on the other hand, tend to have a more quantum mechanical nature. The weakest bonds consist mainly of van der Waals type interactions, and may be difficult to separate from this type of interaction. It should also be noted that the only repulsive component is the exchange component, which hence balances the attractive forces caused by the other contributions.

1.3.2 Structural Definitions

In order to discuss in more detail the nature of the hydrogen bonding present in molecular crystals, it is necessary to be able to characterise the common structural features found. A general hydrogen bond is comprised of a donor group X-H and an acceptor A, and is referred to as X-H A. The hydrogen bond is a long-range interaction, and thus the possibility exists for a donor group to be bonded to more than one acceptor at a time [32]. This is called a *bifurcated* bond. In figures 1.3 and 1.4 an example of a bifurcated donor and a bifurcated acceptor are shown. A further possibility is that of a *chelated* bond; examples of chelated bonds are shown in figure 1.5.

Bifurcated acceptors and donors may arise in systems in which there is an excess of donors (acceptors) relative to the number of acceptors (donors) present. In systems in which weak hydrogen bonds are capable of forming, this leads to bifurcated donors being common [32].

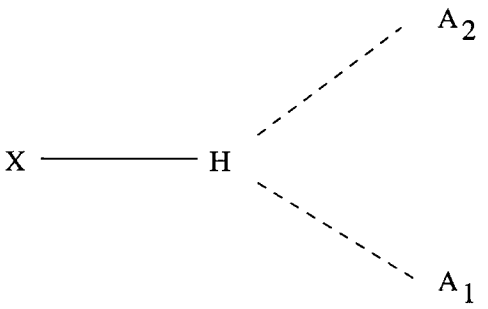

Figure 1.3: Bifurcated hydrogen bond: an example of a bifurcated donor.

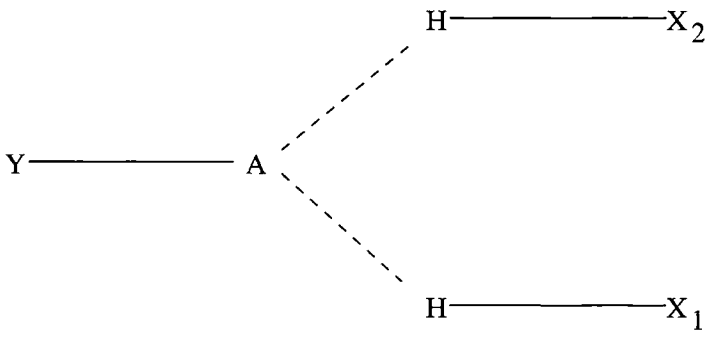

Figure 1.4: Bifurcated hydrogen bond: an example of a bifurcated acceptor.In both of these diagrams, solid lines denote chemical bonds, whilst dashed lines denote a hydrogen bond.

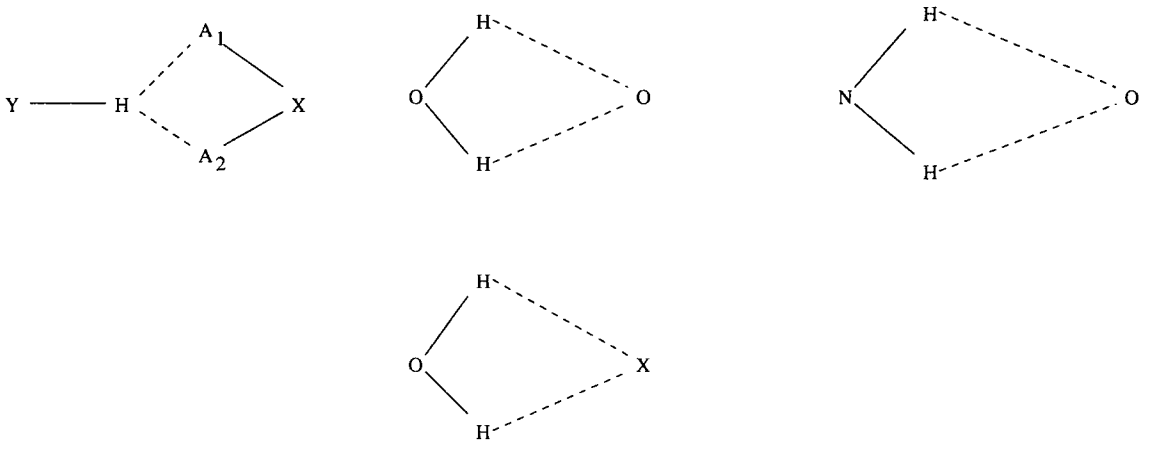

Figure 1.5: Examples of chelated bonds.

1.3.3 Hydrogen Bonds as Group-Pair Interactions

It should be stressed at this stage that the term *hydrogen bond* refers to the group of three atoms involved, X, H and A. In most bonds, the chemical bond X-H is much stronger than the bond H A; however, it is not correct to term the latter as the hydrogen bond. This is because the two entities involved are *not* independent of each other; hydrogen bonds are group-pair interactions, not atom-pair interactions [32]. Similarly, in the case of bifurcated hydrogen bonds, the term hydrogen bond refers to X, H, A_1 and A_2.

1.4 Computational Physics: Empirical versus *ab initio* Methods

In order to investigate theoretically systems as complicated as molecular crystals, it is necessary to model the interactions (of which there may be a hierarchy spread across several energy scales) as accurately as possible, whilst ensuring that the calculations remain computationally feasible. The simplest and crudest approaches to this problem rely upon the useage of empirical potentials; that is potentials which are obtained by fitting to various experimentally obtained properties, such as the lattice constant and bulk modulus. However, although empirical potentials can be of use, they are limited by the accuracy of the parametrisation, and correspondingly, their transferability to other environments can be poor. Further, empirical potentials optimised to accurately obtain quantities such as the lattice parameter accurately, may be inadequate for other properties such as lattice dynamical properties, for which they were not designed, leading to further problems of transferability.

In order to derive an empirical potential, it is usual for some assumption to be made concerning the electronic structure of the system under consideration and the bonding mechanisms present. Modelling interactions with no *a priori* knowledge of the bonding present requires the use of sophisticated *ab initio* methodologies, in which one attempts to solve the Schrödinger equation governing the electronic dynamics. The methodology of choice for such calculations is the density functional theory (DFT); this method is described fully in the next chapter. The *ab initio* approach,

although more computationally intensive, does possess the advantage of being completely transferable, requiring only that the atomic constituents of the system under consideration be specified. It is thus more intellectually appealing, but moreover, this ensures that it may be used to calculate the properties of systems about which no *a priori* knowledge exists. By solving the electronic structure of the system, a deeper understanding of the system's behaviour may be gleaned; furthermore, a knowledge of the electronic structure then allows a range of properties from equilibrium geometries to thermodynamic properties and equations of state to be obtained without recourse to experimental input. One may also use the output of high quality *ab initio* calculations to parametrise classical potentials allowing the computational restrictions associated with *ab initio* methods to be circumvented. It is for these reasons that in this work an *ab initio* approach is preferred to an empirical one.

1.5 Outline of Thesis

This thesis is concerned with the application of density functional perturbation theory calculations to the amino acid molecular crystals alanine, isoleucine, leucine and valine. In order to elucidate the connections between the behaviour of the solid and the constituent molecules, calculations are also carried out on isolated molecules. The first part of the thesis discusses the theoretical techniques used in this work, whilst the second part presents the results.

The work described in this thesis is organised as follows:

Chapter 2

The many-body problem in quantum mechanics is introduced. Single-particle self-consistent field methods (Hartree and Hartree-Fock) are discussed as approximations to the many-body Schrödinger equation. The Hohenberg-Kohn-Sham formulation of density functional theory is introduced, and its implementation within the plane wave pseudopotential formalism discussed. Practical methods of solving the resulting Kohn-Sham equations within the electronic structure code CASTEP are also discussed in detail.

Chapter 3

The motivations for developing a perturbative treatment of DFT are described. A Green's function based method is described, before considering in detail the effects of applying perturbation theory within a variational framework. The resulting $2n+1$-theorem is discussed along with its utility within DFT. The connections between the Green's function method and the $2n+1$-theorem are explicitly discussed. The treatment of lattice dynamics and electric field response is discussed in detail. The macroscopic electric fields set up by long-wave longitudinal phonons in polar materials are also considered, and the correct way to treat this phenomenon is discussed. DFPT offers a natural method for the calculation of IR spectra; accordingly, the basic theory is outlined.

Chapter 4

The implementation of the DFPT scheme outlined in the previous chapter is considered in detail. Particular regard is paid to the treatment of pseudopotentials and exchange and correlation. The conjugate gradients minimisation scheme used is discussed, and the merits of different preconditioning schemes are investigated using simple test systems. Sum rules are introduced as a means of checking the quality of a calculation. The use of symmetry with regard both to Brillouin zone sampling and as a means to calculate symmetry-related elements of the dynamical matrix and permittivity is described in detail. Finally, a series of validation tests is carried out on a series of test systems in order to illustrate the efficacy of the method. Comparison with theoretical and experimental values in the literature shows good agreement. Calculations of IR spectra for a series of molecules reveals that the intensities display a sensitivity to choice of basis set; however, irrespective of basis set, the correct IR-active modes are identified.

Chapter 5

In this chapter the results of calculations determining the structural and electronic properties of amino acids in both the gaseous and solid states are presented. The

similarities and differences exhibited in the geometric structures are discussed, and underlying explanations sought in terms of the electronic structures. It is found that all of the systems under consideration, with the exception of leucine, are found in the non-zwitterionic form in the gaseous phase. All are found as zwitterions in the solid state. A discussion of the reasons for this zwitterionisation in terms of the localisation of the molecular orbitals is presented. The nature of the hydrogen bonds responsible for crystal stabilisation is discussed; extremely good agreement with experimental structures is found, suggesting a largely electrostatic nature for the hydrogen bonds. The differences in geometric and electronic structure exhibited upon crystal formation are investigated and discussed.

Chapter 6

A series of density functional perturbation calculations determining the vibrational and dielectric properties of amino acids is presented. Calculations are carried out both for the solid state and isolated molecules. For the isolated molecules, the molecular polarisabilities, as determined by density functional perturbation theory, are found to be in good agreement with finite difference calculations. Examination of the first order density response to the applied field allows similarities between the different molecules to be found. This indicates that the response is largely determined by the molecular geometry rather than simply the functional groups present. Determination of the normal modes allows the intra-molecular hydrogen bonds to be investigated, and indicates that the reasons for the zwitterionisation of leucine in the gaseous state is due to the possibility of stabilising hydrogen bonds being formed. IR spectra are calculated. Clear differences, due to the different bonds, are found between the zwitterionic and non-zwitterionic cases. The use of dynamical effective charges as a population analysis tool is investigated by comparing with the results of a Mulliken population analysis. This reveals that the Mulliken charges are insensitive to changes in the electronic structure caused by zwitterionisation, in contrast to the dynamical charges. Determination of the normal modes of the molecular crystals reveals that the high frequency vibronic modes undergo the largest modification in frequency, due to the hydrogen bonding present. Low frequency vibronic modes are largely unaffected. The conformational freedom exhibited by molecules with

long sidechains ensures that the low frequency vibrons are close in frequency to the lattice modes. The character of the lattice modes depends upon the system under consideration. The Born effective charges are calculated, and found to alter appreciably between the molecule and the crystal. Mode effective charge three-vectors are calculated in order to identify which modes are responsible for these modifications. The dielectric properties are calculated; examination of first-order electron charge densities allows the effects of the crystalline environment upon the molecular responses to be investigated. These are determined largely by molecular geometry and the character of the intermolecular interactions present.

Chapter 7

In this chapter, conclusions are presented, along with suggestions for further work and investigations.

Chapter 2

The Many Body Problem and Density Functional Theory

The underlying physical laws necessary for the mathematical theory of a large part of physics and the whole of chemistry are thus completely known, and the difficulty lies only in the fact that the exact application of these laws leads to equations much too complicated to be soluble - P. A. M. Dirac

In principle, the properties of a system may be obtained by solving the quantum mechanical wave equation governing the system dynamics. For non-relativistic systems this is simply the Schrödinger equation. As alluded to in the quotation above, this is in practice an impossible task; indeed, the resulting many-body problem has only been solved for a limited number of test systems. In this chapter we outline the many-body problem and why it is intractable, before considering the Hohenberg-Kohn-Sham formulation of density functional theory (DFT) [37, 38]; this reformulates quantum mechanics, using the electron density as its fundamental parameter, rather than the many-electron wavefunction. This takes the N-body problem and instead recasts it as N single-body problems, which is a dramatic simplification. Finally, we briefly consider the methods used to solve this problem. The interested reader may find fuller descriptions in the references [39, 40].

2.1 The Many-Body Problem

The dynamics of a time-independent non-relativistic system are governed by the Schrödinger equation

$$H\Psi = E\Psi \tag{2.1}$$

where Ψ is the many electron wavefunction, E is the system energy and H is the Hamiltonian of the system given by (in atomic units)

$$H = \sum_{i=1}^{N} \Big(-\frac{\hbar^2}{2m}\nabla_i^2 - Ze^2 \sum_R \frac{1}{|\mathbf{r}_i - \mathbf{R}|} \Big) + \frac{1}{2}\sum_{i \neq j} \frac{e^2}{|\mathbf{r}_i - \mathbf{r}_j|}. \tag{2.2}$$

Here $\mathbf{r}_i$ is the position of electron i, whilst the nuclei are clamped at positions $\mathbf{R}$. The first term is the many-body kinetic energy operator which yields the electronic kinetic energies; the second term represents the interaction of the electrons with the bare nuclei. Electron-electron interactions are described by the final term. We have neglected the nuclei-nuclei interaction energy in the above, which would of course have to be added in order to yield the *total* energy of the system. However, the Born-Oppenheimer approximation [41] allows us to decouple the nuclear and electronic degrees of motion; the nuclei are of order $\sim 10^3 - 10^5$ times more massive than the electrons, and therefore may be considered to be stationary on the electronic timescale. As a result of this, it is possible to neglect the nuclear kinetic energy contribution to the system energy.

Although this equation is exact within the non-relativistic regime, it is not possible, except for trivially simple cases, to solve it. There are two reasons for this: one mole of a solid contains $N \sim 10^{28}$ electrons; since the many-electron wavefunction contains $3N$ degrees of freedom, this is simply intractable; further, the electron-electron Coulomb interaction results in the electronic motions being correlated. Consequently the many-body wavefunction is a complicated mathematical object that incorporates the effects of this correlation, preventing a separation of the electronic degrees of freedom into N single-body problems. Further, the interaction is too strong to be treated as a perturbation. Thus we must search for approximations that render the

Schrödinger equation tractable to numerical solution, whilst retaining as much of the key physics as is possible.

2.1.1 Approximate Methods: the Hartree and Hartree-Fock Methods

The simplest approximation is the Hartree approximation [42]. The initial *ansatz* is that we may write the many-body wavefunction as

$$\Psi(\mathbf{r}_1, \mathbf{r}_2, \ldots, \mathbf{r}_N) = \psi_1(\mathbf{r}_1)\psi_2(\mathbf{r}_2)\ldots\psi_N(\mathbf{r}_N) \tag{2.3}$$

from which it follows that the electrons are *independent*, and interact only via the mean-field Coulomb potential. This yields one-electron Schrödinger equations of the form

$$-\frac{\hbar^2}{2m}\nabla^2\psi_i(\mathbf{r}) + V(\mathbf{r})\psi_i(\mathbf{r}) = \epsilon_i\psi_i(\mathbf{r}) \tag{2.4}$$

where $V(\mathbf{r})$ is the potential in which the electron moves; this includes both the nuclear-electron interaction

$$V_{nucleus}(\mathbf{r}) = -Ze^2\sum_R \frac{1}{|\mathbf{r}-\mathbf{R}|} \tag{2.5}$$

and the mean field arising from the $N-1$ other electrons. We smear the other electrons out into a smooth negative charge density $\rho(\mathbf{r}')$ leading to a potential of the form

$$V_{electron}(\mathbf{r}) = -e\int d\mathbf{r}'\rho(\mathbf{r}')\frac{1}{|\mathbf{r}-\mathbf{r}'|} \tag{2.6}$$

where $\rho(\mathbf{r}) = \sum_i |\psi(\mathbf{r})|^2$.

Although these *Hartree* equations are numerically tractable via the self-consistent field method, it is unsurprising that such a crude approximation fails to capture elements of the essential physics. The Pauli exclusion principle demands that the

many-body wavefunction be antisymmetric with respect to interchange of *any* two electron coordinates, *e.g.*

$$\Psi(\mathbf{r}_1, \mathbf{r}_2, \ldots, \mathbf{r}_N) = -\Psi(\mathbf{r}_2, \mathbf{r}_1, \ldots, \mathbf{r}_N) \tag{2.7}$$

which clearly cannot be satisfied by a non-trivial wavefunction of the form 2.3. This *exchange* condition can be satisfied by forming a Slater determinant [43] of single-particle orbitals

$$\Psi(\mathbf{r}_1, \mathbf{r}_2, \ldots, \mathbf{r}_N) = \frac{1}{\sqrt{N}} \mathcal{A} \left| \psi(\mathbf{r}_1)\psi(\mathbf{r}_2)\ldots\psi(\mathbf{r}_N) \right| \tag{2.8}$$

where $\mathcal{A}$ is an anti-symmetrising operator; *i.e.* it ensures that all possible anti-symmetric combinations of orbitals are taken. Again, this decouples the electrons, leading to the single-particle *Hartree-Fock* equations [44] of the form

$$-\frac{\hbar^2}{2m}\nabla^2\psi_i(\mathbf{r}) + V_{nucleus}(\mathbf{r})\psi_i(\mathbf{r}) + V_{electron}(\mathbf{r})\psi_i(\mathbf{r}) - \sum_j \int d\mathbf{r}' \frac{\psi_j^\star(\mathbf{r}')\psi_i^\star(\mathbf{r}')\psi_j(\mathbf{r})}{|\mathbf{r}-\mathbf{r}'|} = \epsilon_i\psi_i(\mathbf{r}). \tag{2.9}$$

The last term on the left-hand side is the *exchange* term; this looks similar to the direct Coulomb term, but for the exchanged indices. It is a manifestation of the Pauli exclusion principle, and acts so as to separate electrons of the same spin; the consequent depletion of the charge density in the immediate vicinity of a given electron due to this effect is called the *exchange hole.* The exchange term adds considerably to the complexity of these equations.

The Hartree-Fock equations deal with exchange exactly; however, the equations neglect more detailed correlations due to many-body interactions. The effects of electronic correlations are not negligible; indeed the failure of Hartree-Fock theory to successfully incorporate correlation leads to one of its most celebrated failures: its prediction that jellium is an insulating rather than a metallic system. The requirement for a computationally practicable scheme that successfully incorporates

the effects of both exchange and correlation leads us to consider the conceptually disarmingly simple and elegant density functional theory.

2.2 Density Functional Theory

The density functional theory (DFT) treats the electron density as the central variable rather than the many-body wavefunction. This conceptual difference leads to a remarkable reduction in difficulty: the density is a function of three variables, *i.e.* the three Cartesian directions, rather than $3N$ variables as the full many-body wavefunction is. An early density functional theory was proposed by Thomas and Fermi [45]. This took the kinetic energy to be a functional of the electron density, but in common with the Hartree and Hartree-Fock methods, only incorporated electron-electron interactions via a mean field potential: as such it neglected *both* exchange and correlation; a subsequent proposal by Dirac [46], formulating an expression for the exchange energy in terms of the electron density failed to significantly improve the method. Here we consider the Hohenberg-Kohn-Sham formulation of DFT; this technique is one of the choice state-of-the-art methods routinely applied in electronic structure theory, and has enjoyed success in fields ranging from quantum chemistry and condensed matter physics to geophysics. It is based upon the following remarkable and deceptively simple theorems:

- Theorem 1. *The external potential is a unique functional of the electron density only. Thus the Hamiltonian, and hence all ground state properties, are determined solely by the electron density.*

The many-body Hamiltonian H fixes the groundstate of the system under consideration, *i.e.* it determines the groundstate many-body wavefunction Ψ, and thus the above theorem ensures that this itself is also a unique functional of the groundstate density. Consequently, the kinetic and electron-electron interaction energies will also be functionals of $n(\mathbf{r})$. One may therefore define the functional $F[n(\mathbf{r})]$

$$F[n(\mathbf{r})] = \langle \Psi | (T + V_{ee}) | \Psi \rangle \tag{2.10}$$

where T is the kinetic energy operator, and V_{ee} is the electron-electron interaction operator. This functional F is a universal functional in the sense that it has the same dependence on the electron density for *any* system, independent of the external potential concerned. The exact density dependence of this functional is, however, unknown.

Using this functional, one may then define, for a given external potential $v(\mathbf{r})$, the energy functional

$$E[n(\mathbf{r})] = \int d\mathbf{r} n(\mathbf{r}) v(\mathbf{r}) + F[n(\mathbf{r})] \tag{2.11}$$

where $F[n(\mathbf{r})]$ is a universal but unknown functional of the electron density. We can write the system energy (for a non-degenerate groundstate) in terms of the groundstate many-body wavefunction Ψ as

$$E[n(\mathbf{r})] = \langle \Psi | H | \Psi \rangle \tag{2.12}$$

with the Hamiltonian given by

$$H = F + V \tag{2.13}$$

where V is the operator corresponding to the external potential, and F is the electronic Hamiltonian

$$F = T + V_{ee}. \tag{2.14}$$

- *Proof:* We proceed by *reductio ad absurdum.* Assume that there are two potentials $v_1(\mathbf{r})$ and $v_2(\mathbf{r})$ that differ by more than an additive constant and further that these two potentials lead to different ground state wavefunctions $\Psi_1(\mathbf{r})$ and $\Psi_2(\mathbf{r})$. Now assume that these both lead to the same ground state density, $n(\mathbf{r})$. The variational principle then asserts that

$$\begin{aligned} E_1 \leq \langle \Psi_2 | H_1 | \Psi_2 \rangle &= \langle \Psi_2 | H_2 | \Psi_2 \rangle + \langle \Psi_2 | H_1 - H_2 | \Psi_2 \rangle \\ &= E_2 + \int n(\mathbf{r}) [v_1(\mathbf{r}) - v_2(\mathbf{r})] \, d\mathbf{r} \end{aligned} \tag{2.15}$$

Note that this inequality applies only to the groundstate and that DFT, as a result, is only rigorously applicable to the groundstate. Interchanging 1 and 2 gives a similar expression, and adding the two inequalities leads to the contradiction

$$E_1 + E_2 \leq E_1 + E_2. \tag{2.16}$$

Thus theorem 1 is proved.

- Theorem 2. *The groundstate energy may be obtained variationally: the density that minimises the total energy is the exact groundstate density.*

- *Proof.* To prove this theorem we introduce the notion of "N-representability": *i.e.* a density is said to be N-representable if it may be obtained from some antisymmetric wavefunction $\psi(\mathbf{r}_1, \mathbf{r}_2, \ldots, \mathbf{r}_N)$ for which we may define the functional [47]

$$F[n] = \min_{\psi \to n} \langle \psi | T + V_{ee} | \psi \rangle \tag{2.17}$$

where the minimum is taken over all ψ that yield the density n. Now, if we introduce $\psi^n_{min}(\mathbf{r})$ for a wavefunction that minimises 2.17 such that

$$F[n] = \langle \psi^n_{min} | T + V | \psi^n_{min} \rangle \tag{2.18}$$

then

$$\begin{aligned} \int V_{ext}(\mathbf{r}) n(\mathbf{r}) d\mathbf{r} + F[n] &= \langle \psi^n_{min} | V + T + V_{ee} | \psi^n_{min} \rangle \\ &\geq E_{GS} \end{aligned} \tag{2.19}$$

with equality at the minimum. Thus the second theorem is proved.

Although these two theorems prove the existence of a universal functional, they do not give any idea as to the nature of the functional, or how to actually calculate the

groundstate density. In order to do so, we must discuss the Kohn-Sham formulation [38]. This is based upon a sleight of hand whereby we map the fully interacting system of N-electrons onto a fictitious auxiliary system of N non-interacting electrons moving within an effective Kohn-Sham potential, $v_{KS}(\mathbf{r})$, thereby coupling the electrons. The single-particle Kohn-Sham orbitals are constrained to yield the same groundstate density as that of the fully-interacting system, so the Hohenberg-Kohn-Sham theorems are still valid.

Variation of the total energy functional in 2.11 with respect to the electron density, subject to the constraint of fixed particle number, *i.e.*

$$\int \delta n(\mathbf{r}) d\mathbf{r} = 0 \tag{2.20}$$

yields

$$\delta\Big[F\left[n(\mathbf{r})\right] + \int v_{ext}(\mathbf{r}) n(\mathbf{r}) d\mathbf{r} - \mu\Big(\int n(\mathbf{r}) d\mathbf{r} - N\Big)\Big] = 0 \tag{2.21}$$

where μ is a Lagrange multiplier associated with our constraint condition 2.20. The Euler-Lagrange equation associated with minimisation of this functional is then

$$\mu = \frac{\delta F\left[n(\mathbf{r})\right]}{\delta n(\mathbf{r})} + v_{ext}(\mathbf{r}). \tag{2.22}$$

The Kohn-Sham formulation allows us to write the universal functional $F\left[n(\mathbf{r})\right]$ as

$$F\left[n(\mathbf{r})\right] = T_s\left[n(\mathbf{r})\right] = E_H\left[n(\mathbf{r})\right] + E_{xc}\left[n(\mathbf{r})\right] \tag{2.23}$$

where the last term is the *exchange-correlation* energy, to which we will return presently, and $T_s\left[n(\mathbf{r})\right]$ is the kinetic energy, which may be written in terms of the *non-interacting* single-particle orbitals as

$$T_s\left[n(\mathbf{r})\right] = -\frac{1}{2}\sum_{i=1}^{N} \int \psi_i^{\star}(\mathbf{r}) \nabla^2 \psi_i(\mathbf{r}) d\mathbf{r}. \tag{2.24}$$

It is important to note that this is the kinetic energy of the auxiliary non-interacting system, *not* the kinetic energy of the actual physical system under consideration. $E_H[n(\mathbf{r})]$ is the classical Hartree energy of the electrons

$$E_H[n(\mathbf{r})] = \frac{1}{2}\int\int \frac{n(\mathbf{r})n(\mathbf{r}')}{|\mathbf{r}-\mathbf{r}'|}d\mathbf{r}d\mathbf{r}' \tag{2.25}$$

which includes a self-interaction term.

Thus the Euler-Lagrange equation 2.21 becomes

$$\mu = \frac{\delta T_s[n(\mathbf{r})]}{\delta n(\mathbf{r})} + v_{KS}(\mathbf{r}) \tag{2.26}$$

where $v_{KS}(\mathbf{r})$ is the effective Kohn-Sham potential

$$v_{KS}(\mathbf{r}) = v_{ext}(\mathbf{r}) + v_H(\mathbf{r}) + v_{xc}(\mathbf{r}). \tag{2.27}$$

The Hartree potential $v_H(\mathbf{r})$ is given by

$$v_H(\mathbf{r}) = \frac{\delta E_H[n(\mathbf{r})]}{\delta n(\mathbf{r})} = \int \frac{n(\mathbf{r}')}{|\mathbf{r}-\mathbf{r}'|}d\mathbf{r}' \tag{2.28}$$

with the exchange-correlation potential $v_{xc}(\mathbf{r})$

$$v_{xc}(\mathbf{r}) = \frac{\delta E_{xc}[n(\mathbf{r})]}{\delta n(\mathbf{r})}. \tag{2.29}$$

The Euler-Lagrange equation is now of exactly the same form as that which leads to the Hartree equations 2.4. Therefore we are required to solve the Schrödinger-type equations

$$\Big(-\frac{1}{2}\nabla^2 + v_{KS}(\mathbf{r})\Big)\psi_i(\mathbf{r}) = \epsilon_i\psi_i(\mathbf{r}) \tag{2.30}$$

where the ϵ_i correspond to the eigenvalues of the single-particle states and the charge density $n(\mathbf{r})$ is constructed from the Kohn-Sham orbitals as

$$n(\mathbf{r}) = \sum_{i=1}^{N} \psi_i^\star(\mathbf{r})\psi_i(\mathbf{r}). \tag{2.31}$$

Similarly, the many-electron wavefunction of the system may be constructed as a Slater determinant of the Kohn-Sham orbitals.

The Kohn-Sham formulation thus succeeds in transforming the N-body problem into N single-body problems, each coupled via the Kohn-Sham effective potential. It is worth noting that formally there is no physical interpretation of these single-particle Kohn-Sham eigenvalues and orbitals: they are merely mathematical artefacts that facilitate the determination of the true groundstate density. The exception is the highest occupied state, for which it can be shown that [47] the eigenvalue corresponding to the highest occupied state yields the ionisation energy of the system.

2.3 The Exchange-Correlation Term

The Kohn-Sham equations in 2.30 are thus far exact: no approximations have yet been made; we have simply mapped the fully interacting system onto an auxiliary non-interacting system that yields the same groundstate density.

As mentioned earlier, the Kohn-Sham kinetic energy is not the *true* kinetic energy; we may use this to define formally the exchange-correlation energy as

$$E_{xc}\left[n(\mathbf{r})\right] = T\left[n(\mathbf{r})\right] - T_s\left[n(\mathbf{r})\right] + E_{ee}\left[n(\mathbf{r})\right] - E_H\left[n(\mathbf{r})\right] \tag{2.32}$$

where $T_s\left[n(\mathbf{r})\right]$ and $E_{ee}\left[n(\mathbf{r})\right]$ are the exact kinetic and electron-electron interaction energies respectively. Physically, this term can be interpreted as containing the contributions of detailed correlation and exchange to the system energy. The definition above is such that it *ensures* that the Kohn-Sham formulation is exact. However, the actual form of E_{xc} is not known; thus we must introduce approximate functionals based upon the electron density to describe this term. There are two common approximations (in various forms) in use: the local density approximation (LDA) [47], and the generalised gradient approximation (GGA) [48]. The simplest approximation is the LDA: this assumes that the exchange-correlation energy at a point $\mathbf{r}$ is simply equal to the exchange-correlation energy of a *uniform electron gas*

that has the same density at the point **r**. Thus we can write

$$E_{xc}[n(\mathbf{r})] = \int \epsilon_{xc}(\mathbf{r})n(\mathbf{r})d\mathbf{r} \tag{2.33}$$

so that the exchange-correlation potential v_{xc} may be written

$$v_{xc}(\mathbf{r}) = \frac{\delta E_{xc}[n(\mathbf{r})]}{\delta n(\mathbf{r})} = \frac{\partial [n(\mathbf{r})\epsilon_{xc}(\mathbf{r})]}{\partial n(\mathbf{r})} \tag{2.34}$$

with

$$\epsilon_{xc}(\mathbf{r}) = \epsilon_{xc}^{hom}[n(\mathbf{r})] \tag{2.35}$$

where in the last equation the assumption is that the exchange-correlation energy is purely local. The most common parametrisation in use for ϵ_{xc}^{hom} is that of Perdew and Zunger [49], which is based upon the quantum Monte Carlo calculations of Ceperley and Alder [50] on homogeneous electron gases at various densities; the parametrisations provide interpolation formulae linking these results.

The LDA ignores corrections to the exchange-correlation energy due to inhomogeneities in the electron density about **r**. It may seem surprising that this is as successful as it is given the severe nature of the approximation in use; to large extent, it appears [40] that this is due to the fact that the LDA respects the sum rule, that is, that exactly one electron is excluded from the immediate vicinity of a given electron at point **r**. The LDA is known to overbind, particularly in molecules. It is for this reason that in this study we have neglected it in favour of the GGA.

The GGA attempts to incorporate the effects of inhomogeneities by including the gradient of the electron density; as such it is a semi-local method. The GGA XC functional can be written as

$$E_{xc}^{GGA}[n(\mathbf{r})] = \int n(\mathbf{r})\epsilon_{xc}^{hom}[n(\mathbf{r})]F_{xc}[n(\mathbf{r}), \nabla n(\mathbf{r})]d\mathbf{r} \tag{2.36}$$

where $F_{xc}[n(\mathbf{r}), \nabla n(\mathbf{r})]$ is known as the enhancement factor. Unlike the LDA, there is no unique form for the GGA, and indeed many possible variations are possible [48, 52, 53, 54], each corresponding to a different enhancement factor. The GGA succeeds in reducing the effects of LDA overbinding [51], and is significantly more successful when applied to molecules. In this work, the PW91 GGA due to Perdew and Wang is used [48].

2.4 Bloch's Theorem

Thus far, the quantum mechanical approaches to solving the many-body problem have been discussed. However, the correlated nature of the electrons within a solid is not the only obstacle to solving the Schrödinger equation for a condensed matter system: for solids, one must also bear in mind the effectively infinite number of electrons within the solid.

One may appeal to Bloch's theorem in order to make headway in obviating this latter problem. Instead of being required to consider an infinite number of electrons, it is only necessary to consider the number of electrons within the unit cell (or half of this number if the electrons are spin degenerate).

Bloch's theorem [55] states that the wavefunction of an electron within a perfectly periodic potential may be written as

$$\psi_{j,\mathbf{k}}(\mathbf{r}) = u_j(\mathbf{r})e^{i\mathbf{k}\cdot\mathbf{r}} \tag{2.37}$$

where $u_i(\mathbf{r})$ is a function that possesses the periodicity of the potential, *i.e.* $u_i(\mathbf{r} + \mathbf{l}) = u_i(\mathbf{r})$, where $\mathbf{l}$ is the length of the unit cell. In 2.37 i is the band index, and $\mathbf{k}$ is a wavevector confined to the first Brillouin Zone. Since $u_i(\mathbf{r})$ is a periodic function, we may expand it in terms of a Fourier series:

$$u_j(\mathbf{r}) = \sum_{\mathbf{G}} c_{j,\mathbf{G}} e^{i\mathbf{G}\cdot\mathbf{r}} \tag{2.38}$$

where the $\mathbf{G}$ are reciprocal lattice vectors defined through $\mathbf{G} \cdot \mathbf{R} = 2\pi m$, where m is an integer, $\mathbf{R}$ is a real space lattice vector and the $c_{i,\mathbf{G}}$ are plane wave expan-

sion coefficients. The electron wavefunctions may therefore be written as a linear combination of plane waves:

$$\psi_{j,\mathbf{k}}(\mathbf{r}) = \sum_{\mathbf{G}} c_{j,\mathbf{k}+\mathbf{G}} e^{i(\mathbf{k}+\mathbf{G})\cdot\mathbf{r}}. \tag{2.39}$$

Given that each electron occupies a state of definite $\mathbf{k}$, the infinite number of electrons within the solid gives rise to an infinite number of k-points. At each k-point, only a finite number of the available energy levels will be occupied. Thus one only needs to consider a finite number of electrons at an infinite number of k-points. This may seem to be replacing one infinity (number of electrons) with another one (number of k-points) to little discernible advantage. However, one does not need to consider all of these k-points; rather, since the electron wavefunctions will be almost identical for values of $\mathbf{k}$ that are sufficiently close, one can represent the wavefunctions over a region of reciprocal space by considering the wavefunction at a single k-point. It is therefore sufficient to consider the electronic states at a finite number of k-points in order to determine the groundstate density of the solid. The net effect of Bloch's Theorem therefore has been to change the problem of an infinite number of electrons to one of considering only the number of electrons in the unit cell (or half that number, depending on whether the states are spin-degenerate or not) at a finite number of k-points chosen so as to appropriately sample the Brillouin Zone; this problem is returned to later.

2.5 Kohn-Sham Equations in Plane Wave Form

Exploiting the lattice periodicity using Bloch's theorem has now led to the one-electron wavefunctions being expressed in terms of a Fourier expansion using plane waves as a basis set. Although plane waves are not the only possible basis set that can be used, for example, one could use atomic wavefunctions as a basis set, plane waves are perhaps more aesthetically appealing. More importantly, a plane wave basis set has the advantage of being mathematically simple, and is in principle complete, that is, it completely spans the Hilbert space. This is in contrast to localised basis sets. Plane waves also possess the advantage of covering all space equally, and are thus not biased to any particular region. This is particularly important when one does not

have any *a priori* knowledge of the form of the electronic wavefunctions. However, it is a double-edged sword in that it results in regions devoid of electron density having equal quality of coverage as regions of high electron density. It is thus, in a sense, inefficient, and it is this that leads to the cubic scaling of plane wave DFT calculations with system size [39, 56]. Accordingly, most efforts at achieving methods that scale linearly with system size have concentrated upon localised basis sets [57, 58, 59].

In principle, the series in 2.39 should be infinite; in practice, the series should be truncated in order that it may be handled computationally. The coefficients for the plane waves have a kinetic energy $\frac{\hbar^2}{2m}|\mathbf{k}+\mathbf{G}|^2$, and plane waves with high kinetic energy typically are less important than those of low kinetic energy. One may thus introduce a kinetic energy cut-off E_{cut} in order to achieve a finite basis set. The kinetic energy cut-off is defined through

$$E_{cut} = \frac{\hbar^2}{2m}|\mathbf{k}+\mathbf{G}|^2 \tag{2.40}$$

and thus this fixes the highest reciprocal lattice vector $\mathbf{G}$ used in the plane wave expansion, resulting in a finite basis set.

Expansion of the electron wave functions in terms of plane waves allows the Kohn-Sham equations to take on the particularly simple and appealing form

$$\sum_{\mathbf{G}'}\left[\tfrac{1}{2}|\mathbf{k}+\mathbf{G}|^2\delta_{\mathbf{G}\mathbf{G}'} + V_{ion}(\mathbf{G}-\mathbf{G}') + V_{xc}(\mathbf{G}-\mathbf{G}') + V_H(\mathbf{G}-\mathbf{G}')\right]\times c_{i,\mathbf{k}+\mathbf{G}'} = \epsilon_i c_{i,\mathbf{k}+\mathbf{G}} \tag{2.41}$$

which may be readily shown by substitution of 2.39 into 2.30. One can see that the reciprocal space representation of the kinetic energy is diagonal, whilst the potentials are described in terms of Fourier components. In principle, this secular equation could be solved by simply diagonalising the Hamiltonian matrix $H_{\mathbf{k}+\mathbf{G},\mathbf{k}+\mathbf{G}'}$ whose matrix elements are given by the terms in brackets above. However, the size of the matrix is determined by the choice of cut-off energy E_{cut}, and for systems containing

valence and core electrons will be intractably large. Discussion of more computationally efficient methods of solving this problem will be returned to later.

2.6 k-point Sampling

We have already discussed how Bloch's theorem allows one to only consider the electrons within the unit cell at an infinite number of k-points within the first Brillouin zone. As alluded to, it is possible to use only a finite number of k-points if these are chosen so as to appropriately sample the reciprocal space. One can therefore write an integrated function $f(\mathbf{r})$ over the Brillouin zone as

$$f(\mathbf{r}) = \frac{\Omega}{(2\pi)^3} \int_{BZ} F(\mathbf{k}) d\mathbf{k} = \sum_j w_j F(\mathbf{k}_j) \tag{2.42}$$

where $F(\mathbf{k})$ is the Fourier transform of $f(\mathbf{r})$, Ω is the cell volume and the w_j are weighting factors. The set of "special" k-points chosen to appropriately sample the Brillouin zone is obtained in this work using the Monkhorst-Pack method [60]. The k-points are distributed uniformly through space as

$$\mathbf{k}_j = x_{1j}\mathbf{b}_1 + x_{2j}\mathbf{b}_2 + x_{3j}\mathbf{b}_3 \tag{2.43}$$

where the $\mathbf{b}_i$ are reciprocal lattice vectors, and

$$x_{ij} = \frac{l_i}{n_j}, j = 1, \ldots, n_j \tag{2.44}$$

where the l_i are lengths of reciprocal lattice vectors, and n_j is an integer determining the number of special points in the set.

In practice, a further computational saving may be made by utilising the point group symmetry of the lattice. This allows one to write the sums as

$$f(\mathbf{r}) = \sum_{j=1}^{P(n_j)} w_j F(\mathbf{k}_j) \tag{2.45}$$

where $P(n_j)$ is the symmetry-dependent number of points in the irreducible wedge of the Brillouin zone. The weights in this equation are in general different to those in equation 2.42; they are simply the ratio of the order of the point group to that of the group of the wavevector $\mathbf{k}_j$ under consideration.

2.7 Pseudopotentials

Although the Kohn-Sham equations have been shown to be tractable when plane waves are used to expand the electron wavefunctions, an all-electron calculation including both core and valence electrons, along with the full Coulombic potential of the nuclei would still be prohibitively expensive using a plane wave basis set. This is because the tightly bound core orbitals, and the highly oscillatory nature of the valence electrons, demand that a high value of E_{cut} and hence number of plane waves be used in order to accurately describe the electronic wavefunctions [40].

However, it is possible to partition the electrons between core and valence states; such a partition is possible because the majority of physical properties of solids depend upon the valence electrons; in contrast, the core electrons are almost environment independent. It is for this reason that the pseudopotential approximation is introduced [61, 62, 63]: the core electrons and ionic potential are removed and replaced with a *pseudopotential* that acts on a set of pseudo wave functions; this is illustrated schematically in figure 2.1.

The pseudopotential is constructed such that that the pseudo wave function has no radial nodes within the core region and that the pseudo wave functions and potential agree with the *true* wave function and potential outside some cut-off radius r_{cut}. Further, the pseudopotential must preserve the atomic properties of the element, including phase shifts on scattering across the core; as these phase shifts will in general be dependent upon the angular momentum state, in general a pseudopotential must be non-local, *i.e.* it must have projectors for the different angular momentum states. The most general form for a pseudopotential is thus [40]

$$V_{ion} = \sum_{lm} |lm\rangle V_l \langle lm| \tag{2.46}$$

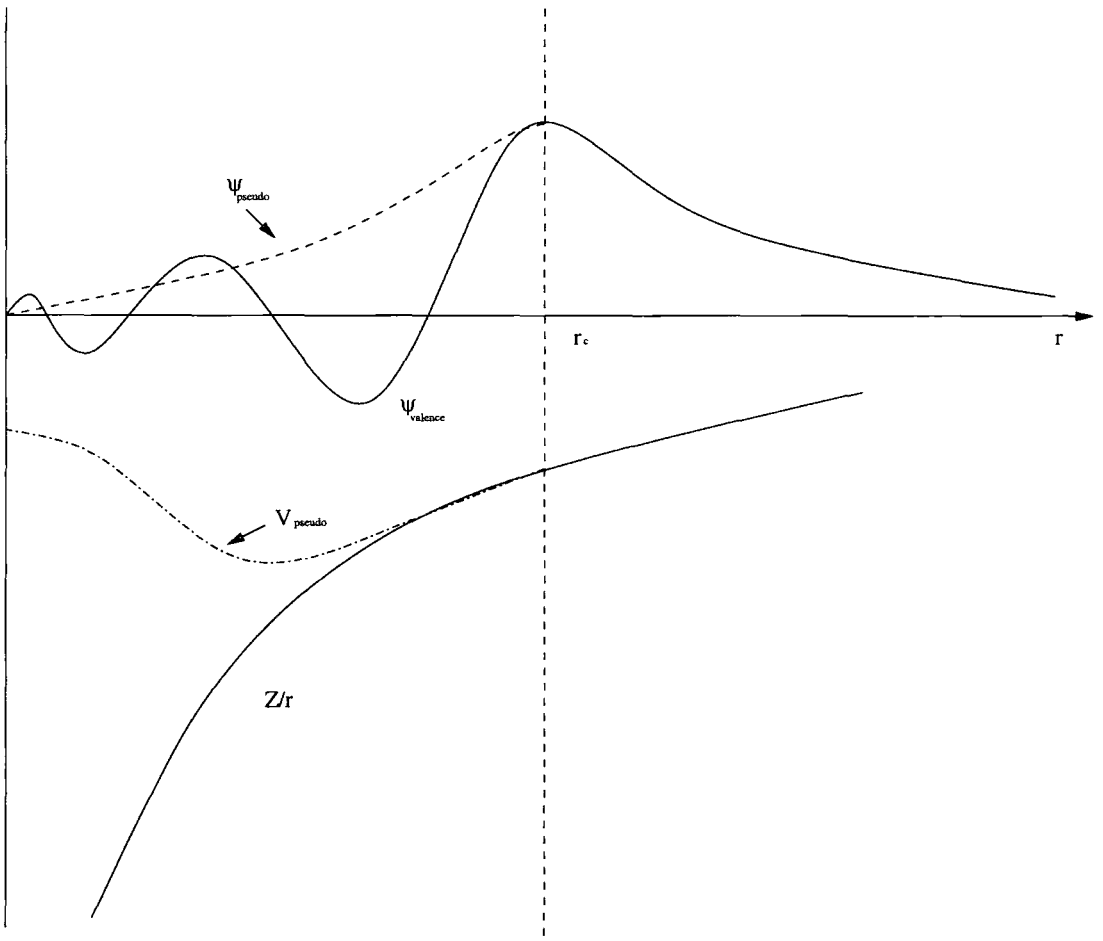

Figure 2.1: Schematic illustration of a pseudopotential

where the $|lm\rangle$ are spherical harmonics, and V_l is the pseudopotential for angular momentum l.

If there are N_{pw} plane waves in the expansion of the electron wavefunction at each k-point, and there are N_k plane waves, then the evaluation of 2.46 will require $N_{pw}N_k(N_{pw}+1)/2$ projectors of the above form to be calculated for each angular momentum component l.

This can be understood as follows: the crystal potential $V_{cr}(\mathbf{r})$ is obtained by placing a pseudopotential at each lattice site, with the structure factor incorporating the crystal symmetry, hence

$$V_{cr}(\mathbf{G}-\mathbf{G}') = \sum_s s_s(\mathbf{G}-\mathbf{G}')V_{ps}(\mathbf{G}-\mathbf{G}') \tag{2.47}$$

where the summation index is over ionic species and the species structure factor is given by

$$s_s(\mathbf{G}-\mathbf{G}') = \sum_i e^{i(\mathbf{G}-\mathbf{G}')\cdot\mathbf{R}_i}. \tag{2.48}$$

The total ion-electron energy is then

$$E_{elec-ion,lm} = \sum_{\mathbf{G}\mathbf{G}'} \langle\psi\,|lm\rangle V_{cr}(\mathbf{G}-\mathbf{G}')\langle lm|\,\psi\rangle \tag{2.49}$$

which leads to an inseparable double sum over both $\mathbf{G}$ and $\mathbf{G}'$. This results in the evaluation of the ion-electron energy scaling as the square of the number of plane waves in the expansion. This will limit the size of any calculation.

2.7.1 Kleinman-Bylander Pseudopotentials

Choosing the Kleinman-Bylander form [64] for the pseudopotential allows the double sum to be split into a product of two single sums. The Kleinman-Bylander form is

$$V_{ion} = V_{loc} + \sum_{lm} \frac{|\psi_{lm}\delta V_l\rangle\langle\delta V_l\psi_{lm}|}{\langle\psi_{lm}\,|\delta V_l|\,\psi_{lm}\rangle} \tag{2.50}$$

where V_{loc} is an arbitrary local potential, ψ_{lm} are the pseudo-atom wavefunctions, and δV_l is defined through

$$\delta V_l = V_{l,non-local} - V_{loc} \tag{2.51}$$

where $V_{l,non-local}$ is the the l angular momentum component of a non-local pseudopotential. Writing the pseudopotential in this form allows the calculation to scale linearly with the size of the basis set.

2.7.2 Norm Conservation and Ultrasoft Potentials

Kleinman-Bylander pseudopotentials are norm-conserving, that is, outside the core, the real and pseudo wavefunctions generate the same charge density. This can be expressed formally as

$$\int_0^{r_c} \psi^{\star}_{AE}(\mathbf{r})\psi_{AE}(\mathbf{r})d\mathbf{r} = \int_0^{r_c} \psi^{\star}_{ps}(\mathbf{r})\psi_{ps}(\mathbf{r})d\mathbf{r} \tag{2.52}$$

where $\psi_{AE}(\mathbf{r})$ is the all electron wavefunction (*i.e.* the Kohn-Sham orbital that would be obtained from a calculation involving all electrons), and $\psi_{ps}(\mathbf{r})$ is the pseudo wavefunction [65]. However, this condition of norm-conservation has meant, in certain cases, notably the O $2p$ orbitals [66], that it is not possible to construct a pseudo wavefunction significantly smoother than the all-electron wavefunction. The compact valence p orbitals of electronegative first row atoms such as F [67], and the d-orbitals of the first row transition elements, present similar problems. Relaxation of the norm conservation condition leads to Vanderbilt ultrasoft potentials [66]; instead, a generalised eigenvalue formalism is adopted. A non-local overlap operator is defined through

$$S = 1 + \sum_{i,j} Q_{ij} \, |\beta_i\rangle\langle\beta_j| \tag{2.53}$$

where β_i are projector functions depending upon ionic positions and the Q_{ij} are the matrix elements

$$Q_{ij} = \langle\psi_i|\psi_j\rangle - \langle\phi_i|\phi_j\rangle. \tag{2.54}$$

Here, the ψ are the all-electron wavefunctions, whilst the ϕ are pseudo wavefunctions. The norm-conservation condition is recovered when $Q_{ij} = 0$. Relaxing this condition results in the introduction of the non-local operator in 2.53. The non-local potential may then be written as

$$V_{non-local} = \sum_{i,j}(B_{ij} + \epsilon_i Q_{ij}) \, |\beta_i\rangle\langle\beta_j| \tag{2.55}$$

where B is the matrix whose elements are formed from

$$B_{ij} = \langle\phi_i|\chi_j\rangle \tag{2.56}$$

and χ is a local wavefunction obtained from

$$|\chi_i\rangle = (\epsilon_i - T - V_{loc})|\phi_i\rangle. \tag{2.57}$$

The ϕ_i are then solutions of the generalised eigenvalue problem

$$(H - \epsilon_i S)|\phi_i\rangle = 0 \tag{2.58}$$

subject to the orthonormality condition

$$\langle\phi_i \, |S| \, \phi_j\rangle = \delta_{ij} \tag{2.59}$$

From this it is readily shown that

$$\langle\phi_i \, |S| \, \phi_j\rangle = \langle\psi_i|\psi_j\rangle \tag{2.60}$$

and thus the pseudo and all electron wavefunction amplitudes are the same beyond the cut-off radius value. Relaxation of the norm conserving condition allows smoother wavefunctions, and hence lower cut-off energies. This is advantageous in reducing the size of the plane wave basis set used, and it is for this reason that Vanderbilt ultra-soft pseudopotentials are amongst the most widely used in the condensed matter community. However, for this work we use the Kleinman-Bylander form instead: this is for technical reasons that will be fully explained in a later chapter.

2.7.3 Pseudopotential Generation

Pseudopotentials are usually generated from all-electron calculations by self-consistently solving the all-electron Schrödinger equation

$$\left(-\frac{1}{2}\nabla^2 + V\right)\psi_l^{AE} = \epsilon_l \psi_l^{AE} \tag{2.61}$$

where ψ_l^{AE} is the all-electron wavefunction with angular momentum quantum number l. The resulting valence eigenvalues are then substituted back into the Schrödinger equation, but with a parameterised pseudo wavefunction. Inversion of the Kohn-Sham equations with this pseudo wavefunction then yields the pseudopotential.

A pseudopotential is not unique: however, it must obey certain criteria:

- 1. the pseudo wavefunction must be the same as the all-electron wavefunction outside a radius r_{cut}.
- 2. the core charge produced by both sets of wavefunctions must be the same. This norm conservation requirement can be relaxed though, as discussed earlier.
- 3. the pseudo wavefunctions must be continuous at the cut-off radius, as must be the first and second derivatives.
- 4. the valence all-electron and pseudopotential eigenvalues must be equal.

2.8 Energy Minimisation

Solution of 2.41 may proceed by several methods. The most obvious is to simply diagonalise the Hamiltonian in that equation. However, conventional matrix diagonalisation procedures are ill-suited to plane wave pseudopotential calculations. This is because the cost of such diagonalisations is $\sim N_{pw}$ where N_{pw} is the number of plane waves in the calculation. An alternative technique is to minimise the Kohn-Sham functional directly. The basic idea is to take a single-particle trial wavefunction, and minimise the contribution of this state to the total energy, whilst maintaining

orthogonality to all other states. The minimisation is achieved by varying the plane wave coefficients. There are various methods available to perform the minimisation procedure.

2.8.1 Steepest Descents

The simplest method to use is that of steepest descents. For a function $F(\mathbf{x})$ the steepest-descent direction $\mathbf{g}$ may be obtained as

$$\mathbf{g} = -\nabla_{\mathbf{x}^1} F \tag{2.62}$$

where $\mathbf{x}^1$ is the point at which the function is evaluated. Once this path of steepest descent has been determined, one may carry out a line minimisation in order to determine the location of the minimum, $\mathbf{x}^2$ along that line. From this point one repeats the procedure until the minimum of the function has been found. The steepest descents algorithm, although it has the advantage of being simple, does not guarantee convergence to a minimum in a finite number of steps [40]. Further, it uses information about the current sampling point only: it fails to use information gleaned from previous iterations in order to guide the minimisation more efficiently.

2.8.2 Conjugate Gradients

The conjugate gradients method [68] is a more efficient method that combines the information from all previous search directions such that a subsequent search direction is independent to all previous search directions, *i.e.* the set of search directions forms a linearly independent set. For an n-dimensional vector space, this guarantees convergence in n iterations, as each minimisation step reduces the dimensionality of the problem by 1; hence after n iterations, the dimensionality of the problem will be zero, and thus the minimum has been reached.

If $\mathbf{g}^m$ is the steepest descents vector associated with iteration m, then the conjugate gradients direction $\mathbf{d}^m$ is given by

$$\mathbf{d}^m = \mathbf{g}^m + \gamma^m \mathbf{d}^{m-1} \tag{2.63}$$

where

$$\gamma^m = \frac{\mathbf{g}^m \cdot \mathbf{g}^m}{\mathbf{g}^{m-1} \cdot \mathbf{g}^{m-1}} \tag{2.64}$$

and $\gamma^1 = 0$.

2.8.3 Preconditioning

The number of plane waves in a calculation is typically of the order $\sim 10^5$, and thus each iteration of a conjugate gradients minimiser could take a long time. In order to remedy this problem, a preconditioning scheme is usually employed in tandem with the minimiser. The Kohn-Sham Hamiltonian is ill-conditioned due to the broad eigenvalue spectrum associated with the basis states; this leads to poor convergence for quadratic functions, for reasons which may be understood as follows [69]: assume a nearly converged trial vector for band m

$$\mathbf{C}_m = \mathbf{E}_m + \sum_{i \neq m} \epsilon_m \mathbf{E}_i, \tag{2.65}$$

i.e. it is a sum of eigenvectors of the Kohn-Sham Hamiltonian. This sum represents the error in $\mathbf{C}_m$. The residual vector

$$H \cdot \mathbf{C}_m - \lambda \cdot \mathbf{C}_m = \sum_{i \neq m} \epsilon_i (\lambda_i - \lambda_m) \mathbf{E}_i \tag{2.66}$$

with

$$\lambda_m = \mathbf{C}_m \cdot H \cdot \mathbf{C}_m \tag{2.67}$$

provides a measure of the error. Ideally, the error vector should be a simple multiple of the steepest descents vector; for then, in principle, one may eliminate the error completely by stepping an appropriately sized step along this direction. However, it can be seen from the above equation that it is not possible to do so, and that this is due to the broad spectrum of eigenvalues. Indeed, only if all the unoccupied

Kohn-Sham orbitals were degenerate would this be the case. Preconditioning offers a solution to this problem: the residual vector is multiplied by an approximate inverse such that a preconditioned steepest-descent vector is obtained that more accurately represents the error vector. The higher-energy eigenstates are dominated by the kinetic energy contributions; hence the energy of these states will be approximately equal to the kinetic energy. Multiplication by a diagonal preconditioning matrix that is essentially the inverse of the kinetic energy operator has the effect of approximately removing the effect of the Hamiltonian upon the residual vector, that is, the eigenvalue spectrum is compressed, and convergence is thus improved. It is important to note that the preconditioning matrix must be a positive definite operator; further, it must be a constant for the low kinetic energy contributions, for which the potential energy is a significant contribution to the total energy. Preconditioning is found to achieve excellent rates of convergence: it is common for problems involving $\sim 10^6$ basis functions to converge in only a few tens of iterations. In this work the preconditioning scheme of Teter *et al.* is used [69]; a more detailed discussion of the merits and demerits of various preconditioning schemes is presented in a later chapter with regard to solving the second-order Kohn-Sham problem.

2.9 Geometry Optimisation

Thus far only total energy calculations for a fixed set of atomic coordinates have been described. However, it is relatively simple to calculate the forces on an atom using the plane wave basis set, and hence move the atom under the influence of these forces. The force on an atom may be obtained through

$$\mathbf{F}_I = -\frac{dE}{d\mathbf{R}_I}. \tag{2.68}$$

As the atom moves to a new position, the electronic wavefunctions must also change: this will contribute to the force on the atom as can be readily seen if the total derivative is expanded:

$$\mathbf{F}_I = -\frac{\partial E}{\partial \mathbf{R}_I} - \frac{\partial E}{\partial \Psi}\frac{d\Psi}{d\mathbf{R}_I} - \frac{\partial E}{\partial \Psi^\star}\frac{d\Psi^\star}{d\mathbf{R}_I}. \tag{2.69}$$

However, since

$$E = \langle \Psi \, | H | \, \Psi \rangle \tag{2.70}$$

the last two terms simply yield

$$E \frac{\partial}{\partial \mathbf{R}_I} \langle \Psi | \Psi \rangle \tag{2.71}$$

which is trivially zero. Thus when Ψ is an eigenstate of the Hamiltonian, the partial derivative of the total energy with respect to atomic position gives the forces acting on that atom.

2.10 The CASTEP code

The calculations described in this thesis are all carried out using the electronic structure code CASTEP. This is a code written in FORTRAN 90 developed by Segall *et al.* [39] and utilises the techniques described in this chapter to solve the Kohn-Sham equations. The DFPT methods discussed in the next chapter were also implemented within the same package.

Chapter 3

Density Functional Perturbation Theory

Many physical properties depend upon a system response to some form of perturbation. Examples include polarisabilities, phonons, Raman intensities and infra-red absorption cross-sections to name but a few. Density functional perturbation theory (DFPT) is a particularly powerful and flexible theoretical technique that allows calculation of such properties within the density functional framework, thereby facilitating an understanding of the microscopic quantum mechanical mechanisms behind such processes, as well as providing a rigorous testing ground for theoretical developments. System responses to external perturbations may be calculated using DFT with the addition of some perturbing potential; however, as such methods involve obtaining the system response through a series of single-point energy calculations carried out at varying strengths of the external perturbation, it can be said that they are somewhat crude and aesthetically unappealing. More fundamentally, such techniques are sometimes restricted in application: for example, they cannot readily be used to calculate the response of crystalline systems to electric field perturbations, and cannot, without large computational effort, calculate phonon responses at arbitrary wavevector; points which will be expounded upon in this chapter. We now consider the application of perturbation theory to DFT, and use this formalism to derive equations allowing the calculation of phonon and electric field responses within crystalline materials.

The two main formalisms of DFPT are due to Baroni [70] and Gonze [71]; although

the two may be shown to be equivalent, there are differences in the implementation that may result in one method being preferable to another. The Baroni formalism is centred upon obtaining a series of equations that may be solved self-consistently using Green's function methods; the Gonze formalism is based rather upon a perturbative expansion of the Kohn-Sham energy functional, leading to a variational problem for even orders of expansion akin to the zeroth order problem.

3.1 The Green's Function Method and Linear Response

The basic *ansatz* behind DFPT is that quantities such as the wavefunction, electron density, or potential may be written as a perturbation series

$$X(\lambda) = X^{(0)} + \lambda X^{(1)} + \lambda^2 X^{(2)} + \dots \tag{3.1}$$

where $X(\lambda)$ is a generic physical quantity that could, for example, be the Kohn-Sham orbitals $\psi(\lambda)$, the Kohn-Sham energy $E(\lambda)$, or the electronic density $n(\lambda)$, and λ is a perturbing parameter, assumed to be small. The expansion coefficients are given by

$$X^{(n)} = \frac{1}{n!}\frac{d^n X}{d\lambda^n}\bigg|_{\lambda=0}. \tag{3.2}$$

The variation in the Kohn-Sham orbitals may be determined by solution of the so-called *Sternheimer* equation [72]

$$(H_{KS}^{(0)} - \epsilon_n^{(0)})|\psi_n^{(1)}\rangle = -(H_{KS}^{(1)} - \epsilon_n^{(1)})|\psi_n^{(0)}\rangle \tag{3.3}$$

where $H_{KS}^{(1)}$ is the first order Kohn-Sham potential given by

$$H_{KS}^{(1)} = T^{(1)} + v_{ext}^{(1)}(\mathbf{r}) + e^2 \int \frac{n^{(1)}(\mathbf{r}')}{|\mathbf{r}-\mathbf{r}'|} d\mathbf{r}' + \int \frac{\delta v_{xc}}{\delta n(\mathbf{r}')} n^{(1)}(\mathbf{r}') d\mathbf{r}'. \tag{3.4}$$

The Sternheimer equation is obtained by expanding the Kohn-Sham equations to first order. It is easy to see how this relates to standard perturbation theory: left

multiplication of 3.3 by $\langle\psi_n^{(0)}|$ and use of the orthogonality condition $\langle\psi_n^{(0)}|\psi_m^{(1)}\rangle = 0$ (the so-called *parallel transport gauge*) leads to

$$\epsilon_n^{(1)} = \langle\psi_n^{(0)}|H_{KS}^{(1)}|\psi_n^{(0)}\rangle. \tag{3.5}$$

The first order change in the wavefunction may be obtained by left multiplication of 3.3 by $\langle\psi_m^{(0)}|$ leading to

$$|\psi_n^{(1)}\rangle = \sum_{m\neq n} C_{nm}^{(1)}|\psi_m^{(0)}\rangle \tag{3.6}$$

where the expansion coefficient $C_{nm}^{(1)}$ is given by

$$C_{nm}^{(1)} = \frac{\langle\psi_m^{(0)}|H_{KS}^{(1)}|\psi_n^{(0)}\rangle}{\epsilon_n^{(0)} - \epsilon_m^{(0)}}. \tag{3.7}$$

These are of course the well-known results from standard perturbation theory, with an additional two terms in the first order perturbed Hamiltonian that reflect the coupling of the electrons to each other via the requirement of self-consistency. These equations form a set of self-consistent equations that must be solved in order to determine the behaviour of the perturbed system. For an N-electron system, the linear dependence of the first order Kohn-Sham Hamiltonian upon the first order density, and hence via this the first order Kohn-Sham orbitals, leads to a coupling of the N equations. Thus the set of $|\psi^{(1)}\rangle$'s is the solution of a problem of dimension $(NM/2 \times NM/2)$, where M is the size of the basis set used.

From equations 3.6 and 3.7, and neglecting spin, the first order electron density may be written as

$$\begin{aligned} n^{(1)}(\mathbf{r}) &= \sum_{n=1}^{N} \psi_n^{(0)\star}(\mathbf{r})\psi_n^{(1)}(\mathbf{r}) + \psi_n^{(1)\star}(\mathbf{r})\psi_n^{(0)}(\mathbf{r}) \\ &= 2\sum_{n=1}^{N}\sum_{m\neq n} \psi_n^{(0)\star}(\mathbf{r})\psi_m^{(0)}(\mathbf{r})\frac{\langle\psi_m^{(0)}|H_{KS}^{(1)}|\psi_n^{(0)}\rangle}{\epsilon_n^{(0)} - \epsilon_m^{(0)}} \end{aligned} \tag{3.8}$$

from which it may be readily seen that the contributions due to products of occupied states cancel; as it is natural within a density functional framework to identify the label n as attaching to valence band states, this ensures that the index m attaches itself only to conduction band states; for this reason the labels v and c, for valence and conduction band states respectively, will be used from now on. This result is equivalent to stating that the electron density only responds to perturbations that couple the valence and conduction manifolds [73].

In order to calculate the projection of the first order wavefunction onto the conduction band manifold the projection operator P_c is introduced, which leads to the Sternheimer equations taking the form

$$P_c(H_{KS} - \epsilon_v^{(0)})P_c|\psi_v^{(1)}\rangle = -P_c H_{KS}^{(1)}|\psi_v^{(0)}\rangle \tag{3.9}$$

where the contribution due to the eigenvalue $\epsilon_v^{(0)}$ vanishes due to the projection of the Kohn-Sham orbitals onto the conduction manifold. The projection operator here takes the form

$$P_c = 1 - \sum_v |\psi_v^{(0)}\rangle\langle\psi_v^{(0)}| = \sum_c |\psi_c^{(0)}\rangle\langle\psi_c^{(0)}| \tag{3.10}$$

and this allows the first order wavefunction to be written as

$$|\psi_v^{(1)}\rangle = G_v H_{KS}^{(1)}|\psi_v^{(0)}\rangle \tag{3.11}$$

where G_v is the Green's function operator projected onto the conduction band

$$G_v = \sum_c \frac{|\psi_c^{(0)}\rangle\langle\psi_c^{(0)}|}{(\epsilon_v^{(0)} - \epsilon_c^{(0)})}. \tag{3.12}$$

Solution of the linear problem defined by the Sternheimer equation requires only knowledge of the occupied states in order to determine the first order correction to the Kohn-Sham orbitals; this is a marked advantage over explicit evaluation using equations 3.6 and 3.7 which require knowledge of the full eigenvalue spectrum. The computational cost of solving this system of linear equations is comparable to that

required to solve the zeroth order Kohn-Sham equations. It should of course be noted that these results have assumed the existence of a finite energy gap, and are hence only applicable to insulators; metallic systems, for which the density of states is non-vanishing at the Fermi energy, may experience a change in occupation number upon application of a perturbation [73]; formulae for metallic systems have been derived by de Gironcoli [74], and such applications are discussed in some detail by Baroni *et al* [70]. It will suffice to note that as the main concern of this work is developing and implementing a DFPT algorithm to calculate electric field and phonon responses, and as the response to an electric field is not defined for metallic systems, only insulating systems will be discussed: the interested reader is referred to the references for details of the application of DFPT to metallic systems.

3.2 The $(2n + 1)$ Theorem

The existence of a "$(2n + 1)$ theorem" in quantum mechanics has been known since the work of Hylleras on two-electron systems in 1930 [75]; simply put, the theorem states that the $(2n + 1)$th derivative of the eigenenergy of a Hamiltonian may be determined with only a knowledge of the change in the eigenfunctions up to order n. Further, Hylleras noted that the second order energy obeyed a minimisation principle with respect to variations in the first order wavefunction. It was not until the work of Dalgarno and Stewart in 1956 [76] that an iterative procedure was proposed that built the $(2n + 1)$th derivative of the eigenenergy from only the knowledge of the change in the eigenfunctions up to order n. This work was then generalised by Dupont-Bourdelet, Tillieu and Guy [77] to Hamiltonians with a dependence upon a small parameter.

Such theorems are not limited to quantum mechanics: Sinanoglu [78] showed that *any* variational principle, when combined with a perturbation expansion will yield even-order variational principles. Although such theorems were known within quantum chemistry, they had generally been calculated on a case-by-case business. The first introduction of these perturbative expansions of the Kohn-Sham energy functional was by Gonze and Vigneron [79] in 1989; it was not until the seminal work of Gonze [71] in 1995 that a unified theoretical approach was achieved that proved

both the existence of even-order variational principles for constrained functionals and provided explicit expressions for these terms.

"Variational" here is meant in the sense of a lower variational bound, that is, the value of the functional for a wave function slightly different from the true wavefunction is higher than the minimal value E_0 for the true wavefunction Φ_0. It is thus possible to say that

$$\forall\Phi, 0 \leq E[\Phi] - E[\Phi_0] \leq K||\Phi - \Phi_0||^2 \tag{3.13}$$

where K is some positive number, under sufficient conditions of differentiability, which are always met in practice. In the following discussion $\hat{E}$ denotes the functional under discussion, and E is the value that it can take.

3.2.1 The Variational Principle and Perturbation Theory

If the functional $\hat{E}$ depends upon a parameter λ, then for λ close to zero, it is possible to define a fixed number K such that

$$\forall\Phi, 0 \leq \hat{E}_{(\lambda)}[\Phi] - \hat{E}_{(\lambda)}[\Phi_0(\lambda)] \leq K||\Phi - \Phi_0(\lambda)||^2. \tag{3.14}$$

It may then be shown that [71]

$$E_0^{(2n+1)} = \left(\hat{E}_{(\lambda)}\left[\sum_{i=0}^{n}\lambda^i\Phi_0^{(i)}\right]\right)^{(2n+1)} \tag{3.15}$$

and

$$E_0^{(2n)} = \min_{\delta\Phi_t}\left(\hat{E}_{(\lambda)}\left[\sum_{i=0}^{n-1}\lambda^i\Phi_0^{(i)} + \lambda^n\delta\Phi_t\right]\right)^{(2n)} \tag{3.16}$$

where $\delta\Phi_t$ is the trial wavefunction. Equation 3.15 is the $2n+1$ theorem, namely that the variation in the energy to order $2n+1$ only, whilst equation 3.16 illustrates the variational property of the even order terms in the perturbation expansion.

Setting m equal to $2n+1$ or $2n$, it is possible to write

$$E_0^{(m)} = \left(\hat{E}_{(\lambda)}\left[\Phi_0^{(0)} + \sum_{i=1}^{n} \lambda^i \Phi_0^{(i)}\right]\right)^{(m)} \tag{3.17}$$

and a Taylor expansion of this yields

$$\begin{aligned} E_0^{(m)} = & \sum_{k=0}^{m-1} \sum_{j=1}^{m-k} \int \dots \int \frac{1}{j!k!} \sum_{i_1,\dots,i_j=1}^{n} \delta(k + i_1 + \dots + i_j - m) \times \\ & \frac{\partial^{j+k} \hat{E}}{(\partial\lambda)^k \partial\Phi(x_1) \dots \partial\Phi(x_j)} \Phi^{(i_1)}(x_1) \dots \Phi^{(i_j)}(x_j) dx_1 \dots dx_j + \\ & \frac{1}{m!} \frac{\partial^m \hat{E}}{\partial\lambda^m}. \end{aligned} \tag{3.18}$$

This result has been derived for a functional *without* constraint; of course, in DFT calculations, the constraint of fixed particle number is imposed. It is therefore necessary to consider how the above expressions are altered when constraints are introduced.

In order to minimise $\hat{E}[\Phi_t]$ under constraint, consider

$$\hat{F}_\Lambda[\Phi_t] = \hat{E}[\Phi_t] - \Lambda \hat{C}[\Phi_t] \tag{3.19}$$

where $\hat{C}[\Phi_t]$ is the functional that places a constraint on the domain of variation of Φ_t:

$$\hat{C}[\Phi_t] = 0. \tag{3.20}$$

Λ is a Lagrange multiplier chosen such that the solution that minimises the functional 3.19 satisfies the constraint condition equation 3.20. It can then be shown [71] that there exists some Ω such that for all possible Φ the variational principle takes the form

$$0 \leq \hat{F}_{\Lambda_0}[\Phi] - \hat{F}_{\Lambda_0}[\Phi_0] + \Omega(\hat{C}[\Phi])^2 \leq K||\Phi - \Phi_0(\lambda)||^2. \tag{3.21}$$

In general, the constraint may also depend upon the variational parameter λ. Taking this into account, then the above equation may be rewritten as

$$0 \leq \hat{E}_{(\lambda)}[\Phi] - \Lambda_0(\lambda)\hat{C}_{(\lambda)}[\Phi] + \Omega(\hat{C}_{(\lambda)}[\Phi])^2 - E_0(\lambda) \leq K||\Phi - \Phi_0(\lambda)||^2. \quad (3.22)$$

The expression for the $2n+1$ theorem is then

$$\begin{aligned} E_0^{(2n+1)} &= \left(\hat{F}_{(\lambda)}\left[\sum_{i=0}^{n}\lambda^i\Phi_0^{(i)}\right]\right)^{(2n+1)} \\ &= \left(\hat{E}_{(\lambda)}\left[\sum_{i=0}^{n}\lambda^i\Phi_0^{(i)}\right] - \Lambda_0(\lambda)\hat{C}_{(\lambda)}\left[\sum_{i=0}^{n}\lambda^i\Phi_0^{(i)}\right]\right)^{(2n+1)} \end{aligned} \quad (3.23)$$

with the even-order variational property

$$E_0^{(2n)} = \min_{\delta\Phi}\hat{F}_{(\lambda)}\left[\sum_{i}^{n-1}\lambda^i\Phi_0^{(i)} + \lambda^n\delta\Phi_t\right]\Big)^{(2n)}. \quad (3.24)$$

Although these expressions illustrate that the energy at order $2n+1$ only requires knowledge of the wavefunction up to order n and that even orders of expansion obey a stationary principle, it is not yet apparent how these relate to DFT. It is therefore necessary to now start to consider the expansion of the Kohn-Sham energy functional.

3.3 Perturbative Treatment of the Kohn-Sham Functional

The Kohn-Sham energy functional may be written as

$$E[\Phi_\alpha] = \sum_{\alpha=1}^{N}\langle\Phi_\alpha|T + v_{ext}|\Phi_\alpha\rangle + E_{Hxc}[n] - \sum_{\alpha,\beta=1}^{N}\Lambda_{\beta\alpha}[\langle\Phi_\alpha|\Phi_\beta\rangle - \delta_{\alpha\beta}] \quad (3.25)$$

where E_{Hxc} is the electron-electron interaction energy, *i.e.* the sum of the Hartree and xc energies, and $\Lambda_{\alpha\beta}$ is a Lagrange multiplier, introduced to ensure the orthonormality of the Kohn-Sham orbitals. It is easy to see what this Lagrange multiplier

is given by: consider the Euler-Lagrange equations associated with minimisation of the above functional

$$H|\Phi_\alpha\rangle = \sum_{\beta=1}^{N} \Lambda_{\beta\alpha}|\Phi_\beta\rangle \tag{3.26}$$

with the Hamiltonian

$$H = T + v_{ext} + v_{Hxc} = T + v_{KS}. \tag{3.27}$$

Taking the scalar product

$$\Lambda_{\alpha\beta} = \langle\Phi_\alpha|H|\Phi_\beta\rangle \tag{3.28}$$

yields the result that the Lagrange multipliers are given by matrix elements of the Hamiltonian. It is worth stressing at this point that these matrix elements *are not* identical to the Kohn-Sham eigenvalues, as a gauge freedom exists: at this point, the orbitals Φ_α have not been chosen to solve the Kohn-Sham equations, but rather solve the "generalised" Kohn-Sham equations 3.26.

It is now useful to begin considering the expansion of the above equations. The density may be expanded as

$$n^{(i)}(\mathbf{r}) = \sum_{j=0}^{i}\sum_{\alpha=1}^{N} \Phi_\alpha^{(j)\star}(\mathbf{r})\Phi_\alpha^{(i-j)}(\mathbf{r}) \tag{3.29}$$

with the orthogonality condition becoming

$$\sum_{j=0}^{i}\langle\Phi_\alpha^{(j)}|\Phi_\beta^{(i-j)}\rangle = 0. \tag{3.30}$$

The generalised Kohn-Sham equations become

$$\sum_{j=0}^{i} H^{(j)}|\Phi_\alpha^{(i-j)}\rangle = \sum_{j=0}^{i}\sum_{\beta=0}^{N} \Lambda_{\beta\alpha}^{(j)}|\Phi_\beta^{(i-j)}\rangle \tag{3.31}$$

where the Hamiltonian expanded at order i is

$$H^{(i)} = T^{(i)} + v_{KS}^{(i)} \tag{3.32}$$

and the Lagrange multipliers at order i become

$$\Lambda_{\beta\alpha}^{(i)} = \sum_{j=0}^{i}\sum_{k=0}^{i}\langle\Phi_{\beta}^{(j)}|H^{(i-j-k)}|\Phi_{\alpha}^{(k)}\rangle. \tag{3.33}$$

Using these then, the variational energy may be written, for $m = 2n$, or $m = 2n+1$ as

$$\begin{aligned} E^{(m)} &= \sum_{\alpha=1}^{N}\sum_{j=0}^{n}\sum_{k=0}^{m}\sum_{l=0}^{n}\delta(m-j-k-l)\langle\Phi_{\alpha}^{(j)}|(T+v)^{(k)}|\Phi_{\alpha}^{(l)}\rangle \\ &+ \frac{1}{m}\frac{d^m}{d\lambda^m}E_{Hxc}\Big[\sum_{\alpha=1}^{N}\Big(\sum_{j=0}^{n}\lambda^j\Phi_{\alpha}^{(j)\star}(\mathbf{r})\Big)\Big(\sum_{k=0}^{n}\lambda^k\Phi_{\alpha}^{(k)}(\mathbf{r})\Big)\Big]\Big|_{\lambda=0} \\ &- \sum_{\alpha,\beta=1}^{N}\sum_{j=0}^{n}\sum_{k=0}^{m}\sum_{l=0}^{n}\delta(m-j-k-l)\Lambda_{\beta\alpha}^{(k)}\langle\Phi_{\alpha}^{(j)}|\Phi_{\beta}^{(l)}\rangle \\ &+ \sum_{\alpha,\beta=1}^{N}\Lambda_{\beta\alpha}^{(m)}\delta_{\alpha\beta} \end{aligned} \tag{3.34}$$

which only requires wavefunctions up to order n, and is fully variational for even orders of expansion.

3.4 Gauge Freedom

In the previous section, it was implied that a gauge freedom exists with regard to the zeroth order occupied orbitals. In order to clarify this issue, consider the generalised Kohn-Sham equations, equation 3.26. These differ from the Kohn-Sham equations as usually presented

$$H|\Psi_{\alpha}^{(0)}\rangle = \epsilon_{\alpha}|\Psi_{\alpha}^{(0)}\rangle. \tag{3.35}$$

Defining a $(N \times N)$ unitary matrix such that

$$U_{\alpha\beta}^{-1} = U_{\alpha\beta}^{\dagger} \tag{3.36}$$

then if another set of occupied orbitals is defined through a unitary transformation

$$|\Phi'_{\alpha}\rangle = \sum_{\gamma=1}^{N} U_{\gamma\alpha}|\Phi_{\gamma}\rangle \tag{3.37}$$

it is clear that both total electronic energies and densities remain the same, whilst the orthonormality condition is still satisfied. This is the result of a $U(N)$ gauge freedom. If one takes the occupied orbitals to be the solution of the Kohn-Sham equations, as will be done for the purposes of this work, then this is equivalent to stating that

$$\Lambda_{\beta\alpha}^{(0)} = \delta_{\beta\alpha}\epsilon_{\alpha}^{(0)} \tag{3.38}$$

and

$$U_{\beta\alpha} = \delta_{\beta\alpha}. \tag{3.39}$$

However, this only applies to the zeroth order wavefunctions. It is necessary to consider the issue of gauge freedom with regard to the higher order wavefunctions. It is most convenient to consider the orthonormalisation condition, which may be written as

$$\sum_{j=0}^{i} \langle \Phi_{\alpha}^{(i)} | \Phi_{\beta}^{(i-j)} \rangle = 0 \tag{3.40}$$

which implies, to first order, $i = 1$

$$\langle \Phi_{\alpha}^{(0)} | \Phi_{\beta}^{(1)} \rangle + \langle \Phi_{\alpha}^{(1))} | \Phi_{\beta}^{(0)} \rangle = 0. \tag{3.41}$$

This though only fixes the real part of the above scalar product; the imaginary part is not fixed, and thus one may impose the stronger condition that

$$\langle \Phi_\alpha^{(0)} | \Phi_\beta^{(i)} \rangle - \langle \Phi_\alpha^{(i)} | \Phi_\beta^{(0)} \rangle = 0. \tag{3.42}$$

This defines the *parallel transport gauge*, and for the first order wavefunctions yields

$$\langle \Phi_\alpha^{(0)} | \Phi_\beta^{(1)} \rangle = 0 \tag{3.43}$$

which determines the projection of the first order wavefunction on the valence manifold. As can be seen, the parallel transport gauge ensures that the first order wavefunction is *completely* orthogonal to the valence manifold. It should be noted that this is not the only gauge possible; it is sometimes useful, if one is interested in obtaining derivatives of the Kohn-Sham eigenenergies, to demand that the Lagrange multiplier matrix is diagonal at all orders. This is the "diagonal" gauge [71], but it is only mentioned in passing here.

3.5 Connection to the Green's Function Method

Having outlined the theoretical framework of the variational DFPT, it is now useful to actually identify the connections with the Green's function method outlined earlier in section 3.1. It is also instructive to consider the relationship between the DFPT and conventional perturbation theory. In order to do so, consider the first order change in the electronic energy, obtained using the $2n + 1$ theorem:

$$E^{(1)} = \sum_{\alpha=1}^{N} \langle \Phi_\alpha^{(0)} | (T + v_{ext})^{(1)} | \Phi_\alpha^{(0)} \rangle + \frac{d}{d\lambda} E_{Hxc}[n^{(0)}] \Big|_{\lambda=0}. \tag{3.44}$$

The last term will be zero unless the Hartree and XC energies *explicitly* depend upon the perturbing parameter, λ. The XC energy, for example, will depend explicitly upon the perturbation when non-linear core corrections are introduced. If the kinetic energy is not dependent upon the perturbation explicitly, which is usually the case,

then

$$E^{(1)} = \sum_{\alpha=1}^{N} \langle \Phi_\alpha^{(0)} | v_{ext}^{(1)} | \Phi_\alpha^{(0)} \rangle \tag{3.45}$$

which is nothing but the familiar Hellmann-Feynman theorem [80] derived *explicitly* within a DFT framework. So it can be seen that the well-known results of perturbation theory are recovered, as one would expect. Indeed, equation 3.44 represents a generalised Hellmann-Feynman theorem.

Appealing to the $2n + 1$-theorem, the second order energy may be obtained from the following expression:

$$\begin{aligned} E^{(2)} = & \sum_{\alpha=1}^{N} [\langle \Phi_\alpha^{(1)} | (T + v_{ext})^{(1)} | \Phi_\alpha^{(0)} \rangle + \langle \Phi_\alpha^{(1)} | (H - \epsilon_\alpha)^{(0)} | \Phi_\alpha^{(1)} \rangle \\ & + \langle \Phi_\alpha^{(0)} | (T + v_{ext})^{(2)} | \Phi_\alpha^{(0)} \rangle + \langle \Phi_\alpha^{(0)} | (T + v_{ext})^{(1)} | \Phi_\alpha^{(1)} \rangle] \\ & + \frac{1}{2} \int \int \frac{\delta^2 E_{Hxc}[n^{(0)}]}{\delta n(\mathbf{r}) \delta n(\mathbf{r}')} n^{(1)}(\mathbf{r}) n^{(1)}(\mathbf{r}') d\mathbf{r} d\mathbf{r}' \\ & + \int \frac{d}{d\lambda} \frac{\delta E_{Hxc}[n^{(0)}]}{\delta n(\mathbf{r})} \Big|_{\lambda=0} n^{(1)}(\mathbf{r}) d\mathbf{r} + \frac{1}{2} \frac{d^2}{d\lambda^2} E_{Hxc}[n^{(0)}] \Big|_{\lambda=0} \end{aligned} \tag{3.46}$$

which may be minimised with respect to variation in the first order wavefunctions. The Euler-Lagrange equations applied to this functional yield [71]

$$P_c (H^{(0)} - \epsilon_\alpha^{(0)}) P_c | \Phi_\alpha^{(0)} \rangle = -P_c H^{(1)} | \Phi_\alpha^{(0)} \rangle \tag{3.47}$$

which is, of course, the Sternheimer equation. Thus equivalence with the Green's function method has been demonstrated. It should be noted that the projection operators ensure that the parallel transport gauge is imposed.

3.6 Non-variational Expressions and Mixed Derivatives

So far, variational expressions for the second order energy have been considered. It is possible, though, to obtain non-variational expressions. If one is at the minimum

of the second order functional, then the first order wavefunctions satisfy the Sternheimer equation, and one may use this to re-write the first order wavefunctions in terms of the zeroth order wavefunctions. It is therefore possible to arrive at the following expressions [81]:

$$E^{(2)} = \sum_{\alpha=1}^{N} [\langle \Phi_\alpha^{(1)} | (T + v_{ext})^{(1)} | \Phi_\alpha^{(0)} \rangle + \langle \Phi_\alpha^{(0)} | (T + v_{ext})^{(2)} | \Phi_\alpha^{(0)} \rangle], \tag{3.48}$$

$$E^{(2)} = \sum_{\alpha=1}^{N} [\langle \Phi_\alpha^{(0)} | (T + v_{ext})^{(1)} | \Phi_\alpha^{(1)} \rangle + \langle \Phi_\alpha^{(0)} | (T + v_{ext})^{(2)} | \Phi_\alpha^{(0)} \rangle] \tag{3.49}$$

and

$$E^{(2)} = \sum_{\alpha=1}^{N} \frac{1}{2} [\langle \Phi_\alpha^{(1)} | (T + v_{ext})^{(1)} | \Phi_\alpha^{(0)} \rangle + \langle \Phi_\alpha^{(0)} | (T + v_{ext})^{(1)} | \Phi_\alpha^{(1)} \rangle + 2\langle \Phi_\alpha^{(0)} | (T + v_{ext})^{(2)} | \Phi_\alpha^{(0)} \rangle]. \tag{3.50}$$

These expressions have the advantage of simplicity compared to the variational expressions, but are unfortunately not variational. They are, however, of use when one considers mixed perturbations, such as arise when one is determining the off-diagonal elements of the dynamical matrix for example.

The formalism already developed can be readily extended to dealing with two or more simultaneous perturbations. Consider the following expansion of the external potential

$$v_{ext}(\lambda) = v_{ext}^{(0)} + \sum_{j_1} \lambda_{j_1} v_{ext}^{j_1} + \sum_{j_1 j_2} \lambda_{j_1} \lambda_{j_2} v_{ext}^{j_1 j_2} + \ldots \tag{3.51}$$

where j_1 and j_2 label the different perturbations, which are Hermitian. Then the mixed derivative of the electronic energy

$$E_{el}^{j_1 j_2} = \frac{1}{2} \frac{\partial^2 E_{el}}{\partial \lambda_{j_1} \partial \lambda_{j_2}} \tag{3.52}$$

is given by

$$E_{el}^{j_1 j_2} = \frac{1}{2}(\tilde{E}_{el}^{j_1 j_2} + \tilde{E}_{el}^{j_2 j_1}). \tag{3.53}$$

Here, $\tilde{E}_{el}^{j_1 j_2}$ is given by [81]

$$\begin{aligned}\tilde{E}_{el}^{j_1 j_2} = \sum_{\alpha}[&\langle \Phi_\alpha^{j_1} | H^{(0)} - \epsilon_\alpha^{(0)} | \Phi_\alpha^{j_2} \rangle + \langle \Phi_\alpha^{j_1} | v_{ext}^{j_2} | \Phi_\alpha^{(0)} \rangle \\ &+ \langle \Phi_\alpha^{(0)} | v_{ext}^{j_1} | \Phi_\alpha^{j_2} \rangle + \langle \Phi_\alpha^{(0)} | v_{ext}^{j_1 j_2} | \Phi_\alpha^{(0)} \rangle] \\ &+ \frac{1}{2}\int\int \left.\frac{\delta^2 E_{Hxc}}{\delta n(\mathbf{r})\delta n(\mathbf{r}')}\right|_{n^{(0)}} n^{j_1}(\mathbf{r}) n^{j_2}(\mathbf{r}') d\mathbf{r} d\mathbf{r}'.\end{aligned} \tag{3.54}$$

Defining a non-variational term, so called because it does not depend upon perturbed wavefunctions

$$E_{non-var}^{j_1 j_2} = \sum_{\alpha} \langle \Phi_\alpha^{(0)} | v_{ext}^{j_1 j_2} | \Phi_\alpha^{(0)} \rangle \tag{3.55}$$

the non-stationary expressions may be written as

$$\begin{aligned} E_{el}^{j_1 j_2} &= \frac{1}{2}\sum_{\alpha}(\langle \Phi_\alpha^{j_2} | v_{ext}^{j_1} | \Phi_\alpha^{(0)} \rangle + \langle \Phi_\alpha^{(0)} | v_{ext}^{j_1} | \Phi_\alpha^{j_2} \rangle) + E_{non-var}^{j_1 j_2} \\ &= \sum_{\alpha} \langle \Phi_\alpha^{j_2} | v_{ext}^{j_1} | \Phi_\alpha^{(0)} \rangle + E_{non-var}^{j_1 j_2} \\ &= \sum_{\alpha} \langle \Phi_\alpha^{(0)} | v_{ext}^{j_1} | \Phi_\alpha^{j_2} \rangle + E_{non-var}^{j_1 j_2}. \end{aligned} \tag{3.56}$$

These have been obtained under the assumption that $\Phi_\alpha^{j_1}$ is known; of course, there is no reason to stipulate this, and one may equally take it that $\Phi_\alpha^{j_2}$ is known exactly instead, in which case one would obtain analogous expressions, but involving $\Phi_\alpha^{j_1}$ instead.

It can seen further that these non-variational expressions provide a generalisation of Dalgarno's interchange theorem [82] to DFT, as

$$\langle \Phi_\alpha^{j_2} | v_{ext}^{j_1} | \Phi_\alpha^{(0)} \rangle = \langle \Phi_\alpha^{(0)} | v_{ext}^{j_1} | \Phi_\alpha^{j_2} \rangle \tag{3.57}$$

which follows trivially from equation 3.56.

3.7 Lattice Dynamics via DFPT

It is now time to begin considering the application of the theoretical framework discussed in the previous sections to the specific problem of determining the lattice dynamics of crystalline systems. It is convenient to express the energy of the crystal as

$$E_{tot}(\Delta\tau) = E_{tot}^{(0)} + \sum_{a\kappa\alpha}\sum_{b\kappa'\beta}\frac{1}{2}\left(\frac{\partial^2 E_{tot}}{\partial\tau_{\kappa\alpha}^a\partial\tau_{\kappa'\beta}^b}\right)\Delta\tau_{\kappa\alpha}^a\Delta\tau_{\kappa'\beta}^b + \ldots \tag{3.58}$$

where the $E_{tot}^{(1)}$ term has been ignored, as this term yields the force acting on the atom, which is, of course equal to zero at the minimum. Here $\Delta_{\kappa\alpha}^a$ is the displacement of atom κ from its equilibrium position τ_κ in the cell labelled a (with lattice vector $\mathbf{R}_a$) in the Cartesian direction α. In the harmonic approximation, this expansion is truncated after the second term. The force on a given atom is then

$$F_{\kappa\alpha}^{ab} = -\sum_{\kappa',\beta} C_{\kappa\alpha,\kappa'\beta}(a,b)\Delta\tau_{\kappa'\beta}^b \tag{3.59}$$

where the matrix of force constants is defined through

$$C_{\kappa\alpha,\kappa'\beta}(a,b) = \left(\frac{\partial^2 E_{tot}}{\partial\tau_{\kappa\alpha}^a\partial\tau_{\kappa'\beta}^b}\right). \tag{3.60}$$

The Fourier transform of this is then

$$\tilde{C}_{\kappa\alpha,\kappa'\beta}(\mathbf{q}) = \frac{1}{N}\sum_{ab} C_{\kappa\alpha,\kappa'\beta}(a,b)e^{-i\mathbf{q}\cdot(\mathbf{R}_a-\mathbf{R}_b)} \tag{3.61}$$

where N is the number of periodic cells in the crystal, and $\mathbf{q}$ is the wavevector of the phonon perturbation. This is connected to the dynamical matrix $\tilde{D}_{\kappa\alpha,\kappa'\beta}(\mathbf{q})$ through

$$\tilde{D}_{\kappa\alpha,\kappa'\beta}(\mathbf{q}) = \tilde{C}_{\kappa\alpha,\kappa'\beta}(\mathbf{q})/(M_\kappa M_{\kappa'})^{1/2}. \tag{3.62}$$

which can be demonstrated by substituting wave-like solutions of the form

$$\Delta\tau_{\kappa\alpha} = \frac{1}{\sqrt{M_\kappa}} e_{m\mathbf{q}}(\kappa\alpha)[e^{i(\mathbf{q}\cdot\tau_\kappa - \omega_m t)} + e^{-i(\mathbf{q}\cdot\tau_\kappa - \omega_m t)}] \tag{3.63}$$

into equation 3.61. This is a Hermitian matrix, as one would expect from Newton's second law, and its eigenvalues yield the phonon frequencies

$$\sum_{\kappa',\beta} \tilde{D}_{\kappa\alpha,\kappa'\beta}(\mathbf{q}) e_{m\mathbf{q}}(\kappa',\beta) = \omega_{m\mathbf{q}}^2 e_{m\mathbf{q}}(\kappa\alpha) \tag{3.64}$$

where $\omega_{m\mathbf{q}}$ is the phonon frequency associated with mode m, and $e_{m\mathbf{q}}(\kappa\alpha)$ is the phonon eigenvector for the same mode. It is easy to see that the connection between the dynamical matrix and the second order energy is then

$$\tilde{C}_{\kappa\alpha,\kappa'\beta}(\mathbf{q}) = 2E_{tot,-\mathbf{qq}}^{\tau^*_{\kappa\alpha}\tau_{\kappa'\beta}} \tag{3.65}$$

where we have adopted the notation

$$E_{tot,-\mathbf{qq}}^{\tau^*_{\kappa\alpha}\tau_{\kappa'\beta}} = \frac{1}{2}\frac{\partial^2 E_{tot,-\mathbf{qq}}}{\partial\tau^*_{\kappa\alpha}\partial\tau_{\kappa'\beta}}. \tag{3.66}$$

The subscript $\mathbf{q}$ labels the phonon wavevector at which the second order energy has been calculated.

3.7.1 Incommensurate Perturbations

It should perhaps be realised that one does not have to rely upon DFPT in order to calculate lattice dynamics as outlined in the previous section: it is possible to do so by finite differences. In this technique, each atom is displaced by some small displacement in each of the Cartesian directions. The force on the atom may be calculated using the Hellmann-Feynman theorem, and then it is straightforward to evaluate the force constant matrix using equation 3.61. One introduces supercells in order to handle perturbations of different $\mathbf{q}$-vectors.

The principal disadvantage of the finite difference approach is that it is not possible to calculate the phonon eigenvectors and eigenvalues at arbitrary $\mathbf{q}$-vectors. Instead,

one is limited to **q**-vectors that are commensurate with the underlying crystal periodicity. One of the major advantages of DFPT is that it is able to calculate responses at arbitrary **q**-vector. This can be seen by considering the following argument: the Sternheimer equation, written in terms of Bloch states is

$$P_{c,\mathbf{k+q}}(H_{KS}-\epsilon_{v\mathbf{k}})P_{c,\mathbf{k+q}}e^{i(\mathbf{k+q})\cdot\mathbf{r}}|u^{(1)}_{v\mathbf{k},\mathbf{q}}\rangle = -P_{c,\mathbf{k+q}}H^{(1)}_{KS}e^{i\mathbf{k}\cdot\mathbf{r}}|u^{(0)}_{v\mathbf{k}}\rangle \tag{3.67}$$

and defining, for a generic operator $\hat{O}$,

$$\hat{O}_{\mathbf{kk'}} = e^{-i\mathbf{k}\cdot\mathbf{r}}\hat{O}e^{i\mathbf{k'}\cdot\mathbf{r'}} \tag{3.68}$$

the Sternheimer equation may be written in terms of lattice periodic functions as

$$P_{c,\mathbf{k+q}}(H_{\mathbf{k+q,k+q}}-\epsilon_{v\mathbf{k}})P_{c,\mathbf{k+q}}|u^{(1)}_{v\mathbf{k},\mathbf{q}}\rangle = -P_{c,\mathbf{k+q}}H^{(1)}_{\mathbf{k+q,k}}|u^{(0)}_{v\mathbf{k}}\rangle. \tag{3.69}$$

The first order Hamiltonian is given by

$$H^{(1)}_{\mathbf{k+q,k}} = v^{(1)}_{ext,\mathbf{k+q,k}} + \int \left.\frac{\delta^2 E_{Hxc}}{\delta n(\mathbf{r})\delta n(\mathbf{r'})}\right|_{n^{(0)}} \bar{n}^{(1)}_{\mathbf{q}}(\mathbf{r'})e^{-i\mathbf{q}\cdot(\mathbf{r}-\mathbf{r'})}d\mathbf{r'} \tag{3.70}$$

with

$$\bar{n}^{(1)}_{\mathbf{q}}(\mathbf{r}) = e^{-i\mathbf{q}\cdot\mathbf{r}}n^{(1)}_{\mathbf{q}}(\mathbf{r}). \tag{3.71}$$

The advantage of equation 3.69 compared to finite difference methods is that only lattice periodic functions are required. Thus the response to *any* **q**-vector may be computed by solving this equation, then simply multiplying the resulting first order periodic function $u^{(1)}_{v\mathbf{k},\mathbf{q}}(\mathbf{r})$ by a phase factor incorporating the relevant **q**-vector. A further useful property of equation 3.69 is that the responses to perturbations at differing wave vectors **q** decouple, allowing one to compute the response to each wave vector separately. Thus the workload involved in determining the lattice dynamics is essentially independent of the phonon wavelength [73].

It is worth noting in passing here that non-commensurate potentials lead, in general, to non-Hermitian first order potentials [83]; however, it is still possible to show that

the second order energy is real, as expected, and that one may still use the theoretical machinery developed above.

3.7.2 Electronic and Ionic Contributions

The dynamical matrix is directly related to the second order variation in the Kohn-Sham energy; of course, this has an electronic and ionic contribution. Correspondingly, it is possible to split the dynamical matrix:

$$\tilde{C}_{\kappa\alpha,\kappa'\beta}(\mathbf{q}) = \tilde{C}_{el,\kappa\alpha,\kappa'\beta}(\mathbf{q}) + \tilde{C}_{Ew,\kappa\alpha,\kappa'\beta}(\mathbf{q}) \tag{3.72}$$

where the second term is that due to the ionic contribution.

Thus far, only a very general form of the second order contribution to the electronic energy has been discussed. It is now necessary to begin to examine how the formulae obtained earlier can be tailored to the specific case of a phonon perturbation.

3.7.3 The Electronic Contribution

Given the discussion above, it is possible to write the electronic contribution to the variational second order energy as [83]

$$\begin{aligned} E^{(2)}_{el,-\mathbf{q},\mathbf{q}}\{u^{(0)};u^{(1)}\} \;=\; & \frac{\Omega_0}{(2\pi)^3}\int_{BZ}\sum_{m}^{occ} s(\langle u^{(1)}_{m\mathbf{k},\mathbf{q}}|H^{(0)}_{\mathbf{k}+\mathbf{q},\mathbf{k}+\mathbf{q}} - \epsilon^{(0)}_{m\mathbf{k}}|u^{(1)}_{m\mathbf{k},\mathbf{q}}\rangle \\ & + \langle u^{(1)}_{m\mathbf{k},\mathbf{q}}|v^{(1)}_{sep,\mathbf{k}+\mathbf{q},\mathbf{k}}|u^{(0)}_{m\mathbf{k}}\rangle + \langle u^{(0)}_{m\mathbf{k}}|v^{(1)}_{sep,\mathbf{k},\mathbf{k}+\mathbf{q}}|u^{(1)}_{m\mathbf{k},\mathbf{q}}\rangle \\ & + \langle u^{(0)}_{m\mathbf{k}}|v^{(2)}_{sep,\mathbf{k},\mathbf{k}}|u^{(0)}_{m\mathbf{k}}\rangle)d\mathbf{k} + 2\pi\Omega_0\sum_{\mathbf{G}}\frac{|\bar{n}^{(1)}_{\mathbf{q}}(\mathbf{G})|^2}{|\mathbf{q}+\mathbf{G}|^2} \\ & + \frac{1}{2}\int_{\Omega_0}([\bar{n}^{(1)}_{\mathbf{q}}(\mathbf{r})]^{\star}\bar{v}^{(1)}_{loc,\mathbf{q}}(\mathbf{r}) + \bar{n}^{(1)}_{\mathbf{q}}(\mathbf{r})\bar{v}^{(1)\star}_{loc,\mathbf{q}})d\mathbf{r} \\ & + \frac{1}{2}\int_{\Omega_0}\left.\frac{dv_{xc}}{dn}\right|_{n^{(0)}(\mathbf{r})}|\bar{n}^{(1)}_{\mathbf{q}}(\mathbf{r})|^2 d\mathbf{r} \\ & + \int_{\Omega_0} n^{(0)}(\mathbf{r})v'^{(2)}_{loc}(\mathbf{r})d\mathbf{r} \end{aligned} \tag{3.73}$$

where v_{sep} refers to the non-local (separable) part of the pseudopotential, and v_{loc}

refers to the local part. Note that in the Hartree contribution, the $\mathbf{G} = \mathbf{0}$ term is included; as $\mathbf{q}$ has been taken to be non-zero, there is no divergence. In the case where $\mathbf{q} = \mathbf{0}$, then the singularities arising from the vanishing denominator of the Hartree term may be dealt with as an homogeneous electric field associated with the atomic displacements. Working at the level of linear response, the response to a linear combination of perturbations is equal to a linear combination of the response of the system to each perturbation. It is therefore possible to calculate the response of the system to a phonon perturbation at $\mathbf{q} = \mathbf{0}$ neglecting the singularities arising from the $\mathbf{G} = \mathbf{0}$ terms, and then to combine this with the system response to an homogeneous field, calculated separately. The treatment of electric fields within DFPT and the method of combining this with a phonon perturbation is elaborated upon in a later section.

3.7.4 The Ionic Contribution

The ionic contribution to the dynamical matrix may be obtained by using the Ewald summation [81, 84, 85]. This is based upon a splitting of the real-space Coulomb summation in real space into two infinite summations, one over reciprocal lattice vectors, and one over real-space lattice vectors:

$$\begin{aligned}\sum_{\mathbf{l}} \frac{1}{|\mathbf{R}_1 + \mathbf{l} - \mathbf{R}_2|} &= \frac{2}{\sqrt{\pi}} \sum_{\mathbf{l}} \int_{\eta}^{\infty} e^{-|\mathbf{R}_1 + \mathbf{l} - \mathbf{R}_2|^2 \rho^2} d\rho \\ &+ \frac{2\pi}{\Omega} \sum_{\mathbf{G}} \int_{0}^{\eta} e^{-\frac{\mathbf{G}^2}{4\rho^2}} e^{i(\mathbf{R}_1 - \mathbf{R}_2)\cdot\mathbf{G}} \frac{1}{\rho^3} d\rho \end{aligned} \tag{3.74}$$

where $\mathbf{l}$ are lattice vectors, and η is a parameter that may be adjusted. The motivation for this splitting is that the long-range of the Coulomb interaction ensures that any direct summation (in real or reciprocal space) will be slowly convergent. The identity in equation 3.74 holds true for any positive value of η, and the value of this can be chosen appropriately such that rapid convergence of the two summations is achieved, typically for only a few reciprocal and real-space lattice vectors.

Using this, and correctly taking into account the exact cancellation that takes place for the $\mathbf{G} = \mathbf{0}$ contributions yields an ion-ion interaction energy

$$E_{ion} = \frac{1}{2}\sum_{I,J} Z_I Z_J e^2 \Big(\sum_{\mathbf{l}} \frac{\mathrm{erfc}(\eta|\mathbf{R}_1 + \mathbf{l} - \mathbf{R}_2|)}{|\mathbf{R}_1 + \mathbf{l} - \mathbf{R}_2|} - \frac{2\eta}{\sqrt{\rho}} + \sum_{\mathbf{G}\neq\mathbf{0}} \frac{4\pi}{\Omega|\mathbf{G}|^2} e^{-\frac{\mathbf{G}^2}{4\rho^2}} \cos[(\mathbf{R}_1 - \mathbf{R}_2)\cdot\mathbf{G}] - \frac{\pi}{\eta^2\Omega} \Big). \tag{3.75}$$

The contribution of the ionic energy to the dynamical matrix may then be obtained using

$$\tilde{C}_{ion,\kappa\alpha,\kappa'\beta}(\mathbf{q}) = \bar{C}_{ion,\kappa\alpha,\kappa'\beta}(\mathbf{q}) - \delta_{\kappa,\kappa'} \sum_{\kappa'} \bar{C}_{ion,\kappa\alpha,\kappa'\beta}(\mathbf{q}=\mathbf{0}) \tag{3.76}$$

where

$$\bar{C}_{ion,\kappa\alpha,\kappa'\beta}(\mathbf{q}) = Z_\kappa Z_{\kappa'} \Big[\sum_{\mathbf{G},\mathbf{K}=\mathbf{G}+\mathbf{q}} \frac{4\pi}{\Omega_0} \frac{K_{\alpha'} K_{\beta'}}{K^2} e^{i\mathbf{K}\cdot(\tau_\kappa - \tau_{\kappa'})} e^{-\frac{K^2}{4\eta^2}} - \sum_a \eta^3 e^{i\mathbf{q}\cdot\mathbf{R}_a} H^{iso}_{\alpha'\beta'}(\eta \mathbf{d}_{a,\kappa\kappa'}) - \frac{4}{3\sqrt{\pi}}\eta^3 \delta_{\kappa\kappa'} \Big] \tag{3.77}$$

with $\mathbf{d}_{a,\kappa\kappa'} = \mathbf{R}_a + \tau_{\kappa'} - \tau_\kappa$, and a a summation index over real-space lattice vectors, and

$$H^{iso}_{\alpha\beta}(x) = \frac{x_\alpha x_\beta}{x^2}\Big[\frac{3}{x^3}\mathrm{erfc}(x) + \frac{2}{\sqrt{\pi}} e^{-x^2}\Big(\frac{3}{x^2} + 2\Big)\Big] - \delta_{\alpha\beta}\Big(\frac{\mathrm{erfc}(x)}{x^3} + \frac{2}{\sqrt{\pi}}\frac{e^{-x^2}}{x^2}\Big). \tag{3.78}$$

3.8 Electric Field Response

It is now time to begin considering how to calculate the response of a crystalline system to an homogeneous electric field. The response of insulators and semiconductors to applied electric fields is of interest as it determines their dielectric, piezoelectric

and ferroelectric behaviour. A full understanding of the lattice dynamics of ionic systems requires that the long-range electric fields associated with long wavelength longitudinal phonons be treated adequately. Further, understanding the electrodynamics of insulators and semiconductors allows the optical properties to be calculated from, and understood in terms of, the electronic structure.

Homogeneous fields present significant difficulties when using Born-von Karmann boundary conditions. In order to understand why this is the case, consider the potential

$$v_{scr}(\mathbf{r}) = \sum_{\alpha} \varepsilon_{mac,\alpha} r_{\alpha} \tag{3.79}$$

where $\varepsilon_{mac,\alpha}$ is the macroscopic field in Cartesian direction α, and $v_{scr}(\mathbf{r})$ is the resulting *screened* potential. This is unbounded from below in an infinite solid, so has no well-defined ground state. There is also an issue of stability of the crystalline band structure when such an external perturbing potential is applied: for large values of ε the possibility exists for valence band electrons to Zener tunnel into the conduction band [86, 88]. The perturbation is, as discussed in some detail by Nenciu [86], non-analytic; upon application of an external field, the discrete band structure of the insulator changes to a continuum of eigenvalues spanning the whole energy axis [87]. This is true even for fields of infinitesimal strength.

The position operator also suffers in that it is *ill-defined* in a periodic crystal. The lattice periodicity ensures that one is dealing with a periodic Hilbert space; thus for an operator to be well-defined in this Hilbert space, the result of acting upon an eigenstate of the system must be a function that still resides in this periodic Hilbert space. The position operator's incompatibility with the underlying lattice periodicity ensures that this condition can not be satisfied, and it is hence not a true operator in periodic systems.

One must therefore attempt to surmount these theoretical difficulties. The first issue to confront is the absence of a groundstate; as discussed by Souza *et al.* [88] this can lead to "runaway" solutions, *i.e.* that the energy may always be lowered by transferring charge from the valence bands in one region to conduction bands

in a distant region. One approach, followed by Gonze and Nunes [89] and Nunes and Vanderbilt [90], is to introduce a finite electric field; for sufficiently small values, Zener tunnelling may be neglected. This preserves the insulating state of the unperturbed crystal, including the band structure and the periodicity of the charge density. One then considers the energy functional

$$E[\{w^{\varepsilon}\}, \varepsilon] = E_{KS} - \Omega\varepsilon \cdot \mathbf{P} \tag{3.80}$$

where Ω is the unit cell volume, $\{w^{\varepsilon}\}$ are real space Wannier functions [1], and $\mathbf{P}$ is the polarisation, which may be obtained using Berry phase methods [91, 92, 93, 94]. Note that the position operator is no longer required. The state underlying this expression is a resonance [89], and as such the energy functional is only well defined for Wannier functions with a finite cut-off distance. An understanding of the resonant nature of the solution of equation 3.80 can be provided as follows: the solution will be that which is generated from the zero field case when the field is adiabatically switched on, whilst retaining the periodicity of the electron density. If the field dependent response of the crystal is measured experimentally, then to measure "static" properties, the field must be switched on on a time scale slow compared to usual electronic processes, but fast compared to the tunnelling rate at the maximum applied field. Thus in reality, the object of experimental study is a long-lived resonance of the finite field Hamiltonian, rather than a true ground state. This corresponds to what equation 3.80 can be physically interpreted as [90].

An alternative is the approach proposed by Souza *et al.* [88], based upon a reciprocal space implementation of the above functional. In this scheme, discretisation of a uniform k-point mesh of $N_1 \times N_2 \times N_3$ k-points within periodic boundary conditions imposes a toroidal topology over a supercell of dimensions $L_i = N_i a_i$ ($i = 1, 2,$

[1] A note on the use of Wannier functions in this functional: because the energy functional in 3.80 represents a resonance rather than a true groundstate, wavefunctions with a finite range must be used to ensure that the problem is well-defined and to prevent Zener tunnelling from conduction band to valence band. Wannier functions, with their exponential decay (in insulators), are ideal for this. Although one could argue that it should be possible to use any set of localised orbitals, in the modern theory of polarisation (MTP) the Berry phase expression used to calculate $\mathbf{P}$ takes a particularly transparent and physically appealing form, as the polarisation is then expressed as the polarisation of the centres of charge of the Wannier functions. In practical applications polarised Bloch orbitals may be used rather than Wannier functions; then a reciprocal space discretisation is required to prevent Zener tunnelling. This is the reciprocal space equivalent of the real-space cut-off required for Wannier functions.

3). In order for a minimum of the energy functional to exist, then the value of ε must be sufficiently small that Zener tunnelling is suppressed. Provided that the distance across which electrons must travel to lower their energy is larger than the ring perimeter, $L_i = N_i a_i$ then this will be true. This can be seen by imagining that the field causes the energy bands of the insulator to spatially tilt; to prevent tunnelling, then $|\varepsilon \cdot \mathbf{a}_i| \leq |\varepsilon_c \cdot \mathbf{a}_i|$ where $e|\varepsilon_c \cdot \mathbf{a}_i| \approx E_{gap}/N_i$ and E_{gap} is the bandgap.

These methods are naturally suited to calculating non-linear responses to electric fields, and indeed, Gonze and Nunes [89] have obtained expressions to arbitrary order. However, in this work it is sufficient to examine the linear response of condensed matter systems to external fields in zero field conditions. By working in zero field conditions, the issues discussed above with respect to band structure stability, and the non-analyticity of the perturbing potential, may be alleviated, with the result that the problem being considered is theoretically well-defined. The sole remaining conceptual difficulty to be overcome is the position operator.

It is possible to obtain a bounded potential that is commensurate with the lattice periodicity by introducing a sinusoidal perturbation and taking the long wavelength limit

$$v(\mathbf{r}) = \lim_{\mathbf{q}\to 0} \lambda \frac{2 \sin \mathbf{q} \cdot \mathbf{r}}{|\,\mathbf{q}\,|} \tag{3.81}$$

which gives a linear potential. Since $\mathbf{q}$ is in the direction of the applied field, this corresponds to a longitudinal field.

3.8.1 Treatment of Electronic Screening

It should be noted that the external potential due to the applied field should be a *screened* potential, that is, one should incorporate the fact that the electrons will be polarised by the bare applied field resulting in an internal change of field. As is discussed in detail in the appendix, the long-wave method can adequately treat the screening, but at the cost of needing to introduce the derivative of the groundstate

wavefunctions with respect to their wave vector, *i.e.*

$$u_{m\mathbf{k}}^{k_\alpha} = \frac{du_{m\mathbf{k}}^{(0)}}{dk_\alpha}. \tag{3.82}$$

Heuristically, this can be understood as the operator d/dk_α is proportional to the position operator in reciprocal space.

3.8.2 Variational Second Order Energy

Substituting the derivative of the ground state wavefunctions with respect to k-vector, as in equation 3.82, for the position operator, a variational expression for the second order energy may now be constructed:

$$\begin{aligned} E_{el}^{\varepsilon_\alpha^\star \varepsilon_\alpha}\{u^{(0)}; u^{\varepsilon_\alpha}\} \;=\; & \frac{\Omega_0}{(2\pi)^3}\int_{BZ}\sum_{m}^{occ} s(\langle u_{m\mathbf{k}}^{\varepsilon_\alpha}|H_{\mathbf{k},\mathbf{k}}^{(0)} - \epsilon_{\mathbf{k}}^{(0)}|u_{m\mathbf{k}}^{\varepsilon_\alpha}\rangle \\ & + \langle u_{m\mathbf{k}}^{\varepsilon_\alpha}|iu_{m\mathbf{k}}^{k_\alpha}\rangle + \langle iu_{m\mathbf{k}}^{k_\alpha}|u_{m\mathbf{k}}^{\varepsilon_\alpha}\rangle)d\mathbf{k} \\ & + \frac{1}{2}\int_{\Omega_0}\left.\frac{dv_{xc}}{dn}\right|_{n^{(0)}(\mathbf{r})}|n^{\varepsilon_\alpha}(\mathbf{r})|^2 \\ & + 2\pi\Omega_0\sum_{\mathbf{G}\neq\mathbf{0}}\frac{|n^{\varepsilon_\alpha}(\mathbf{G})|^2}{|\mathbf{G}|^2} \end{aligned} \tag{3.83}$$

where

$$\langle iu_{m\mathbf{k}}^{k_\alpha}| = (-i)\langle u_{m\mathbf{k}}^{k_\alpha}| \tag{3.84}$$

subject to the constraints

$$\langle u_{m\mathbf{k}}^{(0)}|u_{n\mathbf{k}}^{\varepsilon_\alpha}\rangle = 0. \tag{3.85}$$

To understand the connection between this variational energy and the polarisability, consider the following molecular Hamiltonian

$$H' = H - \mu\cdot\varepsilon \tag{3.86}$$

where H is the unperturbed molecular Hamiltonian, and μ is the molecular dipole moment. Expanding this as

$$\mu_\alpha(\varepsilon_\alpha) = \mu_{0,\alpha} + \sum_{\beta=1}^{3} \alpha_{\alpha\beta}\varepsilon_\beta + \dots \tag{3.87}$$

where $\mu_{0,\alpha}$ is the dipole moment in direction α in the absence of an external field, and $\alpha_{\alpha\beta}$ is the linear polarisability, then it can easily be seen that

$$\alpha_{\alpha\beta} = \frac{\partial \mu_\alpha}{\partial \varepsilon_\beta} \tag{3.88}$$

which can be written as

$$\alpha_{\alpha\beta} = -\frac{\partial^2 E}{\partial \varepsilon_\alpha \varepsilon_\beta}. \tag{3.89}$$

Thus the variational second order energy is directly related to the polarisability. Although this argument has been pursued using a molecular Hamiltonian, there is no reason why the same definition may not be used to calculate the bulk polarisability of a crystalline system.

3.8.3 The Dielectric Permittivity

The dielectric permittivity tensor is defined, in the linear regime, using

$$\mathcal{D}_{mac,\alpha} = \sum_\beta \epsilon_{\alpha\beta}\varepsilon_{mac,\beta} \tag{3.90}$$

which, using simple electrostatics, may be written as

$$\mathcal{D}_{mac,\alpha} = \varepsilon_{mac,\alpha} + 4\pi \sum_\beta \epsilon_{\alpha\beta}\mathcal{P}_{mac,\beta} \tag{3.91}$$

where $\mathcal{D}_{mac,\alpha}$ is the macroscopic displacement field and $\varepsilon_{mac,\beta}$ is the screened macroscopic electric field in directions α and β, respectively, and $\mathcal{P}_{mac,\beta}$ is the macroscopic polarisation. Physically, therefore, the dielectric permittivity tensor can be seen to

incorporate the effect of screening within the solid, as it is the coefficient of proportionality between the external bare field (the displacement field) and the screened field within the crystal itself. Of course, in general the displacement field and the polarisation will include ionic contributions. These will be neglected for now, and considered in a later section. Using equation 3.91, the electronic contribution to the dielectric permittivity tensor, ϵ^{∞} may be written

$$\epsilon^{\infty}_{\alpha\beta} = \delta_{\alpha\beta} + 4\pi \frac{\partial \mathcal{P}_{mac,\alpha}}{\partial \varepsilon_{mac,\beta}} \tag{3.92}$$

which can be connected to the variational second order energy via

$$\epsilon^{\infty}_{\alpha\beta} = \delta_{\alpha\beta} - \frac{4\pi}{\Omega_0} 2E_{el}^{\varepsilon^{\star}_{\alpha}\varepsilon_{\beta}} \tag{3.93}$$

where

$$E_{el}^{\varepsilon^{\star}_{\alpha}\varepsilon_{\beta}} = \frac{1}{2}\frac{\partial^2 E_{el}}{\partial \varepsilon_{\alpha} \partial \varepsilon_{\beta}}. \tag{3.94}$$

3.9 Phonon-Electric Field Coupling: Born Effective Charges

In polar crystals, long range macroscopic electric fields arise that are associated with long wave longitudinal optical phonons. These electric fields are a result of the long range character of the Coulomb interaction [73], and are responsible for the well-known phenomenon of LO-TO splitting, that is, the shift in frequency between longitudinal optical and transverse optical phonons at the Brillouin zone centre.

The origin of this splitting can be understood most readily if one considers an argument due to Yu and Cardona [95]. Consider a long wave TO phonon propagating along the [111] direction in a zinc-blende polar crystal. The positive and negative ions lie on separate planes perpendicular to the direction of propagation. Under excitation of a TO mode, these planes slide past each other, which is analogous to the oppositely charged plates of a capacitor moving past each other whilst their separation is fixed. Now consider the situation when the ions are excited by a LO mode. In this case, the planes move apart, as can be seen in figure 3.1. In the

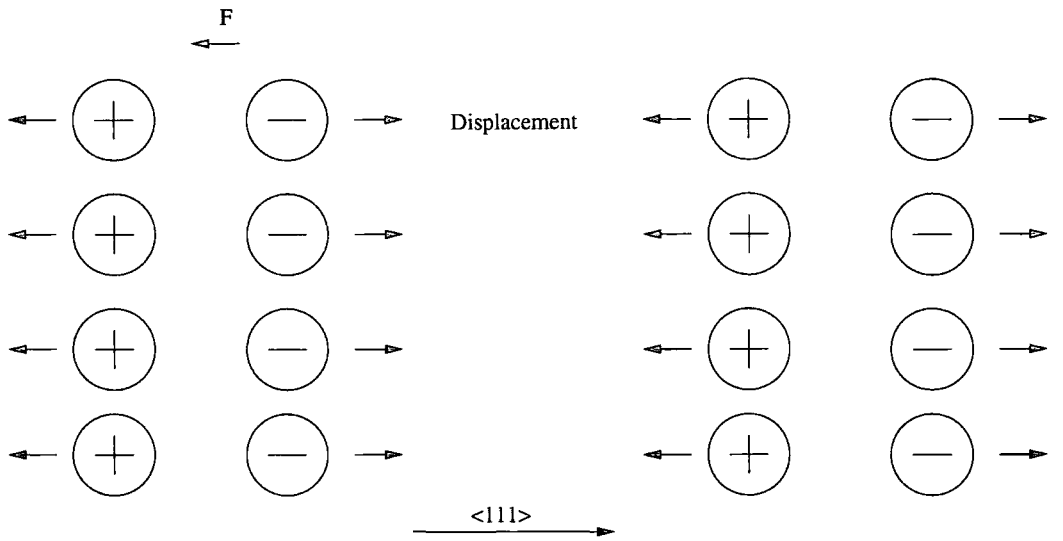

Figure 3.1: Illustration of the displacements of atoms within an ionic crystal during a long-wave longitudinal optical phonon. F is the restoring force due to the displacements of the charges shown. It is this that leads to the LO-TO splitting. Note the similarity to the situation in a parallel-plate capacitor.

capacitor, this increase in separation of the charged plates will be accompanied by an extra force due to the electric field between the plates. Similarly, in the crystal, the LO mode is accompanied by an extra restoring force due to the Coulomb interaction. This additional force then leads to the frequency change.

This coupling between optical phonons and electric fields is quantified by the *Born effective charge*, which is defined through

$$Z^{\star}_{\kappa,\beta\alpha} = \Omega_0 \frac{\partial \mathcal{P}_{mac,\beta}}{\partial \tau_{\kappa\alpha}(\mathbf{q}=\mathbf{0})}, \tag{3.95}$$

i.e. the Born effective charge is the coefficient of proportionality between a change in macroscopic polarisation in direction β caused by an atomic displacement in direction α under conditions of zero external field.

If one considers the electric enthalpy, defined through

$$\tilde{E}[u_{n\mathbf{k}};\varepsilon] = E_{KS} - \Omega_0 \sum_{\alpha} \mathcal{P}_{mac,\alpha}\varepsilon_{\alpha} \tag{3.96}$$

it can be readily seen that

$$\mathcal{P}_{mac,\alpha} = -\frac{1}{\Omega_0}\frac{\partial \tilde{E}}{\partial \varepsilon_\alpha} \tag{3.97}$$

allowing the effective charge to be written as

$$Z^{\star}_{\kappa,\alpha\beta} = -\frac{\partial^2 \tilde{E}}{\partial \varepsilon_\beta \partial \tau_{\kappa,\alpha}} = \frac{\partial F_{\kappa,\alpha}}{\partial \varepsilon_\beta}\bigg|_{\tau_{\kappa\alpha}=0} \tag{3.98}$$

and thus an equivalent definition is as the coefficient of proportionality relating a change in the force in direction α due to an homogeneous electric field applied in direction β with nuclei clamped in place.

The effective charge may be decomposed into ionic and electronic contributions:

$$Z^{\star}_{\kappa,\alpha\beta} = Z_\kappa \delta_{\alpha\beta} + Z^{el}_{\kappa,\alpha\beta} \tag{3.99}$$

where the first term is simply the ionic charge. In the following, discussion will centre around how to calculate the electronic contribution to the effective charge. The three definitions of the effective charge are formally equivalent, but lead to different approaches to the calculation of the effective charge, which will now be considered.

3.9.1 Berry Phase Approach

Taking the effective charge as defined in equation 3.95, then it is possible to calculate it using the King-Smith and Vanderbilt expression [96] for the polarisation

$$\mathcal{P}^{el}_{mac,\alpha} = -\frac{1}{(2\pi)^3} i \sum_n^{occ} s \int_{BZ} \langle u_{n\mathbf{k}} | \partial/\partial k_\alpha | u_{n\mathbf{k}} \rangle d\mathbf{k}. \tag{3.100}$$

This is a *Berry phase* [91, 92], and such objects are discussed in depth in references [92, 93, 94]. Essentially the Berry phase is a geometrical phase that arises in systems in which there is a continuous parameter space through which the system state may travel in a closed path. In crystalline solids, this parameter space is the

reciprocal space bandstructure [92]. The Berry phase is a well-defined gauge invariant quantity [97, 93, 94, 92], even though the individual matrix elements comprising this equation are *not* well-defined. This is because, although working with Bloch's theorem, the phase of wavefunctions at neighbouring points in the Brillouin zone is arbitrary, and will depend upon the diagonalisation routine used. Thus, the phases of wavefunctions at neighbouring k-points are essentially unrelated.

Substituting the King-Smith and Vanderbilt expression for the polarisability into the definition of the effective charge in equation 3.95, and carrying out some algebraic manipulations allows one to write

$$Z^{el}_{\kappa,\alpha\beta} = -2\frac{\Omega_0}{(2\pi)^3} i \sum_n^{occ} s \int_{BZ} \left\langle \frac{\partial u_{n\mathbf{k}}}{\partial \tau_{\kappa,\alpha}} \middle| \frac{\partial u_{n\mathbf{k}}}{\partial k_\beta} \right\rangle d\mathbf{k}. \tag{3.101}$$

Thus it is possible to obtain the Born charge from a knowledge of the first-order wavefunctions with respect to a phonon perturbation, and the derivative of the groundstate Kohn-Sham orbitals with respect to their wavevector.

3.9.2 Mixed Second Derivative of the Electric Enthalpy

Calculating the effective charge as the mixed second derivative of the electric enthalpy allows the following stationary expression to be obtained:

$$\begin{aligned} Z^{el}_{\kappa,\alpha\beta} \;=\; & 2\Big[\frac{\Omega_0}{(2\pi)^3}\int_{BZ}\sum_n^{occ} s(\langle u^{\tau_{\kappa,\alpha}}_{n\mathbf{k},\mathbf{q}=\mathbf{0}}|H^{(0)}_{\mathbf{k},\mathbf{k}} - \epsilon^{(0)}_{n\mathbf{k}}|u^{\varepsilon_\beta}_{n\mathbf{k}}\rangle \\ & + \langle u^{\tau_{\kappa,\alpha}}_{n\mathbf{k},\mathbf{q}=\mathbf{0}}|iu^{k_\beta}_{n\mathbf{k}}\rangle + \langle u^{(0)}_{n\mathbf{k}}|v^{\tau_{\kappa,\alpha}}_{sep,\mathbf{k},\mathbf{k}}|u^{\varepsilon_\beta}_{n\mathbf{k}}\rangle)d\mathbf{k} \\ & + \frac{1}{2}\int_{\Omega_0} v^{\prime\tau_{\kappa,\alpha}}_{loc,\mathbf{q}=\mathbf{0}}(\mathbf{r})[n^{\varepsilon_\beta}(\mathbf{r})]^\star d\mathbf{r} \\ & + \frac{1}{2}\int_{\Omega_0} \frac{dv_{xc}}{dn}\Big|_{n^{(0)}(\mathbf{r})} [n^{\tau_{\kappa,\alpha}}_{\mathbf{q}=\mathbf{0}}(\mathbf{r})]^\star n^{\varepsilon_\beta}(\mathbf{r})d\mathbf{r} \\ & + 2\pi\Omega_0 \sum_{\mathbf{G}\neq\mathbf{0}} \frac{[n^{\tau_{\kappa,\alpha}}_{\mathbf{q}=\mathbf{0}}(\mathbf{G})]^\star n^{\varepsilon_\beta}(\mathbf{G})}{|\mathbf{G}|^2}\Big] \end{aligned} \tag{3.102}$$

which will yield the electronic contribution to the effective charge at the minimum.

3.9.3 Derivative of the Atomic Force

Expressing the effective charge as the derivative of the atomic force, as in equation 3.98, allows one to utilise the Hellmann-Feynman theorem, yielding

$$Z^{el}_{\kappa,\alpha\beta} = 2\Big[\frac{\Omega_0}{(2\pi)^3}\int_{BZ}\sum_{n}^{occ} s\langle u^{(0)}_{n\mathbf{k}}|v^{\tau_{\kappa,\alpha}}_{sep,\mathbf{k},\mathbf{k}}|u^{\varepsilon_\beta}_{m\mathbf{k}}\rangle d\mathbf{k} + \frac{1}{2}\int_{\Omega_0} v^{\prime\tau_{\kappa,\alpha}}_{loc,\mathbf{q}=\mathbf{0}}(\mathbf{r})[n^\beta(\mathbf{r})]^* d\mathbf{r}\Big] \tag{3.103}$$

which requires only a knowledge of the first-order wavefunctions with respect to an electric field perturbation and the first-order pseudopotential with respect to a phonon perturbation.

3.9.4 Equivalence of Methods

These three expressions are formally equivalent, and it is instructive to demonstrate this. From the variational expression, equation 3.102, one has the freedom to assume that either $u^{\varepsilon\alpha}$ or $u^{\tau\kappa,\alpha}$ are known, that is, that the appropriate Sternheimer equations are satisfied. Substituting in these Sternheimer equations allows one to then obtain the non-stationary expressions. The non-stationary expressions, although more sensitive to wavefunction convergence, do share the useful property that they are more convenient to work with. Indeed, they allow the effective charge to be determined in a 'post-process' calculation, immediately following an electric field or phonon linear response calculation.

3.10 Low-Frequency Dielectric Permittivity

Of course, in general, the dielectric permittivity will also have a contribution from the ions. This is because the applied field will cause the ions to move, and hence a polarisation will be induced. This polarisation is directly connected to the Born effective charge. The low-frequency permittivity is then the sum of the electronic

response and the ionic response and may be written [81, 98]

$$\epsilon_{\alpha\beta}(\omega) = \epsilon^{\infty}_{\alpha\beta} + \frac{4\pi}{\Omega_0}\sum_m \frac{S_{m,\alpha\beta}}{\omega_m^2 - \omega^2} \tag{3.104}$$

where $S_{m,\alpha\beta}$ is the mode oscillator strength, which is defined through [81]

$$\begin{aligned} S_{m,\alpha\beta} = &\left(\sum_{\kappa\alpha'} Z^{\star}_{\kappa,\alpha\alpha'} U^{\star}_{m\mathbf{q}=\mathbf{0}}(\kappa\alpha')\right) \\ &\times\left(\sum_{\kappa'\beta'} Z^{\star}_{\kappa',\beta\beta'} U^{\star}_{m\mathbf{q}=\mathbf{0}}(\kappa'\beta')\right). \end{aligned} \tag{3.105}$$

It is thus relatively easy to calculate as part of a post-process step once the normal modes and the response to an external field have been determined.

3.11 LO-TO Splitting

As alluded to earlier, the long range electric fields associated with long-wave longitudinal phonons are responsible for the phenomenon of LO-TO splitting, that is, the removal of degeneracy between the LO and TO phonons at the Brillouin zone centre. In order to deal with this, one must first consider the behaviour of the dynamical matrix as $\mathbf{q} \to \mathbf{0}$. It should be noted that the LO-TO splitting depends upon the direction in which one approaches the Γ-point, and this anisotropy is accessible to experiment. In a later chapter this direction dependence of the LO-TO splitting will be calculated for α-quartz. In the $\mathbf{q} \to \mathbf{0}$ limit, the dynamical matrix may be split [81, 98] into an analytic and non-analytic contribution:

$$\tilde{C}_{\kappa\alpha,\kappa'\beta}(\mathbf{q} \to \mathbf{0}) = \tilde{C}_{\kappa\alpha,\kappa'\beta}(\mathbf{q} = \mathbf{0}) + \tilde{C}^{NA}_{\kappa\alpha,\kappa'\beta}(\mathbf{q} \to \mathbf{0}) \tag{3.106}$$

where the non-analytic term is given by

$$\tilde{C}^{NA}_{\kappa\alpha,\kappa'\beta}(\mathbf{q} \to \mathbf{0}) = \frac{4\pi}{\Omega_0}\frac{(\mathbf{q}\cdot\mathbf{Z}^{\star}_{\kappa})_{\alpha}(\mathbf{q}\cdot\mathbf{Z}^{\star}_{\kappa'})_{\beta}}{\sum_{\alpha\beta} q_{\alpha}\epsilon^{\infty}_{\alpha\beta}q_{\beta}} \tag{3.107}$$

which can be seen to correspond to $1/r^3$ behaviour in real space, corresponding to dipole-dipole interactions [81]. These dipoles are created when the ions within an ionic semiconducting or insulating crystal are displaced in a long-wave longitudinal phonon. It should perhaps be noted that it is possible for the Born effective charge to vanish by symmetry, and non-analytic contributions to the dynamical matrix still exist. This is because, although symmetry may forbid a dipole being formed by an atomic displacement, it does not forbid higher order moments, such as quadrupoles and octupoles being set up. However, these contributions shall not be considered in this work.

In order to simplify the analysis, it will be assumed that the LO eigendisplacements of $\tilde{C}(\mathbf{q} \rightarrow \mathbf{0})$ are the same as those of $\tilde{C}(\mathbf{q} = \mathbf{0})$, even if the corresponding frequencies are not identical. This allows the following relationship to be obtained:

$$\omega_m^2(\mathbf{q} \rightarrow \mathbf{0}) = \omega_m^2(\mathbf{q} = \mathbf{0}) + \left(\frac{4\pi}{\Omega_0}\right) \frac{\sum_{\alpha\beta} q_\alpha S_{m,\alpha\beta} q_\beta}{\sum_{\alpha\beta} q_\alpha \epsilon^\infty_{\alpha\beta} q_\beta} \tag{3.108}$$

which directly connects the LO-TO splitting to the Born effective charge, as promised.

It is worth noting that the above analysis could be extended in order to obtain the Lyddane-Sachs-Teller relationship [81]. However, in this work, consideration will be restricted to the case of the Coulomb gauge, that is, the retardation of the Coulomb interaction will be neglected, and the above analysis of coupling between lattice degrees of freedom and electrical degrees of freedom will suffice.

3.12 Infra-red Spectroscopy

Infra-red (IR) spectroscopy represents a powerful and flexible experimental technique that may be used to characterise materials. It provides direct information about the potential energy surface in the vicinity of the equilibrium position, and thus provides a probe of the structural and bonding characteristics.

In particular, the energy of most molecular vibrational modes corresponds to that of the IR part of the electromagnetic spectrum [99], that is, between around 650 cm^{-1} and 4000 cm^{-1}. IR spectroscopy is therefore a natural tool for the investigation of

molecular structure and bonding. However, in practice, the analysis and assignment of spectral features is difficult [102], and correspondingly, attention is focused instead upon characteristic functional groups and the associated familiar bands . This though, neglects a great deal of the information contained within the IR spectrum.

Ab initio methods provide a solution to this problem: by accurately determining the vibrational spectrum of a system, then it is possible to assign unambiguously the spectral features to actual normal mode oscillations, allowing a deeper understanding of the vibrational spectrum and the bonding and chemical properties of the system under consideration to be gleaned. As it is now possible to routinely carry out high quality *ab initio* calculations on systems of up to 100 atoms on desktop PCs, this potentially allows experimentalists to rapidly analyse experimental spectra.

A wealth of work exists in which *ab initio* methods have been applied very successfully to this problem [100], [101, 102, 103, 104, 105]. Density functional perturbation theory offers a natural route to the accurate determination of the IR spectra, and in this section, the underlying theory used to obtain IR spectra will be discussed.

3.12.1 Basic Theory

The simplest treatment of IR absorption in molecular systems is a semi-classical treatment. Essentially, classical electromagnetism requires that, if a system is to absorb radiation, that it do so by virtue of periodic changes in its electric dipole moment [106]. The frequency of the dipole oscillations must be equal to the frequency of the incident radiation for absorption to occur.

The dipole moment is a vector quantity, thus, absorption may occur provided that at least one component of the dipole moment can oscillate at the incident frequency ν. Of course, as a molecule vibrates, the dipole moment will oscillate at the frequency of the molecular oscillations, as the dipole moment is a function of the nuclear coordinates. In the harmonic approximation used throughout this work, any molecular vibration may be expressed as a sum over normal modes; thus, the dipole moment may only oscillate at these normal mode frequencies, and radiation may only be absorbed at these normal mode frequencies. However, selection rules may ensure

that certain normal modes are so-called "silent" modes, *i.e.* they do not absorb radiation.

Since the molecular dipole moment is a function of the nuclear coordinates, it is possible to expand it as a Taylor series for small displacements:

$$\mu_\alpha = \mu_{0\alpha} + \sum_{\alpha m} \left(\frac{\partial \mu_\alpha}{\partial Q_m} \right)_0 Q_m + \text{higher order terms} \tag{3.109}$$

where α is the Cartesian component under consideration, the subscript 0 denotes quantities that are evaluated at the equilibrium configuration, and the Q_m is the normal coordinate associated with the mth mode. This is related to the atomic displacements via

$$X^m_{\kappa\alpha} = Q_m U_m(\kappa\alpha) \tag{3.110}$$

where $X^m_{\kappa\alpha}$ is the displacement of atom κ in direction α under the action of mode m. Given the following relationship

$$\frac{dA}{dQ_m} = \sum_{\kappa,\alpha} \frac{\partial A}{\partial \tau_{\kappa\alpha}} U_m(\kappa\alpha) \tag{3.111}$$

where A is a generic physical quantity, then it is possible to obtain derivatives with respect to the normal coordinates in terms of derivatives with respect to the Cartesian coordinates [103]. The IR intensity for mode m is then given by [103]

$$I^{IR}_m \propto \sum_\alpha \left| \frac{d\mu_\alpha}{dQ_m} \right|^2 = \sum_\alpha \left| \sum_{\kappa\beta} \frac{\partial \mu_\alpha}{\partial \tau_{\kappa\beta}} U_m(\kappa\beta) \right|^2 \tag{3.112}$$

which, using the definition of the Born effective charge, allows the intensity to be re-written as [100]

$$I^{IR}_m \propto \sum_\alpha \left| \sum_{\kappa,\beta} Z^\star_{\kappa,\alpha\beta} e_m(\kappa\beta) \right|^2 \tag{3.113}$$

i.e. it is proportional to the oscillator strength.

It is easy to see from this how DFPT may be used to obtain the IR spectrum: given the Born effective charge and the normal mode eigenvectors, both of which are naturally obtained from a calculation of the lattice dynamics, it is a trivial task to calculate the oscillator strength.

Selection rules are then obtained from the condition that the oscillator strength does not vanish. Whether the oscillator strength is non-zero or not depends upon the symmetry of the molecule and mode under consideration. For example, consider a simple linear molecule of the form X-Y-X, where the chemical bonds are identical. Carbon dioxide would be a representative molecule. If a normal mode is symmetric, *i.e.* the initial symmetry of the molecule is unchanged, then no change in the dipole moment occurs, and thus the oscillator strength will be vanishing, and the mode will be IR silent. However, if the mode is a non-symmetric mode such that the equilibrium symmetry of the molecule is not preserved, then there is a change in the dipole mode and consequently the oscillator strength is non-vanishing. An important feature to note here is that although the molecule has no dipole moment in its equilibrium geometry, provided that a transition dipole moment is induced by the normal mode oscillations, IR absorption will occur. This is a general feature of IR absorption that applies to more complicated molecules too.

It should be noted that this is a *restricted* selection rule [106]; that is, it depends upon two assumptions: one, that the molecular vibrations are harmonic, allowing a separation of normal modes; and two, that higher order terms in the initial expansion of the dipole moment are negligible. More general selection rules may be derived independent of these approximations by considering the molecular symmetry; these are mentioned in passing for completeness, and will not be discussed in any detail here. The interested reader may find a fuller description in references [106, 107].

3.13 Summary

In this chapter the theoretical framework of DFPT has been expounded in detail. The basic concepts have been introduced through the Green's function-based formalism, where the central issue is to solve a linear problem defined by the Stern-

heimer equation. The existence of a $2n + 1$-theorem in DFT has been discussed; this leads to a variational formalism of DFPT in which one may minimise a second order energy functional. Equivalence to the Green's function-based method has been demonstrated by showing that minimisation of the second order energy functional is equivalent to solving the Sternheimer equation.

The treatment of lattice dynamics within DFPT has been discussed in depth, with the advantages of DFPT versus finite difference methods, viz. the ability to calculate phonon response at arbitrary non-commensurate wavevectors with a workload independent of the perturbation, explicitly discussed. Conceptual problems with electric field perturbations in periodic boundary conditions have been examined, and methods of obviating these within DFPT have been presented. A formalism has been presented that allows the response to homogeneous fields to be calculated; this may be combined with the phonon response to long wavelength perturbations ($\mathbf{q} \rightarrow \mathbf{0}$) in order to calculate the well-known LO-TO splitting in ionic materials arising due to macroscopic fields associated with the atomic displacements.

Finally, application of DFPT to determining IR spectra has been considered. Peaks in the IR spectrum of a material occur at normal mode frequencies possessing a non-zero oscillator strength. The oscillator strength is composed of the Born effective charges and the phonon eigenvectors; thus it is a natural quantity to calculate as a post-process step following a DFPT calculation at little extra computational effort.

The theoretical formalism presented in this chapter provides a framework whereby the response of many-electron systems to phonon and electric field perturbations may be calculated from first principles. However, it has concentrated upon developing the theory at an abstract level, with little discussion of the practicalities of implementing such a formalism. In the next chapter, the detailed implementation and testing of the methodology derived in this chapter within a plane wave pseudopotential framework will be presented.

Chapter 4

Implementation of DFPT Algorithm

Thus far, discussion has centred around DFPT at an abstract level, with little as to how the relevant equations are implemented and solved. A major part of the work in this thesis has been concerned with the implementation of this DFPT formalism within a plane wave pseudopotential framework, and in this chapter, this is discussed in depth, along with efficient techniques for the solution of the second order problem. Although standard minimisation techniques are used that are similar to those used in the solution of the zeroth order Kohn-Sham equations, certain differences arise, particularly with regard to the use of symmetry operations in speeding up calculations, and the choice of k-points. These are discussed in some detail. Finally, a series of test results is presented: by examining the response of a series of test systems to electric field and phonon perturbations, the accuracy of the technique may be illustrated using existing results and finite difference calculations as a comparison.

4.1 Plane Wave Implementation

Plane waves provide a natural basis for DFPT calculations. In addition to the advantages they possess described earlier, it should be noted that as the basis set is fully delocalised over all space, rather than being centred upon individual atoms, perturbations leave the basis set unaltered. This is particularly beneficial as it ensures that one does not need to calculate Pulay-type corrections [108]. The combination

of plane waves with the use of fast Fourier transforms (FFTs) allows one to rapidly change from real to reciprocal space, in order to carry out elements of the calculation in the space most readily suited, for example, the XC term is best dealt with in real space, as it is diagonal in this space; conversely, the kinetic energy is diagonal in reciprocal space, and it is thus most appropriate to deal with it in this space. The DFPT equations take a relatively simple form when expressed in terms of plane waves, and implementing them is a straightforward extension of the method used for the Kohn-Sham equations.

4.1.1 First- and Second-Order Potential Operators

Consider displacements of atoms in the sublattice κ in direction α such that the atomic position changes from $\tau_{\kappa,\alpha}+R_{a,\alpha}$ to $\tau_{\kappa,\alpha}+R_{a,\alpha}+\lambda e^{i\mathbf{q}\cdot\mathbf{R}_a}$ where λ is infinitesimal. The first order change in the potential operator is

$$v^{(1)}_{ext,\mathbf{q}}(\mathbf{r},\mathbf{r}') = \sum_a e^{i\mathbf{q}\cdot\mathbf{R}_a}\frac{\partial}{\partial\tau_{\kappa,\alpha}}v_\kappa(\mathbf{r}-\tau_\kappa-\mathbf{R}_a,\mathbf{r}'-\tau_\kappa-\mathbf{R}_a). \tag{4.1}$$

The local contribution, in reciprocal space, may be written as

$$\bar{v}^{(1)}_{loc,\mathbf{q}}(\mathbf{G}) = \frac{1}{\Omega_0}\frac{\partial}{\partial\tau_{\kappa\alpha}}e^{-i(\mathbf{G}+\mathbf{q})\cdot\tau_\kappa}v^{loc}_\kappa(\mathbf{G}+\mathbf{q}) \tag{4.2}$$

where the phase-factorised potential is defined through

$$\bar{v}^{(1)}_{loc,\mathbf{q}}(\mathbf{r}) = e^{-i\mathbf{q}\cdot\mathbf{r}}v^{(1)}_{loc,\mathbf{q}(\mathbf{r})}. \tag{4.3}$$

Note that this includes the $\mathbf{G}=\mathbf{0}$ term since $\mathbf{q}$ has been taken to be non-zero. The case of $\mathbf{q}\rightarrow\mathbf{0}$ requires, in ionic systems, particular care due to macroscopic electric fields induced by the atomic displacements, as discussed in the previous chapter. This will be considered later.

The first order non-local contribution is given by

$$v^{(1)}_{sep,\mathbf{k}+\mathbf{q},\mathbf{k}}(\mathbf{G},\mathbf{G}') = \frac{1}{\Omega_0}\sum_\mu e_{\mu\kappa}\frac{\partial}{\partial\tau_{\kappa\alpha}}\times$$

$$\left[\left(\sum_G e^{-i(\mathbf{k}+\mathbf{q}+\mathbf{G})\cdot\tau_\kappa}\zeta_{\mu\kappa}(\mathbf{k}+\mathbf{q}+G)\right)\times \left(\sum_{G'} e^{i(\mathbf{k}+\mathbf{G}')\cdot\tau_\kappa}\zeta^\star_{\mu\kappa}(\mathbf{k}+\mathbf{G}')\right)\right] \tag{4.4}$$

where the ζ are short-ranged projectors, *i.e.* the spherical harmonics, and $e_{\mu\kappa}$ is the strength of the angular momentum channel μ for atom κ.

The second order contribution to the local potential is given by

$$v^{\prime(2)}_{loc}(\mathbf{G}) = -\frac{1}{\Omega_0}\frac{1}{2}G^2_\alpha e^{-i\mathbf{G}\cdot\tau_\kappa}v^\kappa_{loc}(\mathbf{G}) \tag{4.5}$$

where the prime denotes the $\mathbf{G} = \mathbf{0}$ term has been set to zero. This is to avoid the divergences associated with this term.

The second order non-local contribution is given by

$$\begin{aligned} v^{(2)}_{sep,\mathbf{k},\mathbf{k}}(\mathbf{G},\mathbf{G}') &= \frac{1}{\Omega_0}\sum_\mu e_{\mu\kappa}\frac{\partial^2}{\partial\tau^2_{\kappa\alpha}}\times \\ &\quad \left[\left(\sum_G e^{-i(\mathbf{k}+\mathbf{G})\cdot\tau_\kappa}\zeta_{\mu\kappa}(\mathbf{k}+G)\right)\times \right. \\ &\quad \left.\left(\sum_{G'} e^{i(\mathbf{k}+\mathbf{G}')\cdot\tau_\kappa}\zeta^\star_{\mu\kappa}(\mathbf{k}+\mathbf{G}')\right)\right]. \end{aligned} \tag{4.6}$$

4.1.2 Ultra-soft Pseudopotentials

The above analysis is dependent only upon the pseudopotential being non-local. No restriction has been placed upon the form of the non-local pseudopotential, save that the pseudopotential may not be ultra-soft. In DFT calculations, ultra-soft non-local pseudopotentials are amongst the most widely used [66]. This is because the orbitals in the core region are allowed to be as "soft" as possible, allowing a low kinetic energy cut-off to be used, although this is at the expense of losing the orthonormality requirements of the atomic orbitals, and the condition of norm conservation. As discussed in chapter 2, the first problem may be solved by considering a generalised

eigenvalue problem, with a generalised orthogonality constraint expressed in terms of an overlap operator S. The second problem may be remedied by the addition of an *augmentation* charge localised within the core regions to the system's charge [66, 73]:

$$\begin{aligned} n(\mathbf{r}) &= 2\sum_{n=1}^{N/2}|\psi_n(\mathbf{r})|^2 + 2\sum_{n=1}^{N/2}\sum_{I}\sum_{ij} Q_{ij}^{I}\langle\psi_n|\beta_i^I\rangle\langle\beta_j^I|\psi_n\rangle \\ &= 2\sum_{n=1}^{N/2}\langle\psi_n|\Lambda(\mathbf{r})|\psi_n\rangle. \end{aligned} \tag{4.7}$$

where the symbols have their usual meanings, as discussed in the previous chapter.

It is because of the existence of this augmentation charge, and the overlap operator S, that care must be exercised when implementing DFPT using ultra-soft pseudopotentials. For example, the orthonormality condition now depends upon the atomic positions through the projectors β^I. Thus, if one applies the Hellmann-Feynman theorem to the generalised eigenvalue problem, one obtains [73]:

$$F_\kappa^\alpha = -\sum_m \left\langle \psi_m \middle| \frac{\partial V_{KS}}{\partial \tau_\kappa^\alpha} - \epsilon_m \frac{\partial S}{\partial \tau_\kappa^\alpha} \middle| \psi_m \right\rangle \tag{4.8}$$

i.e. the changing orthogonality constraint exerts forces. This is similar to the Pulay-type corrections that arise when the Hellmann-Feynman theorem is applied to localised basis sets [108, 109, 110]. Further, the derivative of the Kohn-Sham Hamiltonian itself will acquire extra contributions due to the presence of the augmentation charge.

An ultra-soft implementation of DFPT has been presented by Dal Corso [111, 112] in the context of lattice dynamics, whilst an application to dielectric tensors has been presented by Tobik and Dal Corso and independently by Umari *et al* [114]. The result is that the Sternheimer equation is generalised to

$$(H_{KS}^{(0)} - \epsilon_n^{(0)})P_c|\psi_n^{(1)}\rangle = -P_c^+(H_{KS}^{(1)} - \epsilon_n^{(0)}S^{(1)})|\psi_n^{(0)}\rangle \tag{4.9}$$

where the projector onto the conduction band manifold is defined through

$$P_c^+ = 1 - \sum_n S|\psi_n\rangle\langle\psi_n|. \tag{4.10}$$

It is the presence of these extra terms that ensures that the implementation of DFPT presented in this thesis cannot use ultra-soft potentials. Further, the extra complications involved in actually implementing the additional terms in a sense removes one of the major advantages of ultra-soft pseudopotentials: the gain in efficiency obtained by using a lower kinetic energy cut-off is mitigated to an extent by the necessity of calculating more terms. It is therefore not a major disadvantage to be restricted to norm-conserving pseudopotentials in this study.

4.1.3 The Hartree Contribution

The equations in the previous chapter express the Hartree contribution in the reciprocal space. The Hartree term is diagonal in the reciprocal space, and thus it is more natural to calculate it using this formulation. However, in this work, a real space formulation is used instead. This may seem less efficient in light of the above comments, but the motivation for this can be seen as follows: the local pseudopotential, Hartree and XC contributions can be written down as

$$\frac{1}{2}\int_{\Omega_0} [\bar{v}^{(1)}_{xc,\mathbf{q}}(\mathbf{r}) + \bar{v}^{(1)}_{H,\mathbf{q}}(\mathbf{r}) + \bar{v}^{(1)}_{loc}(\mathbf{r})]\bar{n}^{(1)}_{\mathbf{q}}(\mathbf{r})d\mathbf{r}. \tag{4.11}$$

The advantage of this equation is two-fold: firstly, it can be applied to GGA XC functionals; this is in contrast to the equations in the previous chapter, which were only applicable to the LDA. Secondly, by summing all of the local potentials as above, only a single integral of a first-order local potential multiplied by a first-order density is required. This leads to an overall increase in computational efficiency [115].

4.1.4 Exchange and Correlation

Most implementations of DFPT have been within the LDA [81, 111, 112, 116, 117, 118, 119, 120, 121, 122, 123]. The LDA has the advantage that it is computationally

easy to deal with, as simple analytic expressions for the derivatives of the LDA XC potential may be constructed. However, given the known limitations of the LDA when applied to molecular systems, as mentioned earlier, and also in references [51, 47], in this work the DFPT has been extended to include the GGA.

In determining the second order energy, the second functional derivative of the XC energy is required; as has been discussed by Putrino *et al.* [124], evaluation of this for GGAs is analytically complex and numerically unstable. This is because the derivatives lead to large inverse powers of the electronic density, and one requires a prohibitively fine grid to evaluate these terms accurately and avoid numerical noise. Although in principle a finite difference approach could be adopted, this is not possible for incommensurate perturbations, for which $v_{xc}^{(1)}$ is not a simple derivative.

The starting point for the implementation of GGAs within DFPT is the work of White and Bird [125], who noted that the analytic XC potential has Fourier components not representable on the minimum FFT grid (*i.e.* the smallest grid on which the charge density may be unambiguously represented). Rather, one can define a discrete approximation

$$v_{xc}(\mathbf{R}) = \frac{\partial f_{xc}}{\partial n(\mathbf{R})} + \sum_{\mathbf{R}'} \frac{\partial f_{xc}}{\partial \nabla n(\mathbf{R}')} \cdot \frac{d\nabla n(\mathbf{R}')}{dn(\mathbf{R})} \tag{4.12}$$

where the $\mathbf{R}$ are points on the real space lattice. Here, $f_{xc}(n, \nabla n)$ is the GGA functional being used. One may Taylor expand the above equation, treating $n(\mathbf{R})$ and $\nabla n(\mathbf{R})$ as independent variables. This yields

$$\begin{aligned} \delta v_{xc} \;=\; & \frac{\partial^2 f_{xc}}{\partial n(\mathbf{R}) \partial n(\mathbf{R})} \delta n(\mathbf{R}) + \frac{\partial^2 f_{xc}}{\partial \nabla n(\mathbf{R}) \partial n(\mathbf{R})} \cdot \delta \nabla n(\mathbf{R}) \\ & + \sum_{\mathbf{R}'} \left\{ \frac{\partial^2 f_{xc}}{\partial n(\mathbf{R}') \partial \nabla n(\mathbf{R}')} \cdot \frac{d\nabla n(\mathbf{R}')}{dn(\mathbf{R})} \cdot \delta n(\mathbf{R}') \right. \\ & \left. + \frac{\partial^2 f_{xc}}{\partial \nabla n(\mathbf{R}') \partial \nabla n(\mathbf{R}')} \cdot \frac{d\nabla n(\mathbf{R}')}{dn(\mathbf{R})} \cdot \delta \nabla n(\mathbf{R}') \right\} \end{aligned} \tag{4.13}$$

which can be written as

$$\begin{aligned}\delta v_{xc} &= \frac{\partial^2 f_{xc}}{\partial n(\mathbf{R})\partial n(\mathbf{R})}\delta n(\mathbf{R}) + \frac{\partial^2 f_{xc}}{\partial \nabla n(\mathbf{R})\partial n(\mathbf{R})}\cdot\delta\nabla n(\mathbf{R}) \\ &\quad -\frac{1}{N}\sum_{\mathbf{R}'}\sum_{\mathbf{G}} i\mathbf{G}e^{i\mathbf{G}\cdot(\mathbf{r}-\mathbf{R})}\Big\{\frac{\partial^2 f_{xc}}{\partial n(\mathbf{R}')\partial\nabla n(\mathbf{R}')}\cdot\delta n(\mathbf{R}') \\ &\quad +\frac{\partial^2 f_{xc}}{\partial\nabla n(\mathbf{R}')\partial\nabla n(\mathbf{R}')}\cdot\delta\nabla n(\mathbf{R}')\Big\}. \end{aligned} \tag{4.14}$$

In a DFPT calculation, one uses the phase factorised first-order density $\bar{n}^{(1)}(\mathbf{R})$ rather than $\delta n(\mathbf{R})$, resulting in a discrete approximation for $\bar{v}_{xc}(\mathbf{R})$. These are both complex periodic quantities. In the case of incommensurate perturbations, however, one should use the incommensurate first-order charge density $n^{(1)}(\mathbf{R})$. This is not a cell-periodic quantity, and thus it cannot be implemented upon the FFT grid. Writing the density in terms of $\bar{n}^{(1)}$ as

$$n^{(1)}(\mathbf{R}) = e^{i\mathbf{q}\cdot\mathbf{r}}\bar{n}^{(1)}(\mathbf{R}) \tag{4.15}$$

and applying the chain rule of differentiation to this yields

$$\nabla n^{(1)}(\mathbf{R}) = e^{i\mathbf{q}\cdot\mathbf{r}}(i\mathbf{q}\bar{n}^{(1)}(\mathbf{R}) + \nabla\bar{n}^{(1)}(\mathbf{R})) \tag{4.16}$$

and thus one may use the substitution

$$\delta\nabla n(\mathbf{R}) \Rightarrow \overline{\nabla n^{(1)}(\mathbf{R})} = i\mathbf{q}\bar{n}^{(1)}(\mathbf{R}) + \nabla\bar{n}^{(1)}(\mathbf{R}). \tag{4.17}$$

This is cell-periodic and commensurate and it may thus be evaluated on the FFT grid. However, the GGA depends upon $|\nabla n(\mathbf{R})|$ rather than $\nabla n(\mathbf{R})$, and thus one needs to recast equation 4.14 in terms of this using

$$\frac{\partial f_{xc}}{\partial\nabla n(\mathbf{R})} = \frac{\nabla n(\mathbf{R})}{|\nabla n(\mathbf{R})|}\frac{\partial f_{xc}}{\partial|\nabla n(\mathbf{R})|} \tag{4.18}$$

$$\frac{\partial^2 f_{xc}}{\partial\nabla n(\mathbf{R})\partial n(\mathbf{R})} = \frac{\nabla n(\mathbf{R})}{|\nabla n(\mathbf{R})|}\frac{\partial^2 f_{xc}}{\partial|\nabla n(\mathbf{R})|\partial n(\mathbf{R})} \tag{4.19}$$

and

$$\frac{\partial^2 f_{xc}}{\partial\nabla n(\mathbf{R})\partial\nabla n(\mathbf{R})} = \left(\frac{1}{|\nabla n(\mathbf{R})|} - \frac{\nabla n(\mathbf{R})\nabla n(\mathbf{R})}{|\nabla n(\mathbf{R})|^3}\right)\frac{\partial f_{xc}}{\partial|\nabla n(\mathbf{R})|} + \frac{\nabla n(\mathbf{R})\nabla n(\mathbf{R})}{|\nabla n(\mathbf{R})|^2}\frac{\partial^2 f_{xc}}{\partial|\nabla n(\mathbf{R})|\partial|\nabla n(\mathbf{R})|}. \tag{4.20}$$

It is straightforward to evaluate these derivatives by numerically differentiating the GGA XC expressions. Of course, for the electric field response, which corresponds to the $\mathbf{q} = \mathbf{0}$ case, equation 4.17 simply reduces to $\delta\nabla n(\mathbf{R}) = \nabla n^{(1)}(\mathbf{R})$, and thus one can simply take a numerical derivative of the XC potential.

4.2 Calculation of u^k

The treatment of electric field responses within the long-wave method requires, as discussed in the previous chapter, that the quantity u^k be calculated. One obvious way to do this is using numerical derivatives; however, this is aesthetically unappealing, and its accuracy is limited by the choice of finite step. Indeed, the optimum step would be system dependent, as it would depend upon the topology of the Brillouin zone of the crystal under consideration. A more fundamental difficulty is related to the fact that a naive approach whereby one simply taking numerical derivatives with respect to k-vector encounters problems due to non gauge-invariance. This is because the phase between wavefunctions at neighbouring k-points is random, and the choice of a periodic gauge does nothing to constrain this. Thus the answer obtained will vary from run to run, depending on the phases chosen as a result of the diagonalisation routine. This issue is returned to in more detail in section 4.9. A more elegant method, and one that evades these difficulties, is to appeal to the $2n + 1$ theorem, and formulate the following variational expression

$$E^{k_\alpha k_\alpha}_{m\mathbf{k}} = \langle u^{k_\alpha}_{m\mathbf{k}}|H^{(0)}_{\mathbf{k},\mathbf{k}} - \epsilon^{(0)}_{m\mathbf{k}}|u^{k_\alpha}_{m\mathbf{k}}\rangle + \langle u^{k_\alpha}_{m\mathbf{k}}|T^{k_\alpha}_{\mathbf{k},\mathbf{k}} + v^{k_\alpha}_{sep,\mathbf{k},\mathbf{k}}|u^{(0)}_{m\mathbf{k}}\rangle + \langle u^{(0)}_{m\mathbf{k}}|T^{k_\alpha}_{\mathbf{k},\mathbf{k}} + v^{k_\alpha}_{sep,\mathbf{k},\mathbf{k}}|u^{k_\alpha}_{m\mathbf{k}}\rangle \tag{4.21}$$

where the first order wavefunction is to be obtained subject to the constraints

$$\langle u^{(0)}_{m\mathbf{k}} | u^{k_\alpha}_{n\mathbf{k}} \rangle = 0 \tag{4.22}$$

and the first order kinetic energy operator is given by

$$T^{k_\alpha}_{\mathbf{k},\mathbf{k}}(\mathbf{G},\mathbf{G}') = (G_\alpha + k_\alpha)\delta_{\mathbf{G},\mathbf{G}'}. \tag{4.23}$$

The terms involving the first order kinetic and potential energy operators may be recast into the following convenient form, following Pickard and Payne [126]:

$$H^{k_\alpha}_{\mathbf{k},\mathbf{k}} = ie^{-i\mathbf{k}\cdot\mathbf{r}}[H^{(0)}, r_\alpha]e^{i\mathbf{k}\cdot\mathbf{r}} \tag{4.24}$$

where, for a non-local potential

$$i[H^{(0)}, r_\alpha] = p_\alpha + i[V_{sep}, r_\alpha] \tag{4.25}$$

which is known as the velocity operator.

In order to evaluate the commutator, it is necessary to evaluate matrix elements of the form $\langle\beta|r_\alpha|\psi_{m\mathbf{k}}\rangle$, where the β are the projectors used in the separable part of the pseudopotential. It is most convenient to consider these in reciprocal space. If one takes the matrix element $\langle\beta|e^{i\mathbf{q}\cdot\mathbf{r}}|\psi_{m\mathbf{k}}\rangle$, then for small $\mathbf{q}$

$$\langle\beta|e^{i\mathbf{q}\cdot\mathbf{r}}|\psi_{m\mathbf{k}}\rangle = \langle\beta|\psi_{m\mathbf{k}}\rangle + i\langle\beta|\mathbf{q}\cdot\mathbf{r}|\psi_{m\mathbf{k}}\rangle - \ldots \tag{4.26}$$

and setting $\mathbf{q} = (q, 0, 0)$, then

$$\langle\beta|e^{iqr_1}|\psi_{m,\mathbf{k}}\rangle - \langle\beta|e^{-iqr_1}|\psi_{m,\mathbf{k}}\rangle = 2iq\langle\beta|r_1|\psi_{m,\mathbf{k}}\rangle + O(q^3). \tag{4.27}$$

The advantage of this method for evaluating the matrix elements is that the CASTEP code already has routines for evaluating $\langle\beta|\psi_{m,\mathbf{k}}\rangle$ and therefore evaluating $\langle\beta|e^{i\mathbf{q}\cdot\mathbf{r}}|\psi_{m\mathbf{k}}\rangle$ only requires small shifts in the reciprocal space grid on which $|\beta\rangle$ is calculated. The size of q is chosen such that higher order terms ($O(q^3)$ and higher) become negligible, whilst avoiding errors due to precision limitations.

4.3 Solution of second order equations

As mentioned in the previous chapter, the Gonze formalism of DFPT is a variational method. As such it relies upon the solution of a set of Euler-Lagrange equations arising from minimisation of the second order energy functional (see equation 3.34) $E_{el}^{(2)}$. The equations may either be solved using standard linear algebra methods, or alternatively, by minimising $E^{(2)}$ directly; both methods provide the same solution. For reasons similar to the motivation for solving the Kohn-Sham by direct minimisation, the method adopted here is that of direct minimisation of the second order functional. One important feature is that the expression for $E_{el}^{(2)}$ is an exact quadratic in the space of the first-order wavefunctions; this is in contrast to the Kohn-Sham functional, and makes it easier to implement a minimisation algorithm.

The prerequisite for a DFPT calculation is a set of accurate zeroth order wavefunctions at $\mathbf{k}$ and $\mathbf{k}+\mathbf{q}$. The approach of Gonze [83] is to utilise the groundstate self-consistent wavefunctions which are available on the Monkhorst-Pack grid. This however, has the disadvantage that it limits the phonon wavevector $\mathbf{q}$ to the difference between any pair of Monkhorst-Pack points. To remedy this, in this work, a non-self-consistent bandstructure calculation is used to obtain a set of $\{u^{(0)}_{m\mathbf{k}+\mathbf{q}}\}$ at any required q-point. This allows the response at any wavevector $\mathbf{q}$ to be calculated.

4.3.1 Direct Minimisation: Conjugate Gradients Algorithm

The minimisation algorithm used is similar to that used for the solution of the Kohn-Sham equations. An initial trial vector is used; in practice, since it is assumed that the perturbation being dealt with is small, this is taken to be the null vector. This obviously satisfies the constraint conditions. Specifying the trial wavefunction at iteration m by ψ_α^m, where α is the band index, a steepest descents vector can be determined from

$$\zeta_\alpha^m = -P_c(H^{(0)} - \epsilon_m^{(0)})|\psi_\alpha^{m(1)}\rangle + H^{m(1)}|\psi_\alpha^{(0)}\rangle \tag{4.28}$$

which is obtained by taking the gradient of the energy functional with regard to changes in $\psi_\alpha^{m(1)}$ projected onto the conduction bands. The preconditioned steepest-

descents vector is then

$$\eta_\alpha^m = P_c K \zeta_\alpha^m \tag{4.29}$$

where K is the preconditioning operator. This depends upon the choice of preconditioning scheme, and will be returned to later, in section 4.3.3

The conjugate gradient direction is then given by

$$\phi_\alpha^m = \eta_\alpha^m + \gamma_\alpha^m \phi_\alpha^{m-1} \tag{4.30}$$

with

$$\gamma_\alpha^m = \langle \eta_\alpha^m | \phi_\alpha^m \rangle / \langle \eta_\alpha^{m-1} | \phi_\alpha^{m-1} \rangle \tag{4.31}$$

and $\gamma_\alpha^1 = 0$.

The improved first order wavefunction is then given by

$$\psi_\alpha^{m+1(1)} = \psi_\alpha^{m(1)} + \theta \phi_\alpha^m \tag{4.32}$$

where θ is a parameter determined by the minimisation requirement. The optimum value of θ may be determined using a two-point minimisation algorithm. Given the quadratic form of the second order energy functional in $\psi_\alpha^{(1)}$, one can evaluate the second order energy and gradient vector for some given $\psi_\alpha^{m(1)}$, and again for some $\tilde{\psi}_\alpha^{m(1)}$ where

$$\tilde{\psi}_\alpha^{m(1)} = \psi_\alpha^{m(1)} + c\phi_\alpha^m. \tag{4.33}$$

Here c is some arbitrary, but small, step-size. Given three pieces of information, that is, the value of the second order energy at the original point and the new point, and the gradient at the original point, it is possible to fit a quadratic form. The optimum step size is then given by

$$c_{opt} = \eta_\alpha^m c^2 / (E_{el}^{(2)}\{\psi^{(0)}; \psi^{m(1)}\} - E_{el}^2\{\psi^{(0)}; \tilde{\psi}^{m(1)}\} + \eta_\alpha^m c). \tag{4.34}$$

This is notably simpler than the ground state minimisation algorithm, because the ground state functional is not a simple quadratic form.

The above algorithm is not a true band-by-band minimisation scheme in the spirit of Gonze [83]. That is, one does not decompose $E_{el}^{(2)}$ and the first order Hamiltonian on a band-by-band basis, and then optimise each orbital individually. In principle, one would expect a band-by-band minimiser to be superior, but it would require a separate evaluation of the first-order Hamiltonian for each band considered. The method outlined above optimises the orbitals simultaneously, and thus the first-order Hamiltonian need only be evaluated twice for each iteration; since the evaluation of the first-order Hamiltonian is the most time-consuming step, this is a major computational saving, and save around 20% of the CPU time [115]. Furthermore, as all first order orbitals are being altered simultaneously, there is no requirement for a supplementary self-consistency loop, in contrast to the band-by-band scheme. In practice, it is found that convergence is rapid (within 10-20 iterations) in most cases, and thus it seems justified in using the all-bands minimiser.

It is worth noting here that the same general algorithm may be used for the determination of $u^{k\alpha}$, although in this case, the algorithm is simplified as there is no requirement for self-consistency requirement. Thus it is possible to modify the above algorithm and implement it on a band-by-band, k-point-by-k-point basis.

4.3.2 Conjugate Gradients vs Steepest Descents

In figure 4.1 the performance of a steepest descents minimiser is compared to that of a conjugate gradients minimiser when applied to the determination of $E_{el}^{\epsilon\epsilon}$ for α-quartz. The convergence criterion is that the minimum is taken to be found when the difference between the values of $E_{el}^{\epsilon\epsilon}$ for two subsequent iterations is less than 10^{-4} internal units. Although this is not a particularly tight tolerance, it suffices for the purpose of demonstrating the relative rates of minimisation of the two algorithms. The increased efficiency of the conjugate gradients minimiser is immediately apparent, taking around 45 iterations to find the minimum, in contrast to the steepest descents minimiser, which takes over 100 iterations (although these are not shown on the graph). The steepest descents minimiser's performance is

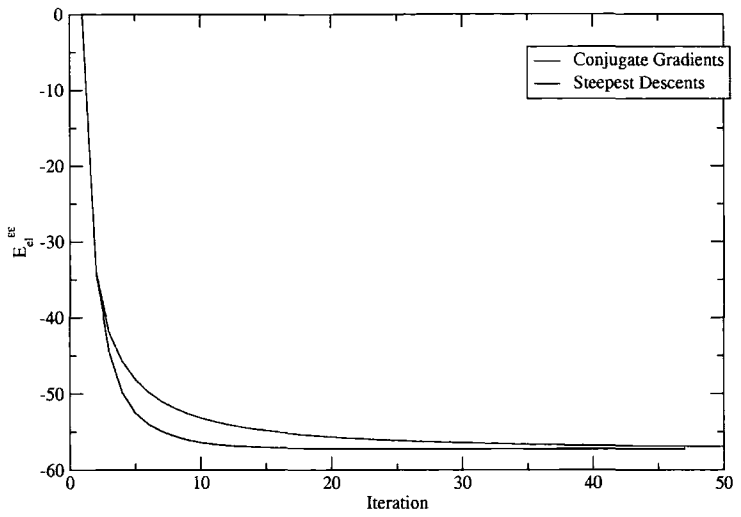

Figure 4.1: Performance of steepest descents minimiser compared to a conjugate gradients minimiser for α-quartz. The units of the second order energy are internal atomic units. No preconditioning has been applied.

initially almost identical to that of the conjugate gradients minimiser, but as the minimum of the energy landscape under consideration is approached, its performance degrades massively. Essentially, this is because as the minimum is approached, the steepest descents minimiser takes no previous steps into account, in contrast to the conjugate gradients method. Thus it fails to "home in" efficiently upon the minimum, and instead oscillates around the environs of it. It is this by-passing of the minimum that accounts for the extraordinarily long time that it takes to converge. The logarithmic plot shown in figure 4.2 illustrates very clearly this difference in performance. In section 4.3.7, the merits of various preconditioners are discussed; the results for α-quartz are presented in figure 4.3. These indicate that although preconditioning improves the performance of the SD scheme such that it reaches the minimum in around 40 iterations compared to 110 without preconditioning, this is still poorer than the CG scheme with the same preconditioning scheme applied, which reaches the minimum in around 20 iterations. It is therefore easy to see that, as is true for the solution of the zeroth order problem, a conjugate gradients algorithm is superior and thus preferable than a simple steepest descents minimiser.

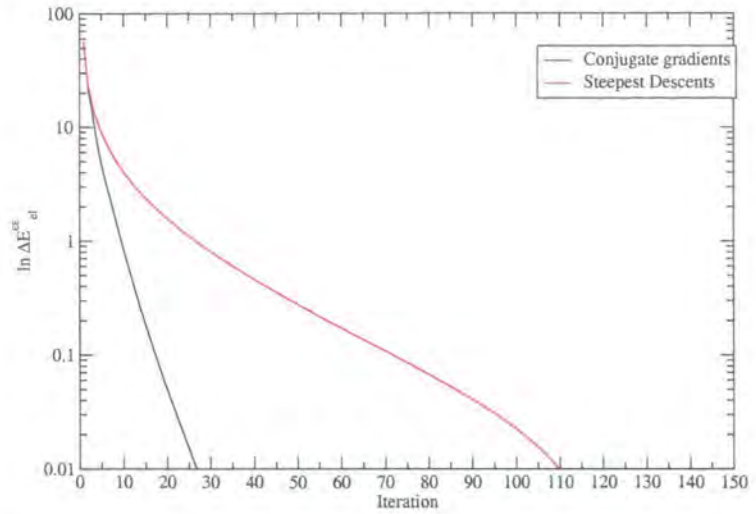

Figure 4.2: Performance of steepest descents minimiser compared to a conjugate gradients minimiser for α-quartz. Logarithmic plot of the difference in the second order energy at each iteration from the final converged value. No preconditioning has been applied.

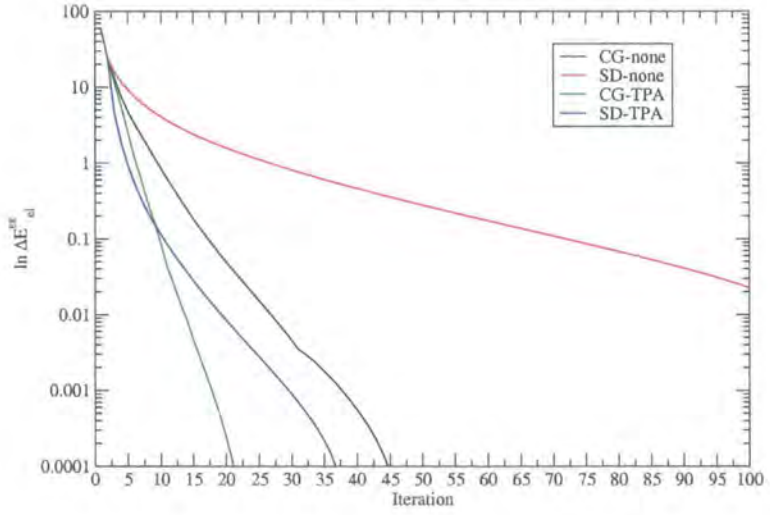

Figure 4.3: Performance of steepest descents minimiser compared to a conjugate gradients minimiser for α-quartz. Performance with and without preconditioning. Logarithmic plot of the difference in the second order energy at each iteration from the final converged value.

4.3.3 Comparison of Preconditioning Methods

As in minimising the Kohn-Sham energy functional, effective preconditioning schemes are essential for efficient solution of the second-order problem. Although the basic concepts behind preconditioning have been outlined in a previous chapter, here a more detailed discussion of the various approaches is presented, and their performances compared.

4.3.4 The TPA Scheme

A standard scheme is that proposed by Teter *et al.* [127]. Here, a preconditioning operator is introduced that is an approximate inverse kinetic energy. The justification for this is quite simple: the high **G** components that lead to the minimisation problem being ill-conditioned are approximately diagonal in the kinetic term. This approximation obviously breaks down for the low **G** components, but as these do not need to be preconditioned, the preconditioning operator is chosen to be approximately constant for small **G**-vectors. Accordingly, the form of the preconditioning operator is

$$K_{\mathbf{G},\mathbf{G}'} = \delta_{\mathbf{G},\mathbf{G}'} \frac{27 + 18x + 12x^2 + 8x^3}{27 + 18x + 12x^2 + 8x^3 + 16x^4} \tag{4.35}$$

where

$$x = \frac{|\mathbf{k} + \mathbf{G}|^2/2}{T_i^m} \tag{4.36}$$

and here T_i^m is the kinetic energy of state m at iteration i. As is easily verified, the matrix elements $K_{\mathbf{G},\mathbf{G}'}$ approach unity as x approaches zero, with vanishing first, second and third derivatives. Thus the small wave-vector components of the trial vector remain unaltered. Above $x = 1$, the matrix elements approach $1/[2(x-1)]$ asymptotically. Thus this factor causes all of the large wave-vector components to converge at nearly the same rate.

In figure 4.4, the effect of preconditioning upon the eigenvalue spectrum is shown; as is clearly seen, the application of the preconditioning matrix K ensures that

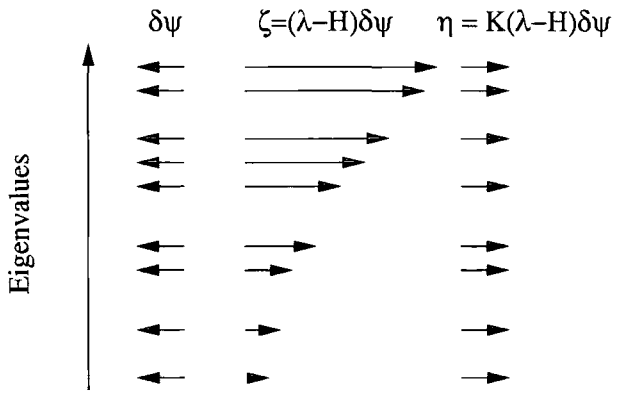

Figure 4.4: Effect of preconditioning upon eigenvalue spectrum. Here $\delta\phi$ is the error in the wavefunction, ζ is the gradient of the wavefunction, and η is the preconditioned gradient vector.

all the high kinetic energy contributions converge at approximately the same rate as the low kinetic energy components. This conditioning of the problem ensures that the preconditioned gradient vector is now a simple multiple of the error in the wavefunction gradient, leading to much improved convergence properties.

4.3.5 The RTPA Scheme

The modified TPA scheme (RTPA) has been proposed by Kresse and Furthmüller [128], and is essentially very similar to the TPA scheme in spirit. The only modification is in the form of the preconditioning matrix, which in this scheme takes the form

$$K_{\mathbf{G},\mathbf{G}'} = \delta_{\mathbf{G},\mathbf{G}'} \frac{2}{3/2T_i^m} \frac{27 + 18x + 12x^2 + 8x^3}{27 + 18x + 12x^2 + 8x^3 + 16x^4} \tag{4.37}$$

with

$$x = \frac{|\mathbf{k} + \mathbf{G}|^2/2}{3/2T_i^m}. \tag{4.38}$$

It is not clear that the slightly different definition of x leads to improved efficiency compared to TPA when applied to minimisation of the Kohn-Sham functional for most materials.

4.3.6 The PSP Scheme

An alternative scheme, and one that is intended specifically for DFPT problems, is that of Putrino, Sebastiani and Parrinello [129]. Here, one wishes to improve the conditioning by finding an inverse of

$$H^{(0)}\delta_{ij} - \langle\phi_i^{(0)}|H^{(0)}|\phi_j^{(0)}\rangle. \tag{4.39}$$

This expression may be simplified by replacing the last term with the trace of the Hamiltonian, and further, by noting that for high $\mathbf{G}$ the dominant contributions come from the kinetic energy, and that this term is diagonal in reciprocal space. Thus one may approximate the previous equation by

$$\frac{1}{2}|\mathbf{G}|^2 + V(\mathbf{G}) - \frac{1}{N}TrH^{(0)}. \tag{4.40}$$

This may be easily inverted to provide the preconditioning matrix; however, it may almost vanish for certain $\mathbf{G}$-vectors. In order to prevent this, one instead transforms to

$$\left[\left(\frac{1}{2}|\mathbf{G}|^2 + V(\mathbf{G}) - \frac{1}{N}TrH^{(0)}\right)^2 + \eta^2\right]^{1/2} \tag{4.41}$$

where η is some small value. The final preconditioner is then simply

$$\left[\left(\frac{1}{2}|\mathbf{G}|^2 + V(\mathbf{G}) - \frac{1}{N}TrH^{(0)}\right)^2 + \eta^2\right]^{-1/2}\delta_{ij}. \tag{4.42}$$

4.3.7 Evaluation of Preconditioning Schemes

In figure 4.5 the performance of the three preconditioning schemes is illustrated for NaCl. As can be seen, the PSP method is slightly better than the TPA and RTPA methods, which have almost identical performances. This performance differential is not significant, and it is likely that the best preconditioning scheme will depend upon the system under consideration. As an example of this, in figure 4.6, the performance of the three schemes is shown for α-quartz. The relative performances

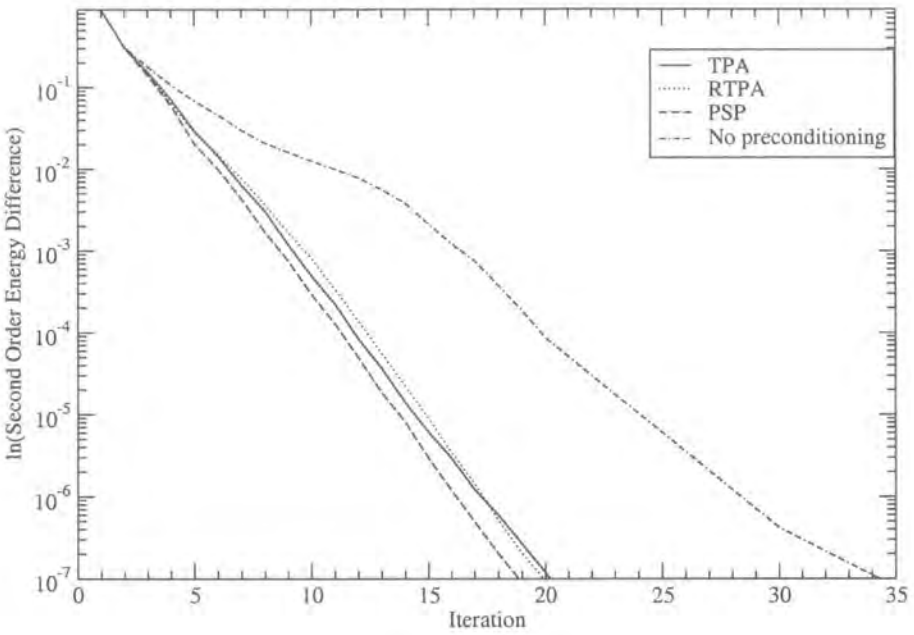

Figure 4.5: Comparison of preconditioning schemes for NaCl

may be seen more clearly in the logarithmic plot presented in figure 4.7. In this case, the TPA and RTPA schemes appear to be most effective, whilst the PSP scheme is least effective. For the remainder of this work, the TPA scheme is used. There are two main reasons for this: at least in some systems, the TPA scheme is superior to the PSP scheme; further, the PSP scheme, although designed specifically for DFPT, requires the potential for every **G**-vector to be stored, which is more expensive than both the TPA and RTPA schemes, for which the kinetic terms only are required. Taken in connection with the first factor, this would seem to justify the use of TPA.

4.4 Off-diagonal Terms and Mixed Perturbations

Thus far, all discussion has centred upon the determination of the diagonal terms of the dynamical matrix and the permittivity tensors by direct minimisation of the second order energy. However, one must also determine the off-diagonal components

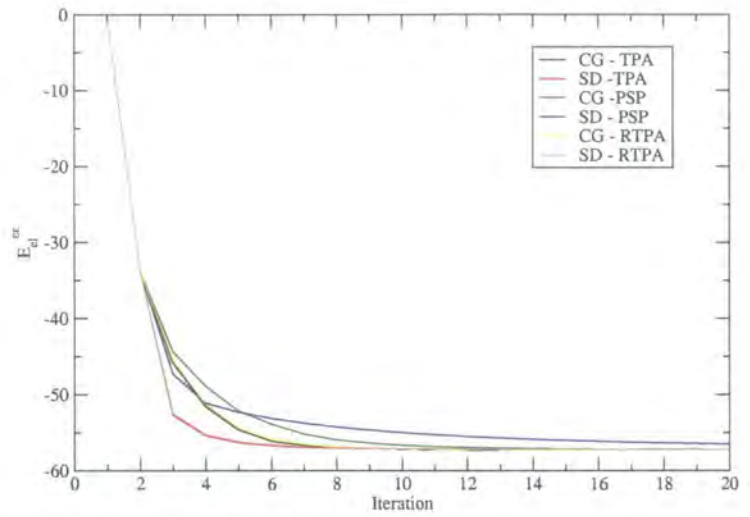

Figure 4.6: Comparison of preconditioning schemes for α-quartz; note the poor performance of the PSP scheme

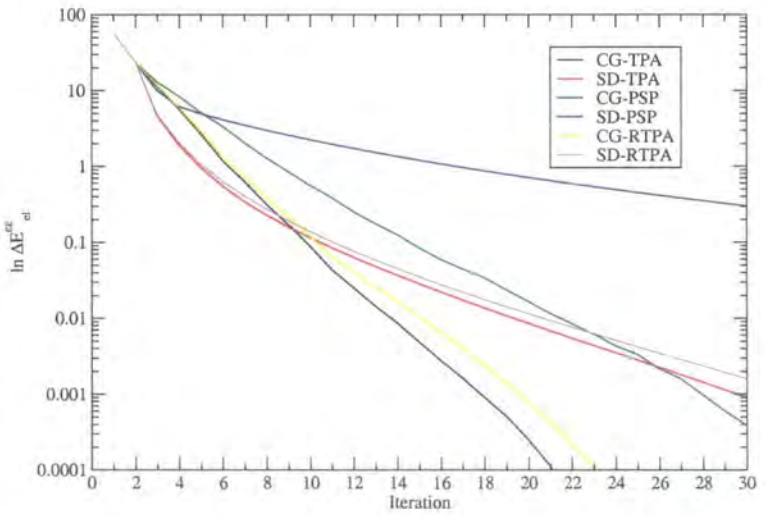

Figure 4.7: Comparison of preconditioning schemes for α-quartz; logarithmic plot.

of these quantities. One could utilise the $2n + 1$ theorem to obtain variational mixed perturbation expressions that could be minimised in the same way as has been outlined for the diagonal terms. However, these expressions would have *two* unknown quantities: the first-order wavefunctions with respect to the two different perturbations in question. A more sensible strategy is instead to obtain the diagonal terms, and hence the set of $\psi^{(1)}$s, and then to combine these first order wavefunctions to construct non-variational expressions in the manner described in the previous chapter. The non-variational expressions consist of simple matrix elements, and are thus relatively inexpensive to calculate; the increase in computational efficiency is worth the decrease in accuracy due to a non-stationary expression being used. Of course, provided that the minimisers used to obtain the first-order wavefunctions are allowed to converge to a sufficiently tight tolerance, then the resulting matrix products can be determined to a sufficient level of accuracy.

4.5 Sum Rules

In addition to the minimisation constraints discussed in the previous sections, sum rules also exist that are imposed by the translational invariance and charge neutrality of the system under consideration. Although in principle these should be exactly satisfied, in practice, they will be broken. This is because of the finite number of plane waves used, the quality of the reciprocal space sampling and the discretisation of the real space integrals used for the XC potential. Thus the extent to which the sum rules are violated provides a measure of the quality of convergence of a calculation with regard to these parameters.

4.5.1 The Acoustic Sum Rule

It is immediately apparent that due to translational invariance, the zone centre dynamical matrix should allow a rigid translation of the solid as an eigenvector with zero eigenfrequency. This leads to the sum rule:

$$\sum_{\kappa'} \tilde{C}_{\kappa\alpha,\kappa'\beta}(q = \mathbf{0}) = 0. \tag{4.43}$$

Use of this sum rule allows one to determine the self-interaction terms of the dynamical matrix, *i.e.* the diagonal terms, $\kappa = \kappa'$, as is easily shown using the previous equation:

$$\tilde{C}_{\kappa\alpha,\kappa\beta} = -\sum_{\kappa' \neq \kappa} \tilde{C}_{\kappa\alpha,\kappa'\beta} \tag{4.44}$$

4.5.2 The Charge Neutrality Condition

In a charge neutral system, the requirement that the acoustic mode frequencies vanish for $\mathbf{q} = \mathbf{0}$ demands that

$$\sum_{\kappa} Z^{\star}_{\kappa,\alpha\beta} = 0 \tag{4.45}$$

which can be seen by comparing the acoustic sum rule with equations 3.106 and 3.107. Although in phenomenological approaches this is imposed as an auxiliary condition, it is possible to show, from a microscopic approach, that this is a consequence of charge neutrality [130].

4.6 Dynamical Matrix Symmetry

In the absence of symmetry (other than the Hermitian character of the dynamical matrix), construction of the dynamical matrix requires $3N$ perturbations and variational minimisations in order to determine the diagonal elements, and $3N/2(3N-1)$ calculations to determine the off-diagonal elements. This may be reduced by exploiting the symmetry of the dynamical matrix consequent upon the space group symmetry of the crystal and the phonon wavevector $\mathbf{q}$. The theory of the symmetry properties of the normal modes and dynamical matrix has been discussed in detail by Maradudin and Vosko [131] and Warren [132] using the irreducible multiplier representations of the space group. A multiplier representation is one in which the following relationship is satisfied between any two members of a set of matrices $\{\mathbf{T}(\mathbf{R})\}$ in one-to-one correspondence with the elements $\{\mathbf{R}\}$ of a group

$$\mathbf{T}(\mathbf{R}_i)\mathbf{T}(\mathbf{R}_j) = \phi(\mathbf{R}_i, \mathbf{R}_j)\mathbf{T}(\mathbf{R}_i\mathbf{R}_j). \tag{4.46}$$

In the context of lattice dynamics, the group elements denoted by $\{\mathbf{R}\}$ are the purely rotational elements of the group of the wavevector $\mathbf{q}$, $G_{\mathbf{q}}$. This is the subgroup of operations of the full crystal space group under which the wavevector $\mathbf{q}$ is invariant. The matrices $\{\mathbf{T}(\mathbf{R})\}$ form a $3N$-dimensional unitary representation of the subgroup $G_{\mathbf{q}}$ and are given by

$$T_{\alpha\beta}(\mathbf{q};\mathbf{R}) = R_{\alpha\beta}\delta(\kappa, F_0(\kappa';R))e^{i\mathbf{q}\cdot[\mathbf{x}(\kappa)-\mathbf{R}\mathbf{x}(\kappa')]} \tag{4.47}$$

where $F_0(\kappa';R)$ is defined through

$$\kappa = F_0^{-1}(K;R) \tag{4.48}$$

which expresses the fact that the index K uniquely labels the atom κ that is brought into position K by the symmetry operation $\{\mathbf{R}|\mathbf{v}(S)+\mathbf{x}(m\}$, where $\mathbf{x}(m)$ is a crystal lattice vector.

The multiplier $\phi(\mathbf{q},\mathbf{R}_i,\mathbf{R}_j)$ is given by

$$\phi(\mathbf{q},\mathbf{R}_i,\mathbf{R}_j) = e^{2\pi i\mathbf{b}(\mathbf{q},\mathbf{R}_i^{-1})\cdot\mathbf{v}_i} \tag{4.49}$$

where the reciprocal lattice vector $\mathbf{b}(\mathbf{q},\mathbf{R}_i^{-1})$ is defined through

$$\mathbf{R}_i^{-1}\mathbf{q} = \mathbf{q} - 2\pi\mathbf{b}(\mathbf{q},\mathbf{R}_i^{-1}). \tag{4.50}$$

If the wavevector $\mathbf{q}$ lies within the first Brillouin Zone, then $\mathbf{b}$ is identically zero, and the multiplier equals unity. Alternatively, if one is dealing with a symmorphic space group such that all $\mathbf{v}(\mathbf{R})$ are equal to zero, then the multiplier will also be equal to unity. In these cases, the multiplier representation will simply be an ordinary representation of $G_{\mathbf{q}}$.

The dynamical matrix transforms under the operations of $G_{\mathbf{q}}$ as

$$D_{\alpha\alpha'}^{\kappa\kappa'}(\mathbf{q}) = \mathbf{T}^{-1}(\mathbf{q};\mathbf{R})D_{\alpha\alpha'}^{\kappa\kappa'}(\mathbf{q})\mathbf{T}(\mathbf{q};\mathbf{R}) \tag{4.51}$$

which may be used to determine the non-zero independent elements of the dynamical matrix. Further conditions may be imposed upon the form of the dynamical matrix if the point group operations include an operation $\mathbf{S}_-$ such that $\mathbf{S}_-\mathbf{q} = -\mathbf{q}$, *i.e.* $-\mathbf{k}$ is in the star of $\mathbf{k}$. Then it can be shown that, for values of $\mathbf{q}$ for which this is true, that

$$\{e^{-i\mathbf{q}\cdot\mathbf{x}(\bar{\kappa})}D^{\bar{\kappa}\kappa'}_{\mu\nu}(\mathbf{q})e^{i\mathbf{q}\cdot\mathbf{x}(\bar{\kappa}')}\}^\star = \sum_{\alpha\beta}(\mathbf{S}_-)_{\mu\alpha}e^{-i\mathbf{q}\cdot\mathbf{x}(\kappa)}D^{\kappa\kappa'}_{\alpha\beta}(\mathbf{q}) \times e^{i\mathbf{q}\cdot\mathbf{x}(\kappa')}(\mathbf{S}_-)_{\nu\beta} \tag{4.52}$$

where $\bar{\kappa}$ and $\bar{\kappa}'$ are the labels of the atoms into which κ and κ' are sent by the operation $\mathbf{S}_-$. One should note that this operation is not limited to the case of a simple inversion. In this particular case, the above simplifies to

$$\{e^{-i\mathbf{q}\cdot\mathbf{x}(\bar{\kappa})}D^{\bar{\kappa}\kappa'}_{\alpha\beta}(\mathbf{q})e^{i\mathbf{q}\cdot\mathbf{x}(\bar{\kappa}')}\}^\star = e^{-i\mathbf{q}\cdot\mathbf{x}(\kappa)}D^{\kappa\kappa'}_{\alpha\beta}(\mathbf{q})e^{i\mathbf{q}\cdot\mathbf{x}(\kappa')}. \tag{4.53}$$

If every ion is at a centre of inversion, such that $\bar{\kappa} = \kappa$ and $\bar{\kappa}' = \kappa'$, then the matrix

$$C^{\kappa\kappa'}_{\alpha\beta}(\mathbf{q}) = e^{-i\mathbf{q}\cdot\mathbf{x}(\bar{\kappa})}D^{\bar{\kappa}\kappa'}_{\alpha\beta}(\mathbf{q})e^{i\mathbf{q}\cdot\mathbf{x}(\bar{\kappa}')} \tag{4.54}$$

is a real symmetric matrix, and accordingly, its eigenvectors may be chosen to be real. It is easy to show from equation 4.53 that elements of the dynamical matrix diagonal in κ and $\bar{\kappa}$ are complex conjugates of one another.

One wishes to utilise the symmetry operations of $G_\mathbf{q}$ in order to determine the minimal subset of the elements of $D^{\kappa\kappa'}_{\alpha\beta}(\mathbf{q})$ and the relationships between elements in order to reconstruct the whole matrix. The algorithm used is as follows: a maximally random dynamical matrix $D^{\kappa\kappa'}_{\alpha\beta;rand}(\mathbf{q})$ of the same dimension as the dynamical matrix is constructed that satisfies all of the invariances of the form of equation 4.51. This is achieved by generating an initial Hermitian matrix $D^{\kappa,\kappa';init}_{\alpha\beta;rand}$ and then generating $D^{\kappa\kappa'}_{\alpha\beta;rand}(\mathbf{q})$ using

$$D^{\kappa\kappa'}_{\alpha\beta;rand}(\mathbf{q}) = \sum_{j=1}^{g(\mathbf{q})}\mathbf{T}^{-1}(\mathbf{q};\mathbf{R})D^{\kappa,\kappa';init}_{\alpha\beta;rand}\mathbf{T}(\mathbf{q};\mathbf{R}). \tag{4.55}$$

A similar procedure is subsequently applied to $D^{\kappa\kappa'}_{\alpha\beta;rand}(\mathbf{q})$ to ensure that it satisfies the inversion and time-reversal symmmetries.

The resulting $D^{\kappa\kappa'}_{\alpha\beta;rand}(\mathbf{q})$ satisfies all of the symmetries of the subgroup $G_{\mathbf{q}}$, but is otherwise random. One may then determine the relationships between elements of the dynamical matrix by analysing the form of $D^{\kappa\kappa'}_{\alpha\beta;rand}(\mathbf{q})$. The relationships between the elements of this matrix may take the form of elements equal to zero, elements which are equal in magnitude and complex phase, elements which are equal in magnitude but of opposite phase, and elements which are equal in magnitude but rotated or counter-rotated in phase. These conditions are satisfied to a large degree of numerical precision. In order to ensure that accidental values of zero are not produced, the initial random elements of $D^{\kappa,\kappa';init}_{\alpha\beta;rand}$ are biased away from zero.

The symmetries present may ensure that certain elements of the dynamical matrix have a fixed phase; this may be either an absolute or $\mathbf{q}$-dependent value. Symmetry-related phases may be determined by generating a new $D^{\kappa,\kappa';init}_{\alpha\beta;rand}$ using an independent sequence of pseudo-random numbers and repeating the above analysis. Phases and phase relationships which are in common are marked as being symmetry determined.

The symmetry information may be used within a calculation of $D^{\kappa\kappa'}_{\alpha\beta}(\mathbf{q})$ to set all elements identically zero to this value immediately. All elements which have equal magnitude are assigned at the first calculation of one of them; the symmetry-related phase information is used to correctly set the phases of these related elements. Upon an element being assigned, a flag is set to "already computed", and subsequent iterations of the atom or direction loops omit any calculations if this flag is set for a particular element.

4.7 Born Effective Charge and Permittivity Tensor Symmetry

The Born effective charge tensors resemble the leading 3×3 block diagonal of the dynamical matrix corresponding to a particular atom with no requirement for Hermiticity. An analysis similar to that described above is therefore possible, although,

since the effective charges require the calculation of the system response to an atomic displacement $u^{\tau_\alpha}_{m,\mathbf{kq}}$, the loops over ions and directions used for the dynamical matrix calculation may only be omitted when both the dynamical matrix and effective charge symmetries permit.

A similar algorithm and analysis may be performed for the symmetry of the permittivity tensor. However, in this case there are some simplifications, as the permittivity is simply a symmetric tensor, rather than being Hermitian. Further, one may simply use the symmetry operations of the *full* crystal point group rather than those of the group of the wavevector $G_\mathbf{q}$. It should also be noted that one does not need to consider phase relations between elements, as the permittivity tensor elements must be real.

4.8 Brillouin Zone Sampling

The choice of k-points used in a DFPT calculation deserves careful consideration. In a single-point calculation, the space group symmetry is used to determine an irreducible set from a Monkhorst-Pack grid of k-points [60]. However, in a DFPT calculation, the perturbations applied break crystalline symmetries, and thus one must instead use a subgroup {S} of the space group that leaves the perturbation invariant. For a perturbation applied in direction α, one must therefore unfold the symmetry irreducible set of k-points determined from the crystal space group up to the *full* Monkhorst-Pack grid. This is not symmetry-reduced, and thus in most cases this will be larger than the 'standard' symmetry-reduced grid used. The operations of the subgroup are then determined by application of the space group symmetry operations and retention of those that leave the perturbation invariant. These operations are then used to construct a new irreducible set of k-points. Of course, as one alters the direction of perturbation (and for phonon calculations in some cases, the atom being perturbed) it will be necessary to determine a new symmetry irreducible set using the above algorithm. In general, these irreducible sets of k-points will be larger than for the SCF calculation, which is expected due to the lower symmetry. An additional consideration is that unless $2\mathbf{q}$ is zero or equal to a reciprocal lattice vector of the crystal time reversal symmetry is broken, and

thus one requires both $\mathbf{k}$ and $-\mathbf{k}$ in the set of k-points.

Given the above discussion, the symmetrised first-order density is constructed according to

$$n_{\mathbf{q}}^{(1)}(\mathbf{r}) = \sum_{S=1}^{N_S} S \sum_{k=1}^{N_k} w_{\mathbf{k}} \sum_{m}^{occ} u_{m,\mathbf{k}}^{(0)\star}(\mathbf{r}) u_{m,\mathbf{k},\mathbf{q}}^{\tau\kappa,\alpha}(\mathbf{r}) \tag{4.56}$$

where S are symmetry operations of the subgroup, and the $w_{\mathbf{k}}$ are the weights associated with each k-point in the irreducible set. The ground state wavefunctions here may be determined by a non-self-consistent bandstructure calculation at the k-points required. Of course, one may reduce the number of calculations required here by utilising the full space group symmetry. The wavefunction coefficients transform in reciprocal space according to

$$c_{m,S\mathbf{k}}(S\mathbf{G}) = e^{-2\pi i S\cdot(\mathbf{k}+\mathbf{G})\cdot\mathbf{v}_S} c_{m\mathbf{k}}(\mathbf{G}) \tag{4.57}$$

under the action of $\{S|\mathbf{v}_S\}$, where $\mathbf{v}_S$ is a translation vector smaller than any primitive lattice translation vector of the crystal.

Further complications arise for terms that involve mixed perturbations. This is because both perturbations will, in general, possess different symmetries. For example, in determining the off-diagonal elements of the dynamical matrix, terms such as the following arise:

$$\sum_{k=1}^{full-BZ} \langle u_{m\mathbf{k}}^{(0)} | v^{\tau\kappa\alpha} | u_{m\mathbf{k},\mathbf{q}}^{\tau\kappa'\beta} \rangle \tag{4.58}$$

where each wavefunction, and the perturbing potential itself, will have been evaluated over different irreducible k-point sets. Given the transformation law in equation 4.57, it can easily be shown that

$$\sum_{k=1}^{full-BZ} \langle u_{m\mathbf{k}}^{(0)} | v^{\tau\kappa\alpha} | u_{m\mathbf{k},\mathbf{q}}^{\tau\kappa'\beta} \rangle = \frac{1}{N_S} \sum_{S=1}^{N_S} \sum_{k=1}^{N_k} w_{\mathbf{k}} e^{-2\pi i \mathbf{q}\cdot\mathbf{v}_S} \langle u_{m\mathbf{k}}^{(0)} | v^{\tau K S\alpha} | u_{m\mathbf{k},\mathbf{q}}^{\tau\kappa'\beta} \rangle \tag{4.59}$$

where K is a symmetry-related atom. The sum on the right-hand side here is taken over the same irreducible set used for the diagonal term.

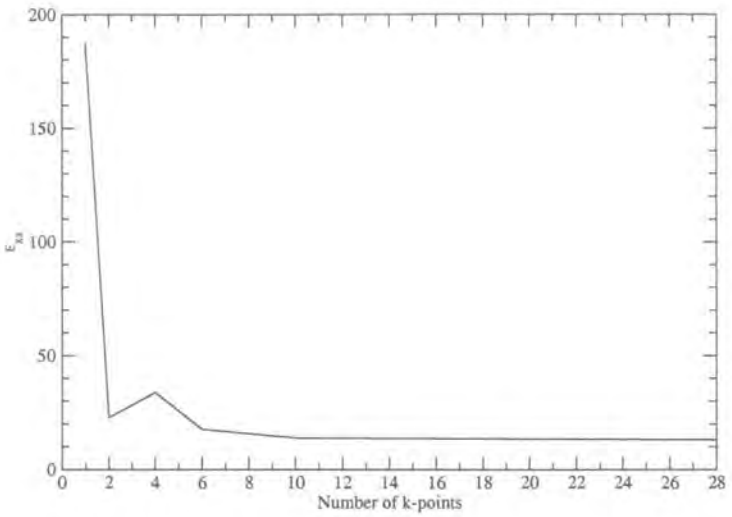

Figure 4.8: Effect of Brillouin zone sampling upon convergence of ϵ_{xx}^{∞} in silicon.

4.8.1 Effect of Brillouin Zone Sampling Upon Convergence

The quality of the DFPT calculation will depend upon the sampling of the reciprocal space. It would be reasonable to expect that, since the accuracy with which the first-order wavefunctions is obtained is sensitive to the accuracy with which the ground state of the system is determined, and further, that because one is obtaining derivatives of the Kohn-Sham energy, that the DFPT calculation may actually be more sensitive to the quality of the Brillouin Zone sampling. As a result, one would perhaps expect that a finer k-point mesh would be required. In figure 4.8 the effect of the sampling is shown for silicon. As can be seen, the permittivity is converged at around 10 k-points. This is no worse than is required for an accurate single-point calculation. One can therefore use the same k-point set for both the single-point and DFPT calculations, provided that it is sufficiently dense to obtain well-converged groundstate properties.

4.9 Phase Issues

In many cases, one needs to run successive minimisers, e.g. in order to determine polarisabilities and dielectric permittivites, first u^k is determined via a minimisation, before this is then used to obtain $E_{el}^{\varepsilon_\alpha \varepsilon_\alpha}$ via another minimiser. Alternatively, if one requires the Born effective charges from a phonon calculation, then it is necessary to perform a subsequent electric field calculation. It is possible to recalculate, via a bandstructure calculation, a new set of $\{u_{\mathbf{k}}^{(0)}\}$ each time in order to avoid the storage and passing of large arrays of wavefunction coefficients from subroutine to subroutine. However, this is found to give inconsistent results. In order to understand this, consider that each time one diagonalises the Kohn-Sham Hamiltonian, a random phase will be chosen for the eigenstates. This is because, as is shown in figure 4.9, the plane wave coefficients possess a $U(N)$ gauge freedom; that is, their orientation in the complex plane is not fixed by the orthonormality condition. However, once a single plane wave phase is fixed for a given k-point, the phases of all of the other plane wave coefficients are fixed relative to this plane wave.

Any first-order wavefunctions obtained must be orthogonalised to a set of Kohn-Sham eigenstates. Thus, at each point in the Brillouin Zone, the phase of the first-order wavefunctions is determined relative to the zeroth-order eigenstates. Now, if two different sets of first order wavefunctions, say $\{u^\varepsilon\}$ and $\{u^k\}$, are obtained relative to different sets of the Kohn-Sham orbitals, then there will, in general, be a non-trivial random phase between them, which will manifest itself in scalar products and matrix elements of the form

$$\langle u_{m\mathbf{k}}^{\varepsilon_\alpha}(\mathbf{r}) | u_{m\mathbf{k}}^{k_\alpha}(\mathbf{r}) \rangle e^{i\phi_{rand}} \tag{4.60}$$

where ϕ_{rand} is the random phase angle. In DFPT calculations, one is often interested in the sum of matrix elements and their Hermitian conjugates, *i.e.*

$$\begin{aligned} \langle u_{m\mathbf{k}}^{\varepsilon_\alpha}(\mathbf{r}) | u_{m\mathbf{k}}^{k_\alpha}(\mathbf{r}) \rangle e^{i\phi_{rand}} + \langle u_{m\mathbf{k}}^{k_\alpha}(\mathbf{r}) | u_{m\mathbf{k}}^{\varepsilon_\alpha}(\mathbf{r}) \rangle e^{-i\phi_{rand}} \\ = 2\langle u_{m\mathbf{k}}^{\varepsilon_\alpha}(\mathbf{r}) | u_{m\mathbf{k}}^{k_\alpha}(\mathbf{r}) \rangle \cos\phi \end{aligned} \tag{4.61}$$

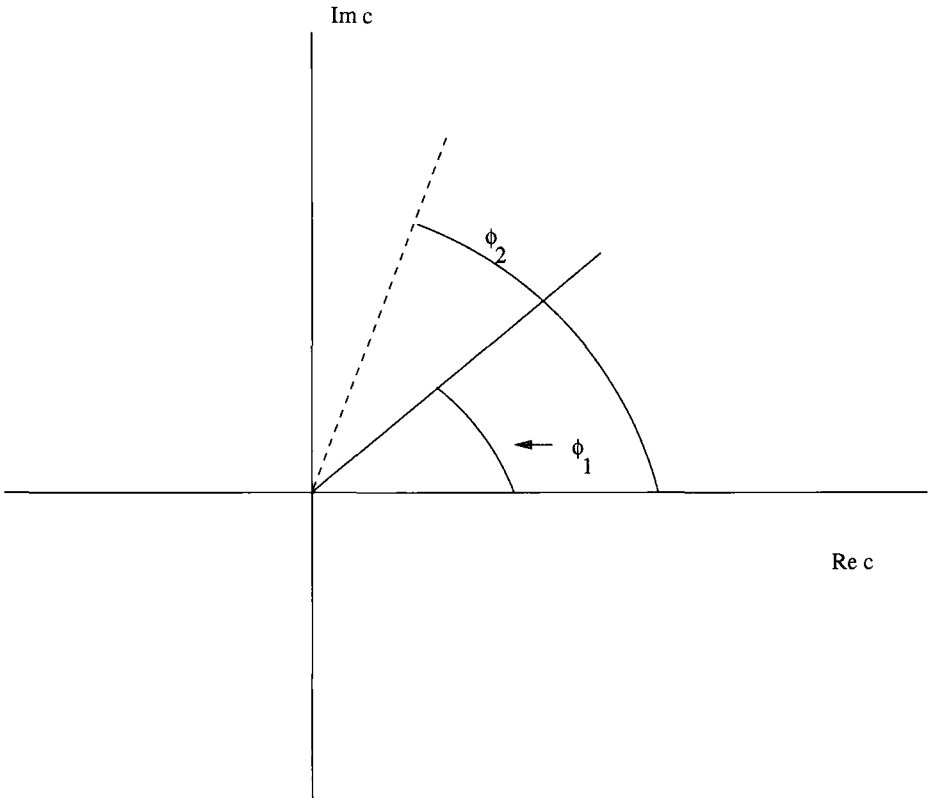

Figure 4.9: Argand plot showing the origin of indeterminacy of phase for the Kohn-Sham eigenstates. Although the magnitude of the plane wave coefficient c is fixed, its orientation, and hence phase, ϕ, is not.

and it is clear that if this phase angle alters from calculation to calculation then inconsistencies will occur. If however, one determines all first-order wavefunctions relative to the same set of Kohn-Sham eigenstates, then the phase in equation 4.60 trivially cancels, and the inconsistencies are removed. The Kohn-Sham orbitals at neighbouring k-points will also have a random phase angle between them, and this phase indeterminacy is one of the reasons for determining u^k by the analytic method described above, as attempting to do so numerically leads to gauge invariance problems similar to those discussed above.

4.10 Scissors Operator

The bandgap problem in DFT associated with LDA is well-known [47], and this has been argued [81] to be the underlying reason why agreement between experimental and LDA-obtained values of the dielectric permittivity tensor is often unsatisfactory. This point is returned to in a later section with regard to silicon. A possible, although slightly unsatisfactory, method to alleviate this problem is to introduce a scissors operator, as done by Levine and Allan [133] and as discussed by Gonze and Lee [81].

The implementation of this is simple. Assuming that the energy band gap must be increased from E_g^{LDA} to $E_g^{LDA} + \Delta$, the expression for the second-order variational energy becomes

$$\begin{aligned} E_{SCI}^{\varepsilon_\alpha^\star \varepsilon_\beta}\{u^{(0)}; u^{SCI,\varepsilon_\alpha}, u^{SCI,\varepsilon_\beta}\} \;=\; & \\ & \frac{\Omega_0}{(2\pi)^3}\int_{BZ}\sum_{m}^{occ} s(\langle u_{m\mathbf{k}}^{SCI,\varepsilon_\alpha}|H_{\mathbf{k},\mathbf{k}}^{(0)} - \epsilon_{m\mathbf{k}}^{(0)} + \Delta|u_{m\mathbf{k}}^{SCI,\varepsilon_\beta}\rangle \\ + \;& \langle u_{m\mathbf{k}}^{SCI,\varepsilon_\alpha}|iu_{m\mathbf{k}}^{k_\beta}\rangle + \langle iu_{m\mathbf{k}}^{k_\alpha}|u_{m\mathbf{k}}^{SCI,\varepsilon_\beta}\rangle)d\mathbf{k} \\ + \;& \frac{1}{2}\int_{\Omega_0}\left.\frac{dv_{xc}}{dn}\right|_{n^{(0)}(\mathbf{r})}[n_{SCI}^{\varepsilon_\alpha}(\mathbf{r})]^\star n_{SCI}^{\varepsilon_\beta}(\mathbf{r})d\mathbf{r} \\ + \;& 2\pi\Omega_0\sum_{\mathbf{G}\neq\mathbf{0}}\frac{[n_{SCI}^{\varepsilon_\alpha}(\mathbf{G})]^\star n_{SCI}^{\varepsilon_\beta}(\mathbf{G})}{|\mathbf{G}|^2}. \end{aligned} \tag{4.62}$$

This may of course be solved by the methods outlined in this chapter. The term involving Δ is positive-definite; thus if Δ is positive, the dielectric permittivity along

any direction will always be smaller in the LDA and scissors approximation than in LDA.

In section 4.12.1, the effects of the scissors operator upon the dielectric permittivity tensor, polarisabilities and effective charges are investigated.

4.11 Parallel Implementation

Thus far, it has been assumed that the code has been implemented in series. In practice, DFPT calculations can be computationally intensive and thus in order to examine large systems, it is necessary to be able to use the code on parallel computers. CASTEP allows two possible parallelisation strategies: parallelisation over either plane wave coefficients or k-points. In the former, the plane wave coefficients $c_{i,\mathbf{k}+\mathbf{G}}$ are distributed over parallel processors. The bands and k-points, the number of which is small in comparison to the number of plane wave coefficients, are then operated on in series. The Achilles heel of all massively parallel implementations is the inter-processor communication; in this scheme, this only occurs when summing over G-vectors when orthogonalising wavefunctions, performing FFTs on the charge density, and in packing/unpacking the wavefunction coefficients in order to construct the charge density. The second possible scheme involves distributing the k-points over the parallel processors; the plane wave coefficients and the electronic bands are then operated upon in serial. In this case, inter-processor communication occurs when performing summations over the Brillouin zone.

The modular design of the CASTEP code in which the DFPT code was implemented, making extensive use of data encapsulation and structured types, ensured that the code was easy to implement for massively parallel execution. For example, the code required for distributing wavefunction coefficients was entirely contained within low-level subroutines; thus the code was **G**-vector parallel by default. Parallelisation over k-point was similarly easy, although some extra calls to low-level subroutines were required in order to perform summations over the Brillouin zone.

Some care is required when implementing the use of symmetry in conjunction with a massively parallel implementation. This can be understood with reference to

equation 4.57, where knowledge of distributed wavefunctions is required. In the serial or k-point parallel case, the FFT grid is mapped onto a 3-dimensional array, and this equation is straightforward to implement. In the case of **G**-vector parallel, more care needs to be exercised, as, in general, the coefficients on either side of equation 4.57 will reside on different processors. Thus one must gather all coefficients onto the master node to reconstruct the FFT grid. One can then carry out the symmetry transformation before distributing the coefficients back to new nodes. In order to limit the additional storage of a full grid on a single processor, this is done on a band-by-band basis.

4.12 Test Results

In order to validate the accuracy of the algorithms and methodologies described in this chapter, a number of calculations on test systems have been carried out. These include crystalline and molecular systems.

4.12.1 Crystalline Systems: silicon

One of the simplest crystalline systems that one may use as a testing ground for the applicability of DFPT methods is cubic silicon. This is the prototypical covalently bonded semiconductor, with the bonding due to sp^3-hybridisation. Further, a wealth of *ab initio* [121, 134, 133, 135, 136] and experimental [137, 138] data exist for silicon, making it easy to compare the results of calculation with existing work. The calculations in this section are carried out using norm-conserving pseudopotentials with cut-off energies of 300 eV, and a $4 \times 4 \times 4$ symmetry-reduced Monkhorst-Pack grid [60] giving 10 k-points in the Brillouin Zone. Exchange and correlation are treated within the GGA, using the parametrisation of Perdew and Wang [48]. The existing *ab initio* work of Giannozzi *et al.* [134, 136] and the experimental results therein are used for the purposes of comparison. In table 4.1 the results of these calculations are summarised.

The agreement between the theoretical values of the Born effective charge is marked, both returning an effectively zero value; this is expected, as the effective charge is a

	This work	Giannozzi *et al.*	Experimental
a	10.20	10.20	10.26
$Z^\star$	7×10^{-2}	$7 \times 10^{-2(a)}$	0
ϵ_∞	13.9	13.6	11.7

Table 4.1: Equilibrium lattice parameter [a, (a.u.)], Born effective charges ($Z^\star$) and static dielectric constants (ϵ_∞) for silicon. Comparison of calculations using DFPT as implemented in this thesis, the calculations of Giannozzi *et al.* and experimental results. (a) denotes a result from reference [136]. The experimental results are as in reference [134].

measure of how ionic a crystal is. The agreement between the values of ϵ_∞ obtained is also good. The differences are probably due to details in the implementation, such as pseudopotentials used, and the choice of XC functionals: the work of Giannozzi *et al.* uses the LDA as opposed to the GGA used in this work. This result also suggests that GGAs cannot be expected to improve upon the accuracy of DFPT calculations when applied to elemental semiconducting systems such as silicon. It is interesting to note the discrepancy between the *ab initio* values of the permittivity tensor and the experimental value. This has previously been attributed to shortcomings in the LDA [121, 139], but these results would seem to suggest that it is a failure related to semi-local functionals in general, rather than just the LDA in particular. There are two possible explanations for this failure: accurate determination of the permittivity is dependent upon accurate first-order wavefunctions. These are implicitly (and may indeed be explicitly) expressed as a sum over conduction band zeroth-order eigenstates. One could perhaps therefore expect that the well-known bandgap problem could lead to errors in the conduction band eigenstates, leading to errors in the permittivity tensor. This has been discussed by Gonze [81], and one suggestion for curing this problem is the use of a so-called scissors operator, as outlined in an earlier section, in order to shift the eigenvalues by a fixed amount such that the experimental bandgap is reproduced. However, given that the conduction band states provide a complete basis set with which to expand the first-order wavefunctions, this is unlikely to be the major reason for the discrepancy.

In order to examine the effects of the scissors operator, calculations have been carried out in order to determine how the inclusion and choice of the scissors operator affects the dielectric permittivity tensor of silicon. In table 4.2, the values of the dielectric

Δ (eV)	ϵ^{∞}	$Z^{\star}_{av}$ (eV)
0.3	12.2	0.150
0.4	11.96	0.216
0.5	11.7	0.278
0.6	11.5	0.339

Table 4.2: Variation in dielectric permittivity and Born effective charge tensors in silicon with scissors operator.

permittivity tensor and the Born effective charges are presented for different values of Δ, the scissors operator.

The LDA bandgap of silicon is 0.56 eV, with the true experimental bandgap being 1.17 eV; thus it would seem that $\Delta = 0.6$ eV is the most appropriate choice for Δ. However, as can be seen in table 4.2, this gives a value of $\epsilon^{\infty} = 11.5$, in contrast to the experimental value of 11.7; it seems therefore that the optimum value of Δ is 0.5 eV. This suggests that the scissors operator does correct the overestimation of the dielectric permittivity. However, in all cases, the value of the Born effective charge is incorrect; experimentally, silicon should not have non-zero effective charge tensors. Clearly, this is unsatisfactory. Further, one would expect that if the bandgap is the fundamental problem, then introducing the scissors operator to "fix" this problem should not then lead to previously well-described aspects of the physics going awry. It therefore seems that the scissors operator is an unsatisfactory "patch-up"; moreover, this suggests that the fundamental reason for the overestimation of the dielectric permittivity tensor within LDA is not due to the bandgap problem, in line with previous discussion.

A more likely explanation is that provided by Gonze *et al.* [140, 141, 142] who argued that, in the presence of an infinitesimal change in external applied field, the XC functional should possess a dependence upon the macroscopic polarisation of the sample. A proof of this has been provided by Ortiz *et al* [143]. In addition, the work of Aulbur *et al.* [144] and van Gisbergen *et al.* [145] lends credence to this interpretation, as they showed specifically that the polarisation dependence of the XC functional leads to extra terms in the Kohn-Sham equations that are absent in the LDA and GGA, which depend only upon the bulk periodic density.

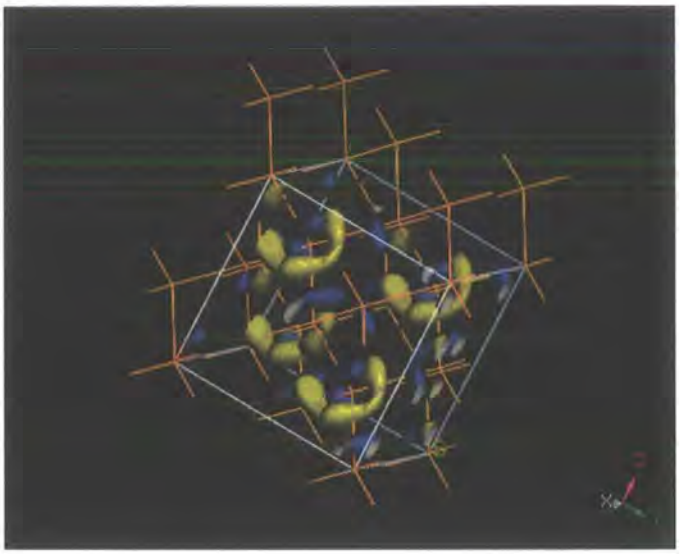

Figure 4.10: First-order change in electron density in silicon in response to an electric field perturbation; the blue represents an augmentation of charge, whilst yellow represents a charge density depletion.

Studying the first-order density may also provide physical insight into the response of a system to an external perturbation. By investigating whether the density response is physically reasonable, it is possible to use this as a further test of the validity and accuracy of a calculation. In figure 4.10, the first order change in the electron density of silicon is shown in response to an electric field perturbing in the y-axis. The blue represents a depletion in charge, whilst the yellow represents an augmentation of the charge. It is clear that this looks physically reasonable: one can see the covalent bonds being polarised strongly, as one would expect.

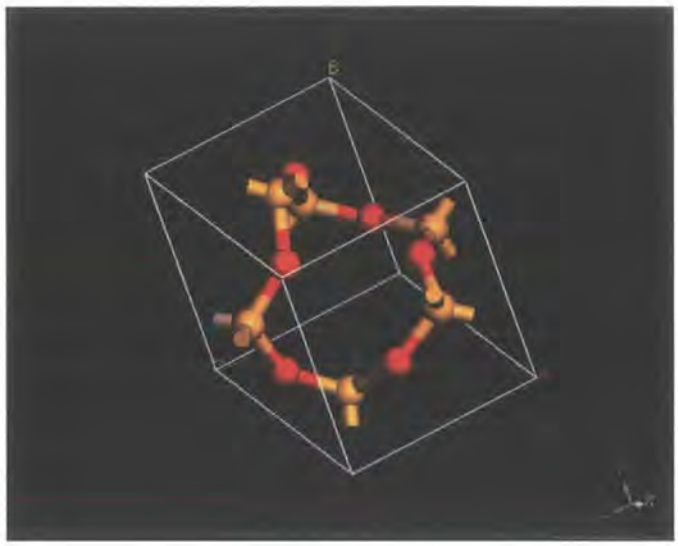

Figure 4.11: Geometric structure of α-quartz.

4.12.2 α-quartz

α-quartz is the simplest tetrahedrally bonded silica (SiO_2). In figures 4.11 and 4.12, its geometric structure is illustrated. Although such silica systems are of technological importance, for example, for the fabrication of optical waveguides, the appeal of studying this system for this work is the existence of both high quality *ab initio* DFPT results [146, 123] and experimental results [147] with which to compare. The strong anisotropy of the Born effective charge and the dielectric permittivity lead to rich behaviour, whilst soft phonon modes are important in the structural phase transitions exhibited [148] . The richness of the physics of quartz makes it an excellent test case for DFPT methods.

The calculations have been carried out using the PBE GGA [149] exchange-correlation functional. Norm-conserving pseudopotentials with a kinetic energy cut-off of 600

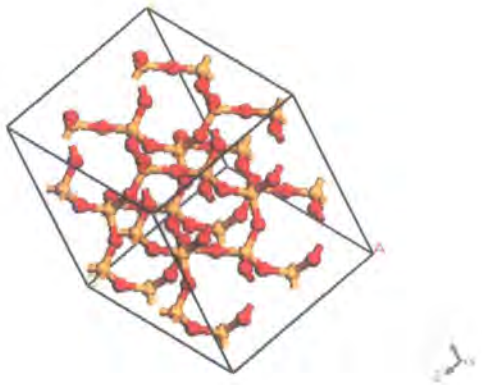

Figure 4.12: α-quartz supercell.

	This work	Gonze *et al.*	Experimental
a	4.811	4.731	4.831
c	5.306	5.230	5.3118

Table 4.3: Equilibrium lattice parameters [a, c (Å)] for quartz. Comparison of calculations using PBE as implemented in this thesis, the calculations of Gonze *et al.* [146] and experimental results. The experimental results are as in reference [146].

eV are used, while a 4×4×4 Monkhorst-Pack grid is used to integrate over the Brillouin zone. The equilibrium geometric structure is determined using the Hellmann-Feynman theorem. In table 4.3, the equilibrium lattice constants are shown and compared with the results of Gonze *et al.* and with experimental values.

The agreement with the experimental values is extremely satisfying; the disagreement between the values reported in this thesis and those of Gonze *et al.* [146] are probably due to their use of the LDA in treating exchange and correlation, and their use of only one special k-point.

In table 4.4 the normal mode frequencies are presented. In order to allow a direct comparison with the work of Gonze *et al.* [146] and Umari *et al.* [123], the Brillouin zone integration is carried out using one k-point at $(1/3, 0, 1/4)$; this is sufficient for obtaining residual forces less than 0.01 eV/Å, which can be considered to be converged. The normal modes require some discussion. The eigenmodes of the analytical part of the dynamical matrix transform according to the irreducible repre-

sentations of the symmetry group D_3: the A_1 and A_2 are non-degenerate, whilst the E are doubly degenerate. The assignment of whether a mode is transverse optical or longitudinal optical is achieved using the method outlined in Umari *et al.* [123]: a three-component mode effective charge vector may be defined as

$$\bar{Z}^n_\alpha = \sum_{\kappa\alpha} Z^\star_{\kappa,\alpha\beta} u^n_{\kappa\beta} \tag{4.63}$$

where the symbols have their usual meanings, u is a dynamical matrix eigenvector, and n is the mode under consideration. If $\mathbf{q} \cdot \bar{\mathbf{Z}}^n = 0$ then the eigenmode of the analytical part of the dynamical matrix is also an eigenmode of the full dynamical matrix with the same frequency, and is hence identified as a TO mode. The LO modes may be identified by taking $\mathbf{q} \parallel \bar{\mathbf{Z}}$ for every $\bar{\mathbf{Z}}^n$.

The A_1 modes are independent of the direction of $\mathbf{q}$, as $\bar{\mathbf{Z}}^n = 0$ for these modes. $\bar{\mathbf{Z}}^n$ is parallel to the optical axis (z-axis) for the A_2 modes, and hence LO-TO splitting occurs for these modes; the A_{2L} modes are, accordingly, obtained by diagonalising the full dynamical matrix with $\mathbf{q}$ parallel to the optical axis, whilst the A_{2T} modes are obtained by diagonalising with $\mathbf{q}$ orthogonal to the optical axis. The E modes are characterised by the $\bar{\mathbf{Z}}^n$ spanning the xy plane. Consequently, for $\mathbf{q}$ orthogonal to the optical axis, a LO-TO splitting occurs, whilst the modes remain degenerate at the E_T frequencies for $\mathbf{q}$ parallel to the optical axis.

Table 4.4 presents the normal mode frequencies calculated in this work, and compares them with results from two other density functional calculations [146, 123] and with two sets of experimental data [147, 150]. The first set of data corresponds to extrapolations to 0K, whilst the second set was obtained at room temperature. The agreement between the experimental and theoretical results is generally good, as is the agreement with the other theoretical values. The differences between theoretical values should probably be attributed to differing lattice constants used, and different XC functionals.

In figure 4.13, the full dispersion curve as calculated by DFPT is presented. The agreement with experimental results is good, and this is an excellent validation of the DFPT technique, as it illustrates that is it possible to obtain highly accurate *ab initio* lattice dynamical and dielectric properties of complex crystalline systems.

	Theory			Experiment	
	Present Work	Umari *et al.*	Gonze *et al.*	Ref. [147]	Ref. [150]
$A1$					
	191.0	193.7	238.9	219	207
	341.1	355.0	339.3	358	356
	449.2	460.1	461.7	469	464
	1094.9	1123.3	1061.0	1082	1085
$A2_T$					
	353.6	366.4	341.4	361.3	
	475.8	489.3	493.4	499	
	774.1	792.2	762.4	778	
	1078.4	1115.4	1056.5	1072	
$A2_L$					
	376.3	391.4	365.7	385	
	530.7	533.8	540.5	553	
	786.3	815.0	784.7	791	
	1248.3	1272.6	1218	1230	
E_T					
	115.7	120.9	133.3	133	128
	252.0	257.3	261.3	269	265
	378.4	390.0	377.6	393.5	394
	431.8	448.0	443.8	452.5	450
	689.0	703.3	690.8	698	697
	791.4	809.6	791.7	799	795
	1078.6	1108.7	1045.0	1066	1072
	1164.9	1190.8	1128.1	1158	1162
E_L					
	117.4	121.0	133.4	133	128
	252.9	258.5	263.2	269	265
	379.4	398.6	389.2	402	401
	434.9	500.2	498.6	512	509
	689.1	708.7	694.5	701	697
	792.1	824.0	803.9	811.5	807
	1087.1	1185.7	1123.9	1155	1162
	1164.9	1270.6	1209.5	1227	1235

Table 4.4: Γ-point vibrational frequencies for α-quartz; all values are in cm^{-1}.

4.12.3 NaCl

Thus far, the tests have been on a prototypical covalent semiconductor (silicon) and an insulator that has significant ionic character (quartz). It is useful to also examine the efficacy of DFPT when applied to a prototypical ionic system. For that reason, the response of sodium chloride (NaCl) to phonon and electric field perturbations

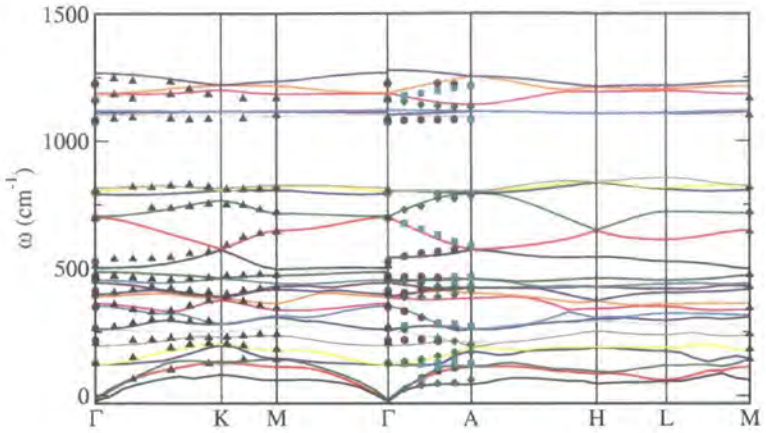

Figure 4.13: Phonon dispersion curve for α-quartz: *ab initio* results via DFPT (solid lines) vs. experimental results.

has been examined. The crystalline structure of NaCl is cubic, and is shown in figure 4.14. The calculations use the LDA XC functional, with norm-conserving pseudopotentials requiring a kinetic energy cut-off value of 500 eV. Brillouin zone integrations are calculated using a mesh of 10 k-points in the irreducible wedge.

In table 4.5 the Γ-point normal mode frequencies are shown. These are compared with the Hartree-Fock results of Prencipe *et al.* [151] using a linear combination of atomic orbitals (LCAO) basis set, and the density functional results of Froyen and Cohen [152]. It can be seen that the results obtained in the present work are in very good agreement with the experimentally determined values. The shortcomings in the results of Prencipe *et al.* can be attributed to the failure of Hartree-Fock methods to incorporate electronic correlation effects. The work of Froyen and Cohen uses a plane wave pseudopotential implementation of DFT in the local density approximation. As with the present work, Brillouin zone integrations use 10 k-points. Froyen and Cohen, in common with Prencipe *et al.* use a finite difference method in order to obtain the normal mode frequencies; the error associated with this is estimated to be 11 cm^{-1}, which suggests that this is responsible for the disagreement. It therefore seems that DFPT can accurately determine the lattice dynamics of ionic systems.

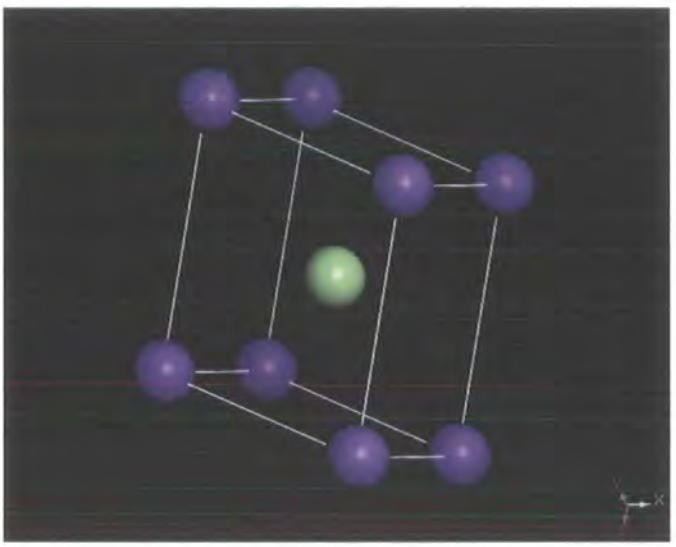

Figure 4.14: Geometric structure of NaCl: unit primitive cell.

$\omega(\text{cm})^{-1}$				
Present Work	Prencipe *et al.* [151]	Froyen [152]	Expt. [153]	Expt. [154]
175.2	156.7	163.9	176.7	172.4

Table 4.5: Γ-point normal modes for NaCl.

	This work	Experimental	Shukla [155]
α (Å^3)	55.44		
ϵ^∞	2.68		
ϵ^0	6.15	6.12[1]	
$Z^\star$ (e) Na	1.06	1	0.985
$Z^\star$ (e) Cl	-1.06	-1	-0.985

Table 4.6: Dielectric properties of NaCl. 1 denotes a value of $\epsilon(\omega)$ for $\omega = 10^4 s^{-1}$. Value taken from [156]

The cubic structure of NaCl leads to the permittivity, polarisability and Born effective charges take the form of diagonal tensors, with all elements the same magnitude. For this reason, only one element of each tensor needs to be quoted. In table 4.6 these quantities are given, along with experimental values, where available. The values of the effective charges are also compared with the work of Shukla [155], where a Wannier function basis set is used in conjunction with Hartree-Fock theory to obtain *ab initio* values.

The agreement demonstrated for the permittivity tensors and the effective charges is pleasing. The result for the effective charges is particularly noteworthy, for not only does it demonstrate that the sum rule is satisfied exactly, but also that the value of the effective charge is equal, within numerical noise, to the nominal ionic charges. This indicates that NaCl is perfectly ionic, and is a satisfying confirmation of the ionic model of solids and simple chemistry. Note that the results of Shukla suggest that one needs to incorporate the effects of electronic correlation in order to obtain accurate values of the Born effective charges.

4.12.4 Molecular Systems

As the ultimate purpose of implementing the DFPT methods described in this chapter is to investigate the dielectric and lattice dynamical properties of molecular crystals, it is necessary to investigate the applicability of DFPT to problems in molecular physics. For this reason, in table 4.7 the harmonic normal mode frequencies are presented for a range of small molecules, as obtained experimentally, and via a range of quantum chemical techniques. The methods compared to are: density functional methods, using a range of XC functionals (BLYP, B3LYP, EDF1, and EDF2). The

	Expt	Present	BLYP	EDF1	B3LYP	EDF2	HF	MP2	CCSD(T)
H_2	4401	3932	4347	4375	4420	4403	4587	4526	4409
HF	4138		3932	4018	4090	4105	4482	4195	4177
CO_2	2397	2440	2328	2379	2416	2439	2564	2439	2395
	1354	1343	1306	1329	1372	1380	1511	1343	1346
	673	715	633	643	671	672	773	661	660
H_2O	3943	3883	3755	3836	3901	3919	4227	3993	3945
	3832	3773	3656	3737	3801	3817	4127	3872	3840
	1649	1598	1611	1624	1639	1631	1743	1651	1668
NH_3	3577	3532	3459	3524	3578	3597	3807	3676	3597
	3506	3401	3348	3404	3462	3476	3685	3537	3471
	1691	1627	1645	1653	1678	1671	1795	1692	1688
	1022	979	1068	1076	1068	1053	1127	1077	1109
HN_3	3336	3444	3368		3481		3733	3576	
	2140	2174	2170		2279		2511	2385	
	1274	1271	1247		1299		1436	1263	
	1150	1133	1134		1180		1254	1129	
	537	593	514		533		677	574	
	522	567	575		603		574	548	
CH_3	3158	3112	3061	3110	3134	3147	3246	3218	3153
	3026	3109	2963	2994	3029	3035	3148	3009	3034
	1567	1529	1531	1535	1564	1555	1666	1600	1571
	1357	1306	1314	1311	1344	1336	1454	1183	1343

Table 4.7: Harmonic frequencies (cm^{-1}) for some small molecules: a comparison of DFPT results with commonly used quantum chemical techniques and experimental values. Data on HN_3 is from [157]; all other data come from [102].

last two named functionals are empirically obtained functionals, optimised for thermochemistry and harmonic frequencies, respectively [102]; and wavefunction-based methods, namely Hartree-Fock, MP2, and coupled cluster theory (CCSD(T)). The data come from references [102, 158, 157]. The results presented in [102] use the Dunning cc-p VTZ basis set [159], whilst those in [158, 157] use the 6-31G** basis set.

Hartree-Fock methods consistently overestimate the harmonic frequencies, often by up to 200 wavenumbers; such poor performance is unsurprising, and reflects the fact that Hartree-Fock methods fail to include any correlation effects. It can be seen that in the majority of cases, the DFPT results are in good agreement with the experimental values, and are often in better agreement than more expensive wavefunction methods such as MP2. It must be born in mind though, when comparing with other *ab initio* results of this form, that it is necessary to take into account

the effects of basis set error. To illustrate this point, consider the EDF2 functional; upon alteration of the basis set used from 6-31+G* to 6-311G**, the error in the normal modes determined for HF can change from -187 cm^{-1} to -5 cm^{-1}; thus the accuracy of the results will to a large extent depend upon the choice of basis set, and what basis set the functional has been optimised for use with. This is a perhaps less than satisfactory state of affairs. Further, one should also consider the fact that localised basis sets of the form used in references [102, 157, 158] cannot, by their very nature, span the entire Hilbert space; this becomes problematical when one requires properties that depend upon derivatives of the groundstate energy. For example, a basis set may be optimised to obtain accurate groundstate geometries, however, upon taking a derivative of the groundstate energy, a localised basis set will suffer the problem that the derivative of the basis set will not be included within the basis set being used. This is in contrast to a plane wave basis set such as that used in the calculations presented in this thesis, for which the derivatives of the basis function still reside within the same Hilbert space.

4.12.5 Molecular Polarisabilities

In table 4.8 the response of a series of test molecules to electric fields is given. In each case, only the trace of the polarisability tensor is quoted. This is because to quote a polarisability tensor in full requires that a frame of reference be defined and specified. The trace, however, is invariant under unitary transformation, and is therefore frame independent. Further, experiments only access the trace, and thus it represents the most natural quantity to quote. The values taken from [160] are carried out using DFPT within the LDA, using ultra-soft pseudopotentials. The present calculations were carried out using the PW91 GGA, and norm-conserving pseudopotentials; this necessitated kinetic energy cut-offs of 600 eV for carbon-containing molecules, 700 eV for ammonia and 400 eV for the hydrogen molecule. In all cases, the equilibrium geometry was obtained via a BFGS relaxation. The agreement between the present values and the experimental values of the polarisability tensors is extremely good, in many cases being better than the values given in [160]. Such agreement is encouraging, and suggests that the DFPT methodology is capable of highly accurate results.

Molecule	Present Work	Ref. [160]	Experiment
H_2O	1.55	1.62	1.43 [160]
CH_4	2.59	2.70	2.59 [160]
NH_3	2.31	2.37	2.21 [160]
H_2	0.89		0.80 [156]
C_2H_6	4.43		4.47 [156]
Benzene	10.73		10.74 [156]
C_{60}	89.2	83 [100]	84.9 [100]

Table 4.8: Molecular polarisabilties. All values are given in $Å^3$.

	ω (cm^{-1})	
Mode	$1T_2$	$2T_2$
Present Work	1306	3112
Porezag and Pederson [103]	1283	3090
Experiment [103]	1357	3158
	I^{IR}	
Mode	$1T_2$	$2T_2$
Present Work	1	0.69
Porezag and Pederson [103]	0.70	1
Experiment [103]	0.57	1

Table 4.9: IR intensities for methane. The values given are relative intensities, with the most intense assigned the value '1'.

4.13 IR Spectroscopy

Thus far, the calculations have indicated that DFPT can reliably and accurately determine the normal mode frequencies and dielectric properties of crystalline and molecular systems. However, if one is to use it to obtain IR spectra, then the accuracy and reliability of the method must be investigated. To this end, in this section, the spectra of a series of representative molecules is obtained and compared to previous calculations and measurements.

The IR spectrum for methane is shown in figure 4.15. In table 4.9, the normal mode frequencies and the corresponding relative IR intensities are presented.

The normal modes are in better agreement with experiment than the results of Porezag and Pederson [103], using a Gaussian basis set. The ratio of intensities between the two theoretical results shows good agreement, and these are in reason-

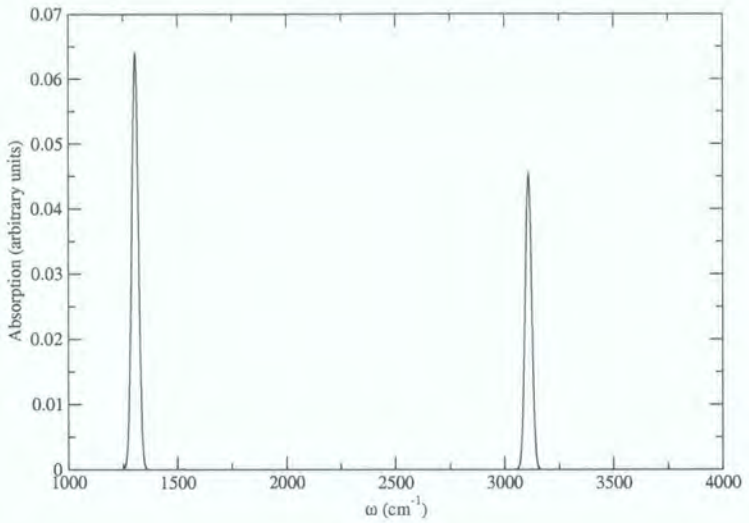

Figure 4.15: IR spectrum of methane as obtained using DFPT. A Gaussian broadening has been applied, as in all the subsequent spectra presented.

able agreement with the experimental values. One noteworthy feature is that the calculations presented in this work disagree over the ordering of the IR intensities for the two IR-active modes. Porezag and Pederson attribute this to a systematic error in the LDA; however, their results are obtained within the GGA using localised basis sets. This makes this contention difficult to support, and suggests that instead, it may be related to the basis set used, and some fortuitous cancellation of errors. Such a contention is supported by the work of Yamaguchi *et al.* [161] who have demonstrated that within Hartree-Fock theory, the ordering of the peaks may alter: for example, the minimal STO-3G basis set predicts that the ratio of intensities between the $1T_2$ and $2T_2$ peaks is 0.0699:1; the 6-311 + + G(3d,3p) basis set, conversely, predicts a reversal of the ordering, with the intensity ratio being 1:0.249. it can therefore be seen that the inclusion of polarisation effects in the basis set can radically alter the intensities and ordering, even within the same *ab initio* method.

In table 4.10 the normal modes and relative IR intensities of ethane are presented. The agreement can be seen to be mixed; although the normal mode frequencies are, on the whole, determined accurately, the relative intensities are not. All the values agree that the $3E_u$ mode is the most intense, although in some cases the intensities

Mode	ω (cm^{-1})			I^{IR}		
	Present	Ref. [103]	Experiment	CASTEP	Ref. [103]	Experiment
$1A_{1u}$	309	297	303	0.0	0.0	
$1E_u$	821	800	822	0.195	0.074	0.050
$1A_{1g}$	1003	998	1016	0.0	0.0	
$1E_g$	1197	1177	1246	0.0	0.0	
$1A_{2u}$	1384	1354	1438	0.002	0.012	0.020
$2A_{1g}$	1390	1361	1449	0.0	0.0	
$2E_u$	1472	1456	1526	0.016	0.166	0.125
$2E_g$	1475	1457	1552	0.0	0.0	
$2A_{2u}$	2988	2973	3061	0.271	0.518	0.411
$3A_{1g}$	2985	2969	3043	0.0	0.0	
$3E_g$	3043	3022	3175	0.0	0.0	
$3E_u$	3067	3055	3140	1.000	1.000	1.000

Table 4.10: Wavenumbers of IR-active modes and relative intensities for ethane. The values given are relative intensities, with the most intense assigned the value '1'.

calculated in this work disagree by an order of magnitude. The full spectrum is shown in figure 4.16.

In table 4.11, the relative IR intensities of water are presented. The full spectrum is given in figure 4.17. Examining the relative intensities, it is apparent that, except for the HF/STO-3G results, the *ab initio* methods agree with the experimental ordering of the peaks. This reinforces the point made with regard to methane concerning the effects of the basis set: the failure to have a sufficiently large basis set may cause incorrect ordering and/or intensities, irrespective of the methods employed. The results also suggest that the effects of correlation are not significant upon determining the relative intensities, at least for water. An important feature to note is that the different methods do not predict that the peaks occur at the same frequencies; the values for the frequencies in table 4.11 are those obtained in this work. Note that in all cases the theoretical methods (save HF/STO-3G) display a tendency to overestimate the intensities of the IR peaks.

In table 4.12 the relative IR intensities of ammonia are presented. The full spectrum is shown in figure 4.18. Again, Hartree-Fock theory with the STO-3G basis set fails to predict the correct ordering, in addition to predicting inaccurate relative intensities. The DFPT results obtained in this work are in broad agreement with

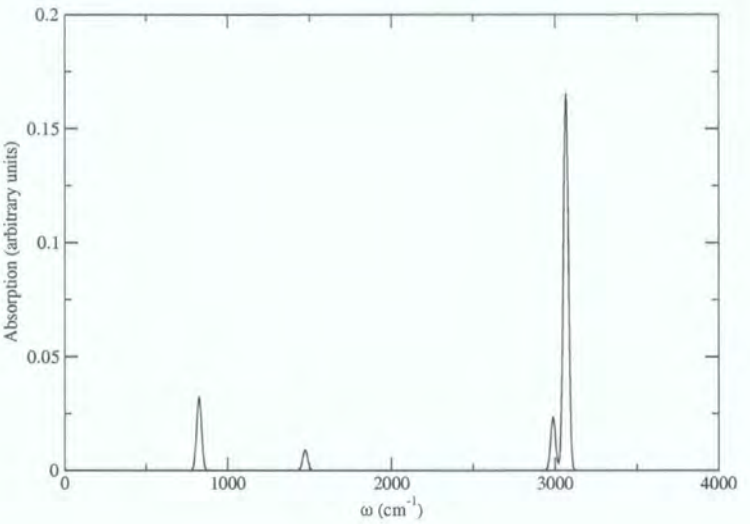

Figure 4.16: IR spectrum of ethane as obtained using DFPT.

ν		Relative Intensities			
(cm^{-1})	Present	HF STO-3G	HF 6-311++G(3d,3p)	MP2 6-31+G(d)	Expt.
1598	1	0.163	1	1	1
3773	0.103	1	0.159	0.110	0.0371-0.0506
3883	0.904	0.677	0.945	0.664	0.860-0.891

Table 4.11: IR intensities for water. The values given are relative intensities, with the most intense assigned the value '1'. Theoretical and experimental values are from Yamaguchi *et al.* [161]. Frequencies are as obtained in this work.

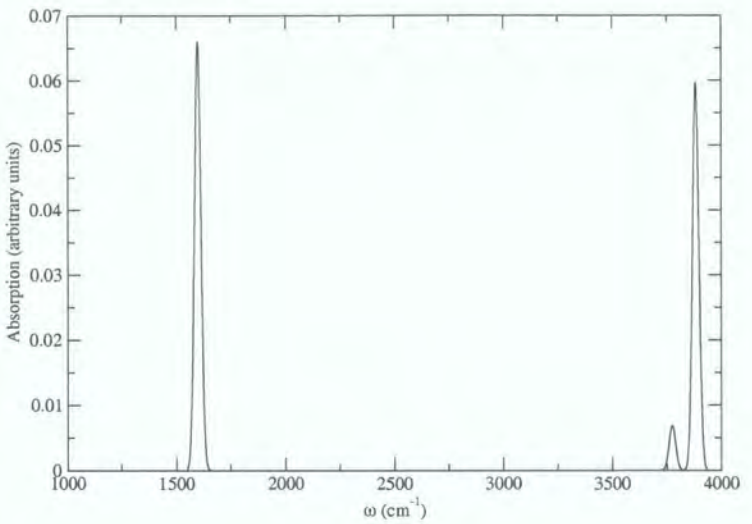

Figure 4.17: IR spectrum of water as obtained using DFPT.

the experimental spectrum, save for a slight overestimation of the intensity of the peak at 1627 cm^{-1}, and a large overestimation occurring at 3532 cm^{-1}. It does however, in common with the HF/6-311++G(3d,3p) and MP2/6-31+G(d) results calculate that this peak should be larger than the peak at 3401 cm^{-1} by an order of magnitude; this is in contrast to the experimental results, which suggest that the ordering of these two peaks should be reversed, with comparable intensities.

In table 4.13 the relative intensities of the IR peaks of hydrazoic acid are presented. The full spectrum is presented in figure 4.19. The calculations of Shen and Durig

ν	Relative Intensities				
(cm^{-1})	Present	HF STO-3G	HF 6-311++G(3d,3p)	MP2 6-31+G(d)	Expt.
979	1	1	1	1	1
1627	0.262	0.041	0.203	0.263	0.088-0.232
3401	0.031	0.099	0.008	0.003	0.028-0.034
3532	0.124	0.124	0.062	0.057	0.018-0.022

Table 4.12: IR intensities for ammonia. The values given are relative intensities, with the most intense assigned the value '1'. Theoretical and experimental values are from Yamaguchi *et al.* [161]. Frequencies are as obtained in this work.

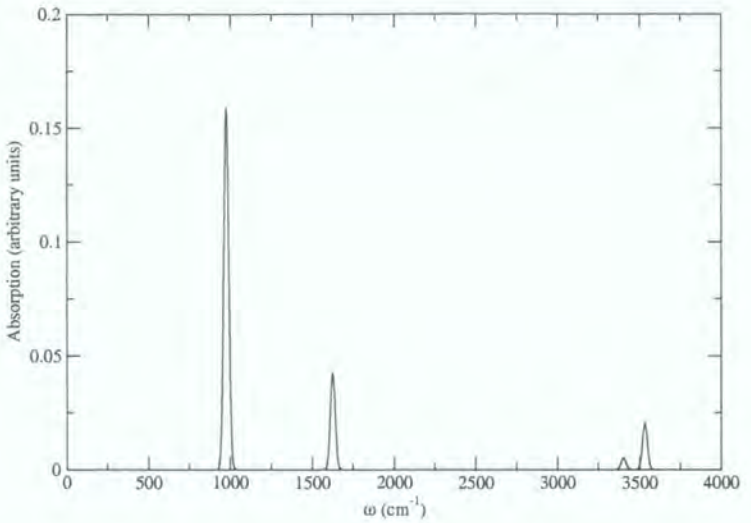

Figure 4.18: IR spectrum of ammonia as obtained using DFPT.

[162] at the MP2/6-31G* level of theory disagree with the other calculations presented as to the ordering of the IR peaks; these authors introduce a scaling factor in order to compensate and restore the "correct" ordering. Again, these results illustrate the importance of choice of basis set. The present work displays a tendency to underestimate the intensities of the peaks compared to the other methods used. The B3LYP results are of interest, as these are obtained within a density functional framework; the intensity of the the NH_3 stretch observed at 3444 cm^{-1} in this work is grossly underestimated, whilst, in contrast, the intensities of the other peaks are overestimated in comparison with the results in this work. This is a further indication of the effects of choice of basis set upon IR intensities.

A more complicated system is benzene. In table 4.14 the normal modes of benzene are presented. Good agreement with experiment and other theoretical calculations is observed for most frequencies, although larger discrepancies of around 100 cm^{-1} with regard to the experimental frequencies are observed for the higher frequency modes. It is noteworthy that the results of Clarke *et al.* [163] share this shortcoming, in contrast to those of Pulay *et al.* [164]. This warrants some comment. The values due to Pulay *et al.* [164] are Hartree-Fock results using a 4-21 basis set;

ν	Relative Intensities			
(cm^{-1})	Present	MP2/6-31G*	MP2/6-311+G**	B3LYP/6-31G*
3444	0.210	0.301	0.292	0.072
2174	1	0.891	1	1
1133	0.529	1	0.765	0.676
567	0.022	0.125	0.102	0.048

Table 4.13: IR intensities for hydrazoic acid. The values given are relative intensities, with the most intense assigned the value '1'. Theoretical and experimental values are from Shen and Durig [162]. The MP2/6-31G* results quoted from this work are the unscaled values. Frequencies are as obtained in this work.

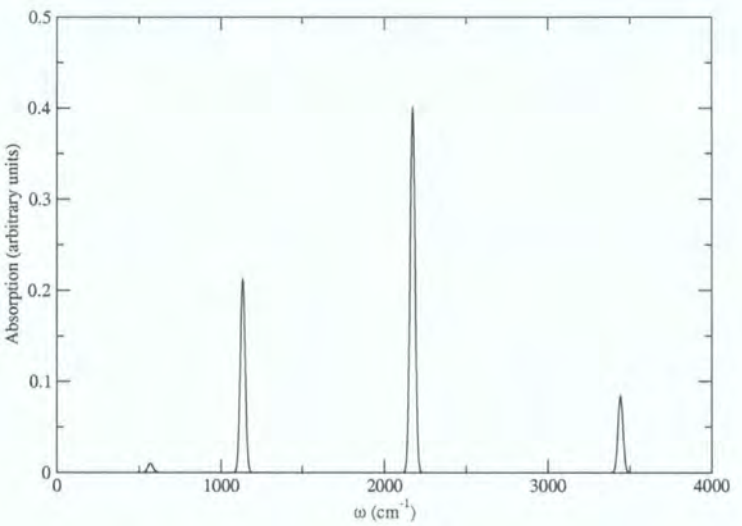

Figure 4.19: IR spectrum of hydrazoic acid as obtained using DFPT.

Assignment	PFB set 1 [164]	Clarke *et al.*[163]	Experiment [165]	Present
op	402		398	402
	607	606	606	612
op	667		673	681
op	701		707	722
op	843		846	849
op	969		967	980
op	996		990	996
	983	993	993	986
	997	1009	1010	1014
	1036	1033	1037	1046
	1162	1140	1146	1175
	1183	1179	1178	1187
	1297	1305	1309	1331
	1365	1479	1350	1372
	1482	1479	1482	1491
	1607	1602	1599	1598
	3051	3135	3057	3127
	3061	3145	3056	3135
	3080	3163	3064	3150
	3095	3178	3073	3159

Table 4.14: Benzene normal mode frequencies (cm^{-1}) and assignments: op denotes out of plane modes.

although this basis set is adequate for calculations of total energies, it systematically overestimates the force constants in benzene, an effect that is due to the neglect of electron correlation inherent in Hartree-Fock methods, and the truncated basis set used. To remedy this, Pulay *et al.* introduce empirical scaling factors that reproduce the high frequency modes accurately; thus it is slightly misleading to consider these results to be truly *ab initio*. The results of Clarke *et al.* are obtained via a classical trajectory study. This takes as its potential energy surface the force constants of Pulay *et al.* [164], with the CH stretch diagonal terms discarded, and the addition of a Morse potential. Interestingly, discarding these terms appears to lead to the same level of discrepancy between the calculated and experimental high frequency modes as is found with DFPT. This, coupled with the fact that the modes in question are C-H stretches, suggests that the issue here is anharmonicity, which is not dealt with at all in the DFPT scheme implemented in this work, based as it is upon a harmonic approximation.

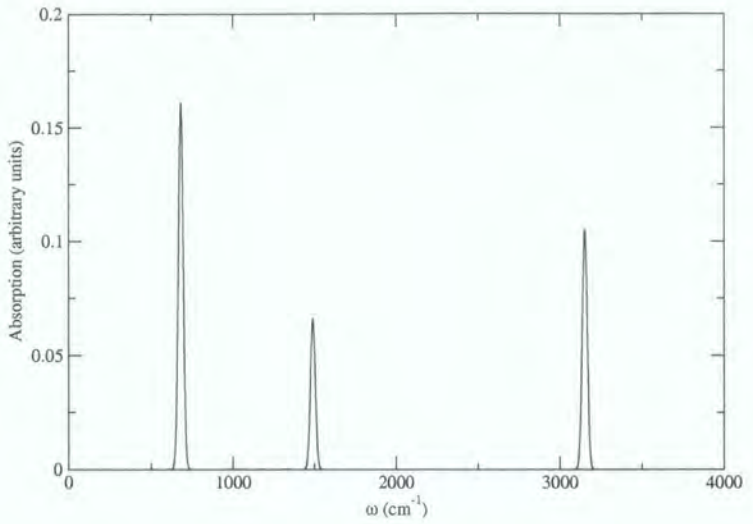

Figure 4.20: IR spectrum of benzene as obtained using DFPT.

In figure 4.20 the calculated IR spectrum of benzene is illustrated. This is in good agreement with the experimental spectrum, with the maximum intensity peak occurring at around 680 cm^{-1}. This is due to an out-of-plane wagging motion of all the C-H bonds. A peak at 1500 cm^{-1} is correctly predicted, although its relative intensity with respect to the peak at 3200 cm^{-1} is slightly wrong; the peak at 1500 cm^{-1} should be slightly more intense than that at 3200 cm^{-1}, in contrast to what is predicted. The peak at 1500 cm^{-1} is due to stretching of the C-C bonds in the aromatic ring. However, the spectrum does not include the smaller intensity peaks that should occur between 1500 and 200 cm^{-1}.

The calculations of IR spectra presented here seem to suggest that although DFPT can be used to obtain IR spectra, the results should be treated with caution. Certainly, it correctly predicts which modes are silent or IR-active, and in general predicts relative intensities in good agreement with other high level methods. There are, however, a minority of cases in which it does however, give inconsistent results as to the relative intensities, sometimes failing to predict these (as in ethane), or at other times correctly obtaining the intensities, but getting the ordering of the peaks wrong (as in methane).

The results presented, in particular the IR spectra of water, methane and hydrazoic acid, indicate that the relative intensities are extremely sensitive to the choice of basis set; indeed, even when using the same method in two calculations, a different basis set may lead to vastly different values of the intensities and/or the ordering of the peaks altering. It is therefore possible that the problems encountered with regard to methane and, to a lesser extent, ethane, could be due to problems with the basis set used, rather than to any inherent problem with the theoretical method used. One could perhaps expect such problems with localised basis sets, especially using sets that are too small to include polarisation effects; it seems more surprising that such problems could occur using plane waves. It is, of course, possible to suggest that the problems could arise, at least in part, from failures of the harmonic approximation inherent in determining the molecular normal modes. However, the evidence would appear to refute this; for example, in the case of methane, the normal mode frequencies obtained in this work are in closer agreement with experimental values than those of Porezag and Pederson [103] and yet the ordering of the IR peaks is not correct. This therefore suggests, in conjunction with Porezag and Pederson's use of the PW GGA [103, 48] and a localised Gaussian basis set, that it is indeed a basis set problem. Furthermore, it also implies that one may have a basis set that is well converged with respect to groundstate properties and normal modes, and yet not be appropriate for accurate determination of IR spectra. This can probably be attributed to the fact that one is dealing with a derivative of the groundstate dipole moment. Calculations have also been carried out to verify that the size of the supercell chosen does not affect the IR spectra, provided that the supercell is sufficiently large that calculations may be converged with regard to groundstate and structural properties (*i.e.* forces are smaller than 0.01 eV/Å).

The question of whether a mode is IR-active or not is largely down to the symmetry of the effective charge tensor and the dynamical matrix eigenvectors; as this is independent of the quality of the calculation, it is not surprising that this is correctly predicted. It would therefore seem that while the DFPT spectra can be used to correctly indicate where IR peaks will occur, that conclusions based upon the predicted intensities should be treated with caution.

4.14 Summary and Conclusions

In this chapter, the detailed implementation of density functional perturbation theory within a plane wave pseudopotential formalism has been described. The treatment of the first order potentials has been discussed, as has the treatment of exchange and correlation within the GGA using a numerical derivative. The use of this numerical derivative is numerically more stable than an analytical derivative, and allows the use of non-local XC functionals without modification.

The appropriate choice of minimisation scheme and preconditioner has been examined; it is found that conjugate gradients minimisation techniques offer the best convergence properties. The optimum preconditioner depends upon the system in question; in α-quartz, the TPA scheme is most effective, whilst in NaCl, the PSP scheme is the best performing. However, even when the PSP scheme performs best, the TPA performance is not significantly worse, with the difference being only 1-2 iterations; conversely, when TPA is the most effective, the performance of the PSP scheme is significantly worse. Thus the optimum choice, neglecting a detailed and impractical investigation of the optimum preconditioner for each system under consideration, is the TPA scheme, even though this is a groundstate preconditioning scheme, and is not optimised for DFPT calculations.

The use of symmetry to reduce the computational workload has been discussed in detail. Utilising the reduced symmetry of the perturbing wavevector allows a symmetry-reduced set of k-points to be determined; this will, in general, be larger than the unperturbed minimal set. Symmetry may also be used to determine the symmetry-related elements of the dynamical matrix, and therefore reduce the number of calculations required. The algorithm used has been presented, and a simplified version, applicable for the determination of the symmetry-related elements in the dielectric permittivity and polarisability tensors, has been described as well.

A series of test calculations on a range of representative systems (ionic, covalent, and molecular) in order to determine the accuracy of DFPT compared to other theoretical methods and experimental measurements has been presented. The agreement is, in the most part very good. There are known discrepancies, particularly with

regard to dielectric properties, but the reasons for this are understood to arise from an inadequacy in the treatment of of macroscopic fields within LDA and GGA XC functionals. The satisfying agreement indicates that DFPT is capable of obtaining high quality results for the dielectric and lattice dynamical properties of a range of different, and in some cases, complex systems.

The test calculations of IR spectra indicate that whilst DFPT can successfully predict the IR silent and active modes, the ordering and intensities of these peaks may not always be correct. Therefore it seems that although calculating the IR spectrum can help yield insight into a system on the basis of identifying the active modes, that one should exercise caution when attempting to draw conclusions based upon the actual intensities.

The work in this chapter therefore represents a good basis for investigating the lattice dynamical and dielectric properties of amino acid molecular crystals, for which no experimental values seem to exist; given the accuracy demonstrated in this work, one can be confident about using DFPT as a predictive tool in its own right rather than merely using it to confirm experimental results.

Chapter 5

Structural and Electronic Properties of Amino Acids

Any attempt to understand the relationship between the molecular crystal and its constituent molecules must begin with an understanding of the geometric and electronic structures of the two different cases. This may then serve as a foundation for more advanced investigations. In this chapter, therefore, the results of calculations determining the groundstate geometries and electronic structures of the amino acids under consideration in both the gaseous and solid state are presented. The aim is then to understand how and why the geometric and electronic structures are altered upon modification of the molecular environment. To this end, the intermolecular interactions responsible for stabilisation of the molecular crystals are identified, and their effects upon the molecular electronic structure analysed.

This is, to the best of the author's knowledge, the first time such a study has been carried out on the amino acids. As noted earlier in chapter 1, most *ab initio* work concerning amino acids has comprised of conformational studies on a limited number of small molecules. Even less exists on the molecular crystals: only the shielding tensors of carbon-13 in amino acid molecular crystals [30, 31] have been investigated using *ab initio* methods. A thorough investigation of the structural and electronic properties of these systems is therefore long overdue.

Within the Born-Oppenheimer approximation, the equilibrium geometries may be obtained using the Hellmann-Feynman theorem as outlined in chapter 2. All inter-

nal degrees of freedom are optimised using a BFGS algorithm, taking experimentally determined structures to determine the initial atomic positions. The single-particle Kohn-Sham equations are then solved at a series of reciprocal space points of high symmetry in order to determine the crystal eigenvalue spectrum, *i.e.* the band-structure. Population analyses are performed on both the molecular crystals and isolated crystals. The electron-ion interactions are described using non-local norm-conserving pseudopotentials of the Kleinman-Bylander form [64]. This is necessary because later work will involve subjecting these systems to DFPT calculations; therefore, in the interests of consistency, ultrasoft pseudopotentials are not used. Coupled with the presence of oxygen atoms, this does though necessitate that the the valence electron wavefunctions be expanded up to a kinetic energy cut-off of 1000 eV. This ensures convergence of total energy properties to better than 1meV/atom. Reciprocal space integrations are carried out over varying numbers of symmetry-reduced k-points, with the same energy convergence tolerance as used for the plane-wave cut-off. Exchange and correlation effects are treated using the GGA due to Perdew and Wang [48]; this is known to perform significantly better for hydrogen-bonded molecular systems than the LDA [101, 47]. The calculations on isolated molecules use the same parameters, except a supercell of $10 \times 10 \times 10$Å is used in order to impose false periodicity; this is found to be sufficient to ensure that the molecular energy levels are dispersionless to within 1 meV, and hence only the Γ-point need be used in integrating over the Brillouin zone.

In order to investigate the structural parameters in more detail, it is useful here to discuss the labelling conventions used in assigning labels to atoms. In figure 5.1 the (zwitterionic) structure of valine is illustrated, along with the numbering convention used throughout. In all cases, the numbering of the carbon atoms labels that in the carboxy group as '1', then proceeds along the sidechain in sequence.

5.1 Structural Relaxation

The object of a structural relaxation is to obtain the groundstate relaxed geometry of the system under consideration. This may include the equilibrium lattice constants. For a given ionic configuration, a self-consistent single-point calculation is

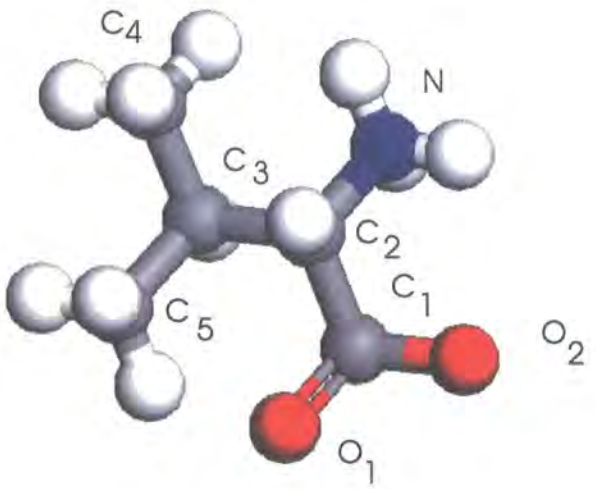

Figure 5.1: Valine: the numbering convention used in this study.

carried out, and from this, the forces obtained. If these forces are greater than some minimum tolerance, then the ions are moved in the direction of the forces. This procedure is repeated until an equilibrium structure, with vanishing forces (within the numerical tolerance) is obtained. The lattice constants may also be varied by determining the stresses acting, and obtaining an equilibrium structure with vanishing stresses.

5.2 Population Analysis

A useful tool in studying the electronic structure is population analysis. In this chapter, extensive use will be made of this method; it is therefore useful at this juncture to discuss at some length the basic theory underpinning this technique. Population analysis is based upon a decomposition of the electronic density into atomic contributions, such that nominal charges may be assigned to each atom. The absolute values of these charges are not physically meaningful, being extremely sensitive to the choice of basis set used in the calculation [166, 167, 168, 169, 170], in addition to which, no unique single decomposition exists. However, the trends revealed by population analysis are useful.

Plane wave basis sets do not naturally lend themselves to such localised atom-based decompositions due to the extended nature of the basis states. Instead, one must project the Kohn-Sham eigenstates obtained from a PW calculation onto a localised basis set. In this work, the choice of localised basis sets is that of atomic pseudo-orbitals generated from the pseudopotential. The projection technique of Sanchez-Portal *et al.* [169, 170] is used in conjunction with the implementation of Segall *et al.* [166, 167, 168].

An overlap matrix $\mathbf{S}(\mathbf{k})$ may be defined through

$$S_{\mu\nu}(\mathbf{k}) = \langle \phi_\mu(\mathbf{k}) | \phi_\nu(\mathbf{k}) \rangle \tag{5.1}$$

where the $|\phi_\mu(\mathbf{k})\rangle$ is a localised orbital. Such an overlap is calculated in reciprocal space; the application of a phase factor suffices to allow overlaps between orbitals on different atomic sites to be evaluated.

The quality of the localised basis set used is quantified by the spilling parameter

$$\mathcal{S} = \frac{1}{N_\alpha} \sum_{\mathbf{k}} w_k \sum_{\alpha} \langle \psi_\alpha(\mathbf{k}) | (1 - \hat{p}(\mathbf{k})) | \psi_\alpha(\mathbf{k}) \rangle \tag{5.2}$$

where N_α is the number of plane wave eigenstates, w_k is the weight associated with each k-point in the Brillouin zone integration, and $\hat{p}(\mathbf{k})$ is the projection operator into the subspace of Bloch orbitals, $\psi_\alpha(\mathbf{k})$, at wavevector $\mathbf{k}$ generated by the atomic basis:

$$\hat{p}(\mathbf{k}) = \sum_{\mu} |\phi_\mu(\mathbf{k})\rangle \langle \phi^\mu(\mathbf{k})|. \tag{5.3}$$

Here, the $|\phi^\mu(\mathbf{k})\rangle$ are the duals of the atomic basis set such that

$$\langle \phi_\mu(\mathbf{k}) | \phi^\nu(\mathbf{k}) \rangle = \langle \phi^\mu(\mathbf{k}) | \phi_\mu(\mathbf{k}) \rangle = \delta_{\mu\nu} \tag{5.4}$$

and

$$|\phi^\mu\rangle = \sum_{\nu} (\mathbf{S}^{-1})^\star_{\mu\nu} |\phi_\nu\rangle. \tag{5.5}$$

The projector is defined in this way because the atomic orbitals used are non-orthogonal; although these are more cumbersome to handle, as the above equations indicate, they do possess the advantage of being more transferable and less environment-dependent [169], with a shorter range of interactions.

The spilling parameter may vary in value between 1, denoting complete orthogonality between the localised basis set and the plane wave eigenstates, and 0, meaning that the localised basis set perfectly reproduces the plane wave states.

A density operator may be defined through

$$\hat{\rho}(\mathbf{k}) = \sum_{\alpha}^{occ} n_{\alpha} |\chi_{\alpha}(\mathbf{k})\rangle\langle\chi^{\alpha}(\mathbf{k})| \tag{5.6}$$

where the n_α are the occupancies of the plane wave states and $|\chi_\alpha(\mathbf{k})\rangle$ are the projected eigenstates $\hat{p}(\mathbf{k})|\psi_\alpha(\mathbf{k})\rangle$. This allows the density matrix for the atomic basis set to be written

$$P_{\mu\nu}(\mathbf{k}) = \langle\phi^{\mu}(\mathbf{k})|\hat{\rho}(\mathbf{k})|\phi^{\nu}(\mathbf{k})\rangle \tag{5.7}$$

from which the Mulliken charge [171] for atom A is given by

$$Q_M(A) = \sum_{\mathbf{k}} w_k \sum_{\mu}^{onA} \sum_{\nu} P_{\mu\nu}(\mathbf{k}) S_{\nu\mu}(\mathbf{k}) \tag{5.8}$$

and the overlap charge between atoms A and B is

$$n_M(AB) = \sum_{\mathbf{k}} w_k \sum_{\mu}^{onA} \sum_{\nu}^{onB} 2P_{\mu\nu}(\mathbf{k}) S_{\nu\mu}(\mathbf{k}) \tag{5.9}$$

By examining the atomic Mulliken charges, it is possible to analyse in more detail the effects of zwitterionisation upon the molecular structure, and hence to understand the underlying reasons for this. Further, examination of the overlap charge between atoms allows one to investigate the nature of the bonding. A positive value of the overlap population indicates that the atoms are bonded; a negative value is indicative that the atoms are in an antibonding state. Of course, the values also

	Crystal symmetry	Z
L-alanine	$P2_12_12_1$	4
L-leucine	$P2_1$	4
L-isoleucine	$P2_1$	4
L-valine	$P2_1$	4

Table 5.1: Crystal symmetries and numbers of molecules per unit cell (Z) for the molecular crystals L-alanine, L-isoleucine, L-leucine and L-valine as determined experimentally in references [173, 174, 175, 176].

	a		b		c	
	Theory	Experiment	Theory	Experiment	Theory	Experiment
L-alanine	6.18	6.03	12.29	12.34	5.83	5.78
L-leucine	14.72	14.67	5.29	5.32	9.60	9.61
L-isoleucine	10.20	9.68	5.31	5.30	14.48	13.96
L-valine	9.71	9.68	5.23	5.25	12.51	11.93

Table 5.2: Structural parameters of the molecular crystals L-alanine, L-isoleucine, L-leucine, and L-valine; experimental (cited above) versus theoretical (this study) results. All lattice parameters are quoted in angstrom.

yield information on the strengths of the bonds present. This allows a quantitative investigation of the bonding mechanisms present within the molecular crystal, both inter- and intra-molecular.

5.3 Crystalline Systems

The determination of the structure of molecular crystal systems is a formidable problem, as has been discussed by Gdanitz [172]: although one may optimise the intramolecular structure relatively easily, the intermolecular structure represents a more challenging task due to the nature of the intermolecular forces and the large number of degrees of freedom typically present. Indeed, no method currently exists that can reliably determine molecular crystal structures from the constituent molecules' structures. In order to bypass this problem, experimentally determined structures [173, 174, 175, 176] are employed to provide initial atomic positions and crystal symmetries, after which one may then minimise the atomic forces to determine an equilibrium geometry consistent with the system symmetry.

The symmetries and numbers of molecules per unit cell are given in table 5.1.

	x		y		z	
	Experiment	Theory	Experiment	Theory	Experiment	Theory
H(1)	-0.301	-0.285	0.064	0.064	-0.806	-0.797
H(2)	-0.231	-0.214	0.179	0.198	-0.777	-0.780
H(3)	-0.401	-0.404	0.150	0.156	-0.957	-0.971
H(4)	-0.558	-0.559	0.239	0.248	-0.654	-0.646
H(5)	-0.778	-0.772	0.108	0.109	-0.856	-0.852
H(6)	-0.847	-0.833	0.103	0.103	-0.590	-0.558
H(7)	-0.685	-0.660	0.014	0.005	-0.694	-0.681
C(1)	-0.439	-0.428	0.142	0.141	-0.398	-0.390
C(2)	-0.523	-0.513	0.161	0.162	-0.644	-0.632
C(3)	-0.725	-0.706	0.091	0.091	-0.698	-0.684
N	-0.344	-0.341	0.138	0.143	-0.814	-0.805
O(1)	-0.271	-0.270	0.084	0.080	-0.372	-0.368
O(2)	-0.550	-0.528	0.185	0.188	-0.239	-0.230

Table 5.3: Theoretically determined atomic positions for L-alanine compared to the experimentally determined positions [173].

In figure 5.2 the structure of L-valine is shown. One can observe that the molecules have formed *zwitterions*; that is, the amino and carboxy functional groups ionise, forming oppositely charged functional groups, via the donation of a proton from the carboxy group to the amino group; the resulting amino group is now NH_3, whilst the carboxy group is CO_2. This is expected, as it is well-known that these zwitterions are stabilised in the solid state by electrostatic, polarisation and hydrogen bonding interactions with the crystalline environment [177]. This is in contrast to the gaseous phase, as can be seen by examining figure 5.2(b) illustrating the structure of an isolated valine molecule. In the crystal one can see that the molecules have arranged themselves such that the negatively ionised amine functional groups are in close proximity to the positively ionised carboxy groups of neighbouring molecules. This is readily understood via classical electrostatics: a bond between molecules may be formed via these charged functional groups. The molecules may also be bound by hydrogen bonding between the carboxy groups and the amine groups. Such bonding is well-known to take place in these molecular systems [32, 33]. It can be seen in figure 5.2 that the crystal structure allows oxygen atoms in the carboxy groups to participate in multiple hydrogen bonds; this is common in such structures [32]. However, such bonds are not generally of the same strength, and this is reflected in different bond lengths. For example, the O-H bonds between neighbouring molecules

	x		y		z	
	Experiment	Theory	Experiment	Theory	Experiment	Theory
H(1)	0.625	0.623	0.528	0.503	0.959	0.956
H(2)	0.507	0.507	0.246	0.213	0.870	0.859
H(3)	0.579	0.578	0.061	0.085	0.984	0.990
H(4)	0.587	0.589	0.039	0.008	0.802	0.820
H(5)	0.747	0.744	0.162	0.136	0.810	0.813
H(6)	0.743	0.740	0.175	0.168	0.993	0.994
H(7)	0.800	0.800	0.609	0.584	0.816	0.806
H(8)	0.744	0.741	0.750	0.739	1.033	1.029
H(9)	0.863	0.859	0.780	0.788	1.026	1.025
H(10)	0.817	0.819	0.534	0.537	1.122	1.123
H(11)	0.941	0.956	0.517	0.480	0.898	0.904
H(12)	0.914	0.907	0.230	0.213	0.817	0.818
H(13)	0.930	0.914	0.244	0.232	1.000	1.002
C(1)	0.618	0.615	0.512	0.495	0.738	0.731
C(2)	0.636	0.636	0.389	0.370	0.880	0.874
C(3)	0.736	0.734	0.283	0.273	0.898	0.895
C(4)	0.810	0.809	0.485	0.470	0.905	0.901
C(5)	0.807	0.807	0.649	0.644	1.030	1.026
C(6)	0.903	0.902	0.345	0.341	0.908	0.906
N	0.575	0.574	0.164	0.153	0.887	0.886
O(1)	0.587	0.582	0.382	0.358	0.639	0.634
O(2)	0.636	0.635	0.743	0.723	0.731	0.719

Table 5.4: Theoretically determined atomic positions for L-leucine compared to experimentally determined positions [174].

in the a-axis, where the H atom forms part of a donor group common to both bonds, and both oxygen atoms are in the same carboxy group, range from 1.71 to 1.82 $\mathring{A}$.

This though does not address why it is energetically favourable for the molecules to form zwitterions: valine has a non-zero dipole moment; therefore the possibility of forming bonds with neighbouring molecules must exist via dipole-dipole interactions. However, to form a zwitterion must involve some energetic penalty: therefore, why is it energetically favourable to zwitterionise? This is a point that is returned to later on, when discussing the electronic structure of L-valine. One consequence of the molecular arrangement, as shown in figure 5.2, is the formation of "layers" in the z-axis, which one would expect to be weakly bonded to each other, in contrast to the dipolar interactions and hydrogen bonding of the intra-layer arrangement.

One may contrast this structure with that of L-alanine, shown in figure 5.3. Again,

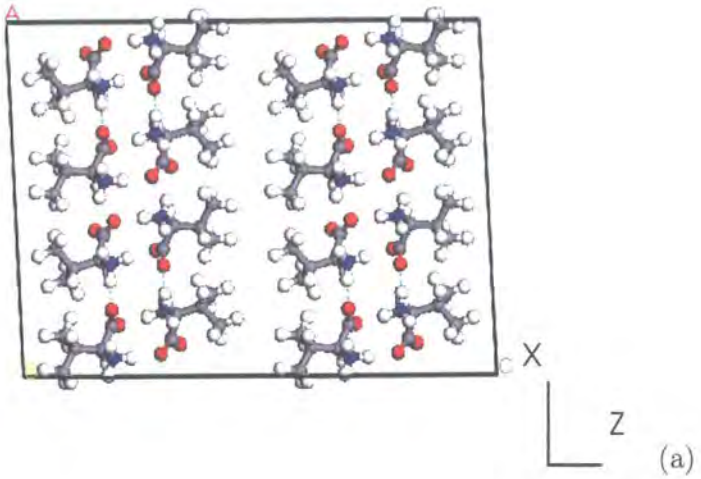

(a)

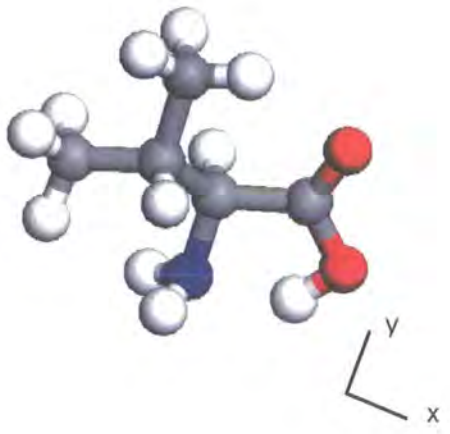

(b)

Figure 5.2: . The structure L-valine: supercell used in this study in (a); isolated molecule in (b). Note the "layer" formation in (b). Oxygen atoms are shown as red, carbon as grey, hydrogen as white, and nitrogen as blue. This colour convention is used throughout.

	x		y		z	
	Experiment	Theory	Experiment	Theory	Experiment	Theory
H(1)	0.303	0.288	-0.348	-0.336	0.396	0.383
H(2)	0.452	0.451	-0.286	-0.255	0.415	0.391
H(3)	0.359	0.349	-0.197	-0.182	0.480	0.477
H(4)	0.419	0.408	0.133	0.173	0.394	0.385
H(5)	0.438	0.425	-0.142	-0.113	0.254	0.247
H(6)	0.337	0.304	0.357	0.401	0.223	0.214
H(7)	0.493	0.468	0.287	0.339	0.252	0.248
H(8)	0.466	0.449	0.380	0.413	0.088	0.080
H(9)	0.343	0.331	0.177	0.175	0.070	0.065
H(10)	0.499	0.494	0.085	0.098	0.100	0.100
H(11)	0.198	0.189	-0.261	-0.263	0.239	0.243
H(12)	0.250	0.238	-0.186	-0.152	0.144	0.136
H(13)	0.163	0.140	-0.003	0.038	0.196	0.204
C(1)	0.206	0.198	0.131	0.157	0.384	0.385
C(2)	0.347	0.330	0.018	0.047	0.367	0.359
C(3)	0.363	0.343	-0.019	0.018	0.259	0.254
C(4)	0.408	0.383	0.231	0.264	0.216	0.209
C(5)	0.431	0.416	0.217	0.236	0.109	0.108
C(6)	0.230	0.221	-0.128	-0.096	0.204	0.207
N	0.366	0.354	-0.228	-0.199	0.420	0.405
O(1)	0.116	0.119	-0.017	0.019	0.413	0.424
O(2)	0.185	0.176	0.360	0.382	0.364	0.362

Table 5.5: Theoretically determined atomic positions for L-isoleucine compared to experimentally determined positions [175].

the molecules form zwitterions but the molecular arrangement differs from that of L-valine. Examining a $2 \times 2 \times 2$ supercell, looking along the a-axis reveals a pattern of interlocking "layers", each two molecules "thick" of oppositely aligned molecules. This arrangement allows the interaction energy between the oppositely ionised functional groups of neighbouring molecules to be minimised, hence making this arrangement energetically favourable. It is worth noting that in contrast to L-valine, no weakly bonded layers appear in the structure. This is significant, as it may explain why, for example, the agreement between experiment and theory (shown in table (5.2)) is so much better for L-alanine as opposed to that exhibited for L-valine. This can be understood as follows: charge localisation means that it is unlikely that the inter-layer bonding in L-valine is due to any form of charge overlap. Further, the "interfaces" of each layer are composed of CH_3 groups, so dipolar interactions are unlikely to be significant. Thus one could reasonably assume that non-local van der

	x		y		z	
	Experiment	Theory	Experiment	Theory	Experiment	Theory
H(1)	0.678	0.690	0.439	0.461	0.385	0.387
H(2)	0.541	0.520	0.379	0.384	0.409	0.408
H(3)	0.643	0.649	0.302	0.281	0.486	0.492
H(4)	0.569	0.559	-0.021	-0.052	0.379	0.381
H(5)	0.523	0.517	0.255	0.268	0.226	0.231
H(6)	0.514	0.507	-0.078	-0.070	0.091	0.095
H(7)	0.612	0.622	-0.243	-0.259	0.167	0.174
H(8)	0.467	0.457	-0.181	-0.190	0.210	0.220
H(9)	0.690	0.683	0.290	0.290	0.081	0.090
H(10)	0.760	0.762	0.380	0.405	0.195	0.210
H(11)	0.792	0.800	0.128	0.096	0.152	0.164
C(1)	0.779	0.779	-0.031	-0.040	0.363	0.371
C(2)	0.634	0.636	0.083	0.078	0.347	0.351
C(3)	0.597	0.599	0.132	0.126	0.222	0.232
C(4)	0.543	0.543	-0.111	-0.113	0.167	0.177
C(5)	0.719	0.718	0.242	0.237	0.157	0.171
N	0.624	0.624	0.326	0.318	0.412	0.413
O(1)	0.873	0.871	0.112	0.105	0.400	0.409
O(2)	0.794	0.795	-0.262	-0.265	0.335	0.345

Table 5.6: Theoretically determined atomic positions for L-valine compared to the experimentally determined positions [176].

Waals-type interactions are responsible for the inter-layer bonding. Semi-local XC functionals such as the GGA are poor at describing such non-local interactions, and thus one could expect some inaccuracy to be present. Contrariwise, in L-alanine, no such layers exist; the inter-molecular and inter-layer interactions appear to be primarily dipolar and hydrogen bond-like, which are accurately described by GGAs. One would therefore expect to find the agreement that is indeed found. This is also the most likely explanation for the fact that in some circumstances, the theoretical lattice constants (shown in table 5.1) have been found to be greater than the experimental lattice constants; for in principle, one would expect the exact reverse: that the experimentally determined lattice constants, which implicitly incorporate thermal effects, should be greater than the theoretically determined ones. In connection with this though, it should be noted that GGAs are occasionally responsible for underbinding in solids, resulting in lattice constants that are slightly too long [51].

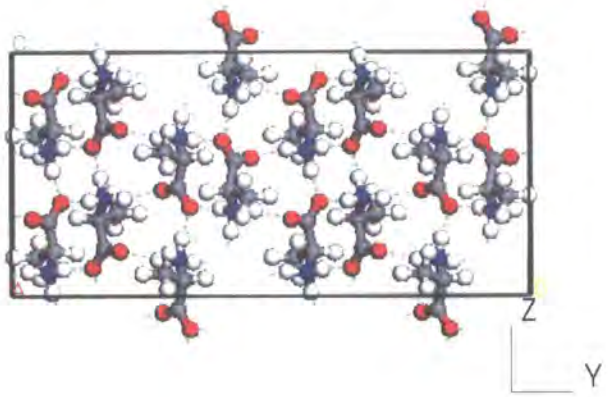

Figure 5.3: Structure of alanine supercell. Note the percolating network of hydrogen bonds.

Examination of the atomic positions as determined experimentally and theoretically in tables 5.3, 5.4, 5.5 and 5.6 lends credence to this view, as in all cases individual intra-molecular degrees of freedom can be dealt with satisfactorily; evidence for this is the good agreement found for the atomic positions of an individual molecule of the crystal. Rather, this suggests that, in accordance with the above discussion, it is the inter-molecular interactions that can be problematic.

L-isoleucine appears structurally to be similar to L-valine, as shown in figure 5.4. One may immediately note the interesting manner in which the functional groups on one molecule "lock horns", so to speak, with their oppositely charged counterparts on the neighbouring molecule. Thus individual molecules within the unit cell are bound by two hydrogen bonds. Again, like L-valine, examining a supercell shows the same layer formation. One may postulate the following explanation for such formations occurring: L-alanine possesses a short sidechain; therefore it is possible for the molecules to "interlock" to a greater extent than is possible if the functional groups are attached to a long sidechain. It should also be noted that this interlocking manifests itself in the percolating network of hydrogen bonds that can be observed in figure 5.3. Thus it appears to be an issue of packing: the shorter the side chain, the closer the molecules can be packed, and therefore the greater the number of bonds that can be made between functional groups on neighbouring molecules. Considering

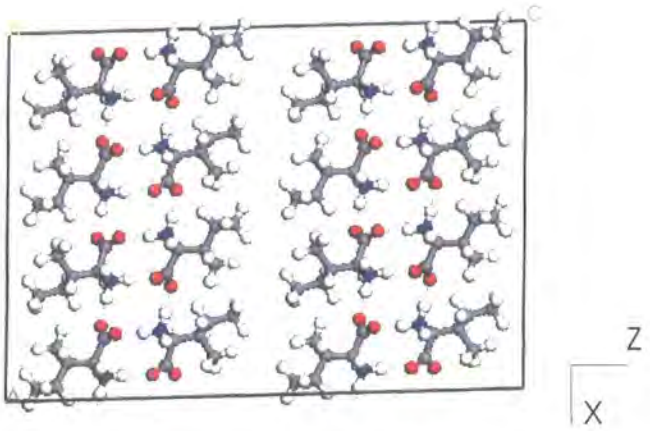

Figure 5.4: Structure of isoleucine supercell.

an example where one has a large sidechain, then one can see that the packing arrangements are limited to the case where the functional groups can "lock horns" with a molecule opposite, and perhaps form a bond to a molecule lying parallel to itself, resulting in " layer formation". Perhaps unsurprisingly, L-leucine appears to be largely similar, and one may make the same observations for this structure as have been made for the previous ones. In this case though, one gets hydrogen bonded layers forming in both the a and c axes, which account for the discrepancies observed between the experimental and theoretically determined lattice constants.

Current methods of carrying out calculations on molecular crystals [16] frequently use free molecule structures and parameters, such as charge densities, in order to simulate the crystal, *i.e.* a free molecule is placed in the field due to the other molecules within the unit cell and then a calculation is carried out: the above raises serious issues about the validity of such an approach, for clearly it is inappropriate to assume that the molecule does not relax its internal degrees of freedom in the solid state.

5.4 Electronic Structure

In figure 5.5 the band structure for L-valine is presented. Despite the existence of the well-known bandgap problem [47] (LDA and GGA XC functionals commonly underestimate bandgaps), the qualitative topology of DFT-obtained bandstructures is generally considered to be correct, and it is therefore justified to use this concept to understand the electronic structure. Certain features are immediately apparent, namely the wide bandgap of 5.27 eV. It may also be noted that the occupied states display little dispersion, and therefore are likely to correspond closely to the molecular orbitals, *i.e.* to be localised to individual molecules within the unit cell, as one would expect for a molecular crystal. It implies that the inter-molecular attraction, and hence the geometric structure, is not primarily dictated by electronic bonding, differing from that of the isolated molecules, but is rather due to either van der Waals forces, hydrogen bonding or dipole-dipole interactions. The non-zero dipole moment of valine, coupled with the polar nature of the functional groups involved, and their known tendency to form hydrogen bonds, strongly suggests that dipole-dipole and hydrogen bonding interactions may be expected to dominate. This provides an explanation of the point alluded to in the previous section concerning the zwitterionisation of L-valine in the solid state: namely that the only way in which a stable crystal may form is by increasing the dipole-dipole interaction by zwitterionisation: this is because of the localisation of the electron charge distribution to individual molecules. Further, zwitterionisation has implications for the nature of the hydrogen bond between the amino and carboxyl groups. In principle, it would seem that a hydrogen bond could form between these groups irrespective of whether the functional groups are ionised or not; however, the hydrogen bond that forms is stronger if the zwitterionisation occurs. This can be understood if one examines the geometry of the molecules involved: donation of a proton to the amino group from the carboxyl group allows a relatively straight hydrogen bond to form: this is characteristic of a strong bond, whereas such a straight and hence strong bond could not form if the zwitterionisation did not occur.

A Mulliken population analysis allows this argument to be placed upon a more quantitative basis: the nitrogen atoms have a negative overall charge of -0.78e, as

opposed to a charge of -0.68e on the oxygen atoms. Such a result is indicative of the nitrogen atom being more electronegative than the oxygen atom, and suggests that the proton bonded to the nitrogen atom will be deshielded more than it would be if it were covalently bonded to the oxygen atom in the carboxyl group. This deshielding then can account for the formation of a stronger hydrogen bond. It is further interesting to note that by zwitterionisation, the possibility occurs for the carboxyl group to take part in more hydrogen bonds than would otherwise be the case, as can be seen in figure 5.2. This in itself will act as a further stabilising influence.

Examination of the electron charge density of L-valine is supportive of the above conclusions. Figure 5.6(a) shows a constant density isosurface, and as expected, it displays a marked localisation on individual molecules. It may also be noted that some level of charge overlap does occur between the amide and carboxy functional groups of neighbouring molecules. This is suggestive of a hydrogen bond forming between these molecules, via these oppositely ionised functional groups, and is consistent with the discussion above on the reasons for zwitterionisation occurring in the solid state.

A bond population analysis of the O-H bonds strengthens the above analysis. The shortest bonds have a length of 1.69-1.71 Å; if one guardedly uses as a criterion for hydrogen bonding the requirement that the sum of the van der Waals radii of the atoms involved must be greater than the separation of the atoms, then this indeed does qualify as a hydrogen bond. The bond contains a population of 0.1-0.13e.

In figure 5.6(b) we show the density corresponding to the highest occupied orbital of the system. It can be seen that this appears to be "p-like" in nature and is primarily localised on the oxygen atoms. These are the are lone pair electrons on the oxygen atoms that take place in hydrogen bonding, in line with the discussion above on hydrogen bond formation.

The partial density of states is a useful construct to introduce at this point; it

decomposes the total density of states, defined through

$$N(E) = \sum_j \delta(E - \epsilon_j), \tag{5.10}$$

into contributions due to different angular momentum components (*i.e.* whether the levels are s-like, p-like etc.). It may be defined through

$$N_\mu = \sum_j |\langle \chi_\mu | \phi_j \rangle|^2 \delta(E - \epsilon_j) \tag{5.11}$$

where χ_μ is the angular momentum component concerned and ϕ_j is a Kohn-Sham orbital, with ϵ_j the corresponding Kohn-Sham eigenvalue. In practice, the delta functions in equations (5.10) and (5.11) are evaluated using a Gaussian function as an approximation with an appropriately chosen smearing width. In this work, a width of 0.2 eV is found to be sufficient. Although examination of orbitals is useful, and provides insight, the partial density of states provides a more rigorous identification of the nature of the orbitals. Figure 5.7 shows the the partial density of states for valine; the highest occupied orbitals are primarily p-like in character, which is consistent with the analysis based upon the orbitals.

It is mentioned here in passing that the band structures for isoleucine (figure 5.8) and leucine (figure 5.9) are largely similar to that of valine. Band gaps are 4.68 eV and 5.05 eV, respectively. The electron densities and orbitals also appear to exhibit the same behaviour, as can be deduced by examination of the partial densities of states shown in figures 5.10 and 5.11; for this reason, these are not presented. Given the similarity between these molecules in terms of their geometric structures and in terms of the functional groups present, these similarities are not surprising.

L-alanine (figure 5.12) deserves more detailed attention, as its band structure is markedly different. It possesses a wide bandgap, of 5.07 eV, as do the other three systems examined. The band structure appears shows more dispersion in both the valence and conduction band manifolds possibly because of the closer packing that alanine takes part in. Examining the density in figure 5.13 does not show a noticeable degree of delocalisation, which one would expect in order to produce dispersion; rather, the density is largely localised to individual molecules, with electron overlap

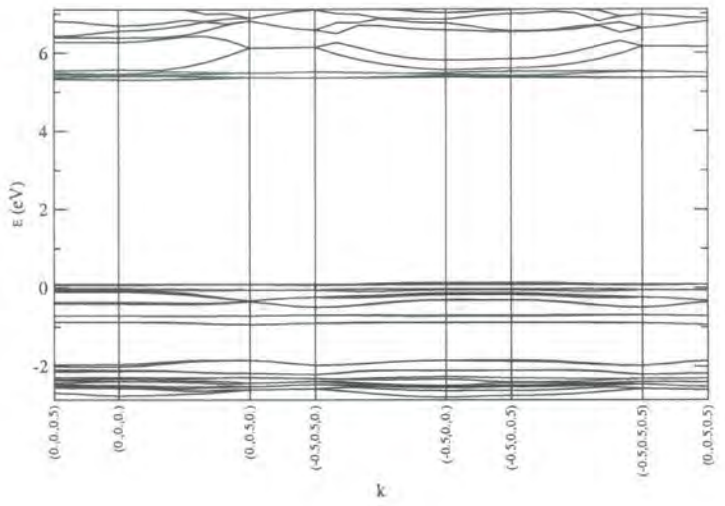

Figure 5.5: The electronic band structure of L-valine.

confined to the region of the inter-molecular hydrogen bonds. The density of states reinforces this conclusion, as does the partial density of states in figure 5.14. The carbon-oxygen bonds are slightly asymmetric, having lengths of 1.24 and 1.26 Å; suggesting that the two hydrogen bonds are not of the same strength. Population analysis suggests that the closest distance oxygen-carbon bonds are of length 1.74 Å, a characteristic hydrogen bond length, and that these bonds have net positive populations of $0.12e$. It is worth noting here that this compares to hydrogen bond distances of around 1.7 Å for L-valine: this suggests that the strength of the hydrogen bonds is approximately constant from system to system. Examination of the orbitals reveals that they are similar to those of the other systems, with the highest orbitals being primarily oxygen p-type orbitals; this is again consistent with hydrogen bonding, and means that the electronic structure of L-alanine is broadly similar to those of the other systems considered.

5.5 Comparison with Isolated Molecules

The most obvious point when comparing the properties of the molecular crystal with the isolated molecules is that, except for leucine, the isolated molecules are found in

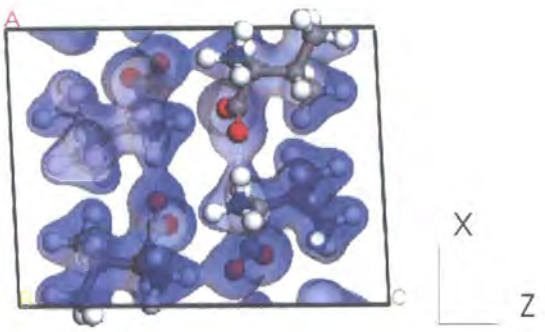

(a)

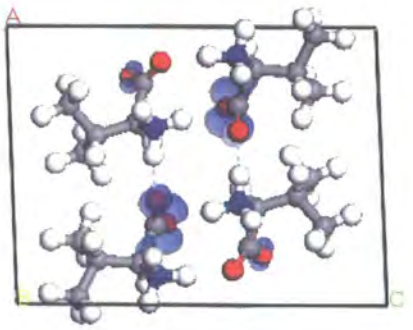

(b)

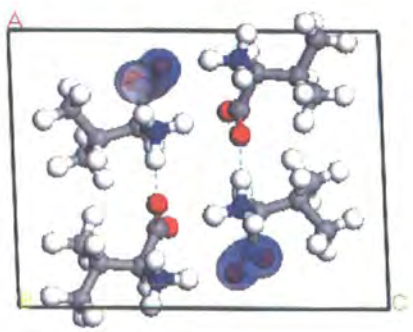

(c)

Figure 5.6: The ground state density of valine (a), highest occupied orbital (b), and lowest occupied orbital (c).

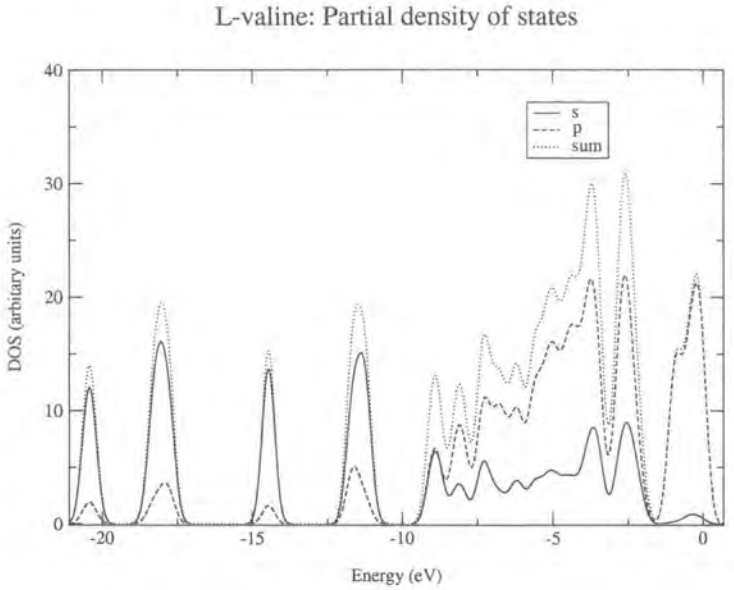

Figure 5.7: The partial density of states for L-valine. A Gaussian smearing of 0.2 eV has been applied.

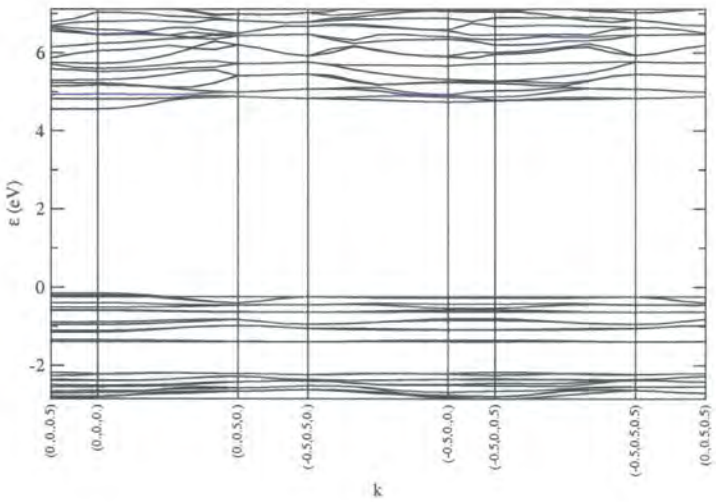

Figure 5.8: The electronic band structure of L-isoleucine.

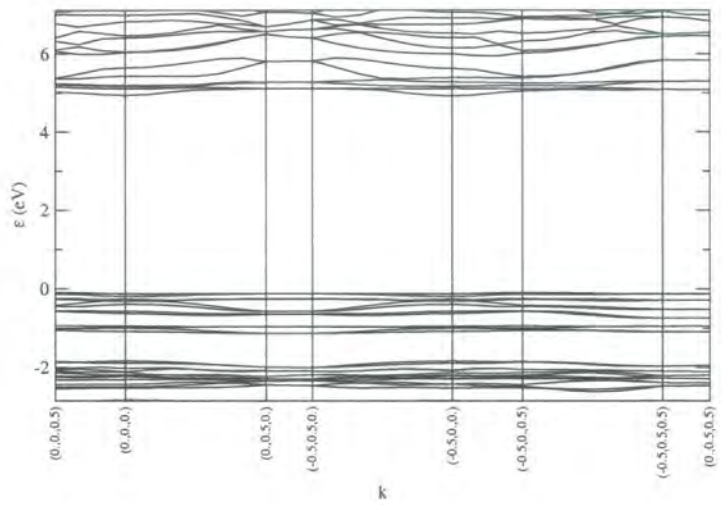

Figure 5.9: The electronic band structure of L-leucine.

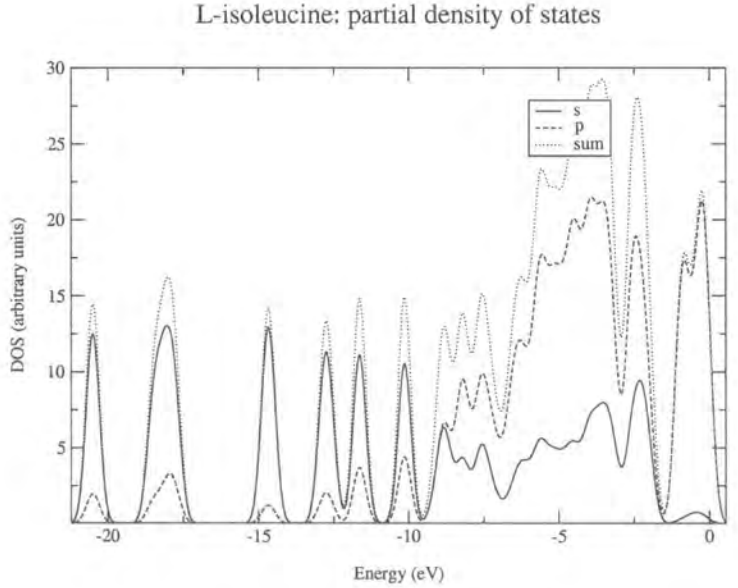

Figure 5.10: Partial density of states for L-isoleucine

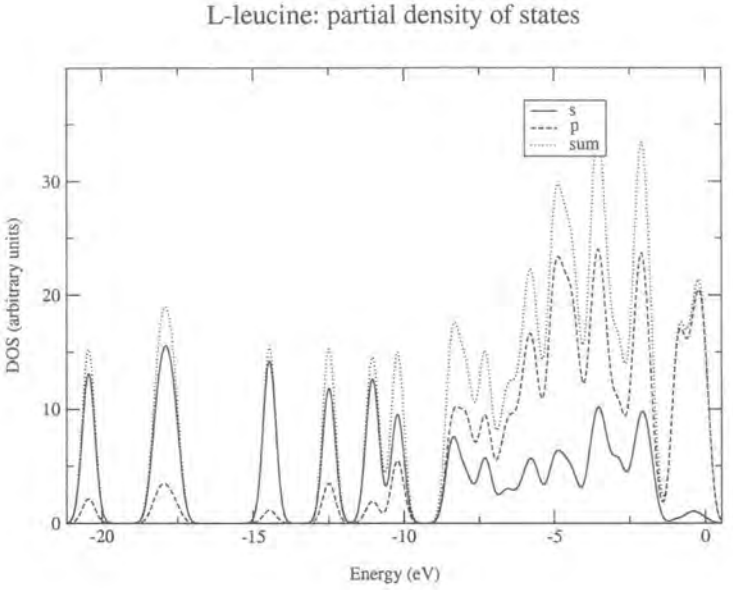

Figure 5.11: Partial density of states of L-leucine.

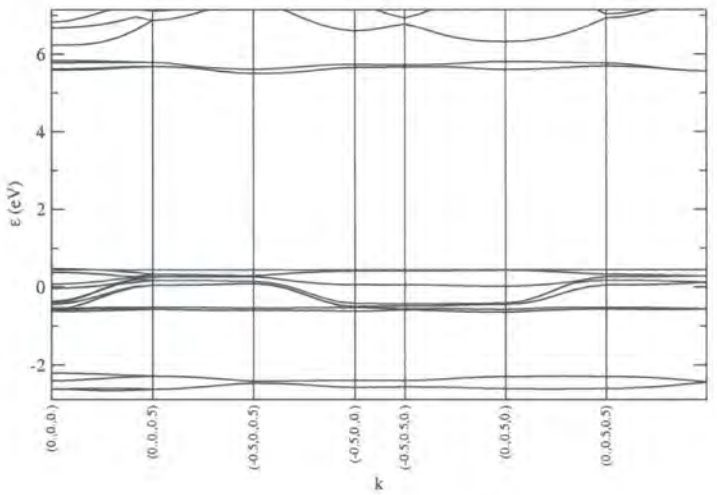

Figure 5.12: The electronic band structure of L-alanine.

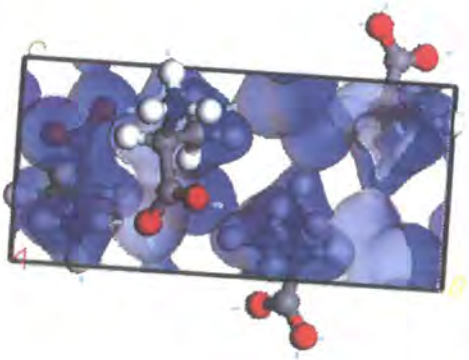

Figure 5.13: The ground state density of alanine. Note the localised nature of the density, with significant overlap only occurring in the vicinity of the amino and carboxy groups involved in hydrogen bonding.

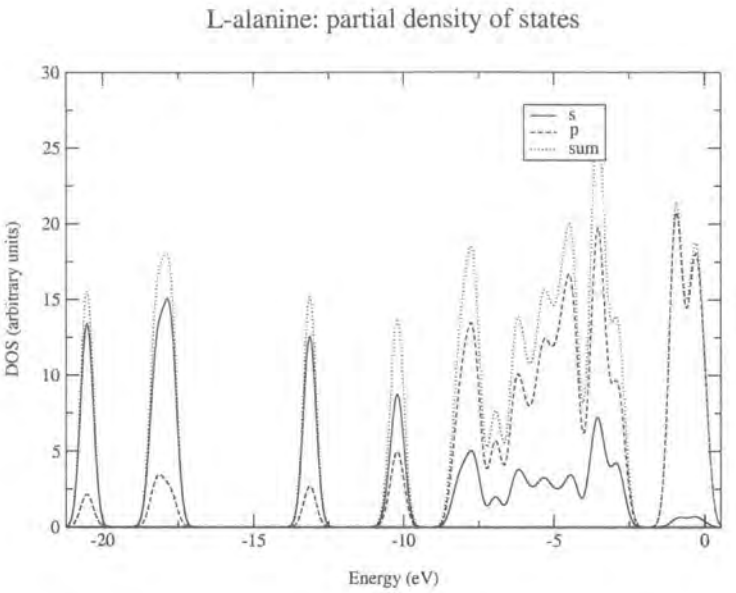

Figure 5.14: Partial density of states of alanine.

	Free molecule		Crystal	
	Length (Å)	Population (e)	Length (Å)	Population (e)
$C_1 = O_1$	1.19	1.07	1.26	0.88
$C_1 - O_2$	1.32	0.66	1.24	0.95
$C_2 - N_1$	1.47	0.61	1.48	0.54
$C_1 - C_2$	1.54	0.76	1.53	0.75
$C_2 - C_3$	1.51	0.68	1.51	0.69

Table 5.7: Variation in bond lengths and populations in alanine: comparison between the free molecule and the solid state.

the non-zwitterionic state. This immediately suggests that one could expect there to be both major differences in the geometric and electronic structures between the two cases considered. In order to investigate this, it is useful to examine the geometric parameters such as bond lengths, and their variation between the free molecule and the molecule in the solid state. It is also useful to examine the Mulliken charges in order to investigate the effect of the solid state environment upon the molecular properties. In tables 5.7, 5.8, 5.9 and 5.10, the lengths and populations of certain bonds are presented. The notation labelling the atoms is that illustrated in figure 5.1.

	Free molecule		Crystal	
	Length (Å)	Population (e)	Length (Å)	Population (e)
$C_1 = O_1$	1.21	1.05	1.24	0.93
$C_1 - O_2$	1.33	0.67	1.26	0.89
$C_2 - N_1$	1.47	0.62	1.48	0.55
$C_3 - C_4$	1.52	0.69	1.52	0.75
$C_4 - C_5$	1.51	0.67	1.52	0.68
$C_3 - C_6$	1.52	0.69	1.52	0.72
$C_2 - C_3$	1.54	0.76	1.54	0.74
$C_1 - C_2$	1.55	0.77	1.53	0.76

Table 5.8: Variation in bond lengths and populations in isoleucine: comparison between the free molecule and the solid state.

	Free molecule		Crystal	
	Length (Å)	Population (e)	Length (Å)	Population (e)
$C_1 = O_1$	1.21	1.06	1.24	0.93
$C_1 - O_2$	1.33	0.66	1.25	0.90
$C_2 - N_1$	1.47	0.62	1.49	0.55
$C_3 - C_4$	1.52	0.69	1.52	0.71
$C_3 - C_5$	1.52	0.70	1.52	0.72
$C_2 - C_3$	1.53	0.75	1.54	0.74
$C_1 - C_2$	1.54	0.77	1.53	0.76

Table 5.9: Variation in bond lengths and populations in valine: comparison between the free molecule and the solid state.

It is immediately apparent that the geometrical parameters are similar for all the non-zwitterionic systems considered. This is not entirely surprising. More importantly, it is noticeable that the C-C bonds do not alter significantly upon zwitterionisation. This suggests that the molecular structure remains largely unaltered between the free molecule and the molecular solid cases. The only significant changes occur in the carboxy functional group. Here, one can clearly see that in the free molecule, the C=O bond is significantly shorter than the C-O bond, and has a greater population, reflecting the double nature of the bond. Upon zwitterionisation, the bond lengths "equalise", resulting in two bonds that are of approximately the same length with similar populations. Given that the deprotonated oxygen now has a free unbound electron, such a contraction in the C-O bond is not surprising. The accompanying population increase in the bond is unsurprising. A more unexpected result is the alteration in the C=O bond length and population. This is explicable if one considers that this oxygen atom may also participate in hydrogen bonding; thus one could expect an accompanying depletion of charge in the region of the C=O bond, and instead a charge accumulation in the region between the carbon atom and the hydrogen involved in the hydrogen bond. The charge densities shown earlier support such an argument.

Examining leucine in table 5.10, which is zwitterionic as a free molecule, one sees, as in the non-zwitterionic case, very little change in the carbon "backbone" of the molecule. This is unsurprising in light of the previous discussion and the zwitterionic nature of the molecule. The bonds between the carbon and oxygen atoms remain unaltered; again, this is unsurprising. A slight alteration in the population of the $C_1 - O_2$ bond occurs, from $0.94e$ to $0.91e$; given that the bond length remains constant, it is likely that this is simply a numerical artefact and not physically significant.

In tables 5.11, 5.12 and 5.13 the Mulliken charges are presented for the alanine, isoleucine and valine. The effective charges of the carbon atoms comprising the backbones of the molecules alter only slightly upon formation of the molecular solid. More significant are those changes that arise due to zwitterionisation. The O_1 atom, *i.e.* the atom double bonded to the C_α atom, undergoes a significant change in its Mulliken charge, changing from -0.57e to -0.67e; such an accumulation of charge

	Free molecule		Crystal	
	Length (Å)	Population (e)	Length (Å)	Population (e)
$C_1 = O_1$	1.25	0.93	1.25	0.92
$C_1 - O_2$	1.25	0.94	1.25	0.91
$C_2 - N_1$	1.51	0.48	1.49	0.55
$C_3 - C_4$	1.53	0.73	1.52	0.75
$C_4 - C_5$	1.52	0.70	1.52	0.70
$C_4 - C_6$	1.52	0.70	1.52	0.72
$C_1 - C_2$	1.57	0.67	1.53	0.75

Table 5.10: Variation in bond lengths and populations in leucine: comparison between the free molecule and the solid state.

is consistent with the reduction in the bond population noted earlier. It is also consistent with the possibility existing for these double-bonded oxygen atoms to participate in hydrogen bonding. Interestingly, the deprotonated O atom undergoes no change at all in its Mulliken charge. This is perhaps surprising; one would expect the removal of a covalent bond to be accompanied by a change in the electronic structure of the atom involved, rather than simply an alteration in bond lengths and populations, as happens. The formation of the NH_3^+ upon crystallisation is accompanied by an alteration in the Mulliken charge of the N atoms from around -0.9e to around -0.79e; this can be easily understood as occurring because of the formation of an extra covalent bond between the N atom and the extra H atom now present.

In table 5.14 the Mulliken charges are presented for leucine in the molecular and solid states. Since this molecule is already zwitterionised, one observes little change in the values of the charges present in the carboxy group. It is interesting to note that the N atom undergoes a change in charge from -0.85e to -0.78e; this is is probably associated with the slight alteration in the C-N bond, and the corresponding bond population alteration from 0.48e in the molecular case to 0.55e in the crystalline case. More surprisingly, the values of the C_5 and C_6 atoms present change greatly, from -0.80e to -0.70e; there appears to be little explanation for such a large alteration, which is not observed for any other carbon atoms present. Further, there is no molecular distortion occurring that would account for such a large alteration in the Mulliken charge.

	Mulliken charge (e)	
	Free molecule	Crystal
C_1	0.68	0.65
C_2	-0.22	-0.18
C_3	-0.82	-0.74
N	-0.94	-0.78
O_1	-0.57	-0.67
O_2	-0.67	-0.67

Table 5.11: Variation in Mulliken charges in alanine: comparison between the free molecule and the solid state.

These results are of interest as they clearly show that the major changes in the molecular structure of amino acids when they crystallise are not due to the effects of the crystalline environment, but are due instead to the zwitterionisation process that allows the crystal to be stabilised. Correspondingly, these changes are manifested in the functional groups involved in zwitterionisation. The changes are both structural and electronic, and would seem to indicate that, at least for those molecules that are found to be non-zwitterionic in the gaseous phase, free molecule properties would be inappropriate in order to attempt to simulate the solid.

The case of leucine is more intriguing. It could be expected, in light of the above discussion, that, since GGA calculations predict that leucine is a zwitterion as an isolated molecule, that perhaps one would be justified in assuming very little change upon crystallisation. However, despite the fact that the geometric structure appears to change very little upon crystallisation, the Mulliken charges suggest that the electronic structure undergoes significant alteration and this consequently implies that any treatment of the crystalline structure should fully account for these changes.

5.6 Summary

In conclusion, this chapter has investigated the geometric and electronic structures of the four amino acids alanine, valine, leucine and isoleucine in both the solid state and as isolated molecules with a view to understanding how these depend upon the molecular environment. Although amino acids in both forms have been extensively studied by a variety of experimental techniques, such as X-ray diffraction

	Mulliken charge (e)	
	Free molecule	Crystal
C_1	0.67	0.64
C_2	-0.21	-0.19
C_3	-0.24	-0.21
C_4	-0.49	-0.46
C_5	-0.79	-0.75
C_6	-0.79	-0.72
N	-0.90	-0.79
O_1	-0.57	-0.69
O_2	-0.66	-0.66

Table 5.12: Variation in Mulliken charges in isoleucine: comparison between the free molecule and the solid state.

	Mulliken charge (e)	
	Free molecule	Crystal
C_1	0.67	0.64
C_2	-0.21	-0.17
C_3	-0.24	-0.20
C_4	-0.79	-0.73
C_5	-0.79	-0.74
N	-0.91	-0.78
O_1	-0.57	-0.68
O_2	-0.66	-0.66

Table 5.13: Variation in Mulliken charges in valine: comparison between the free molecule and the solid state.

	Mulliken charge (e)	
	Free molecule	Crystal
C_1	0.64	0.64
C_2	-0.21	-0.17
C_3	-0.53	-0.47
C_4	-0.25	-0.22
C_5	-0.80	-0.70
C_6	-0.80	-0.71
N	-0.85	-0.78
O_1	-0.69	-0.68
O_2	-0.70	-0.66

Table 5.14: Variation in Mulliken charges in leucine: comparison between the free molecule and the solid state.

[173, 174, 175, 176], little work appears to have been carried out on investigating the relationship between the properties of the molecular crystal, and those of the constituent molecules.

The molecular crystals are broadly understood to be zwitterionic and stabilised largely by hydrogen bonding between the amino and carboxy functional groups, although little theoretical work has been carried out to verify the validity of this picture. In this chapter, the geometric and electronic structures of these four crystals have been calculated using first principles methods. In general, the geometric structures have been found to be in good agreement with the experimentally determined structures allowing for finite temperature effects and van der Waals bonding. It is found that the inter-molecular interactions that stabilise the crystals must be primarily electrostatic in nature, for it is well-known that DFT accounts well for such interactions: this has implications too for the hydrogen bonding, suggesting a primarily electrostatic nature, which is consistent with the current understanding of the nature of the typical bonds that predominate in these crystals, *i.e.* C=O-H-N [32]. The cases where agreement is poor between theoretical and experimentally determined lattice constants are most likely due to van der Waals forces being responsible for binding: these cases almost always involve interactions between widely separated CH_3 groups, for which other forms of interaction are unlikely to occur.

The gross features of the electronic structure appear to be largely the same from system to system; this is perhaps not entirely surprising, given that they all share the same functional groups; rather the only differences appear to stem mainly from the differing side chains. As an example, the band structures, densities of states, both complete and partial, and electronic orbitals appear broadly similar. However, the differences manifest themselves in how these molecules pack together to form crystals; alanine is notably different, in main because its much shorter side chain allows a greater degree of close packing than is possible in the other three systems, all of which possess much longer side chains. However, in all cases the bonding mechanisms appear to be the same. It is interesting to note that the structures of individual molecules within the crystal structure are so different from the gas phase conformers; this is largely due to the zwitterionisation that occurs; however, it does have implications for how calculations are carried out on these systems: it is clearly

not appropriate to use the isolated gas phase molecular conformers and subject these to the crystal field of the surrounding molecules, for this completely neglects the structural and electronic changes that take place upon zwitterionisation.

Comparison with the structures of isolated molecules reveals that the molecular structures alter due to zwitterionisation upon crystallisation (save for leucine), and that these changes are confined to the functional groups that are directly involved in the zwitterionisation. Corresponding changes in the electronic structure are confined to these functional groups. Leucine is found to be zwitterionic as an isolated molecule; accordingly the geometric structure changes little upon crystallisation. The electronic structure does show significant changes though.

This work has produced results that are broadly consistent with interpretative models. It is to be hoped that such first principles techniques will find wider application to these important systems, and help to place our understanding of them and the interactions responsible for their formation on a much firmer theoretical footing. It is to this end that this work is intended to serve as a foundation for further investigations such as the vibrational and dielectric properties of these important crystals.

Chapter 6

Dielectric and Vibrational Properties of Amino Acids

Although a complete understanding of the physical properties of a system depends upon accurate determination of the groundstate electronic structure, a wide variety of phenomena in crystalline systems depends upon the lattice dynamical and dielectric behaviour. Examples include: IR, Raman and neutron-diffraction spectra, specific heats, thermal expansion and heat conduction; phenomena involving electron-phonon coupling such as superconductivity, the resistivity of metals, transport properties, and the temperature dependence of optical spectra [73]. Furthermore, the central quantity of interest in a lattice dynamical calculation, *viz.* the dynamical matrix, is intimately related to the nature of the chemical bonding present. Investigating the lattice dynamical behaviour can, therefore, yield insights into the bonding mechanisms prevalent in molecular crystalline systems.

The first step in developing a thorough understanding of these phenomena in amino acids in the solid state is therefore an accurate determination of these properties and their relation with those of the constituent molecules. To this end, this chapter presents the results of such calculations. The normal modes and polarisabilities of the isolated molecules are determined initially, and then compared to the results of calculations on the crystals themselves.

6.1 Molecular Properties

6.1.1 Computational Approach

The molecular calculations fall into three distinct stages: firstly, the geometrical structures at equilibrium are obtained by minimising all internal degrees of freedom using the Hellmann-Feynman theorem. The polarisabilities are then obtained using DFPT, before the molecular normal modes and effective charges are determined.

The interactions between the valence electrons and the atomic nuclei are treated using norm-conserving pseudopotentials with cut-off energies of 1000 eV. This adds considerably to the computational effort required, but as explained earlier, the use of ultra-soft pseudopotentials within DFPT is problematical, with several technical issues needing to be addressed. Artificial periodicity is imposed through the use of cubic supercells of $10 \times 10 \times 10$Å; this is found to be sufficiently large so as to ensure that the molecular energy levels are non-dispersive. Consequently, one only has to consider the Γ-point when carrying out integrations over the Brillouin zone. Exchange and correlation are treated within the GGA of Perdew and Wang [48].

6.1.2 Polarisabilities

In order to validate the accuracy and efficacy of DFPT when applied to molecular problems, the polarisability tensor has been calculated by two independent methods: by DFPT itself, and by finite differences. The finite difference method is based upon the following expansion of the molecular dipole moment

$$\mu_\alpha(\varepsilon) = \mu_{0\alpha} + \sum_\beta \alpha_{\alpha\beta}\varepsilon_\beta + \ldots \tag{6.1}$$

where α and β run over the Cartesian axes, and $\mu_{0\alpha}$ is the zero field molecular dipole moment.

As can be seen in table 6.1, good agreement between the two methods is found not only for the average of the trace but also for individual diagonal components; such agreement is edifying, and demonstrates convincingly that DFPT can obtain molecular polarisabilities. It is likely that errors originate mainly in the finite difference

Molecule	$\alpha^{DFPT}(\text{Å}^3)$			$\alpha_{av}^{DFPT}(\text{Å}^3)$	$\alpha^{FD}(\text{Å}^3)$			$\alpha_{av}^{FD}(\text{Å}^3)$
	9.30	-0.12	-0.86	8.67	9.62	-0.1	-0.87	9.14
Alanine	-0.12	9.50	0.29		-0.16	10.28	0.33	
	-0.86	0.29	7.23		-0.89	0.25	7.53	
	18.50	-0.21	-0.12	15.37	17.95	-0.1	-0.19	15.49
Leucine	-0.21	13.03	0.63		-0.19	13.77	0.61	
	-0.12	0.63	14.57		-0.22	0.64	14.75	
	17.19	-0.61	0.01	14.73	18.02	-0.57	0.11	15.33
Isoleucine	-0.61	13.71	1.72		-0.59	14.19	1.77	
	0.01	1.72	13.29		0.1	1.80	13.77	
	14.34	0.05	-0.55	12.72	14.27	0.04	-0.52	13.03
Valine	0.05	13.18	1.36		0.26	13.75	1.40	
	-0.53	1.36	10.64		-0.55	1.45	11.06	

Table 6.1: Amino acid polarisability components: finite differences (FD) versus DFPT; all values are in Å^3.

treatment, as one is effectively taking a numerical derivative; the quality of such a result will depend upon the number of points used to evaluate the polarisability. It can also be seen that the agreement is at times much less satisfactory for the off-diagonal elements. This is because the off-diagonal elements, in contrast to the diagonal elements, are obtained via a non-variational calculation. As such, they will be extremely sensitive to the quality and convergence of the calculation. It should be noted that the DFPT off-diagonal elements are constrained by symmetry, i.e. element $\alpha\beta$ is the same as $\beta\alpha$. The finite difference calculations do not have such a constraint, and thus, although in general one finds that it is satisfied to within the second decimal place, it is not always. In this case, one can consider the DFPT result to be the more reliable value. In figure 6.1 we show typical curves displaying dipole moment as a function of applied field for alanine.

The first-order electronic density gives the linear variation in the electronic density caused by the external perturbing field. In figures 6.2-6.5 and 6.6-6.9, the molecular structure and first order densities obtained by DFPT calculations for alanine and valine are shown. These are presented as being representative of the types of behaviour found. The contributions of the carboxy and amino functional groups may be clearly seen; what is equally clear is that these functional groups are not equally polarisable in different molecular environments; these contributions shall now be discussed in more detail, and an attempt to elucidate possible connections between

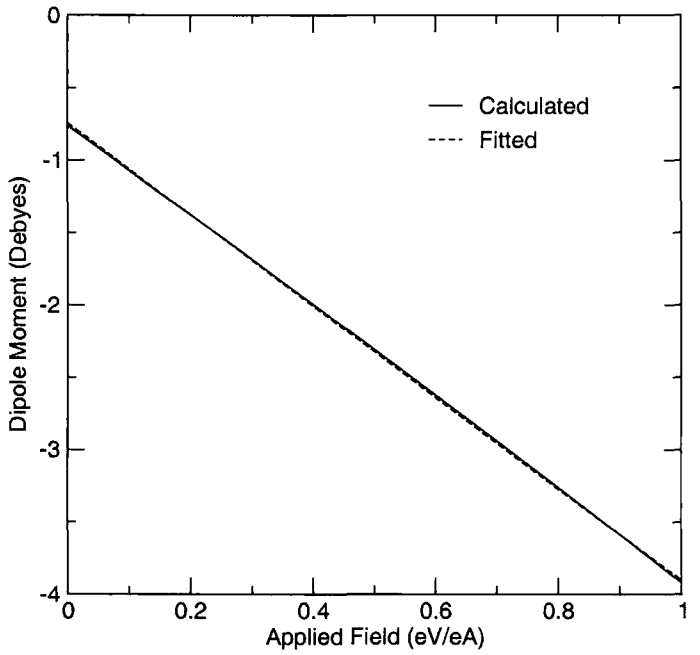

Figure 6.1: The variation in the dipole moment $\mu(x)$ as a function of applied field in the x-axis for alanine.The fit used is a linear fit.

molecules in terms of shared geometric and structural factors will be made.

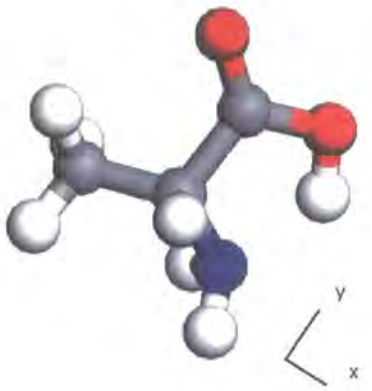

Figure 6.2: Molecular geometry of alanine.

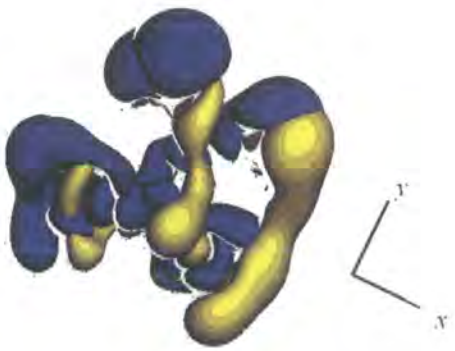

Figure 6.3: Alanine: first order electron density. Response to a perturbation in the x axis. Blue represents where charge is being displaced to, whilst yellow represents a depletion of charge caused by the applied field.

6.1.3 Relation to Geometric Structure

The most noteworthy structural difference between the molecules under consideration is that leucine forms a zwitterion in the gaseous state, in contrast to the other

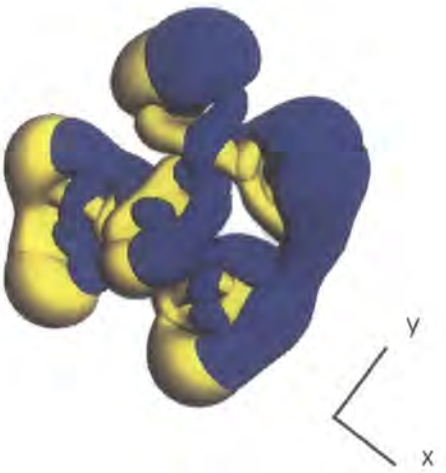

Figure 6.4: Alanine: response to perturbation in y-axis. Colours as before.

three molecules. The reason for this is connected to intra-molecular hydrogen bonds. In the neutral molecules, there is a hydrogen bond that forms between the hydrogen atom of the carboxy group and the nitrogen of the amine group. The bond lengths, and populations as obtained from a Mulliken population analysis, can be seen in table 6.2. These suggest that the three bonds are of approximately the same strength, which is perhaps not unexpected. These intramolecular bonds will act so as to stabilise this conformer. However, the position of the amine group with respect to the carboxy group in leucine is such that it is not possible to form a hydrogen bond between these two groups of the same strength; this is essentially because the amine group does not lie in the same plane as the carboxy group. Instead, by zwitterionising, it is possible for the amine group to form two hydrogen bonds, each bond involving different oxygen atoms in the carboxy group. It is thus energetically favourable for zwitterionisation to occur. As can be seen in table 6.2, in leucine

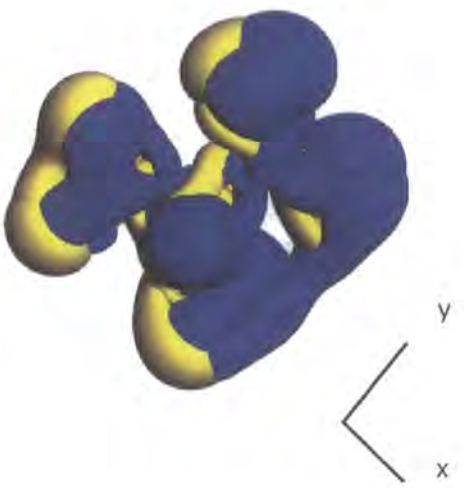

Figure 6.5: Alanine: first order electron density. Response to perturbation z-axis. Colours as before.

these hydrogen bonds are longer, suggesting that they are weaker, a conclusion that is reinforced by the substantially smaller populations of these bonds.

	Length (Å)	Population (e)
alanine	1.81	0.12
leucine (1)	2.49	0.03
leucine (2)	2.71	0.01
isoleucine	1.72	0.14
valine	1.74	0.13

Table 6.2: Hydrogen bond lengths and populations. Bond 1 refers to the bond between the deprotonated oxygen atom and its nearest neighbour hydrogen; similarly, bond 2 refers to the bond between the remaining oxygen atom and its nearest neighbour hydrogen.

In support of such a hypothesis, note that for the neutral molecules alanine and

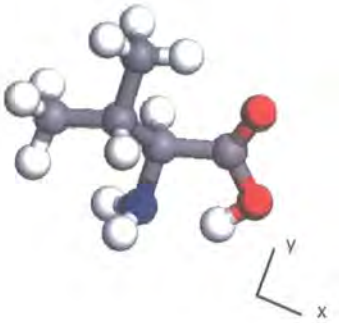

Figure 6.6: Molecular structure of valine.

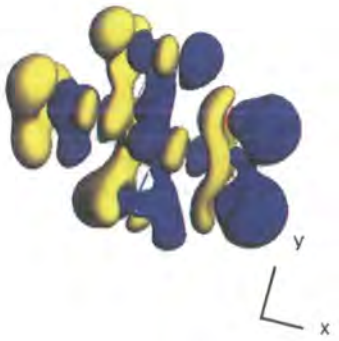

Figure 6.7: Valine: first order density, response to perturbation in x-axis. Colours as before.

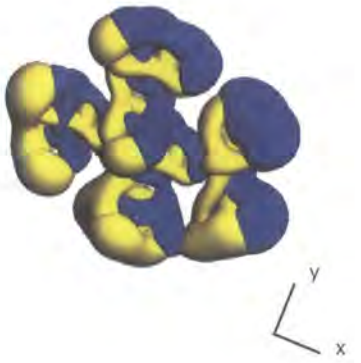

Figure 6.8: Valine: response to perturbation in y-axis. Colours as before.

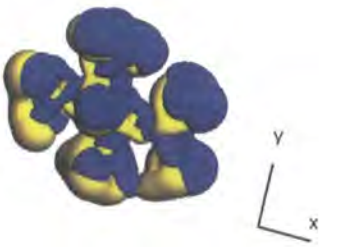

Figure 6.9: Valine: response to perturbation in z-axis, respectively. The colours have the same significance as in the previous diagrams.

valine, a depletion/augmentation of charge may be seen in the region between the amino and carboxy groups (figures 6.3 and 6.7), suggesting the existence of a hydrogen bond between these two functional groups. A similar feature is observed for leucine.

For valine, leucine and isoleucine, the behaviour of the electron density appears to be broadly similar in each case, which considering the zwitterionisation of leucine, is an interesting point. Given the geometric similarities between valine, leucine and isoleucine, this is perhaps expected, but it does suggest that the geometric structure plays a part in helping to determine the electronic response to external fields. Reinforcing this belief is the observation that in alanine, although neutral, as are isoleucine and valine, the electron density response is rather different. This is significant, and suggests that assuming that the polarisability will be determined by the functional groups present in a molecule is mistaken.

6.1.4 Vibrational Properties

In table 6.3, the normal mode frequencies and assignments as calculated using DFPT are presented. The normal modes may be used to investigate the nature of the intramolecular hydrogen bonds present in these systems. It is interesting to note that in the alanine and isoleucine, there are modes in the range 380-465 cm^{-1} that correspond to oscillations of the hydrogen bond existing between the amine and carboxy groups. The fact that these oscillations occur in the same frequency range for both molecules suggests that this particular hydrogen bond is of around the same strength in both of these molecules. This is is agreement with the population analysis and bond lengths described in the previous section. In valine the same oscillatory motions are observed in the frequency range 350-450 cm^{-1}. Examining table 6.3 indicates that in leucine, oscillations in this frequency range do not correspond to hydrogen bond distortions, rather they consist of oscillations of the carbon sidechain, although some of these oscillations suggest the existence of a weak hydrogen bond between the hydrogens on the C_β atom and the carboxy group. In leucine one can observe oscillations of the three-centre hydrogen bond between the amine and carboxy groups in the frequency range 198-266 cm^{-1}; this suggests a weaker hydrogen bond than in

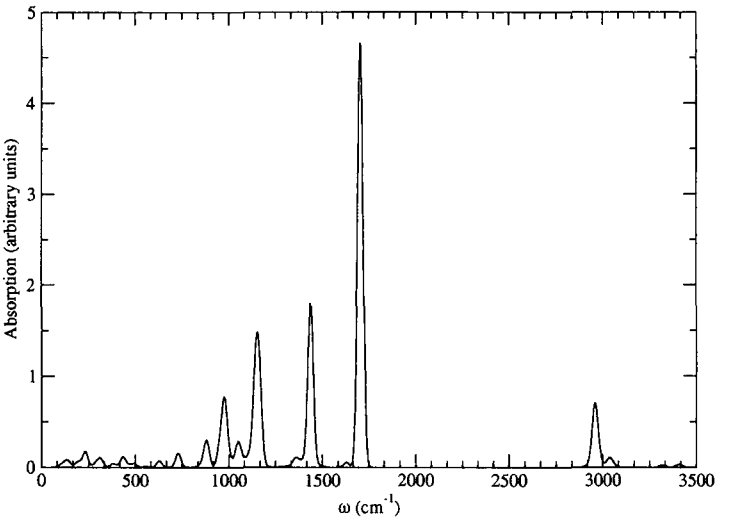

Figure 6.10: IR spectrum of isoleucine; a Gaussian broadening corresponding to 300K has been applied.

the neutral molecules, in agreement with the previous discussion. The identification of these hydrogen bonds is consistent with the discussion in the previous section regarding the reasons for the zwitterionisation of leucine.

Knowledge of the normal modes and the effective charges for the molecules under consideration allows the IR absorption spectra to be calculated. In figures 6.10 and 6.11 the spectra of isoleucine and leucine, respectively, are presented. The IR-active modes are obtained using the oscillator strengths calculated according to equation 3.113. A Gaussian thermal broadening using a Boltzmann factor is then be applied in order to produce a full spectrum.

The spectrum for isoleucine is representative of that of the non-zwitterionic molecules, and therefore only this one is presented, in order to discuss its features with regard to those exhibited in the zwitterionic case. It is interesting to note the contrast between this and the spectrum calculated for leucine, which is zwitterionic. Examination of the phonon eigenvectors for the individual peaks allows one to assign peaks to actual atomic motions. The peak at around 3000 cm^{-1} corresponds to oscillation of the O-H bond. As expected, no such peak appears for the zwitterion leucine.

Alanine		Isoleucine		Leucine		Valine	
Freq	Assign	Freq	Assign	Freq	Assign	Freq	Assign
188	$\tau COOH$	100	sidechain rocking	92	sidechain twist	110	sidechain rocking
264	τCH_3	127	sidechain "breathing" mode	140	sidechain rocking	159	"breathing" mode
278	δCCC	144	$\tau COOH$	146	sidechain rocking	231	sidechain flexing
385	$\delta COH; \delta CNN$	193	sidechain flexing	199	sidechain flexing	265	sidechain flexing
433	ρNH_2	232	sidechain flexing	254	ρCH_3; ρNH_3	272	$\delta CHCHCOOH$
438	δCCN	286	δCCH_3	265	tw CH_3; δCN	324	sidechain flexing
529	δCCO	312	sidechain flexing	274	tw CH_3	355	$\delta C-O; \delta CHCH_3$
581	$\delta CN; \delta COH$	326	ρCH_3	310	tw CH_3	365	$\delta CH-NH_2$; $\delta C-O$
747	ωCOO	365	sidechain rocking; $\rho COOH$	329	ρCH	443	as above
804	$\nu CCOOH$	383	δCNH_2	350	ρCH_2	449	ρNH_2
879	δCN	433	$\nu NCOOH$	407	$\delta_s CH_3CHCH_3$	467	sidechain twisting
939	δCN	464	ρNH_2	441	twNH_3	547	$\delta C=O$
995	δOH	495	sidechain flexing	468	$\delta_s CH_3CHCH_2$	593	$\rho COOH$
1018	δCCC	555	$\delta CCOOH$	547	$\delta CHCH_2$	715	$\delta COOH$
1077	νCH_3CH	628	δCOH	679	ρCNH_3	835	$\nu_s CH_3CHCH_3$; $\nu C-C$
1128	νCN	729	$\delta COOH_s$	780	νCNH_3	838	$\delta CCOOH$
1180	νCOH	765	$\delta_{as} CH_2$	810	ρCH_2; $\delta CCOO$	905	$\nu_s CH_3CHCH_3$; δCN
1220	δCH_3CH	827	sidechain stretching	819	$\nu_s CH$; $\nu CCOO$	932	$\nu CHCH$
1285	δOH	857	sidechain rocking	855	$\nu_s CH_3CHCH_3$	967	$\nu_{as} CH_3CHCH_3$
1362	τCN	881	$\rho_{as} CH_2CHCHN$ νCNH_2	887	$\tau CCOO$	998	$\nu CCCC$
1386	νCCH_3	950	sidechain flexing; δCNH_2	923	$\nu_{as} CHCH_2-$ $-CHNH_3$	1033	δOH
1423	$\nu C-O; \rho OH$	976	$\nu_{as} CHCHN-$ $-COOH$	934	$\nu_{as} CH_3CHCH_2$	1053	νCN
1463	$\delta_{as} CH_3$	1001	$\nu CHCH_3$; δCH_2CH_3	966	$\nu CHCH_3$	1093	$\nu CHCH$
1471	$\delta_{as} CH_3$	1040	δOH	1000	νCH_2CHNH_3	1129	$\nu_{as} CHCH_3$; $\delta CCCOOH$
1635	δNH_2	1053	$\rho CHNH_3$	1048	νCH_2CHNH_3	1160	$\nu_s CCC$
1723	$\nu C=O$	1073	νCH_2CH_3	1084	νCH_2CHNH_3	1189	$\nu_{as} CCC$
2969	$\nu_s CH_3$	1104	νCN	1121	$\nu CHCH_3$	1202	$\delta CHCH$
2976	$\nu_s CH_3$	1136	ρCH_2CHCHN	1175	$\nu_s CHCH_2-$ $-CHNH_3$	1255	ρCH
3042	$\nu_{as} CH_3$	1146	νCOH; sidechain rocking	1191	$\nu CHCH_2$	1319	ρCH
3069	$\nu_{as} CH_3; \nu OH$	1163	νCOH; sidechain rocking	1218	ρCH	1340	δCH
3075	$\nu_{as} CH_3; \nu OH$	1201	$\tau CCOOH$	1257	ωCH_2; ρCH	1353	δCH
3315	$\nu_{as} NH_2$	1235	$\rho CHCHCH_2$	1266	$\nu CCOO$	1383	$\delta_s CH_3$
3400	$\nu_{as} NH_2$	1277	$\delta CHCHCH_2$	1307	$\delta CHNH_3$	1407	$\delta_s CH_3$

Isoleucine		Leucine		Valine	
Freq	Assign	Freq	Assign	Freq	Assign
1318	$\nu CHCH$	1331	ρCH	1431	$\nu O-H; \delta OH$
1327	$\nu CHCH_3 \delta C-H$	1350	ρCH	1458	$\delta_{as} CH_3$
1354	sidechain stretching	1368	$\nu CHNCH_2$; $\nu CH_3 CHCH_3$	1461	$\delta_{as} CH_3$
1358	$\tau CHNH_2$	1377	sidechain flexing	1476	$\delta_{as} CH_3$
1388	νCCH_3; $\nu CH_2 CH_3$	1401	$\nu CH_3 CH$	1490	$\delta_{as} CH_3$
1399	νCCH_3; $\nu CCH_2 CH_3$	1412	$\delta_s NH_3$	1630	δNH_2
1436	$\nu OH; \rho OH$	1439	$\delta_s CH_2$	1709	$\nu C=O$
1455	δCH_2	1462	$\delta_s CH_3$	2911	νCH
1469	$\delta_s CH_3$	1467	$\delta_{as} CH_3$	2947	νCH
1471	$\delta_s CH_3$	1484	$\delta_{as} CH_3$	2963	$\nu_s CH_3$
1480	$\delta_{as} CH_3 \delta CH_2$	1505	$\delta_{as} CH_3$	2967	$\nu_s CH_3$
1496	$\delta_{as} CH_3$	1578	$\nu C-O$	2988	$\nu O-H$
1630	δNH_2	1626	δNH_3	3025	$\nu_{as} CH_3$
1705	$\nu C=O$	1633	$\nu C=O$	3031	$\nu_{as} CH_3$
2910	νCH	2927	$\nu_s CH_3$	3048	$\nu_{as} CH_3$
2933	$\nu_s NH_2; \nu CH$	2935	νCH	3091	$\nu_{as} CH_3$
2954	νCH	2951	$\nu_s CH_2$	3319	$\nu_s NH_2$
2960	νOH	2962	$\nu_s CH_3$	3413	$\nu_{as} NH_2$
2963	$\nu_s CH_3$	2995	$\nu_{as} CH_3$		
2969	$\nu_s CH_3$	3007	$\nu_{as} CH_2$		
2984	$\nu_{as} CH_2$	3023	$\nu_{as} CH_3$		
3031	$\nu_{as} CH_3$	3025	νCH		
3036	$\nu_{as} CH_3$	3028	$\nu_{as} CH_3$		
3050	$\nu_{as} CH_3$	3042	$\nu_{as} CH_3$		
3081	$\nu_{as} CH_3$	3160	$\nu_s NH_3$		
3319	$\nu_s NH_2$	3241	$\nu_{as} NH_3$		
3409	$\nu_{as} NH_2$	3282	$\nu_{as} NH_3$		

Table 6.3: (Continued table from previous page) Amino acid normal modes; all frequencies are in cm^{-1}. The notation for the various motions of atoms within the normal modes is defined as follows: ν, stretching; δ, bending; ω, wagging; ρ, rocking; τ, torsion; s, symmetric; as, asymmetric.

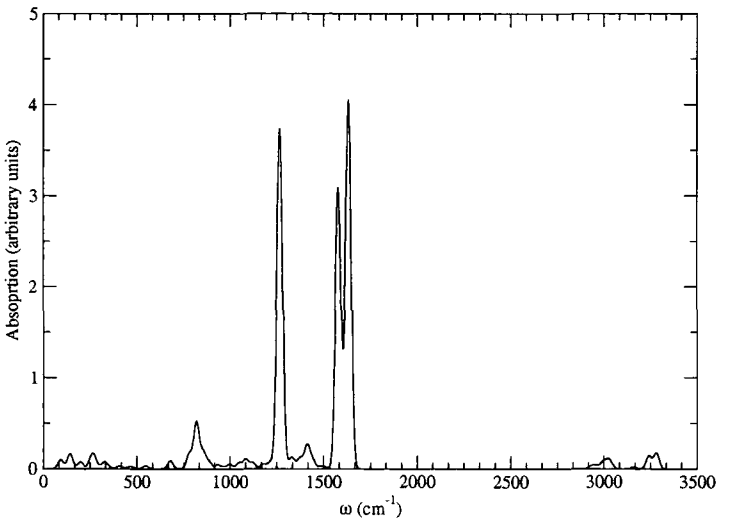

Figure 6.11: IR spectrum of leucine; Gaussian broadening corresponding to 300K applied.

The large peak present at around 1600 cm^{-1} is due to stretching of the C=O bond. This peak does occur for leucine, but it is striking that in this case, a doublet forms, with a slightly smaller, but closely separated peak present. This doublet is due to the oscillation of the bond between the carbon atom and the deprotonated oxygen atom and the C=O bond, and it is thus not surprising that they are almost equally intense. Correspondingly, one would expect that this peak is absent from the spectra of the neutral molecules, and instead, one observes a peak at around 1400 cm^{-1} due to the stretching of the C-O bond and "rocking" of the O-H bond. This peak is around half as intense as that of the C=O bond stretching. In the zwitterionic case, one observes another strong peak at 1266 cm^{-1}; this is due to simultaneous excitation of the $C_\alpha - C$ bond and the carbon-oxygen bonds within the carboxylic acid group. In the non-zwitterionic case, a peak around half as small is observed at around 1150 cm^{-1} corresponding to oscillations of the carbon sidechain, including stretching of the $C - O$ bond.

6.1.5 Effective and Mulliken Charges

In table 6.4, the effective charges for the nitrogen and oxygen atoms in each molecule are presented. It is immediately noticeable that all four molecules possess effective charges that display marked off-diagonal components. It is noteworthy that in all cases except leucine, the average effective charges are approximately the same. The off-diagonal components depend upon the orientation of the molecule concerned with respect to the Cartesian axes. This is not constant from molecule to molecule, and therefore it is only possible to compare the traces meaningfully. It is not entirely surprising, in light of the discussion above regarding the zwitterionisation of leucine in the gaseous phase, that leucine displays markedly different effective charges, and that this is particularly true for the nitrogen atom. It is easy to understand this: the effective charge is directly related to the vibrational properties of the molecule, and quantifies how the electronic structure changes under atomic displacement; it is therefore related directly to the chemical bonds present, and in leucine, the nitrogen atom bonds to three hydrogen atoms, rather than two, as is true for the other three molecules. The oxygen atoms also possess effective charges that are closer in value to each other than is the case in the other molecules. Again, this can be explained with reference to the zwitterionisation of the molecule, which results in both oxygen atoms forming double bonds with the C_α atom, rather than just one as in the neutral case. These bonds will be identical and thus one would expect to see similar, if not identical, effective charges. In support of this, it should perhaps be noted that in leucine, the nominal charges as calculated by population analysis for both oxygen atoms are almost identical (-0.69e versus -0.70e); no such agreement is found for the other three neutral molecules.

It is also interesting to note that the nominal atomic charges determined by Mulliken population analysis [171] display a constancy from molecule to molecule. This is suggestive that the electronic structures of each molecule are similar. This is interesting, as it implies that the geometric structure and the sidechain of the amino acid under consideration have minimal impact upon the electronic structure of the molecule, and that further, that this is dictated in main by the functional groups present.

Molecule		$Z_{\kappa,\beta\alpha}$(e)			Z_{av}(e)	Z_{nom} (e)
		-0.61	-0.03	0.15	-0.49	-0.92
	N	0.03	-0.58	-0.69		
		0.21	-0.06	-0.27		
		-1.09	0.15	0.39	-0.78	-0.66
Alanine	O(1)	-0.25	-0.77	0.075		
		0.39	-0.06	-0.49		
		-0.80	0.25	0.20	-0.74	-0.57
	O(2)	0.37	-0.94	-0.19		
		0.20	-0.11	-0.46		
		-0.67	0.10	-0.01	-0.52	-0.90
	N	0.15	-0.49	-0.27		
		0.02	-0.26	-0.40		
		-0.92	0.37	0.14	-0.83	-0.66
Isoleucine	O(1)	0.12	-0.94	0.48		
		-0.19	-0.35	-0.63		
		-0.88	-0.17	-0.29	-0.77	-0.57
	O(2)	-0.06	-0.70	-0.33		
		0.23	-0.39	-0.75		
		-0.35	-0.02	-0.05	-0.18	-0.85
	N	-0.12	-0.13	0.08		
		0.04	0.12	-0.30		
		-0.89	-0.08	-0.13	-0.90	-0.70
Leucine	O(1)	0.11	-1.06	-0.46		
		-0.02	-0.42	-0.76		
		-1.34	0.45	0.22	-0.94	-0.69
	O(2)	0.39	-0.84	-0.27		
		0.21	-0.30	-0.63		
		-0.63	0.01	0.10	-0.50	-0.91
	N	0.05	-0.61	-0.22		
		0.12	-0.18	-0.27		
		-1.00	0.37	0.24	-0.83	-0.66
Valine	O(1)	0.04	-1.04	-0.30		
		0.02	-0.34	-0.44		
		-0.77	-0.29	-0.09	-0.75	-0.57
	O(2)	-0.14	-1.01	-0.29		
		-0.04	-0.29	-0.47		

Table 6.4: Effective charges and nominal atomic charges from population analysis for the molecules considered in this work. By average effective charge, we mean the average of the trace. O(1) is the oxygen atom bonded to a hydrogen; O(2) is double-bonded to the carbon chain. For the zwitterionic leucine, O(1) is the deprotonated oxygen.

It also suggests that zwitterionisation does not substantially alter the population of the nitrogen atom involved, but rather only alters the population of the oxygen atom that donates a proton, as discussed above.

Discrepancies exist between the effective charges and the nominal charges. It is instructive to consider these discrepancies and to attempt to understand their origin. The discrepancies are most marked in dealing with the nitrogen atoms, as the effective charge is almost always around half of the value of the nominal charge; for leucine the disagreement is even more marked. Further, the nominal charges show, in all cases, that the nitrogen has more negative charge than the oxygen atoms. This is in agreement with nitrogen being more electronegative than oxygen. It is noticeable though that this trend is not followed by the effective charges, which in all cases show the reverse, that the nitrogen effective charge is less than that of the oxygen atoms. Of course, it should be understood that such discrepancies may arise from the fact that the effective charge and the nominal charge encapsulate complementary, but different, aspects of the physics involved: the nominal charge is based upon a decomposition of the Kohn-Sham eigenstates into localised atomic orbitals, and as such yields information on the electronic density; the effective charge, on the other hand, yields information on the vibrational properties, and hence chemical bonding of the molecule concerned. The two are not therefore directly comparable, but rather, are more usefully used as complementary techniques. It can therefore be said that the fact that the effective charges for nitrogen are consistently less negative than those of the oxygen atoms present is due to the differences in chemical bonding.

The discrepancies occurring between the nominal charges and the effective charges do raise some interesting questions: often in molecular mechanics simulations, atomic charges obtained from Mulliken population analysis are used. This though relies upon an arbitrary partitioning of charge; other partitioning techniques are equally valid. More importantly, perhaps, the results discussed, particularly leucine, seem to indicate that Mulliken population analysis does not always reflect the physics in the system under consideration: examining the nominal charges alone, one would not be able to identify leucine as being zwitterionic, but this does appear to be reflected in the effective charges calculated. Further, the effective charge is obtained from the dynamics of the system: in a simulation where atoms are subjected to

external fields, it would perhaps be more appropriate to use effective charges rather than charges obtained from population analyses. This is an interesting point and deserves further investigation.

6.2 Molecular Crystals

Having determined the normal mode behaviour for the case of isolated molecules, it is now time to examine the lattice dynamical properties of the molecular crystal in detail, and attempt to understand how the two relate. One would expect that there will be two major factors in determining this relationship: the zwitterionisation of the constituent molecules in the solid state leading to alterations in the molecular electronic and geometric structure; and secondly, the influence of the inter-molecular interactions responsible for binding the solid upon the vibrational spectrum.

Generally, in most molecular crystals, the intra-molecular forces will be greater than the inter-molecular forces by an order of magnitude [179]. Consequently, internal molecular modes will have higher frequencies of oscillation than the intra-molecular lattice modes. It is therefore often a justifiable approximation to treat the motions as separable, and hence to assume that the molecule moves under the influence of the lattice modes as a rigid body. These rigid motions may take two forms: translational motions, analogous to phonons in a conventional crystal, and orientational, or librational motions in which the molecular centre-of-mass is stationary. This approach is very much in the spirit of molecular physics, *i.e.* one treats individual molecules as being perturbed by the crystalline environment. However, dealing with librational motions using such a scheme is cumbersome, as one must explicitly include such terms in the Hamiltonian. Similarly, if coupling arises between internal and lattice modes, or between internal modes on neighbouring molecules, this again must be included explicitly in the Hamiltonian.

Such a treatment has been outlined in detail by Venkatarman and Sahni [178] and Schnepp and Jacobi [179], and has had numerous successes. However, it is apparent that in situations where the molecules possess a large degree of conformational flexibility (indicating that the separation of the normal modes approximation breaks

down) that this approach is inadequate. An accurate treatment of the low-frequency lattice modes, which are sensitive to intermolecular interactions, demands that a full treatment of the crystal be provided, rather than simply treating it as a molecule perturbed by the effects of the crystal field [180].

Amino acids are able to undergo many conformational changes, as mentioned previously, and as such, an accurate treatment of the lattice dynamics requires a full *ab initio* treatment of the crystal. DFPT is a natural candidate for this work. DFPT possesses further advantages over the molecule-centred approach: because the normal modes are obtained by examining the system response to a perturbation of every atom in each Cartesian direction, the lattice and internal modes are treated on exactly the same footing, and any couplings between them are implicitly incorporated. Similarly, librational motions and any possible couplings with the translational degrees of freedom are implicitly incorporated. This approach is very much in keeping with the traditional solid state physics approach whereby lattice dynamics are discussed in terms of cooperative vibrations of all atoms within the crystal. In principle, it suffers the disadvantage that the conceptually simple picture of a molecule undergoing librational and translational motions is lost, but this picture can be constructed retrospectively by examining the system eigenvectors.

6.2.1 Computational Approach

The response of each molecular crystal to electric field and atomic displacement perturbations is obtained using the same DFPT techniques as discussed earlier. The theoretically determined structures of the previous chapter are used. However, DFPT calculations on such large systems (of the order of 200 electrons) are extremely computationally demanding; thus it has only been possible to calculate the normal modes at the Γ-point, rather than being able to obtain a full phonon dispersion curve. Computational restrictions have also meant that, in all cases except L-alanine, only the Γ-point has been used in determining the self-consistent Kohn-Sham groundstate via a single-point energy calculation. The first restriction is disappointing, as it would be interesting to be able to examine the full vibrational spectrum, as this has not, to the best of the author's knowledge, been investigated by

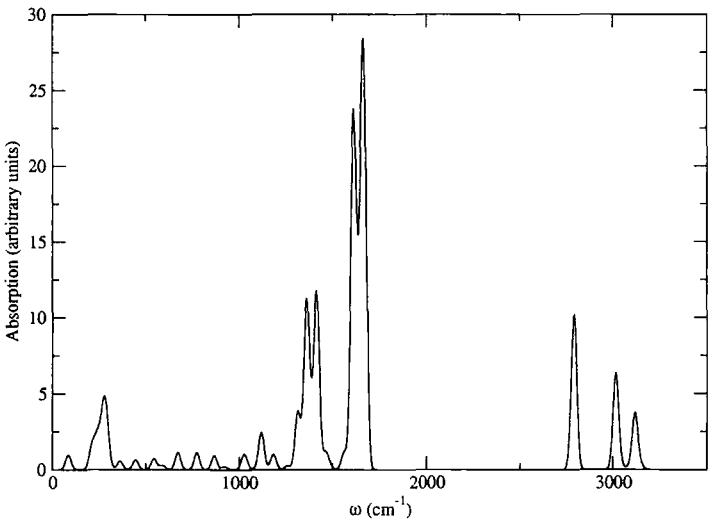

Figure 6.12: IR spectrum of L-alanine.

ab initio methods. However, the zone centre phonons are still extremely useful physically, as a knowledge of them is vital for investigating the IR and Raman spectra. The second restriction is more problematic, and slightly unsatisfying, as it means that the groundstate density will be less well determined, leading to an inherent error when the response of the system to a perturbation is considered. However, it is possible to estimate the resulting error in the predicted normal mode frequencies by using L-alanine, which is fully converged, as a benchmark.

6.2.2 Lattice Dynamics

Given that L-alanine represents the most converged calculation carried out, it makes sense to analyse this one initially. It is useful to examine the validity of the rigid molecule approximation, and whether the internal normal modes are separable from the external lattice modes. In order to attempt to illustrate this discussion, rather than simply providing a rather dry table of normal mode frequencies (which would be prohibitively long!), in figure 6.12 the IR spectrum of L-alanine is presented.

This is noticeably different from the IR spectrum of a free molecule presented ear-

lier. This is not surprising, given that the molecule in the solid state is found as a zwitterion. The presence of three peaks at around 3000 cm^{-1} is noticeable, in contrast to the one peak in the molecular case. These are due to stretching of the N-H bonds present. These oscillations are, unsurprisingly, decoupled from motions of the lattice, and constitute pure vibronic (internal) modes. The doublet that occurs in the spectrum at 1610-1683 cm^{-1} is common to zwitterionised amino acids; a similar feature was observed in the spectrum of isolated (zwitterionic) leucine. This is due to oscillations of the C-O bond and the bond between the deprotonated oxygen and the C_α atom. Correspondingly, it is not surprising that these peaks are of almost equal intensity. A further doublet occurs at 1364-1420 cm^{-1}. These correspond to oscillations of the C-C bonds that form the sidechain of the molecules. These modes can legitimately be termed internal modes. However, for the lower-lying modes, the distinction between vibronic and lattice modes is less clear. For example, the peak at 272 cm^{-1} originates from a motion that in the plane of the carboxy group looks like a rocking of the carboxy group fixed about the C_α atom, that is due to bending of the C-C bonds forming the sidechain. This causes stretching of the O N-H hydrogen bonds present, and thus it can be seen that this corresponds to an admixture of inter and intramolecular motion. This is a direct consequence of the flexibility of the carbon sidechain.

The lowest lying modes occur at frequencies of less than 100 cm^{-1}; these can be identified in the main as lattice modes, although a mode occurs at 79 cm^{-1} that appears to arise largely from CH_3-C_α bond rocking. A translational mode occurs at 89 cm^{-1} in which pairs of molecules oscillate anti-phase with the neighbouring pair in the direction of the *a*-axis. The highest frequency lattice mode occurs at 142 cm^{-1}; this is a pure translation mode in which neighbouring molecules oscillate anti-phase in the *a*-axis. Given that the lowest normal mode of the isolated alanine molecule has a frequency of 188 cm^{-1}, this suggests that a degree of coupling may be expected between external and internal modes. Indeed, modes such as that occurring at 107 cm^{-1} and 124 cm^{-1} appear to be an admixture of librational motions and C_α-C bond bending and rocking. This is consistent with the conformational flexibility of amino acid molecules. A further manifestation of this flexibility is found with the presence of several low-lying soft phonons. This opens up the possibility of phonon-mediated

phase transitions occurring between phases in which the constituent molecules adopt different conformations.

The presence of soft phonon modes in molecular crystals is not surprising. However, unambiguously identifying soft phonon modes is problematical because it is the low-lying lattice modes that are likely to be soft, and these very modes are the most difficult to accurately describe. This is because these modes have small frequencies - of the order of less than 100 cm^{-1} - and therefore the error on the calculated frequencies is, in some cases, of the order of the frequency itself. An illustration of this can be provided by examining the lowest lying modes of L-alanine. Imposition of the sum rule drastically changes the frequencies of the lowest 11 modes; in fact from mode 7 to 11, there is actually a sign change: this suggests that significant error is present. Therefore, in order to ascertain whether modes are genuinely soft, or the negative frequencies obtained in the calculation are a numerical artifact, atoms have been displaced from their equilibrium positions by a small amount in the direction of the phonon eigenvectors of the modes in question. Single-point energy calculations are then carried out for these new geometries, and the resulting system energy compared to that obtained at the relaxed geometry. Of course, if the mode is not soft, and the negative frequency is merely an indication of a poorly converged result, then the system energy will be greater for the displaced structures. However, if the mode is a genuine soft mode, then the reverse will be true, and the energy should decrease upon atomic displacement under the action of these modes.

These calculations have verified the existence of two soft phonon modes amongst these low-lying lattice modes: that occurring at 79 cm^{-1} and that at 107 cm^{-1}. These both refer to the frequencies without the acoustic sum rule explicitly imposed. These modes correspond to rigid unit rotations of the molecules involved around the axis defined by the $C_1 - C_2$ bond. The presence of these soft modes opens up the possibility of phonon-mediated phase transitions occurring: this is an intriguing prospect, and deserving of further investigation.

In order to attempt to understand whether the majority of the changes in the vibrational behaviour arise from, *i.e.* from the crystalline environment, the zwitterionisation of the molecules, or some combination, it is useful to examine the behaviour of

L-leucine in detail. This is zwitterionic as an isolated molecule, thus allowing one to probe the effects of the crystalline environment alone on the vibrational properties.

In figure 6.13 the IR spectrum of L-leucine in the solid state is shown. This shows some similarities with that of the isolated molecule, but there are some noticeable differences present. For example, the modes at around 3000 cm^{-1} have larger IR peaks than in the case of the isolated molecule. The peak at 3176 cm^{-1} arises due to asymmetric stretching of the N-H bonds present; a symmetric stretching mode of the same bonds occurs at 3126 cm^{-1}. This compares to values of 3241 and 3282 cm^{-1} for the asymmetric mode and 3028 cm^{-1} for the symmetric mode. This is a significant change in the frequencies, and it is also noteworthy that in the solid state, the difference in frequencies between the asymmetric and symmetric modes is less. This suggests that the crystalline environment has a noticeable effect on these high frequency vibronic modes; this is not surprising, as the H atoms involved in these oscillations are also responsible for hydrogen-bonding with neighbouring molecules. Thus one could expect there to be an observable alteration in frequency due to the presence of the hydrogen bonds. That these oscillations occur at frequencies very similar to those in L-alanine suggests two important things: firstly, that the strength of the hydrogen bonds is approximately constant between systems, which is consistent with the discussion in the preceding chapter based upon population analysis of the bonds; and secondly, even though only the Γ-point has been used for sampling of the Brillouin zone, that this is sufficient to describe the vibronic modes adequately. The modes that are most sensitive to the convergence of the groundstate calculation are the low-lying lattice modes, which is unsurprising. A remedy to this problem may be provided by imposing the acoustic sum rule artificially as a post-process step. This has the effect of constraining the low frequency modes, thereby improving the vibrational spectrum. A further N-H stretching mode may be seen at 2707 cm^{-1}.

The characteristic doublet that occurs at around 1500 cm^{-1} in zwitterionic systems is present, but slightly more complicated in structure in L-leucine. The peak at 1595 cm^{-1} arises from asymmetric oscillations of the C-O bonds present, with a symmetric oscillation of the same bonds present at 1415 cm^{-1}. Again, this differs from the frequencies of 1578 and 1633 cm^{-1} observed in the isolated molecule, and

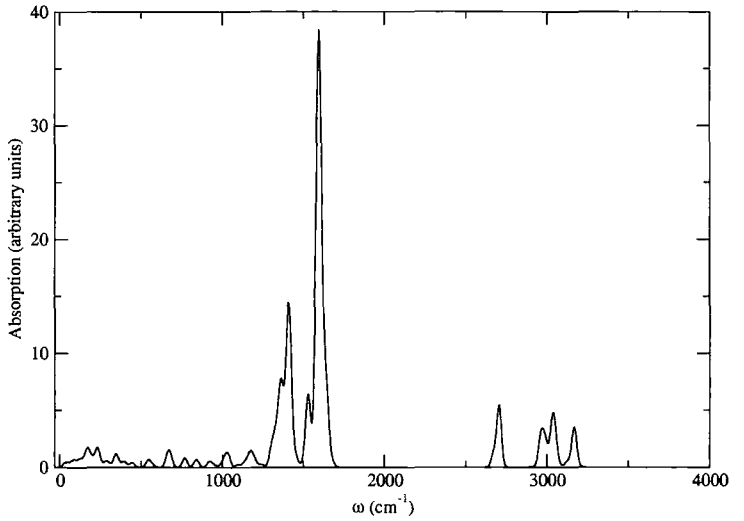

Figure 6.13: IR spectrum of L-leucine.

one can invoke the hydrogen bonds to help explain this discrepancy. It is likely that the hydrogen bonds and the crystal field are also responsible for the large difference in the relative intensities of these peaks in contrast to L-alanine, where the peaks are of similar intensity. However, an interesting feature not observed in the isolated molecule is the small peak at 1530 cm^{-1} due to wagging of the N-H bonds present. Again, this will involve the hydrogen bonds, although this will act more to bend them than to stretch them.

The low-lying modes appear to be largely librational motions, with no translational modes present. Interestingly, these modes appear to have little in the way of mixed internal/external mode character, being almost entirely purely external in character. Given that the lowest lying molecular modes occur at 92 cm^{-1}, this appears unexpected. However, modes occur at 101 and 148 cm^{-1} that appear to exhibit the same behaviour as those occurring at 92, 140 and 146 cm^{-1} in the isolated molecule. This suggests that the intermolecular interactions are not significant in perturbing the low lying internal modes. This is not entirely surprising, given that these modes consist of flexing and rocking motions of the sidechains, and that the atoms involved in these motions are not involved in the bonding mechanisms prevalent in these crys-

tals. The high frequency vibrons, conversely, involve atoms intimately connected to the bonding mechanisms present; thus one would expect that these modes show the greatest variation. This acts as a further confirmation that hydrogen bonds are dominant in determining the molecular structure, as deduced by examining the electronic structure in the previous chapter.

It is now possible to understand the relative contributions of zwitterionisation and intermolecular interactions to the modification of the free molecule normal modes. It is clear from examining the spectrum of L-alanine that modifications do occur due to zwitterionisation; for example, the doublet occurring at around 1600 cm^{-1}. However, there are also features present such as the peaks occurring in the vicinity of 3000 cm^{-1}, that do not occur for a zwitterionic isolated molecule. This is indicative of the effects of the crystalline environment and intermolecular interactions.

The spectrum of L-leucine also shows modification of the normal modes relative to those of the isolated molecule, for example, the more complicated structure of the carboxy doublet at around 1500 cm^{-1} compared to that of the isolated molecule, and the peaks occurring at 3000 cm^{-1}, indicate the influence of intermolecular, in particular hydrogen bonding, interactions.

It therefore appears that the effects of the crystalline environment may be decoupled from those of zwitterionisation: the former is responsible for modification of the highest frequency vibronic modes, and results in extra structural features being observable in the IR spectrum at around 1500 cm^{-1}; the latter is responsible for the appearance of this doublet.

One can now examine the spectra and vibrational behaviour of L-valine and L-isoleucine in order to verify that this general trend is true. In figure 6.14 the IR spectrum of L-valine is presented. It is immediately apparent that the spectrum is similar to that of L-leucine, with a similar form of doublet structure arising at around 1600 cm^{-1}. This is interesting, as it illustrates the effect of the crystalline environment in line with the discussion above. The general vibrational behaviour is very similar to that of L-leucine, with the exception that the low lying lattice modes include translational modes at 96.2 cm^{-1}, and a coupled translational-librational mode at 42 cm^{-1}, in contrast to L-leucine, where the low-lying modes are libronic.

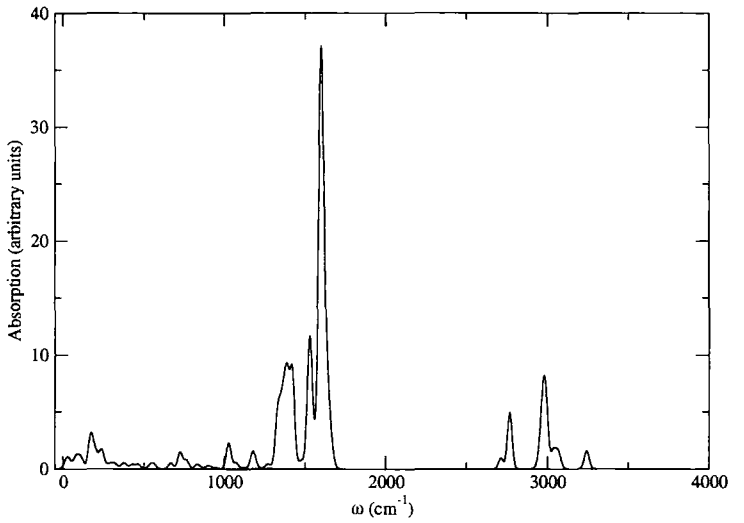

Figure 6.14: IR spectrum of L-valine.

The lowest vibronic modes are little affected by the crystalline environment: the sidechain rocking mode occurring at 110 cm^{-1} in the isolated molecule occurs at 118 cm^{-1} in the crystal. One would expect such behaviour for the same reasons as in L-leucine.

The spectrum of L-isoleucine, presented in figure 6.15, is slightly different to those of L-leucine and L-valine. The most noticeable difference is the structure of the peaks at around 1500 cm^{-1}. As in the other cases, the higher frequency peak is due to antisymmetric oscillations of the oxygen atoms in the carboxy group, whilst the lower frequency peak arises from a symmetric oscillation of the same bonds. However, it is noticeable that these form two distinct peaks, in contrast to the other cases. The intensity of the lower frequency peak is also only around half that of the more intense peak; a major contrast to the situation arising in both L-leucine and L-valine. One also finds that in all cases, the antisymmetric oscillation is accompanied by "wagging" of the N-H bonds. However, in L-isoleucine, unlike the other three systems, the symmetric oscillation is accompanied by excitation of the C-C bonds between the end atoms of the sidechain. It therefore appears that in L-isoleucine, this motion is more of a superposition of vibronic modes, rather than a pure vibron,

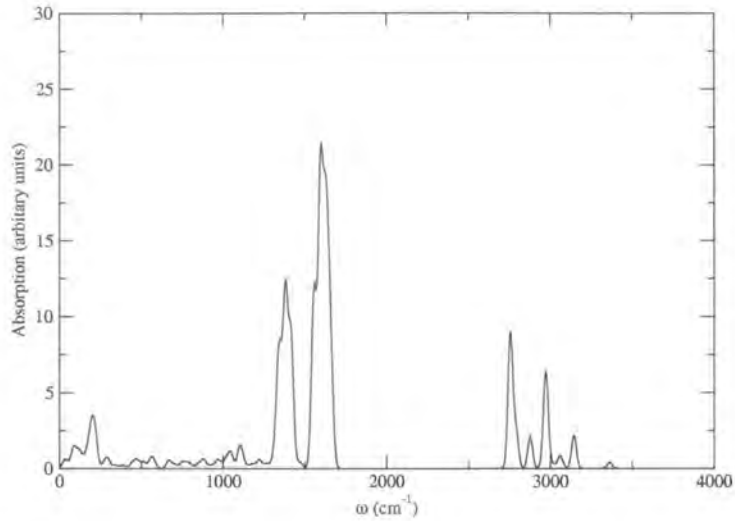

Figure 6.15: IR spectrum of L-isoleucine.

as it is in the other systems. This mixed character may account for the discrepancy observed.

The high frequency vibrons occurring in the vicinity of 3000 cm^{-1} behave slightly differently also. Each of the major peaks, at 3147 cm^{-1}, 2974 cm^{-1} and 2756 cm^{-1} consists of a single N-H stretch, in contrast to L-leucine, for example, where one observes an IR-active antisymmetric stretch of these modes. An IR-silent symmetric stretch does occur at 2867 cm^{-1}, in contrast to 2933 cm^{-1} in the isolated molecule. The highest frequency vibrons, occurring at 3162 cm^{-1}, are single N-H stretching modes. This is in contrast to the isolated molecule, where the highest frequency modes occur at 3319 and 3409 cm^{-1}, and are symmetric and antisymmetric N-H stretching modes respectively. Thus the effect of the crystal is to change both the frequency and the fundamental character of the highest frequency vibrons. The reasons for this can be understood in terms of the fact that every H bonded to the N atom in the crystal may participate in a hydrogen bond with a neighbouring molecule.

The low frequency lattice modes are libronic; no translational modes appear to exist. It is noticeable that a libronic mode occurs at 103 cm^{-1}; thus the lattice modes and

Molecule		$Z_{\kappa,\beta\alpha}$(e)			Z_{av}(e)	Z_{nom} (e)
		-0.70	-0.15	-0.12	-0.45	-0.92
	N	-0.09	-0.65	0.01		
		-0.03	-0.04	0.01		
		-1.54	0.70	0.09	-1.31	-0.66
L-alanine	O(1)	0.77	-1.44	-0.01		
		-0.19	0.13	-0.95		
		-1.21	0.59	0.16	-1.43	-0.57
	O(2)	0.63	-1.14	-0.23		
		0.50	-0.60	-1.95		

Table 6.5: Born effective charges in the L-alanine crystal. The nominal charge refers to that obtained via Mulliken population analysis.

the lowest lying vibronic modes almost overlap. This is a natural and expected consequence of the conformational flexibility inherent in a long carbon sidechain. From 110 cm^{-1} one obtains vibronic modes, in this case, sidechain rocking motions, compared to the same occurring at 100 cm^{-1} in the isolated molecule. Similarly a vigorous twisting of the carboxy group is observed at 145 cm^{-1} compared to 144 cm^{-1} for the isolated molecule. Thus, as expected, the low-lying vibrons are largely unaffected by the crystalline environment.

6.3 Born Effective Charges

Having analysed in detail the effects of the crystalline environment upon the normal modes of the molecules, it is useful now to turn attention to the Born effective charges and to investigate how these are affected. In table 6.5, the effective charge tensors of the N and O atoms in L-alanine are presented.

These values show some marked differences from those obtained for the isolated molecule. Given the effects of zwitterionisation, and the presence of the crystalline environment, such variations are expected. Interestingly, the average of the effective charge for nitrogen, -0.45e, is close to that obtained for the isolated molecule, -0.49e. This is unexpected, especially given that the nitrogen atom gains a chemical bond with an extra hydrogen atom in the crystal. However, the hydrogen atoms bonded to this atom are involved in the hydrogen bonds responsible for binding the crystal; as discussed above, these hydrogen bonds lead to a modification of the normal modes of

the constituent molecules. Given that the effective charge is intimately related to the normal modes of the system under consideration, it is possible that the changes due to the extra chemical bond present are cancelled to some degree by the modification of the vibronic modes that arises because of the hydrogen bonds.

In common with the free molecule, it is again found that the effective charges of the oxygen atoms are more negative than those of the nitrogen atoms. This is in contrast to what one would expect on the basis of electronegativites. As in the case of the free molecule, the Mulliken charges follow the trend of electronegativities.

In order to investigate the effects of the crystalline environment on the Born charges, and attempt to understand which modes contribute to it, it is useful to calculate the mode effective charge vector, defined through [114]

$$\bar{Z}^m_\alpha = \sum_{\kappa\beta} Z^\star_{\kappa,\alpha,\beta} U_{m,\mathbf{q}=\mathbf{0}}(\kappa\beta) \tag{6.2}$$

where m is the mode under consideration, $U_{m,\mathbf{q}=\mathbf{0}}$ is the corresponding phonon eigenvector, α, β label Cartesian directions and κ labels atoms. Calculation of this quantity is equivalent to projecting the Born effective charge onto the space of dynamical matrix eigenvectors, and allows the actual change in polarisation due to each mode to be obtained. It therefore amounts to decomposing the Born effective charge into contributions from each normal mode. Such a decomposition is useful as it yields valuable information on the character of the modes present. For example, vibronic modes are very often associated with excitations of intramolecular chemical bonds, and therefore determination of the mode effective charge vector provides insights into the nature of the chemical bonds, such as the level of ionicity or covalency present.

In table 6.6 the mode effective charge vectors of some of the normal modes present in L-alanine are given. Of interest is the behaviour of the highest frequency vibrons; those that are associated with the stretching of the N-H bonds. It can be seen that those at 3148 and 3117 cm^{-1} have $|\bar{Z}_m|$ values of 0.53 eÅ and 1.87 eÅ, respectively. This indicates that these modes contribute significantly to the Born effective charges, and further, that these modes possess a significant ionic character. Given that the

ω (cm^{-1})	Character	$\bar{Z}^m$		
3148	LO	-0.53	0.00	0.00
3117	TO	0.00	-1.87	0.00
1663	LO	-4.89	0.00	0.00
1607	TO	0.00	4.59	0.00
1412	TO	0.00	-0.03	0.00
1358	TO	0.00	-0.26	0.00
1357	LO	0.21	0.00	0.00
270	LO	0.89	0.00	0.00
206	LO	1.18	0.00	0.00
106	LO	-0.06	0.00	0.00

Table 6.6: Mode effective charge vectors in L-alanine. The character of the mode can be established by noting that $\mathbf{q} \rightarrow \mathbf{0}$ along the x-axis.

hydrogen and nitrogen atoms are involved in hydrogen bonding, one would expect that there should be an accumulation of charge on the nitrogen atom; thus a level of ionicity is expected in these bonds.

Similarly, the modes arising due to stretching of the carbon-oxygen bonds, namely those occurring at 1663 and 1607 cm^{-1} possess large mode effective charge vectors; the magnitudes being 4.89 eÅ and 4.59 eÅ, respectively. This is unsurprising, given the above discussion, as the oxygen atoms involved in these oscillations are also involved in hydrogen bonds. The large values of these three-vectors suggest that the major changes occurring in the Born effective charges are due to the hydrogen bonds that form in the molecular crystal. Of course, implicit in this is the effect of zwitterionisation, for it is this that allows the hydrogen bonds to form, as discussed in the previous chapter.

One would perhaps expect that in this case the effective charges due to the atoms in the sidechain are largely unaffected by the crystal environment. In table 6.7 this is clearly not the case; the C(1) atom can be seen to undergo a significant change, in line with the preceding discussion. The C(2), *i.e.* the C_α, atom undergoes some change, with the average of the effective charge being modified from 0.18 e to 0.23 e. The C(3) atom also undergoes modification, with the values changing from -0.01 e to -0.06 e. These changes can be understood in terms of the lattice modes present; the long-range fields associated with these modes will lead to modifications of the free molecule Born charges, which are only associated with internal modes. In line

	Free Molecule				Crystal			
	$Z_{\kappa,\beta\alpha}$(e)			Z_{av}(e)	$Z_{\kappa,\beta\alpha}$(e)			Z_{av}(e)
	1.41	-0.34	-0.60	1.04	1.61	-1.10	-0.26	1.52
C(1)	-0.09	1.20	0.01		-1.08	1.07	0.40	
	-0.61	0.06	0.50		-0.20	0.54	1.87	
	0.39	-0.10	-0.05	0.18	0.39	0.10	-0.52	0.23
C(2)	-0.21	-0.06	0.18		0.03	0.16	0.04	
	-0.10	0.22	0.22		-0.41	0.02	0.15	
	-0.13	0.06	0.05	-0.01	-0.08	-0.02	0.13	-0.06
C(3)	-0.01	0.03	-0.04		-0.02	0.003	0.05	
	0.03	-0.04	0.06		0.002	0.02	-0.10	

Table 6.7: Born effective charges of the carbon atoms in alanine; comparison between values in the crystal and free molecule.

with this, it can be seen in table 6.6 that the lattice modes may possess values of $\bar{Z}^m$ as large as those of the vibronic modes.

The discussion above suggests that the formation of hydrogen bonds is responsible for the modifications to the Born effective charges in L-alanine; however, the ability to form these hydrogen bonds is due to the fact that the molecules zwitterionise. Therefore the changes are due to both effects, and it is difficult to separate and decouple the two effects. Turning to L-leucine, any changes are due solely to the formation of the intermolecular hydrogen bonds. It is therefore an interesting case, as it allows one to investigate the effects of the crystal environment unadulterated by the effects of zwitterionisation.

In table 6.8, the effective charges in L-leucine are given. Again, large changes to the effective charge tensors occur. It can be expected that these changes are due to the intermolecular hydrogen bonds. It is interesting that in L-leucine, the value of the effective charge tensor of nitrogen is not close to that of the same atom in the isolated molecule. This is in contrast to the situation in L-alanine, as mentioned previously. The values of the effective charge tensors for the oxygen atoms are -1.43e and -1.39e, which is similar to the values in L-alanine; this suggests that the effects of the hydrogen bonds upon the effective charges are similar in the two cases.

Again, an examination of the mode effective charge vectors given in table 6.9 indicates that the major changes in polarisation are associated with the high frequency

Molecule		$Z_{\kappa,\beta\alpha}$(e)			Z_{av}(e)	Z_{nom} (e)
		-0.631	0.124	0.012	-0.755	-0.85
	N	-0.004	-0.672	0.222		
		-0.077	0.136	-0.962		
		-1.281	-0.441	-0.268	-1.43	-0.69
L-leucine	O(1)	-0.408	-1.464	-0.295		
		-0.560	-0.580	-1.541		
		-0.645	-0.164	-0.120	-1.39	-0.70
	O(2)	-0.385	-2.333	-0.143		
		-0.106	0.295	-1.192		

Table 6.8: Born effective charges in the L-leucine crystal. The nominal charge refers to that obtained via Mulliken population analysis.

ω (cm^{-1})	$\|\bar{Z}^m\|$
3172	1.63
3126	0.63
2707	2.32
1596	5.07
1415	0.40
148	0.58
101	0.22

Table 6.9: Mode effective charge vectors in L-leucine.

vibrons corresponding to oscillations of the N-H and carbon-oxygen bonds. This is similar to the findings in L-alanine, and similarly, imply that these bonds possess a level of ionicity consistent with hydrogen bonding.

In table 6.10 the averages of the effective charge tensors are presented for the atoms in the molecular sidechain. The C(1) atom, that is, the carbon atom in the carboxy group, undergoes the largest change; in light of the discussion so far, this is unsurprising, as this atom is bonded to atoms involved in hydrogen bonding. It is noteworthy as well that the effective charges of the atoms further along the sidechain, *i.e.* further away from the C_α atom, display less variation. This can be understood if one considers that these atoms are not involved in intermolecular interactions, and therefore the properties possessed by these atoms in the free molecule undergo little modification. It does, however, seem to imply that the lattice modes contribute little to the Born charges. This can be understood by recalling that the lattice modes in L-leucine were found to be libronic in nature; such modes will not contribute to long

Atom	$Z^*_{av,crystal}$	$Z^*_{av,molecule}$
C(1)	1.544	1.182
C(2)	0.203	0.139
C(3)	0.067	0.019
C(4)	0.164	0.128
C(5)	0.018	0.019
C(6)	0.023	0.020

Table 6.10: Averages of the Born effective charge tensors for the carbon atoms in leucine: comparison between values for the isolated molecule and the crystal.

range electric fields set up in the crystal.

Finally, having analysed L-alanine and L-leucine in detail, attention can be focused upon the remaining two systems, L-isoleucine and L-valine. Examining L-isoleucine, the effective charge tensors are given in table 6.11. The changes can be explained within the same framework used for the other systems. The average of the effective charges of the carbon atoms are given in table 6.12; it can be seen that these are very close to those in L-leucine. This is unsurprising, given the similarities between these molecules, and suggests that the effects of the crystalline structure upon the long range non-analytic contribution to the dynamical matrix will be similar in each case. It can be seen though that there is a greater variation in the effective charges moving from the free molecule to the crystalline case in L-isoleucine than is true in L-leucine. If one bears in mind though that leucine was found to be zwitterionic as a free molecule, largely due to the different inter-molecular hydrogen bonds present, then one would expect this to be reflected in the molecular effective charges; thus the differences can be attributed to the differences in the molecular state, rather than differences in the crystal.

In table 6.13 the Born effective charges of the nitrogen and oxygen atoms in L-valine are given. The values are broadly similar to those in the other systems under consideration; this suggests that the same mechanism is behind the modifications, *i.e.* the intermolecular hydrogen bonds. This implies that the hydrogen bond strengths are approximately constant between the systems. This is unsurprising, given that the functional groups responsible for these bonds are the same in all cases, and is consistent with the findings in the previous chapter, which were based upon an analysis

Molecule		$Z_{\kappa,\beta\alpha}$(e)			Z_{av}(e)	Z_{nom} (e)
		-0.973	0.135	0.147	-0.847	-0.79
	N	0.185	-0.643	0.045		
		0.104	-0.129	-0.925		
		-1.189	-0.456	0.709	-1.334	-0.69
L-isoleucine	O(1)	-0.145	-1.362	0.541		
		0.340	0.606	-1.451		
		-1.411	0.487	0.056	-1.527	-0.66
	O(2)	0.180	-2.410	0.511		
		0.097	0.175	0.761		

Table 6.11: Born effective charges in the L-isoleucine crystal. The nominal charge refers to that obtained via Mulliken population analysis.

Atom	$Z^{\star}_{av,crystal}$	$Z^{\star}_{av,molecule}$
C(1)	1.53	1.072
C(2)	0.204	0.180
C(3)	0.168	0.078
C(4)	0.135	0.077
C(5)	0.002	0.033
C(6)	0.018	0.029

Table 6.12: Averages of the Born effective charge tensors for the carbon atoms in isoleucine: comparison between values for the isolated molecule and the crystal.

Molecule		$Z_{\kappa,\beta\alpha}$(e)			Z_{av}(e)	Z_{nom} (e)
		-0.970	0.012	-0.078	-0.734	-0.78
	N	0.133	-0.707	-0.059		
		0.006	0.064	-0.526		
		-1.424	-0.568	-0.599	-1.360	-0.68
L-valine	O(1)	-0.254	-1.425	-0.417		
		-0.273	-0.475	-1.232		
		-1.267	0.349	-0.027	-1.458	-0.66
	O(2)	-0.090	-2.414	-0.448		
		-0.060	-0.228	-0.693		

Table 6.13: Born effective charges in the L-valine crystal. The nominal charge refers to that obtained via Mulliken population analysis.

Atom	$Z^{\star}_{av,crystal}$	$Z^{\star}_{av,molecule}$
C(1)	1.553	1.059
C(2)	0.203	0.174
C(3)	0.191	0.106
C(4)	0.053	-0.010
C(5)	0.024	0.002

Table 6.14: Averages of the Born effective charge tensors for the carbon atoms in valine: comparison between values for the isolated molecule and the crystal.

of bond lengths and populations. Looking at the averages of the effective charges for the carbon atoms, presented in table 6.14, it can be seen that the effective charges of the carbon atoms in the sidechain undergo greater changes than is the case for L-leucine and L-isoleucine; this can be attributed to the presence of translational lattice modes, which will cause long-range electric fields to be induced. The effect of these will be to modify the sidechain effective charges.

6.4 Response to Electric Fields

Finally, attention will now be turned to examining the dielectric properties of the crystals under consideration by calculating their response to homogeneous electric fields. Given the difficulties discussed in chapter 3 with regard to the handling of electric field effects within crystalline solids, the calculations are carried out using DFPT, and there are no finite difference calculations to compare with. However, given that DFPT has been shown to be able to accurately determine the electric field

α (Å^3)			α_{av} (Å^3)	ϵ^{∞}			ϵ^{∞}_{av}	$\epsilon(\omega \to 0)$			$\epsilon_{av}(\omega \to 0)$
46.52	0.00	0.00	46.27	2.32	0.00	0.00	2.31	2.41	0.00	0.00	2.39
0.00	43.26	0.00		0.00	2.23	0.00		0.00	2.30	0.00	
0.00	0.00	49.03		0.00	0.00	2.39		0.00	0.00	2.47	

Table 6.15: Dielectric properties of L-alanine.

response of the isolated molecules, and given the results on test systems presented in chapter 4, it is possible to be confident in the accuracy of the results presented here.

Examination of the crystal response to an electric field, and in particular, visualisation of the corresponding first order change in the electronic density, facilitates an understanding of the origin of the dielectric properties exhibited by the crystal. As has been discussed, understanding these properties is essential if one is to correctly describe the long wave lattice dynamics. In molecular crystals, investigation of the first-order densities allows one to examine how the response of the crystal as a whole is related to that of the constituent molecules. This facilitates an insight into the effects of the crystalline environment upon the response of the constituent molecules.

In table 6.15 the polarisability and dielectric permittivity tensors of L-alanine are presented. The first obvious difference between the isolated molecule and the crystal is that the tensors for the crystalline system are diagonal; this is a consequence of the unit cell symmetry. The average of the polarisability tensor is, at 46.27 Å^3, greater than that of the isolated molecule at 8.67 Å^3. This is unsurprising, given that there are four molecules per unit cell, and that the molecules have formed zwitterions. Furthermore, a simplistic calculation of the crystal polarisability using the molecular value yields a value of 34.68 Å^3; this implies that the zwitterionic form is more polarisable, and illustrates the problems inherent in attempting to calculate crystalline properties using molecular properties. It can also be seen that the ionic (low-frequency) contribution to the dielectric permittivity is of the same order as the electronic contribution; given the effective charges discussed in the previous section, this is not surprising.

In figures 6.16, 6.17 and 6.18, the first-order change in the electronic density in response to electric field perturbations in the x-, y- and z-axes respectively, are

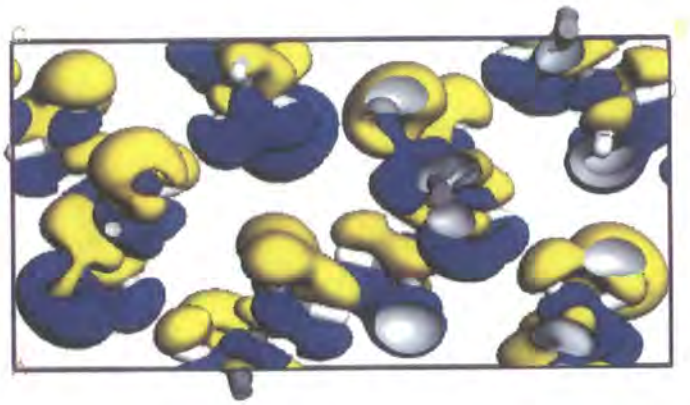

Figure 6.16: L-alanine: response of the electronic density to an electric field in the x-direction. Blue denotes regions in which the density is augmented; conversely yellow denotes those regions where depletion of the electronic density occurs.

illustrated. It can be seen that the density response is primarily localised to each molecule; further the polarisation of individual functional groups present can be seen. Comparing these figures to the first-order density isosurfaces of the isolated alanine molecule presented in figures 6.3-6.5, it is apparent that their are significant differences in the electric field response. This can be attributed to the effects of zwitterionisation and the crystalline environment. The results presented for the isolated molecules suggested that the zwitterionisation of a molecule is less significant in determining its polarisability than the actual geometric structure of the molecule. Given that the actual structure of the alanine molecules changes little upon zwitterionisation, this then implies that the majority of the changes must be due to the effects of inter-molecular interactions. Indeed, in figures 6.16, 6.17 and 6.18 significant polarisation can seen occurring between carboxy and amino groups involved in hydrogen bonding. This is effectively polarisation of the hydrogen bonds in the system, and is supportive of the above conclusions.

In table 6.16 the dielectric properties of L-isoleucine are presented. The first order densities are presented in figures 6.19, 6.20 and 6.21. As in the case of L-alanine,

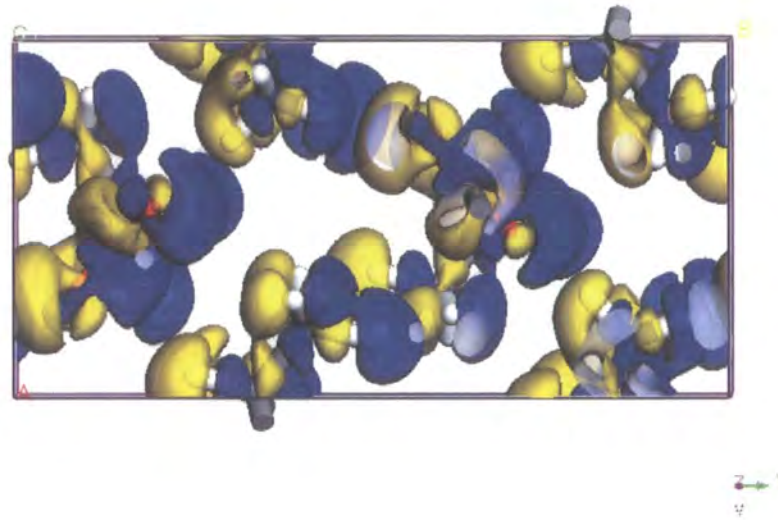

Figure 6.17: L-alanine: response of the electronic density to an electric field in the y-direction. Colour convention as in the previous diagram.

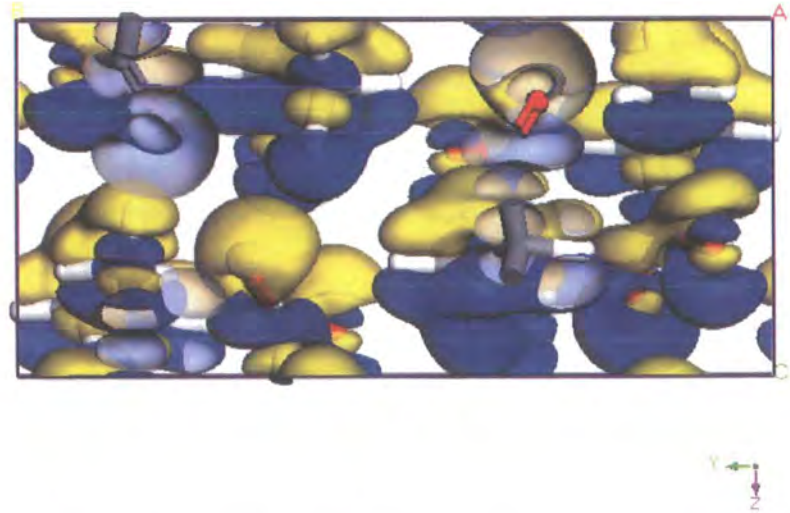

Figure 6.18: L-alanine: response of the electronic density to an electric field in the z-direction. Colour convention as before.

α (Å^3)			α_{av} (Å^3)	ϵ^{∞}			ϵ^{∞}_{av}	$\epsilon(\omega \to 0)$			$\epsilon_{av}(\omega \to 0)$
77.55	0.00	-4.95	74.39	2.24	0.00	-0.08	2.19	3.11	0.00	-0.11	3.00
0.00	70.18	0.00		0.00	2.13	0.00		0.00	3.09	0.00	
-4.95	0.00	75.44		-0.08	0.00	2.21		-0.11	0.00	2.80	

Table 6.16: Dielectric properties of L-isoleucine.

significant polarisation of the hydrogen bonds present can be deduced. In figure 6.21, it appears that the response of the electronic density to a field applied along the axis of the molecule is similar in both the crystalline and isolated molecule cases. This is probably because the only parts of the molecule that are involved in bonding, and can hence be expected to have a different response, are the amino and carboxy functional groups; the rest of the molecule, that is the sidechain, can be expected to have the same response in each environment as these are not involved in intermolecular interactions. Note that the calculations involving L-isoleucine, L-leucine and L-valine have only used the Γ-point to sample the Brillouin zone; this is for the same reasons of computational effort as was the case for the phonon calculations. However, the first-order density isosurfaces presented indicate that the calculations are at least qualitatively correct; therefore the results presented are still useful in gaining an understanding of the dielectric properties of these crystals.

In order to better determine the effects of intermolecular interactions upon the density response to electric fields, it is useful to examine L-leucine in detail, as this is zwitterionic as both an isolated molecule, and in the crystal. In table 6.17, the dielectric properties of this crystal are presented. It is difficult though to gain much insight by simply examining numbers in a table; to this end, it is more fruitful to examine the first-order density isosurfaces, which are shown in figures 6.22, 6.23 and 6.24. Again, the response along the axis of the molecules, *i.e.* the x-axis, is similar to that of the isolated molecule, with some differences occurring in the region of the hydrogen bonds. Interestingly, the first-order densities presented are very similar to those of L-leucine; given the discussions on the relationship between the polarisability and the molecular shape, this is not surprising. It further implies that the effects of the intermolecular interactions are similar in these cases, and are certainly more important than the zwitterionisation of the molecules. Note as well that, as with the isolated molecules, L-leucine is more polarisable than either L-

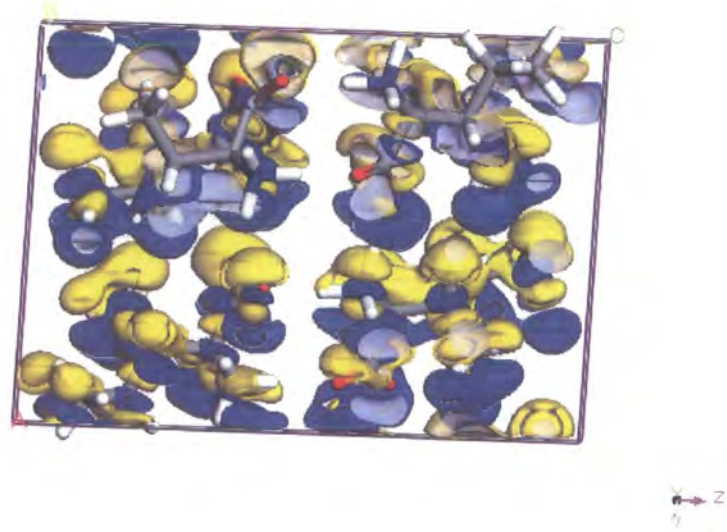

Figure 6.19: L-isoleucine: response of the electronic density to an electric field in the x-direction. Blue denotes regions in which the density is augmented; conversely yellow denotes those regions where depletion of the electronic density occurs.

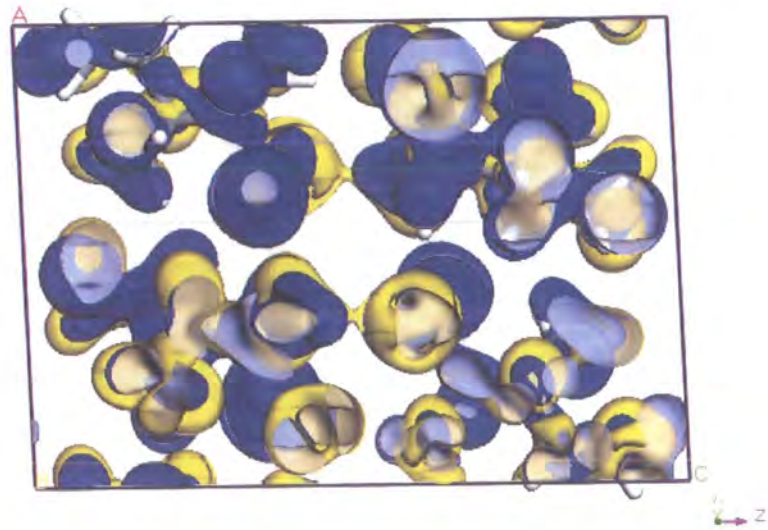

Figure 6.20: L-isoleucine: response of the electronic density to an electric field in the y-direction. Colour convention as in the previous diagram.

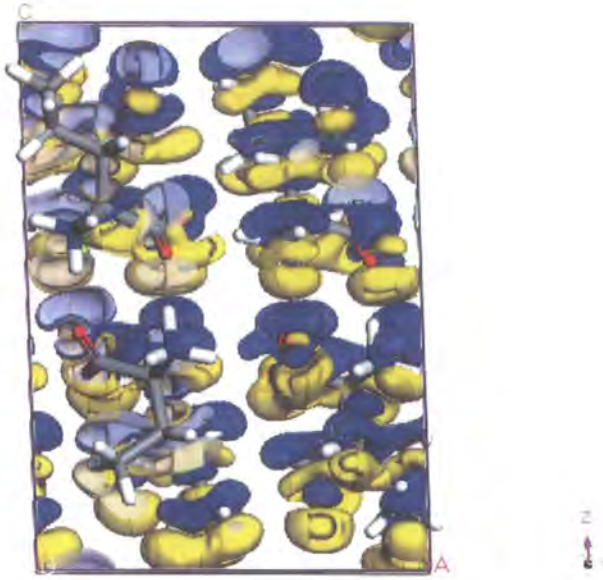

Figure 6.21: L-isoleucine: response of the electronic density to an electric field in the z-direction. Colour convention as before.

α (Å^3)			α_{av} (Å^3)	ϵ^{∞}			ϵ^{∞}_{av}	$\epsilon(\omega \to 0)$			$\epsilon_{av}(\omega \to 0)$
73.44	0.00	4.44	76.27	2.24	0.00	0.07	2.29	2.73	0.00	0.09	3.20
0.00	79.19	0.00		0.00	2.34	0.00		0.00	3.74	0.00	
4.44	0.00	76.18		0.07	0.00	2.29		0.09	0.00	3.12	

Table 6.17: Dielectric properties of L-leucine.

isoleucine or L-alanine, a fact that is related to the larger volume of the L-isoleucine crystal.

Finally, in table 6.18, attention is focused upon L-valine. The first-order density isosurfaces are shown in figures 6.25, 6.26 and 6.27. Again, the behaviour is broadly similar to that exhibited in L-leucine and L-isoleucine. Note that in figure 6.27, the centre of the figure not only shows clear polarisation in the region of the carboxy and amino groups, but in the x-axis an overlap between neighbouring molecules can be seen (*i.e.* the first-order density appears to be shared between two molecules); this is clear evidence of the influence of the intermolecular interaction upon the density response. Indeed this suggests that the major modifications to the molecular response due to the crystal environment occur in the functional groups that participate in these intermolecular interactions. In the amino acids, these will be the amino and

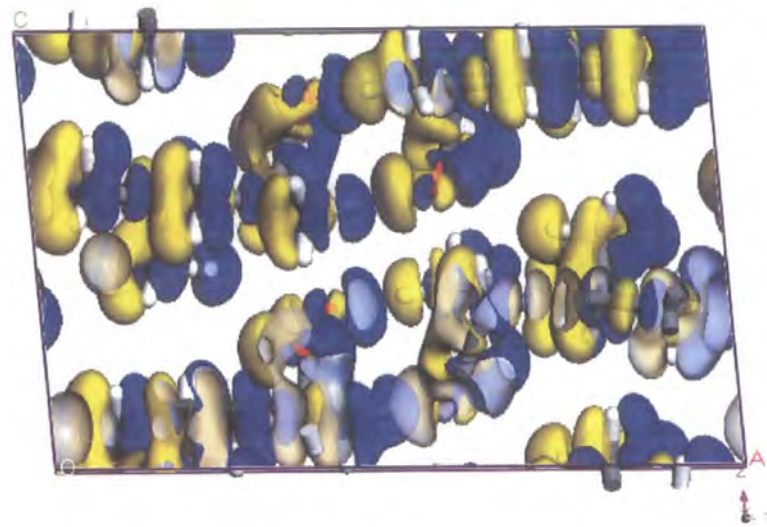

Figure 6.22: L-leucine: response of the electronic density to an electric field in the x-direction. Blue denotes regions in which the density is augmented; conversely yellow denotes those regions where depletion of the electronic density occurs.Grey denotes the interior surface of an isosurface.

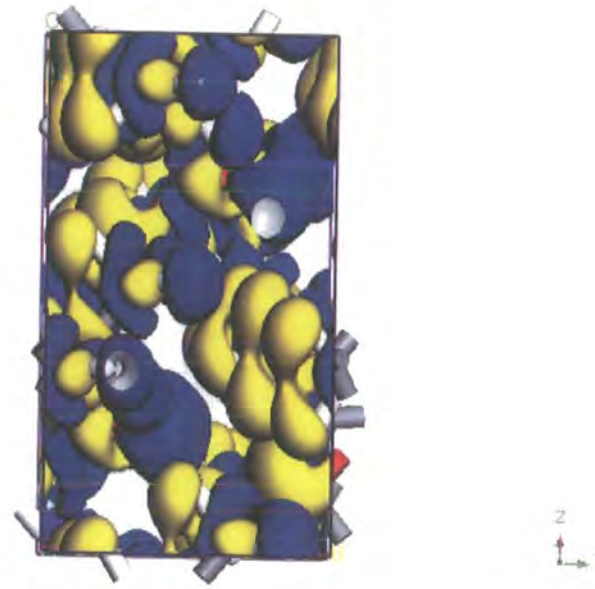

Figure 6.23: L-leucine: response of the electronic density to an electric field in the y-direction. Colour convention as in the previous diagram.

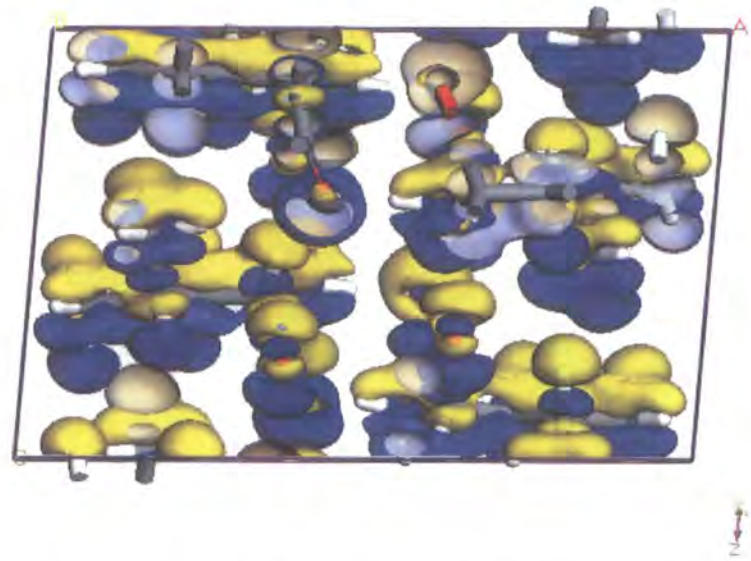

Figure 6.24: L-leucine: response of the electronic density to an electric field in the z-direction. Colour convention as before.

α (Å^3)			α_{av} (Å^3)	ϵ^{∞}			ϵ^{∞}_{av}	$\epsilon(\omega \to 0)$			$\epsilon_{av}(\omega \to 0)$
66.97	0.00	4.35	66.12	2.33	0.00	0.09	2.27	2.42	0.00	0.08	3.35
0.00	69.22	0.00		0.00	2.37	0.00		0.00	5.45	0.00	
4.35	0.00	62.17		0.09	0.00	2.23		0.08	0.00	2.19	

Table 6.18: Dielectric properties of L-valine.

carboxy groups; the carbon sidechains can be expected to behave similarly in both environments, as these are not involved in intermolecular interactions.

6.5 Conclusions

We have calculated the dielectric and vibrational properties of the amino acid molecules alanine, valine, leucine and isoleucine using density functional perturbation theory. We find that the polarisability tensors show good agreement with values determined by finite difference calculations, whilst analysis of the first order densities indicates that the contributions of the various functional groups to the polarisability are influenced by the geometrical structure of the molecule. It would thus seem that the polarisabilities of each functional group are not transferable,

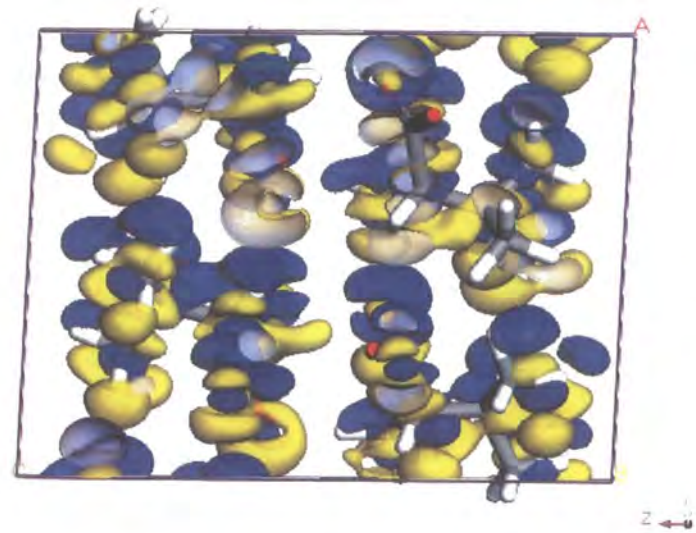

Figure 6.25: L-valine: response of the electronic density to an electric field in the x-direction. Blue denotes regions in which the density is augmented; conversely yellow denotes those regions where depletion of the electronic density occurs.Grey denotes the interior surface of an isosurface.

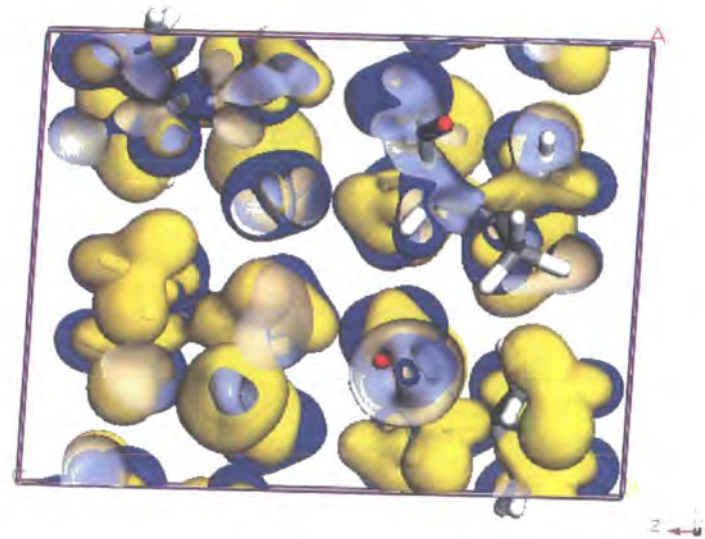

Figure 6.26: L-valine: response of the electronic density to an electric field in the y-direction. Colour convention as in the previous diagram.

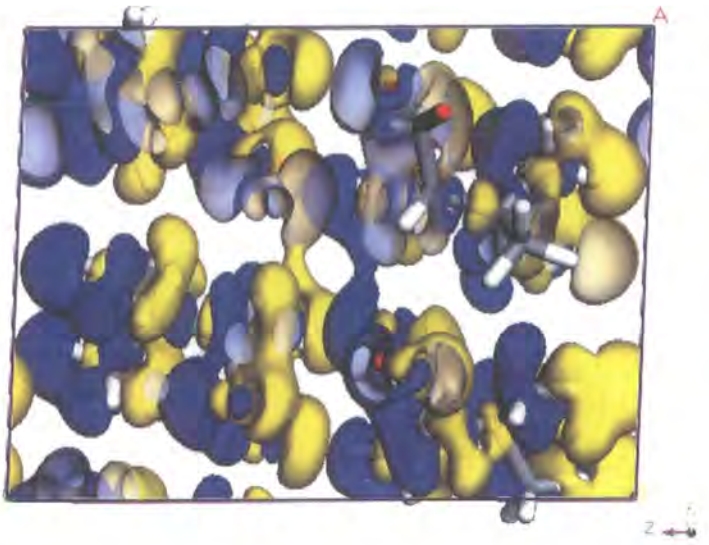

Figure 6.27: L-valine: response of the electronic density to an electric field in the z-direction. Colour convention as before.

rendering an additive approach to molecular polarisabilties difficult to justify.

The normal modes are broadly similar for the non-zwitterionic molecules, and differ significantly from the behaviour observed in the zwitterionic case. This is most clearly seen when one examines the IR spectra for the two distinct cases. In contrast to the dielectric properties, it seems that the most important factor in determining the vibrational behaviour is whether the molecule in question is zwitterionic or not; the different chemical bonds present and the resultant differences in the nature of the hydrogen bonding between the two cases result in very different spectra. Given that the normal modes are a direct reflection of the nature of the chemical bonding present, this is not surprising. The differences in the hydrogen bonding explain the zwitterionisation of leucine.

We have also considered the use of the effective charge as a measure of the charge possessed by the constituent atoms of each molecule, and compared this to charges derived from Mulliken population analysis. We have found that the Mulliken charges are approximately constant from molecule to molecule, independent of zwitterionisation; thus it seems to fail to reflect changes in electronic structure upon zwitteri-

onisation that one would perhaps expect. The effective charges do show a marked change upon zwitterionisation, which reflects the different chemical bonds formed. It seems that agreement between the two is not always obtained, probably because each is obtained from different physical properties.

The normal modes of the molecular crystal forms of the same amino acids have been determined using DFPT. The high frequency vibronic modes are found to be modified by the crystalline environment; this can be explained in terms of the intermolecular hydrogen bonds present between the carboxy and amine functional groups. In L-alanine, the low-lying modes are found to be an admixture of internal and external motions; this is explained by the flexibility of the carbon sidechain, and that these atoms are nearest neighbours to atoms involved in intermolecular interactions. The lowest lattice modes are translational in nature, with some librational modes occurring. The presence of soft phonon modes has been confirmed in L-alanine, raising the possibility of phonon-mediated phase transitions; as mentioned earlier, this is deserving of further detailed investigation. It is likely that such modes occur in the other systems under consideration; however, these have not been pursued due to the limitations imposed upon the accuracy of the lattice dynamical calculations by computational issues.

The other three systems that have been considered display high frequency vibronic modes that have been modified by the hydrogen bonds present. These vibronic modes are associated with stretching of N-H and carbon-oxygen bonds, and always occur at around 3000 cm^{-1}, implying that the hydrogen bonds in all cases are of approximately the same strength. In molecules with a long sidechain, it appears that the low-lying vibronic modes do not couple with the external modes; further the low frequency vibrons do not alter significantly between the crystalline and molecular cases. This is because these vibronic modes are associated with oscillations of the atoms comprising the sidechain, and therefore do not involve intermolecular interactions. The lattice modes are found to be largely libronic in character. The convergence criteria of the calculations with respect to Brillouin zone integration are less than ideal because of computational limitations. The lattice modes are therefore described poorly in comparison to the vibronic modes; it is found that the acoustic sum rule must be imposed explicitly in order to adequately describe these modes. It

would seem therefore that whilst these modes are described adequately qualitatively, that the quantitative description, that is, the actual values of the frequencies, may be inaccurate, and therefore little weight should be put on these numbers.

Examining the IR spectra of the crystals allows the effects of the crystalline environment to be decoupled from those of zwitterionisation. The latter is responsible for peaks occurring in the IR spectra at around 1500 cm^{-1} that do not occur in the non-zwitterionic molecular species; the former, on the other hand, is responsible for the IR-active vibrons at around 3000 cm^{-1}. The crystalline environment is also responsible for fine structure occurring between the major peaks at around 1500 cm^{-1} in L-leucine and L-isoleucine; these can be attributed to wagging of N-H bonds.

The Born effective charges change considerably between the free molecule and the crystal. Determination of the mode effective charge vector suggests that the modification of the high frequency vibrons due to hydrogen bonds is responsible for the changes exhibited by the atoms in the carboxy and amine functional groups. The carbon atoms comprising the sidechain are not involved in intermolecular interactions; thus modifications occurring to these atoms indicate the effect of long-range electric fields arising from the lattice modes upon the effective charges. In L-alanine and L-valine, these indicate that the lattice modes contribute to modifying the long-range fields induced in the crystal. In L-leucine and L-isoleucine, the lattice modes are libronic in character; these do not contribute to the long-range fields set up, and therefore these two crystals have similar values for the effective charges of the sidechain carbon atoms.

The dielectric properties of the molecular crystals have been calculated, and first-order electron densities have been examined in order to investigate the relationship between the response of the constituent molecules in the crystal to an electric field, and that of the isolated molecules. This indicates that, with the exception of L-alanine, the responses appear to be similar. However, modifications occur in the responses of the amino and carboxy functional groups. It would seem that the reason for the differences in the response of alanine molecules in the crystal versus those of isolated molecules is due to the geometrical arrangement of the molecules within the crystal. The molecules are not aligned along one axis of the crystal, in contrast to

the situation prevalent in the other three systems under consideration. Furthermore, the sidechain in L-alanine is short; this allows the molecules to arrange themselves in a three-dimensional percolating network of hydrogen bonds, as discussed in the previous chapter. The close-packing resulting from this means that the sidechain atoms in neighbouring molecules are in close proximity to each other; the result is that the molecular response is perturbed by the intermolecular interactions. In the other systems under consideration, the existence of long sidechains prevents such close packing, ensuring that only the amino and carboxy functional groups can be significantly perturbed. These geometrical arguments are in line with those advanced previously in this chapter concerning the polarisabilities of isolated molecules: the dominant feature appears to be the geometrical structure of the molecule. This implies furthermore that the zwitterionisation of the molecules that occurs upon formation of the crystal plays little part in altering the molecular response. Rather, the governing features appear to be the geometrical arrangement and structure of the molecules in the crystal and the nature of the intermolecular interactions.

Conclusions and Future Work

The aim of this thesis was to implement an efficient density functional perturbation theory algorithm in order to investigate the dielectric and lattice dynamical properties of amino acid molecular crystals and to elucidate the connections between the behaviour of the crystal as a whole and that of the constituent molecules. The amino acids have, to a large degree, been neglected, and relatively few *ab initio* calculation have been carried out on them. Certainly, no work appears to exist on their crystalline forms. Therefore, there was a need to examine using high level theoretical techniques the behaviour of these systems. However, as was outlined in chapter 3, in order to investigate the lattice dynamics and dielectric behaviours of solid state systems requires the use of sophisticated density functional perturbation theory techniques, rather than crude finite difference methods.

The implementation of such a perturbation theory scheme was discussed in depth in chapter 4; it was shown that it is relatively easy to implement such a scheme within the plane wave pseudopotential framework when working within a structured code such as CASTEP. The structure of the DFPT code is such that it is relatively easy to extend; for example, various XC functionals, aside from LDA and GGA could be implemented with only a little effort. Potentially, this allows the inclusion of exact exchange or WDA functionals; such work has not been carried out before, and it would be interesting to investigate how this affects notable shortcomings of the DFPT formalism, such as the overestimation of dielectric permittivity tensors, a failing which is often attributed to shortcomings in the present widely used functionals such as GGAs and LDA. The test results presented provide convincing evidence that DFPT is able to obtain the lattice dynamical and dielectric behaviours of a range of systems, from covalently bonded semiconductors, to molecular systems. Further,

it allows access to quantities that are otherwise difficult to obtain, such as bulk polarisabilities in solids.

A simple extension to DFPT has been presented in order to calculate IR absorption spectra; this allows unambiguous assignment of IR-active modes, and yields insights into the normal modes of the system under consideration. It appears that the IR-active modes and their frequencies are predicted reliably; unfortunately, intensities are sensitive to choice of basis set, and although they are satisfactory for the majority of test systems considered in this work, problem cases, such as methane, do exist. However, DFPT also lends itself naturally to the calculation of Raman spectra. The theory underlying this is slightly more involved, requiring extension of DFPT to cover third-order responses; a methodology for this involving density matrices has been proposed [181]. Obtaining Raman spectra would provide a complementary picture to that provided by IR spectra of the lattice dynamics. Further extensions allowing a richer understanding of the behaviour of condensed matter systems are also conceivable: for example, by extending DFPT to the third order, the effects of anharmonicities and finite phonon lifetimes could be investigated; other extensions involve extending the formalism to include phonon-electron coupling terms. Unfortunately, time constraints have meant that such extensions have been left unexplored; however, they represent potentially fruitful future avenues of research.

In chapters 5 and 6, the structural, electronic, lattice dynamical and dielectric properties of the amino acids in both the solid state and as isolated molecules were obtained. Accurate calculations of the equilibrium geometry adopted by the molecular crystals indicated that the primary intermolecular interaction was hydrogen bonding of a primarily electrostatic nature; furthermore, it is the ability of the molecule to form such bonds that dictates the geometrical structure of the molecule. Formation of these bonds is responsible for the zwitterionisation of the molecules upon forming the crystal. In turn, the structure of these bonds is dictated by the shape of the molecule under consideration.

The presence of these hydrogen bonds is responsible for modifications observed in the high frequency vibronic modes; indeed the low-lying vibronic modes appear to be largely unaffected in the molecular environment. The effects of zwitterionisation

are manifested in the appearance of IR-active modes absent in spectra from non-zwitterionic species; the crystal environment leads to fine structure around these peaks. The character of the lattice modes alters from system to system. The response of the molecules to electric fields is primarily determined by the geometrical structure of the molecule; zwitterionisation is a less significant feature. Correspondingly, the response of the molecular crystal is modified by the presence of hydrogen bonds rather than zwitterionisation, and by the geometrical arrangement and structure of the molecules within the unit cell.

In conclusion, the modifications arising in physical properties between isolated molecules and molecular crystals appear to arise mainly because of intermolecular hydrogen bonds, and the geometrical structure of the molecules themselves. The latter is dominant in determining the response to electric fields; but on a deeper level, it is responsible for the network of intermolecular hydrogen bonds possible, and hence for the arrangement of the molecules within the unit cell.

The work presented in this thesis is by no means an exhaustive investigation into the lattice dynamical and dielectric properties of amino acid molecular crystals. However, it is to be hoped that it represents a firm foundation for deeper and more advanced investigations into these systems. For example, determination of the full phonon dispersion curve is desirable, but unfortunately has been beyond the scope of this study due to computational limitations. Further information on the vibrational behaviour of the systems under consideration could be obtained by theoretical predictions of the Raman spectra; this though requires further developmental work of the DFPT. A knowledge of the full vibrational spectrum would also allow the interplay between the electronic and lattice degrees of freedom, *i.e.* electron-phonon interactions, to be investigated, whilst inclusion of anharmonicities would allow access to finite lifetime phonon phenomena; such anharmonic contributions could be expected to yield useful information on the nature of the hydrogen bonds in these systems. Further fruitful investigations could include a thorough examination of the potential surfaces associated with the lowest phonon modes in order to systematically identify soft phonon modes in these crystals; further, by combining this with similar studies of different phases of the crystals concerned, it may be possible to identify possible phonon-assisted phase transitions and the underlying mechanisms

responsible.

Appendix A

Proof of the $2n+1$-theorem

Consider the expansion of the exact wavefunction

$$\Phi_0(\lambda) = \sum_{i=0}^{\infty} \lambda^i \Phi_0^{(i)} \tag{A.1}$$

and the trial wavefunction

$$\begin{aligned} \Phi_t &= \sum_{i=0}^{n} \lambda^i \Phi_0^{(i)} + \lambda^{n+1} \delta\Phi_t \\ &= \Phi_0(\lambda) - \lambda^{n+1} \Big(\sum_{i=n+1}^{\infty} \lambda^{i-n-1} \Phi_0^{(i)} - \delta\Phi_t \Big). \end{aligned} \tag{A.2}$$

The last equation is exact up to order n. Substituting this last equation into equation 3.14 and using equation A.1 yields

$$\begin{aligned} 0 &\leq \hat{E}_\lambda \Big[\sum_{i=0}^{n} \lambda^i \Phi_0^{(i)} + \lambda^{n+1} \delta\Phi_t \Big] - E_0(\lambda) \\ &\leq K^{2n+2} \Big|\Big| \sum_{i=n+1}^{\infty} \lambda^{i-n-1} \Phi_0^{(i)} - \delta\Phi_t \Big|\Big|^2 \end{aligned} \tag{A.3}$$

which is valid for all $\delta\Phi_t$. Choosing $\delta\Phi_t$ to be zero in particular yields

$$\begin{aligned} 0 &\leq \hat{E}_\lambda\Big[\sum_{i=0}^{n}\lambda^i\Phi_0^{(i)}\Big] - E_0(\lambda) \\ &\leq K^{2n+2}\Big|\Big|\sum_{i=n+1}^{\infty}\lambda^{i-n-1}\Phi_0^{(i)}\Big|\Big|^2 \end{aligned} \tag{A.4}$$

and thus knowledge of the perturbation series of $\Phi_0(\lambda)$ up to an including order n leads to an error in the evaluation of the exact energy of the order λ^{2n+2}. Further, if one considers only terms up to order $2n+1$, then the quantity between the inequality signs is equal identically to zero, and thus one obtains equation ??, which is the familiar $2n+1$-theorem.

If one considers equation A.2 at order $2n+2$, then one obtains

$$\begin{aligned} 0 &\leq \Big\{\hat{E}_{(\lambda)}\Big[\sum_{i=0}^{n}\lambda^i\Phi_0^{(i)} + \lambda^{n+1}\delta\Phi_t\Big]\Big\}^{(2n+2)} - E_0^{(2n+2)} \\ &\leq K||\Phi_0^{(n+1)} - \delta\Phi_t||^2 \end{aligned} \tag{A.5}$$

which is a variational bound for the $(2n+2)$-order derivative of the energy when the wavefunction is known up to order n. Since n is a dummy argument, one can shift to $n-1$, leading to

$$\begin{aligned} 0 &\leq \Big\{\hat{E}_{(\lambda)}\Big[\sum_{i=0}^{n-1}\lambda^{(i)}\Phi_0^{(i)} + \lambda^{n}\delta\Phi_t\Big]\Big\}^{(2n)} - E_0^{(2n)} \\ &\leq K||\Phi_0^{(n)} - \delta\Phi_t||^2 \end{aligned} \tag{A.6}$$

which can be reworked to give equation 3.16. Thus the $2n+1$-theorem and the variational nature of the perturbation expansion of the Kohn-Sham energy functional have been demonstrated.

Appendix B

Treatment of Electronic Screening within the Long-Wave Method

In order to deal with the long-wave limit of an incommensurate perturbation correctly, and deal formally with the issue of screening, the first order potential is written

$$v^{(1)}_{ext,\mathbf{q}}(\mathbf{r},\mathbf{r}') = e^{i\mathbf{q}\cdot\mathbf{r}}\delta(\mathbf{r}-\mathbf{r}') \tag{B.1}$$

which corresponds to the phase factorised local potential

$$\bar{v}^{(1)}_{loc,\mathbf{q}} = 1. \tag{B.2}$$

Noting that one may write

$$\int_{\Omega_0} \bar{n}^{(1)}_{\mathbf{q}}(\mathbf{r})d\mathbf{r} = \Omega_0 \bar{n}^{(1)}_{\mathbf{q}}(\mathbf{G}=\mathbf{0}) \tag{B.3}$$

the variational second order energy can be written

$$E^{(2)}_{el,-\mathbf{q},\mathbf{q}}\{u^{(0)};u^{(1)}\} = \frac{\Omega_0}{(2\pi)^3}\int_{BZ}\sum_{m}^{occ} s\langle u^{(1)}_{m\mathbf{k},\mathbf{q}}|H^{(0)}_{\mathbf{k}+\mathbf{q},\mathbf{k}+\mathbf{q}} - \epsilon^{(0)}_{m\mathbf{k}}|u^{(1)}_{m\mathbf{k},\mathbf{q}}\rangle d\mathbf{k}$$
$$+\frac{\Omega_0}{2}[\bar{n}^{\star(1)}_{\mathbf{q}}(\mathbf{G}=\mathbf{0}) + \bar{n}^{(1)}_{\mathbf{q}}(\mathbf{G}=\mathbf{0})]$$

$$+\frac{1}{2}\int_{\Omega_0}\left.\frac{dv_{xc}}{dn}\right|_{n^{(0)}(\mathbf{r})}|\bar{n}^{(1)}(\mathbf{r})|^2 d\mathbf{r} + 2\pi\Omega_0\sum_{\mathbf{G}}\frac{|\bar{n}^{(1)}(\mathbf{G})|^2}{|\mathbf{q}+\mathbf{G}|^2}. \quad \text{(B.4)}$$

The first order Hamiltonian is then

$$\bar{H}^{(1)}_{\mathbf{q}}(\mathbf{G}) = \delta_{\mathbf{G},0} + 4\pi\frac{\bar{n}^{(1)}_{\mathbf{q}}(\mathbf{G})}{|\mathbf{G}+\mathbf{q}|^2} + \bar{v}^{(1)}_{xc,\mathbf{q}}(\mathbf{G}) \quad \text{(B.5)}$$

which in the limit $\mathbf{q} \to \mathbf{0}$, for $\mathbf{G} = \mathbf{0}$, can be written as

$$\bar{H}^{(1)}_{\mathbf{q}}(\mathbf{G}=\mathbf{0}) = 1 + 4\pi\frac{\bar{n}^{(1)}_{\mathbf{q}}(\mathbf{G}=\mathbf{0})}{|\mathbf{q}|^2}, \quad \text{(B.6)}$$

i.e. in this limit the Hamiltonian consists of the bare potential and the screening due to the Hartree term. Note that the *xc* term may be neglected, as this term is well-behaved in the small $\mathbf{q}$ limit.

The divergence in the Hartree term may be treated as follows. One may define an auxiliary second order energy functional $\tilde{E}^{(2)}_{el,-\mathbf{q},\mathbf{q}}$ which is equal to equation B.4, save for the exclusion of the $\mathbf{G} = \mathbf{0}$ terms. The first order wavefunctions for this functional will be denoted $\tilde{u}^{(1)}_{m,\mathbf{k},\mathbf{q}}$. This functional may be minimised subject to the orthonormality constraints

$$\langle u^{(0)}_{m,\mathbf{k}+\mathbf{q}}|\tilde{u}^{(1)}_{n,\mathbf{k},\mathbf{q}}\rangle = 0 \quad \text{(B.7)}$$

where m and n run over occupied states.

The first order Hamiltonian in the long-wave limit is given by

$$\begin{aligned}\tilde{H}^{(1)}_{\mathbf{q}}(\mathbf{G}) &= 4\pi\frac{\tilde{n}^{(1)}_{\mathbf{q}}(\mathbf{G})}{|\mathbf{G}+\mathbf{q}|^2} + \tilde{v}^{(1)}_{xc,\mathbf{q}}(\mathbf{G}) \qquad \text{when} \quad \mathbf{G} \neq \mathbf{0} \\ &= 1 \qquad \text{when} \quad \mathbf{G} = \mathbf{0}\end{aligned} \quad \text{(B.8)}$$

where

$$\tilde{n}^{(1)}_{\mathbf{q}}(\mathbf{r}) = \frac{2}{(2\pi)^3}\int_{BZ}\sum_{m}^{occ} s u^{\star(0)}_{m\mathbf{k}}\tilde{u}^{(1)}_{m\mathbf{k},\mathbf{q}}(\mathbf{r})d\mathbf{k}. \tag{B.9}$$

It can thus be seen that for $\mathbf{G} = \mathbf{0}$ the screening due to the Hartree term is removed.

At the minimum of both energy functionals, the Sherman-Morrison formula allows one to write:

$$E^{(2)}_{el,-\mathbf{q},\mathbf{q}} = \tilde{E}^{(2)}_{el,-\mathbf{q},\mathbf{q}}\left(1 + \frac{4\pi}{q^2}\bar{n}^{(1)}_{\mathbf{q}}(\mathbf{G}=\mathbf{0})\right) \tag{B.10}$$

which demonstrates that the rate of change of $E^{(2)}_{el,-\mathbf{q},\mathbf{q}}$ with respect to the long wave part of $\bar{H}^{(1)}_{\mathbf{q}}(\mathbf{G}=\mathbf{0})$ (*i.e.* to an electric field), is the same as that of $\tilde{E}^{(2)}_{el,-\mathbf{q},\mathbf{q}}$ to a bare applied field. This allows one to connect the auxiliary problem to the actual physical problem under consideration.

If one now takes the limit that $\mathbf{q} \to \mathbf{0}$, then the zeroth-order and first-order wavefunctions may be expanded as

$$u^{(0)}_{m\mathbf{k}+\mathbf{q}} = u^{(0)}_{m\mathbf{k}} + q\frac{du^{(0)}_{m\mathbf{k}}}{dk_\alpha} + O(q^2) \tag{B.11}$$

and

$$\tilde{u}^{(1)}_{m\mathbf{k},\mathbf{q}} = \tilde{u}^{(1)}_{m\mathbf{k},\mathbf{0}} + q\frac{d\tilde{u}^{(1)}_{m\mathbf{k},\mathbf{0}}}{dq_\alpha} + O(q^2) \tag{B.12}$$

To lowest order in q, the auxiliary functional can be satisfied by taking

$$\tilde{u}^{(1)}_{m\mathbf{k},\mathbf{0}} = 0 \tag{B.13}$$

and thus expansions of $\tilde{n}^{(1)}_{\mathbf{q}}$, $\tilde{v}^{(1)}_{xc,\mathbf{q}}$ and $\tilde{H}^{(1)}_{\mathbf{q}}$ only begin with the term linear in q.

To first order in q, the orthonormality constraint can be expressed as

$$\left\langle u^{(0)}_{m\mathbf{k}} \middle| \frac{d\tilde{u}^{(1)}_{n\mathbf{k},\mathbf{0}}}{dq_\alpha} \right\rangle \tag{B.14}$$

which ensures that the expansion of $\tilde{n}^{(1)}(\mathbf{G}=\mathbf{0})$ only begins at the second order. It also ensures that the expansion of $\tilde{E}^{(2)}_{el,-\mathbf{q},\mathbf{q}}$

$$\tilde{E}^{(2)}_{el,-\mathbf{q},\mathbf{q}} = \tilde{E}^{(2)}_{el,-\mathbf{q},\mathbf{q}}\Big|_{q\to 0} + q\frac{d\tilde{E}^{(2)}_{el,-\mathbf{q},\mathbf{q}}}{dq_\alpha}\Big|_{q\to 0} + \frac{1}{2}q^2\frac{d^2\tilde{E}^{(2)}_{el,-\mathbf{q},\mathbf{q}}}{dq_\alpha^2}\Big|_{q\to 0} \tag{B.15}$$

only begins at second order

$$\tilde{E}^{(2)}_{el,\mathbf{q},\mathbf{q}} = \frac{1}{2}q^2\frac{d^2\tilde{E}^{(2)}_{el,-\mathbf{q},\mathbf{q}}}{dq_\alpha^2}\Big|_{q\to 0}. \tag{B.16}$$

Given the second order expansion of the orthonormality constraint

$$\left\langle u^{(0)}_{m\mathbf{k}}\middle|\frac{d^2\tilde{u}^{(1)}_{n\mathbf{k},\mathbf{0}}}{dq_\alpha^2}\right\rangle + \left\langle \frac{d\tilde{u}^{(0)}_{m\mathbf{k}}}{dk_\alpha}\middle|\frac{d\tilde{u}^{(1)}_{n\mathbf{k},\mathbf{0}}}{dq_\alpha}\right\rangle = 0 \tag{B.17}$$

along with its complex conjugate, the following variational expression can be obtained

$$\begin{aligned}\frac{1}{2}\frac{d^2\tilde{E}^{(2)}_{el,-\mathbf{q},\mathbf{q}}}{dq_\alpha^2}\Big|_{q\to 0}\left\{u^{(0)};\frac{d\tilde{u}^{(1)}}{dq_\alpha}\right\} = {} & \frac{\Omega_0}{(2\pi)^3}\int_{BZ}\sum_m^{occ} s\Bigg(\left\langle\frac{d\tilde{u}^{(1)}_{m\mathbf{k},\mathbf{q}}}{dq_\alpha}\middle|H^{(0)}_{\mathbf{k}+\mathbf{q},\mathbf{k}+\mathbf{q}} - \epsilon^{(0)}_{m\mathbf{k}}\middle|\frac{d\tilde{u}^{(1)}_{m\mathbf{k},\mathbf{q}}}{dq_\alpha}\right\rangle \\ & -\left\langle\frac{d\tilde{u}^{(1)}_{m\mathbf{k},\mathbf{q}}}{dq_\alpha}\middle|\frac{du^{(0)}_{m\mathbf{k}}}{dk_\alpha}\right\rangle - \left\langle\frac{du^{(0)}_{m\mathbf{k}}}{dk_\alpha}\middle|\frac{d\tilde{u}^{(1)}_{m\mathbf{k},\mathbf{q}}}{dq_\alpha}\right\rangle\Bigg)d\mathbf{k} \\ & +\frac{1}{2}\int_{\Omega_0}\frac{dv_{xc}}{dn}\Big|_{n^{(0)}(\mathbf{r})}\left|\frac{d\tilde{n}^{(1)}_{\mathbf{q}}(\mathbf{r})}{dq_\alpha}\right|^2 \\ & +2\pi\Omega_0\sum_{\mathbf{G}\neq\mathbf{0}}\left|\frac{d\tilde{n}^{(1)}_{\mathbf{q}}(\mathbf{G})}{dq_\alpha}\right|^2/|\mathbf{G}|^2\end{aligned} \tag{B.18}$$

and the connection with the equations presented in section 3.8.2 can be made by identifying

$$u^{\varepsilon_\alpha}_{m\mathbf{k}} = \frac{q_\alpha}{i|\mathbf{q}|}\frac{d\tilde{u}^{(1)}_{m\mathbf{k},\mathbf{0}}(\mathbf{r})}{dq_\alpha}. \tag{B.19}$$

Appendix C

Publications

Much of the work submitted in this thesis has been published, or submitted for publication. The references are listed here:

Keith Refson, Paul Tulip and Stewart J. Clark, *Implementation of DFPT within the CASTEP electronic structure code*, to be submitted.

P. R. Tulip and S. J. Clark, *Geometric and Electronic Properties of L-amino Acids*, submitted, Phys. Rev. B.

P. R. Tulip and S. J. Clark, *Dielectric and Vibrational properties of Amino Acids*, J. Chem. Phys. **121**, 5201 (2004).

Work not included in this thesis, but submitted for publication has been included in the following:

Guang Zheng, S. J. Clark, P. R. Tulip, S. Brand and R. A. Abram, *Lattice Dynamics of Poly-para-Phenylene Vinylene: an ab initio study*, submitted.

James A. Chisholm, P. R. Tulip, Simon Parsons and Stewart J. Clark, *An ab initio Study of Observed and Hypothetical Polymorphs of Glycine*, submitted.

Bibliography

[1] Edgar A. Silinsh and V. Capek, *Organic Molecular Crystals: Interaction, Localization and Transport Phenomena*, AIP Press, New York (1994).

[2] G. U. Kulkarni, R. S. Gopalan, and C. N. R. Rao, J. Molec. Struct.: Theochem **500**, 339 (2000).

[3] C. Rovira and J. J. Novoa, J. Chem. Phys. **113**, 9208 (2000).

[4] Yu. A. Abramov, A. V. Volkov and P. Coppens, Chem. Phys. Lett. **311**, 81 (1999).

[5] T. Tada and Y. Aoki, Phys. Rev. B **65**, 113113 (2002).

[6] R. C. Haddon, X. Chi, M. E. Itkis, J. E. Anthony, D. L. Eaton, T. Siegrist, C. C. Mattheus and T. T. M. Palstra, J. Phys. Chem. B **106**, 8288 (2002).

[7] Yu. A. Abramov, A. Volkov, G. Wu and P. Coppens, J. Phys. Chem. B **104**, 2183 (2000).

[8] R. Dovesi, M. Causa', R. Orlando, C. Roetti and V. R. Saunders, J. Chem. Phys. **92**, 7402 (1990).

[9] E. V. Tsiper and Z. G. Soos, Phys. Rev. B **64**, 195124 (2001).

[10] Z. G. Soos, E. V. Tsiper and R. A. Pascal Jr., Chem. Phys. Lett. **342**, 652 (2001).

[11] G. Bussi, A. Runi, E. Molinari, M. J. Caldas, P. Puschnig and C. Ambrosch-Draxl, App. Phys. Lett. **80**, 4118 (2002).

[12] Y. C. Cheng, R. J. Silbey, D. A. da Silva Filho, J. P. Calbert, J. Cornil and J. L. Bredas, J. Chem. Phys. **118**, 3764 (2003).

[13] E. V. Tsiper and Z. G. Soos, Phys. Rev. B **68**, 085301 (2003).

[14] A. Gavezzotti, Current Opinion in Solid State and Materials Science **1**, 501 (1996).

[15] G. R. Desiraju, Current Opinion in Solid State and Materials Science **2**, 451 (1997).

[16] A. Gavezzotti, Mod. Sim. Mat. Sci. Eng. **10**, R1 (2002).

[17] http://www.ornl.gov/sci/techresources/Human_Genome/home.shtml

[18] G. C. Barrett and D. T. Elmore, *Amino Acids and Peptides*, Cambridge University Press, Cambridge (1998).

[19] M. D. Segall, J. Phys.: Condens. Matter **14**, 2957 (2002).

[20] C. Dekker and M. Ratner, Phys. World **14** (2001).

[21] N. C. Greenham, S. C. Moratti, D. D. C. Bradley, R. H. Friend and A. B. Holmes, Nature **365**, 628 (1993).

[22] A. G. Csaszar, J. Mol. Struc. **346**, 141 (1995).

[23] M. T. S. Rosado, M. L. R. S. Duarte and R. Fausto, J. Mol. Stuct. **410-411**, 343 (1997).

[24] A. G. Csaszar, J. Phys. Chem. **100**, 3541 (1996).

[25] A. G. Csaszar, A. Perczel, Prog. Biophys. Mol. Biol. **71**, 243 (1999).

[26] M. Cao, S. Q. Newton, J. Pranata and L. Schäfer J. Mol. Structure: Theochem **332**, 251 (1995).

[27] V. Barone, C. Adamo, F. Lelj, J. Chem. Phys. **102**, 364 (1995)

[28] K. Frimand, H. Bohr, K. J. Jalkanen and S. Suhai, Chem. Phys. **255**, 165 (2000).

[29] G. F. Nobrega, J. R. Sambrano, A. R. de Souza, J. J. Queralt and E. Longo, J. Mol. Struct.: Theochem **544**, 151 (2000).

[30] G. Zheng, J. Z. Hu, X. D. Zhang *et al.*, Acta Chim Sinica, **55**(8), 729 (1997).

[31] Y. He, D. H. Wu, L. F. Shen *et al.*, Magn. Reson. Chem., **33**(9), 701 (1995).

[32] G. R. Desiraju and T. Steiner, *The Weak Hydrogen Bond In Structural Chemistry and Biology*, OUP (1999).

[33] G. A. Jeffrey, *An Introduction to Hydrogen Bonding*, OUP (1997).

[34] T. Steiner and W. Saenger, J. American. Chem. Soc. **115**, 4540 (1993).

[35] C. A. Coulson, *Valence*, Oxford University Press, Oxford (1952).

[36] K. Morakuma, J. Phys. Chem. **55**, 1236 (1971).

[37] P. Hohenberg and W. Kohn, Phys. Rev. **136**, B864 (1964).

[38] W. Kohn and L. J. Sham, Phys. Rev. **140**, A1133 (1965).

[39] M. D. Segall, P. J. D. Lindan, M. J. Probert, C. J. Pickard, P. J. Hasnip, S. J. Clark and M. C. Payne, J. Phys.: Cond. Matt. **14**, 2717 (2002).

[40] M. C. Payne, M. P. Teter, D. C. Allan, T. A. Arias and J. D. Joannopoulos, Rev. Mod. Phys. **64**, 1045 (1992).

[41] M. Born and J. R. Oppenheimer, Ann. Phys. (Leipzig) **84**, 457 (1927).

[42] D. R. Hartree, Proc. R. Soc. London 113, 621 (1928).

[43] J. C. Slater, Phys. Rev. **81**, 385 (1951).

[44] V. Fock, Z. Phys. **61**, 126 (1930).

[45] L. H. Thomas, Proc. Cambridge Philos. Soc.**23**, 542 (1927); E. Fermi, Z. Phys. **48**, 73 (1928).

[46] P. A. M. Dirac, Proc. Cambridge Philos. Soc. **26**, 376 (1930).

[47] R. O. Jones and O. Gunnarsson, Rev. Mod. Phys. **61**, 689 (1989).

[48] J. P. Perdew and Y. Wang, Phys. Rev. B **46**, 12947 (1992).

[49] J. P. Perdew and A. Zunger, Phys. Rev. B **23**, 5048 (1981).

[50] D. M. Ceperley and B. J. Alder, Phys. Rev. Lett. **45**, 566 (1980).

[51] P. P. Rushton, *Towards a Non-local Description of Exchnage and Corrlation*, PhD Thesis, University of Durham (2002).

[52] A. D. Becke, J. Chem. Phys. **38**, 3098 (1988).

[53] J. P. Perdew, K. Burke, and M. Ernzerhof, Phys. Rev. Lett. **77**, 3865 (1996).

[54] J. P. Perdew, K. Burke, and M. Ernzerhof, Phys. Rev. Lett. (E) **78**, 1396 (1997).

[55] N. W. Ashcroft and N. D. Mermin, *Solid State Physics*, Holt Saunders, Philadelphia, p. 113 (1976).

[56] M. D. Segall, J. Phys.: Condens. Matter **14**, 2957 (2002).

[57] J. M. Soler, E. Artacho, J. D. Gale, A. Garcia, J. Junquera, P. Ordejon and D. Sanchez-Portal, J. Phys.: Condens. Matter **14**, 2745 (2002).

[58] D. R. Bowler, T. Miyazaki and M. J. Gillan,J. Phys.: Condens. Matter **14**, 2781 (2002).

[59] S. Goedecker, Rev. Mod. Phys. **71**, 1085 (1999).

[60] H. J. Monkhorst and J. D. Pack, Phys. Rev. B **13**, 5188 (1976).

[61] J. C. Phillips, Phys. Rev. **112**, 685 (1958).

[62] J. C. Phillips and L. Kleinman, Phys. Rev. **116**, 287 (1959).

[63] M. L. Cohen and V. Heine, Solid State Physics **24**, 37 (1970).

[64] L. Kleinman and D. M. Bylander, Phys. Rev. Lett. **4**, 1425 (1982).

[65] S. J. Clark, *Complex Structures in Tetrahedrally Bonded Semiconductors*, PhD Thesis, University of Edinburgh, p. 33 (1994).

[66] D. Vanderbilt, Phys. Rev. B. **41**, 8412 (1990).

[67] Y. Bar-Yam, S. T. Pantelides and J. D. Joannopoulos, Phys. Rev. B **39**, 3396 (1989).

[68] E. Polak, *Computational Methods in Optimisation*, Academic Press, New York (1970).

[69] M. P. Teter, M. C. Payne and D. C. Allan, Phys. Rev. B **40**, 12255 (1989).

[70] S. Baroni, P. Giannozzi and A. Testa, Phys. Rev. Lett. **58**, 1861 (1987).

[71] X. Gonze, Phys. Rev. A **52**, 1086 (1995); X. Gonze, Phys. Rev. A **52**, 1096 (1995).

[72] R. M. Sternheimer, Phys. Rev. **96**, 951 (1954); R. M. Sternheimer, *ibid.* **84**, 244 (1951); and R. M. Sternheimer and H. M. Foley, *ibid.*, **92**, 1460 (1953).

[73] S. Baroni, S. de Gironcoli and A. Dal Corso, Rev. Mod. Phys. **73**, 515 (2001).

[74] S. de Gironcoli, Phys. Rev. B **51**, 6773 (1995).

[75] E. A. Hylleras, Z. Phys. **65**, 209 (1930).

[76] A. Dalgarno and A. L. Stewart, Proc. R. Soc. London Ser. A **238**, 269 (1956).

[77] F. Dupont-Bourdelet, J. Tillieu and J. Guy, J. Phys. Radium **21**, 776 (1960).

[78] O. Sinanoglu, J. Chem. Phys. **34**, 1237 (1961).

[79] X. Gonze and J.-P. Vigneron, Phys. Rev. B **39**, 13120 (1989).

[80] R. P. Feynman, Phys. Rev. **56**, 340 (1939).

[81] X. Gonze and C. Lee, Phys. Rev. B **55**, 10355 (1997).

[82] A. Dalgarno and A. L. Stewart, Proc. R. Soc. London Ser. A **247**, 245 (1958).

[83] X. Gonze, Phys. Rev. B **55**, 10337 (1997).

[84] W. Pickett, Comput. Phys. Rep. **9**, 115 (1989).

[85] P. P. Ewald, Ann. Phys. (Leipzig) **54**, 519 (1917); P. P. Ewald, Ann. Phys. (Leipzig) **54**, 557 (1917); and P. P. Ewald, Ann. Phys. (Leipzig) **64**, 253 (1921).

[86] G. Nenciu, Rev. Mod. Phys. **63**, 91 (1991).

[87] J. Avron and J. Zak, Phys. Rev. B **9**, 658 (1974).

[88] I. Souza, J. Iniguez, and D. Vanderbilt, Phys. Rev. Lett. **89**, 117602 (2002).

[89] R. W. Nunes and X. Gonze, Phys. Rev. B **63**, 155107-1 (2001).

[90] R. W. Nunes and D. Vanderbilt, Phys. Rev. Lett. **73**, 712 (1994).

[91] M. V. Berry, Proc. R. Soc. London, Ser. A **392**, 45 (1984).

[92] J. Zak, Phys. Rev. Lett. **62**, 2747 (1989).

[93] R. Resta, Rev. Mod. Phys. **66**, 899 (1994).

[94] R. Resta, J. Phys.: Condens. Matter **12**, R107 (2000).

[95] P. Y. Yu and M. Cardona, *Fundamentals of Semiconductors: Physics and Materials Properties*, pp 104, Springer-Verlag, Berlin (1996).

[96] R. D. King-Smith and D. Vanderbilt, Phys. Rev. B **47**, 1651 (1993).

[97] P. Ghosez and X. Gonze, J. Phys.: Condens. Matter **12**, 9179 (2000).

[98] G. K. Horton and A. A. Maradudin (eds) *Dynamical Properties of Solids Volume 1*, North-Holland Publishing Company, Amsterdam (1974).

[99] D. H. Williams and I. Fleming *Spectroscopic methods in Organic Chemistry*, McGraw-Hill, London (1980).

[100] P. Giannozzi and S. Baroni, J. Chem. Phys. **100**, 8537 (1994).

[101] P. R. Tulip and S. J. Clark, J. Chem. Phys. **121**, 1501 (2004).

[102] C. Y. Lin, M. W. George and P. M. W. Gill, Aust. J. Chem. **57**, 365 (2004).

[103] D. Porezag and M. R. Pederson, Phys. Rev. B **54**, 7830 (1996).

[104] J. Hafner, J. Mol. Struct. **651-653**, 3 (2003).

[105] A. Alparone, A. Millefiori and S. Millefiori, J. Mol. Struct. (Theochem) **640**, 123 (2003).

[106] L. A. Woodward, *Introduction to the Theory of Molecular Vibrations and Vibrational Spectroscopy*, OUP, London (1972).

[107] H. F. Jones, *Groups Representations and Physics*, IoP, London (1998).

[108] P. Pulay, Mol. Phys. **17**, 197 (1969).

[109] S. Yu. Davrasov, Phys. Rev. Lett. **69**, 2819 (1992).

[110] M. Scheffler, J.-P. Vigneron and G. B. Bachelet, Phys. Rev. B **31**, 6541 (1985).

[111] A. Dal Corso, A. Pasquarello and A. Baldereschi, Phys. Rev. B **56**, R11369 (1997).

[112] A. Dal Corso, Phys. Rev. B **64**, 235118 (2001).

[113] J. Tobik and A. Dal Corso, J. Chem. Phys. **120**, 9934 (2004).

[114] P. Umari, X. Gonze and A. Pasquarello, Phys. Rev. B **69**, 235102 (2004).

[115] K. Refson, P. R. Tulip and S. J. Clark, to be submitted.

[116] C. Parlak and R. Eryigit, Phys. Rev. B **66**, 165201 (2002).

[117] P. Giannozzi and S. Baroni, J. Chem. Phys. **100**, 8537 (1994).

[118] P. Giannozzi and W. Andreoni, Phys. Rev. Lett. **76**, 4915 (1996).

[119] Ph. Ghosez, E. Cockayne, U. V. Waghmare and K. M. Rabe, Phys. Rev. B **60**, 836 (1999).

[120] X. Gonze, D. C. Allan and M. P. Teter, Phys. Rev. Lett. **68**, 3603 (1992).

[121] S. Baroni and R. Resta, Phys. Rev. B **33**, 5969 (1986).

[122] P. Giannozzi, S. de Gironcoli, P. Pavone and S. Baroni, Phys. Rev. B **43**, 7231 (1991).

[123] P. Umari, A. Pasquarello and A. Dal Corso, Phys. Rev. B **63**, 094305 (2001).

[124] A. Putrino *et al* J. Chem. Phys. **113**, 17, 7102 (2000).

[125] J. A. White and D. M. Bird, Phys. Rev. B **50**, 4954 (1994).

[126] C. J. Pickard and M. C. Payne, Phys. Rev. B **62**, 4383 (2000).

[127] M. P. Teter, M. C. Payne and D. C. Allan, Phys. Rev. B **40**, 12255 (1989).

[128] G. Kresse and J. Furthmüller, Phys. Rev. B **54**, 11169 (1996).

[129] A. Putrino, D. Sebasitiani and M. Parrinello, J. Chem. Phys. **113**, 7102 (2000).

[130] R. M. Pick, M. H. Cohen and R. M. Martin, Phys. Rev. B **1**, 910 (1970).

[131] A. A. Maradudin and S. H. Vosko, Rev. Mod. Phys. **40**, 1 (1968).

[132] J. L. Warren, Rev. Mod. Phys. **40**, 38 (1968).

[133] Z. H. Levine and D. C. Allan, Phys. Rev. Lett. **63**, 1719 (1989).

[134] P. Giannozzi, S. de Gironcoli, P. Pavone and S. Baroni, Phys. Rev. B **43**, 7231 (1991).

[135] S. Baroni and R. Resta, Phys. Rev. B **33**, 5969 (1986).

[136] S. Baroni and P. Giannozzi, Phys. Rev. Lett. **58**, 1861 (1987).

[137] R. A. Faulkner, Phys. Rev. **184**, 713 (1969).

[138] H. W. Icenogle, B. C. Platt and W. L. Wolfe, Appl. Opt. **15**, 2348 (1976).

[139] M. S. Hybbertson and S. G. Louie, Phys. Rev. B **35**, 5585 (1987).

[140] X. Gonze, Ph. Ghosez and R. W. Godby, Phys. Rev. B **74**, 4035 (1995).

[141] X. Gonze, Ph. Ghosez and R. W. Godby, Phys. Rev. Lett. **78**, 294 (1997).

[142] X. Gonze, Ph. Ghosez and R. W. Godby, Phys. Rev. Lett. **78**, 2029 (1997).

[143] G. Ortiz, I. Souza and R. M. Martin, Phys. Rev. Lett. **80**, 353 (1998).

[144] W. G. Aulber, L. Jönsson and J. W. Wilkins, Phys. Rev. B **54**, 8540 (1996).

[145] S. J. A. van Gisbergen, P. R. T. Schipper, O. V. Gritensko, E. J. Baerends, J. G. Snijders, B. Champagne and B. Kirtman, Phys. Rev. Lett. **83**, 694 (1999).

[146] X. Gonze, D. C. Allan and M. P. Teter, Phys. Rev. Lett. **68**, 3603 (1992).

[147] F. Gervais and B. Piriou, Phys. Rev. B **11**, 3944 (1975).

[148] F. S. Tautz, V. Heine, M. T. Dove and X. J. Chen, Phys. Chem. Min. **18**, 326 (1991).

[149] J. P. Perdew, K. Burke and M. Ernzerhof, Phys. Rev. Lett. **77**, 3865 (1996).

[150] J. D. Masso, C. Y. She and D. F. Edwards, Phys. Rev. B **1**, 4179 (1970).

[151] M. Prencipe, A. Zupan, R. Dovesi, E. Apra and V. R. Saunders, Phys. Rev. B **51**, 3391 (1995).

[152] S. Froyen and M. L. Cohen, Phys. Rev. B **29**, 3770 (1984).

[153] R. P. Lowndes and D. H. Martin, Proc. R. Soc. London A **308**, 473 91969).

[154] G. Raunio, L. Almqvist and R. Stedman, Phys. Rev. **178**, 1496 (1969).

[155] A. Shukla, Phys. Rev. B **61**, 13277 (2000).

[156] *Handbook of Physics and Chemistry 70th Edition*, CRC Press, Boca Raton (1990).

[157] W. Zhadong,J. Mol. Struct.: THEOCHEM **434**, 1 (1998)

[158] B. J. Costa Cabral and M. L. Costa, J. Mol. Struct.: THEOCHEM **343**, 31 (1995).

[159] D. E. Woon and T. H. Dunning, J. Chem. Phys. **98**, 1358 (1993).

[160] P. Umari, X. Gonze and A. Pasquarello, Phys. Rev. B **69**, 235102 (2004).

[161] Y. Yamaguchi, M. Frisch, J. Gaw, H. F. Schaeffer and J. S. Brinkley, J. Chem. Phys. **84**, 2262 (1986).

[162] S. Shen and J. R. Durig, J. Mol. Struct. **661-662**, 49 (2003).

[163] D. L. Clarke and M. A. Collins, J. Chem. Phys. **86**, 6871 (1987).

[164] P. Pulay and G. Fogarasi, J. Chem. Phys. **74**, 3999 (1981).

[165] H. W. Schranz, http://rsc.anu.edu.au/ harry/ECCC2/Paper36/ (1998).

[166] M. D. Segall, *An ab initio Study of Biological Systems*, PhD Thesis, University of Cambridge (1997).

[167] M. D. Segall, C. J. Pickard, R. Shah and M. C. Payne, Molecular Physics **89**, 571 (1996).

[168] M. D. Segall, R. Shah, C. J. Pickard and M. C. Payne, Phys. Rev. B **54**, 16317 (1996).

[169] D. Sanchez-Portal, E. Artacho and J. M. Soler, J. Phys.: Condens. Matter **8**, 3859 (1996).

[170] D. Sanchez-Portal, E. Artacho and J. M. Soler, Solid State Communications **95**, 685 (1995).

[171] R. S. Mulliken, J. Chem. Phys. **23**, 1833 (1955).

[172] R. J. Gdanitz, Current Opinion in Solid State and Materials Science **3**, 414 (1998).

[173] H. J. Simpson and R. E. Marsh, Acta Crystallogr., **20**, 550 (1966).

[174] M. Coll *et al.*, Acta Crystallogr. Sect. C: Cryst. Struct. Comm, **42**, 599 (1986).

[175] C. H. Gorbitz and B. Dalhus, Acta Crystallogr. Sect. C: Cryst. Struct. Comm, **52**, 1464 (1996).

[176] B. Dalhus and C. H. Gorbitz, Acta Chem. Scand., **50**, 544 (1996).

[177] A. G. Csaszar, J. Phys. Chem. B, **100**, 3541 (1996).

[178] G. Venkatarman and V. L. Sahni, Rev. Mod. Phys. **42**, 409 (1970).

[179] G. K. Horton and A. A. Maradudin (eds) *Dynamical Properties of Solids Volume 2*, pp 153, North-Holland Publishing Company, Amsterdam (1974).

[180] M. Plazanet, M. R. Johnson, J. D. Gale, Y. Yildirim, G. J. Kearley, M. T. Fernandez-Diaz, D. Sanchez-Portal, E. Artacho, J. M. Soler, P. Ordejohn, A. Garcia and H. P. Trommsdorff, Chem. Phys. **261**, 189 (2003).

[181] M. Lazzeri and F. Mauri, Phys. Rev. B **68**, 161101 (2003).